SEDIMENT-ASSOCIATED CONSTITUENT RELEASE AT THE MUD-WATER INTERFACE DUE TO MONOCHROMATIC WAVES

By

YIGONG LI

A DISSERTATION PRESENTED TO THE GRADUATE SCHOOL
OF THE UNIVERSITY OF FLORIDA IN PARTIAL FULFILLMENT
OF THE REQUIREMENTS FOR THE DEGREE OF
DOCTOR OF PHILOSOPHY

UNIVERSITY OF FLORIDA

1996

ACKNOWLEDGMENT

First of all, I would like to express my deepest gratitude to my advisor and the chairman of my supervisory committee Professor Ashish J. Mehta, for his constructive direction, enthusiasm, advice and unflagging support throughout this four year study, which has been a challenging, joyful and unforgettable experience in my life.

I wish to thank Professors Kirk Hatfield and Robert G. Dean for their continuously valuable advice, suggestions and discussions. Thanks are also due to the other committee members, including Professor Peter Y. Sheng and Professor Brij M. Moudgil for their advice, comments and patience in reviewing this dissertation.

Appreciation is extended to all other faculty members in the department, as well as those in the Department of Aerospace Engineering Mechanics and Engineering Science, Civil Engineering, Agricultural Engineering, Soil Science and Chemical Engineering for supplying various components of knowledge essential for the pursuit of this study through their creative teaching efforts.

Gratitude is due to departmental staff, especially, Mr. Sydney Schofield, Mr. Jim Joiner and Mr. George Chappell at the Coastal Engineering Laboratory for their coorperation and help during the experimental phase of this research. Support also came from many friends and fellow research assistants.

Special thanks go to Sandra Bivins, Becky Hudson, Lucy Hamm, Cynthia Vey, John Davis and Helen Twedell for their kindness, which helped directly or indirectly in the completion of this study. Deep appreciation goes to Dr. Feng Jiang, Dr. Xinjian Chen and Dr. Say-Chong Lee, with whose help I got through the hard initial period of my stay in Gainesville. Appreciation also goes to Mr. Paul Devine, Mr. Ahmad Tarigan, Mr. Hogo Rodriguez, Ms. Xu Wang, Ms. Jie Zheng, Dr. Taerim Kim, Mr. Eduardo Yassuda, Mr. Mike Krecic and Mr. Albert Browder for their assistance and useful discussions.

Funding for this work came from U.S. Army Engineer Waterways Experiment Station at Vicksburg, Mississippi. The contaminant portion of the work was funded by contract DACW39-95-K-0023 through the Environmental Laboratory, and the sediment part by contract DACW39-95-K-0022 through the Hydraulics Laboratory. Assistance provided especially by Dr. Mark Dortch and Dr. T.M. Parchure in processing the contracts, managing them and providing valuable technical guidance is sincerely acknowledged.

My final acknowledgement is reserved for those whom I probably owe the most, my wife, Wendy S. Tan, for her love, support, encouragement and patience throughout these four years, and my parents, who instilled in me the work ethic and values that have allowed me to make it this far, and have supported me all my life.

TABLE OF CONTENTS

ACKNOWLEDGMENT ii

LIST OF FIGURES viii

LIST OF TABLES xiii

LIST OF SYMBOLS xv

ABSTRACT xxx

1 INTRODUCTION 1
1.1 Problem Statement 1
1.2 Objective, Tasks and Scope 5
1.3 Outline of Presentation 7

2 BACKGROUND INFORMATION 9
2.1 Introduction 9
2.2 Mud Rheology and Wave-Mud Interaction Modeling 9
2.2.1 Mud Rheology 10
2.2.2 Wave-Mud Interaction Modeling 19
2.3 Mud Fluidization and Fluid Mud 23
2.4 Processes Governing the Vertical Structure of Suspension 28
2.4.1 Settling 28
2.4.2 Diffusion 31
2.4.3 Deposition Rate 35
2.4.4 Entrainment 36
2.5 Sorption Models 40
2.5.1 Equilibrium Sorption Isotherm 40
2.5.2 Kinetic Sorption Models 43
2.5.3 Advanced Sorption Models 46
2.6 Sediment-Associated Contaminant Transport 49
2.6.1 Contaminant Transport in Water 49
2.6.2 Contaminant Transport in Bottom Sediment 52
2.6.3 Fluxes Across the Sediment-Water Interface 58

2.6.4 Fluxes Across the Fluid Mud-Bed Interface 62

3 MUD FLUIDIZATION BY WAVES 64
3.1 Introduction 64
3.2 Mechanics of Fluidization 65
3.2.1 Vertical and Horizontal Motions of Bed under Waves 65
3.2.2 Bed Failure by Horizontal Forces 66
3.2.3 Bed Fluidization by Vertical Forces 68
3.2.4 A Heuristic Criterion for Bed Fluidization Under Waves 70
3.3 Voigt and Extensional-Voigt Models 72
3.4 Bed as a Spring-Dashpot-Mass System 74
3.4.1 Case 1: G_n, and μ_n Independent of Depth 75
3.4.2 Case 2: G_n, and μ_n Increase with Depth 77
3.5 Dynamic Response of Bed 79
3.5.1 Wave over Bed: One-Degree of Freedom 79
3.5.2 Wave over Fluid Mud above Bed: Two-Degrees of Freedom 80
3.6 Fluidization Depth 83
3.6.1 Model Results 83
3.6.2 Comparison with Data 90
3.7 Application to Field Data 93
3.7.1 Field Conditions 93
3.7.2 Model Application 96
3.8 Conclusions 99

4 SEDIMENT TRANSPORT MODELING 102
4.1 Introduction 102
4.2 Three-Layered System 102
4.3 Wave-Averaged Transport Equation for Constituent Transport 103
4.4 Sediment Transport Model 107
4.4.1 Vertical Fine-grained Sediment Transport Equation 107
4.4.2 Boundary Conditions 110
4.5 Fluid Mud Entrainment Rate 112
4.5.1 Entrainment Rate Formulation 112
4.5.2 Laboratory Experiment 115
4.5.3 Critical Global Richardson Number for Entrainment 118
4.5.4 Comparison with Experimental Data 124
4.6 Laboratory Simulations 128
4.7 Model Application to Field Data 132
4.7.1 Coast of Louisiana 133
4.7.2 Southwest Coast of India 142

5 SORPTION KINETICS 152
5.1 Introduction 152

5.2 Dyes, Sediments and Fluid Characteristics 153
5.3 Sorption Test Procedure 155
5.3.1 Sampling of Sediment-Dye-Water Mixture 155
5.3.2 Photographic Method for Dye Concentration Determination in Water 156
5.3.3 Calibration Experiments 158
5.4 Results and Discussion 160
5.4.1 Sorption Isotherms 160
5.4.2 Sorption Kinetics 164
5.4.3 Discussion 169

6 CONSTITUENT TRANSPORT MODELING 174
6.1 Introduction 174
6.2 Constituent Transport Model 174
6.2.1 Formulation 174
6.2.2 Governing Equations 176
6.2.3 Boundary and Interfacial Connective Conditions 178
6.3 Wave-Induced Diffusivity in Fluid Mud, K_{22} 184
6.4 Mass Transfer Coefficient, K_{12c} 190
6.5 Solution Technique 196

7 FLUME EXPERIMENTS 198
7.1 Introduction 198
7.2 Experimental Equipment 198
7.2.1 Wave Flume 198
7.2.2 Colorimeter 199
7.3 Test Conditions and Procedure 204
7.3.1 Test Conditions 204
7.3.2 Procedure 204
7.4 Data Analysis 206
7.4.1 Suspended Sediment 206
7.4.2 Dye Release in Water 215

8 RESULTS, DISCUSSION AND CONCLUSIONS 225
8.1 Introduction 225
8.2 Results of Model Simulations and Calibrations 225
8.2.1 Model Conditions 225
8.2.2 Suspended Sediment Concentrations 230
8.2.3 Dye Concentrations 233
8.3 Analysis and Discussion 238
8.3.1 Release Flux and Sub-fluxes 238
8.3.2 Effects on Release Sub-fluxes 243
8.4 Summary and Conclusions 250

8.5 Recommendations for Future Studies 254

APPENDICES

A FLUME EXPERIMENTAL DATA 257

B SIMULATED AND MEASURED SUSPENDED SEDIMENT AND DYE CONCENTRATION PROFILES 269
B.1 Suspended Sediment Profiles 269
B.2 Dye Concentration Profiles in Water 280

BIBLIOGRAPHY 296

BIOGRAPHICAL SKETCH 313

LIST OF FIGURES

1.1 Total contaminant flux and sub-fluxes. 2
2.1 Common two-parameter viscoelastic models. 13
2.2 Jeffrey models. 14
2.3 A typical wave-mud system (after Hwang, 1989) 23
2.4 Schematic of instantaneous stress profile in a wave-mud system (after Mehta et al., 1994). 24
2.5 Three-layered water-fluid mud-bed system and vertical sediment transport processes under waves. 25
2.6 A schematic description of settling velocity and flux variation with suspension concentration (after Hwang, 1989). 29
2.7 Sediment-associated contaminant transport processes. 49
3.1 Forces on a particle or floc. 68
3.2 Bed simulated as a S-D-M system with known vertical distributions of bed density, ρ, extensional elastic modulus, G_n, and extensional viscous coefficient, μ_n. ... 74
3.3 Bed layer represented by a one-degree of freedom system. 80
3.4 Fluid mud and bed layers represented by a two-degrees of freedom system. 81
3.5 A schematic description of the criterion for equilibrium fluidization depth, z'_e. ... 83
3.6 Fluidization depth variation with wave frequency and amplitude with negligible cohesion and without considering initial fluid mud effects. 84
3.7 Fluidization depth variation with wave frequency and bed elastic modulus with negligible cohesion and without considering initial fluid mud effects. ... 85
3.8 Fluidization depth variation with wave frequency and bed viscous coefficient with negligible cohesion and without considering initial fluid mud effects. 85
3.9 Fluidization depth variation with wave frequency and amplitude with negligible cohesion, but including initial fluid mud effects. 87
3.10 Fluidization depth variation with wave frequency and bed elastic modulus with negligible cohesion, but including initial fluid mud effects. 87
3.11 Fluidization depth variation with wave frequency and bed viscous coefficient with negligible cohesion, but including initial fluid mud effects. 88
3.12 Fluidization depth variation with wave frequency and cohesion parameter. 89
3.13 Comparison between calculated and flume-measured fluidization depths. 92
3.14 Bathymetric map of Lake Okeechobee. Depth are relative to a datum which is 3.81 m above msl (after Mehta and Jiang, 1990). 94
3.15 Mud thickness contour map of Lake Okeechobee (after Kirby et al., 1989). 95
3.16 A representative bottom mud density profile in Lake Okeechobee. 97

3.17 Calculated fluidization depth as a function of water depth in Lake Okeechobee and band of measured values. 98
3.18 An example of fluidization depth calculation for Lake Okeechobee at a site where water depth was 1.43 m. 98
4.1 Three-layered system and vertical sediment transport processes considered. 102
4.2 Side view of wave flume used in entrainment experiments. 115
4.3 Critical Richardson Number for entrainment by waves. 121
4.4 Critical Richardson Number estimated from the experiments of Maa (1986). 121
4.5 Dimensionless entrainment rate as a function of Richardson Number. 125
4.6 Entrainment flux as a function of wave height and mud viscosity. 127
4.7 Comparison between simulated and measured data for Run 4 of Maa (1986). 130
4.8 Comparison between simulated and measured data for Run 5 of Maa (1986). 130
4.9 Comparison between simulated and measured data for Run 6 of Maa (1986). 131
4.10 Location map of the study area of Kemp (1986). 135
4.11 Simulated and measured data (Kemp, 1986) for the Louisiana coast during frontal passage. 139
4.12 Simulated and measured data (Kemp, 1986) for the Louisiana coast during the post-frontal period. 140
4.13 Location map of the study area of Mathew (1992) off Alleppey in the State of Kerala, India. 143
4.14 A conceptual model of mudbank evolution 143
4.15 Settling velocity data used for mudbank turbidity simulation. 150
4.16 Simulated suspended sediment concentration profiles and data of Mathew (1992) in the vicinity of Alleppey Pier. 151
5.1 Schematic diagram of the sorption procedure. 156
5.2 Schematic diagram for photography in sorption tests. 157
5.3 Procedure for determining dye concentration 157
5.4 Calibration curve for Rhodamine B solutions. 159
5.5 Calibration curve for Erioglaucine A solutions. 160
5.6 Linear isotherm of Rhodamine B sorbed onto kaolinite. 161
5.7 Linear isotherm of Rhodamine B sorbed onto AK mud. 161
5.8 Linear isotherm of Erioglaucine A sorbed onto kaolinite. 162
5.9 Linear isotherm of Erioglaucine A sorbed onto AK mud. 163
5.10 Effect of temperature on sorption of Rhodamine B on kaolinite 163
5.11 Comparison between kinetic sorption model and experimental data. 167
5.12 Comparison between kinetic sorption model and experimental 167
5.13 Comparison between kinetic sorption model and experimental data. 168
5.14 Comparison between kinetic model and experimental results. 168
5.15 Comparison between kinetic sorption model and experimental data. 169
5.16 Chemical structures of Rhodamine B and Erioglaucine A. 169
5.17 Idealized clay geometries of kaolinite and attapulgite. 170
6.1 Sediment-associated contaminant transport processes considered. 175
6.2 Contaminant fluxes across the water-fluid mud and fluid mud-bed interfaces. 179

6.3 Schematic representation of the mode of indirect dissolved and particulate contaminant transport across the water-mud interface 183
6.4 Schematic of energy transport and dissipation, velocity distribution and momentum transport, and constituent concentration distribution and momentum-analogous constituent mass transport. 188
6.5 Schematic shown of bottom diffusive sub-layer and wave boundary layer in water, and direct convective flux. 191
7.1 Wave flume used in experiments. 199
7.2 Relationship between incident wave length and transmittance for Rhodamine B. . 201
7.3 Relationship between incident wave length and transmittance for Erioglaucine A. 201
7.4 Calibration of Rhodamine B concentration with selected light wave length, L_{RB} = 550 nm. 202
7.5 Calibration of Erioglaucine A concentration with selected light wave length, L_{EA} = 625 nm. 202
7.6 Suspended sediment concentration profile variations with time at B, C and D in the duration range of 240 ~ 480 minutes. 207
7.7 Suspended sediment concentration profile variations with time at A and E in the duration range of 240 ~ 480 minutes. 208
7.8 Suspended sediment concentration profile variations with time at B, C and D in the duration range of 480 ~ 720 minutes. 209
7.9 Suspended sediment concentration profile variations with time at A and E in the duration range of 480 ~ 720 minutes. 210
7.10 Comparison between the calculated suspended sediment concentration using three methods (Eqs. 7.7, 7.10 and 7.11). 214
7.11 Dye concentration profile variations with time at B, C and D in the duration range of 0 ~ 240 minutes. 215
7.12 Dye concentration profile variations with time at A and E in the duration range of 0 ~ 240 minutes. 217
7.13 Dye concentration profile variations with time at B, C and D in the duration range of 240 ~ 480 minutes. 218
7.14 Dye concentration profile variation with time at A and E in the duration range of 240 ~ 480 minutes. 219
7.15 Dye concentration profile variations with time at B, C and D in the duration range of 480 ~ 720 minutes. 220
7.16 Dye concentration profile variations with time at B, C and D in the duration range of 480 ~ 720 minutes. 221
7.17 Comparison between calculated dye concentration using three methods (Eqs. 7.12, 7.15 and 7.16). 223
8.1 Comparison between simulated and measured depth-averaged suspended sediment concentrations in Test 2. 230
8.2 Comparison between simulated and measured depth-averaged suspended sediment concentrations in Test 3. 231

8.3 Comparison between simulated and measured depth-averaged suspended sediment concentrations in Test 4. 231
8.4 Comparison between simulated and measured depth-averaged suspended sediment concentrations in Test 5. 232
8.5 Comparison between simulated and measured depth-averaged suspended sediment concentrations in Test 6. 232
8.6 Comparison between simulated and measured depth-averaged dye concentrations in Test 1. 235
8.7 Comparison between simulated and measured depth-averaged dye concentrations in Test 2. 235
8.8 Comparison between simulated and measured depth-averaged dye concentrations in Test 3. 236
8.9 Comparison between simulated and measured depth-averaged dye concentrations in Test 4. 236
8.10 Comparison between simulated and measured depth-averaged dye concentrations in Test 5. 237
8.11 Comparison between simulated and measured depth-averaged dye concentrations in Test 6. 237
8.12 Dye release flux and sub-fluxes in Tests 1-1 (0~240 min) and 1-2 (240~480 min). 238
8.13 Dye release flux and sub-fluxes in Tests 2-1(0~240 min), 2-2 (240~480 min) and 2-3 (480~600 min). 239
8.14 Dye release flux and sub-fluxes in Tests 3-1 (0~240 min) and 3-2 (240~480 min). 239
8.15 Dye release flux and sub-fluxes in Test 4 (0~720 min). 240
8.16 Dye release flux and sub-fluxes in Tests 5-1(0~240 min), 5-2 (240~480 min) and 5-3 (480~600 min). 240
8.17 Dye release flux and sub-fluxes in Tests 6-1(0~240 min), 6-2 (240~480 min) and 6-3 (480~600 min). 241
8.18 Schematic shown characteristic profiles and coefficients related to release fluxes. 244
8.19 Relationship between the direct convective flux coefficient, α_{12c}, and the bottom boundary layer Richardson Number, Ri_w. 246
8.20 Relationship between dimensionless diffusivity in fluid mud, D_f/ν_1, and the dimensionless wave damping parameter, $H^2k_i/(h_2-h_1)$ 248
B.1 Comparison between simulated and measured suspended sediment profiles in Test 2-2. 269
B.2 Comparison between simulated and measured suspended sediment profiles in Test 2-3. 270
B.3 Comparison between simulated and measured suspended sediment profiles in Test 3-2. 271
B.4 Comparison between simulated and measured suspended sediment profiles In Test 3-3. 272

B.5 Comparison between simulated and measured suspended sediment profiles in Test 4-1 during time range of 0 ~ 300 min. 273
B.6 Comparison between simulated and measured suspended sediment profiles in Test 4-1 during time range of 300 ~ 660 min. 274
B.7 Comparison between simulated and measured suspended sediment profiles in Test 5-2 during time range of 240 ~ 480 min. 275
B.8 Comparison between simulated and measured suspended sediment profiles in Test 5-3 during time range of 480 ~ 720 min. 276
B.9 Comparison between simulated and measured suspended sediment profiles in Test 6-1 during time range of 0 ~ 240 min. 277
B.10 Comparison between simulated and measured suspended sediment profiles in Test 6-2 during time range of 240 ~ 480 min. 278
B.11 Comparison between simulated and measured suspended sediment profiles in Test 6-3 during time range of 480 ~ 720 min. 279
B.12 Comparison between simulated and measured dye profiles in Tests 1-1. 280
B.13 Comparison between simulated and measured dye profiles in Tests 1-2. 281
B.14 Comparison between simulated and measured dye profiles in Tests 2-1. 282
B.15 Comparison between simulated and measured dye profiles in Test 2-2. 283
B.16 Comparison between simulated and measured dye profiles in Test 2-3. 284
B.17 Comparison between simulated and measured dye profiles in Test 3-1. 285
B.18 Comparison between simulated and measured dye profiles in Test 3-2. 286
B.19 Comparison between simulated and measured dye profiles in Test 3-3 287
B.20 Comparison between simulated and measured dye profiles in Test 4 during time range of 0 ~ 300 min. 288
B.21 Comparison between simulated and measured dye profiles in Test 4 during time range of 300 ~ 660 min. 289
B.22 Comparison between simulated and measured dye profiles in Test 5-1 during time range of 0 ~ 240 min. 290
B.23 Comparison between simulated and measured dye profiles in Test 5-2 during time range of 240 ~ 480 min. 291
B.24 Comparison between simulated and measured dye profiles in Test 5-3 during time range of 480 ~ 720 min. 292
B.25 Comparison between simulated and measured dye profiles in Test 6-1 during time range of 0 ~ 240 min. 293
B.26 Comparison between simulated and measured dye profiles in Test 6-2 during time range of 240 ~ 480 min. 294
B.27 Comparison between simulated and measured dye profiles in Test 6-3 during time range of 480 ~ 720 min. 295

LIST OF TABLES

2.1 Diffusion coefficients for some tracers in some typical marine mud beds. 57
3.1 Wave and bed conditions and calculated and measured fluidization depths. 91
3.2 Summary of selected fluid mud generation experiments in flumes from Ross(1988) and Lindenberg et al. (1989). 91
3.3 Flume tests of Lindenberg et al. (1989) without fluid mud generation 93
4.1 Experimental results for determination of the critical entrainment condition. 117
4.2 Equilibrium depth-averaged suspended sediment concentrations for specified wave conditions. 119
4.3 Parameters for simulating Runs 4, 5 and 6 of Maa (1986). 134
4.4 Measured wave and suspended sediment data from Louisiana coast (based on Kemp, 1986). 136
4.5 Parameters for simulating data from the Louisiana coast. 138
4.6 Parameters for simulating field data of Mathew (1992) from the southwest coast of India. 147
5.1 Physical and chemical properties of Rhodamine B and Erioglaucine A. 153
5.2 Chemical compositions of kaolinite and attapulgite (%). 154
5.3 Chemical composition of tap water. 155
5.4 Equilibrium sorption distribution coefficient, K_d (l/g) 161
5.5 First order rate coefficient for sorption kinetics. 172
7.1 Tests Conditions 203
8.1 Characteristic parameters for modeling of Tests 1 and 2. 227
8.2 Characteristic parameters for modeling of Tests 3 and 4. 228
8.3 Characteristic parameters for modeling for Tests 5 and 6. 229
A.1 Sediment concentration (g/l) data for Test 1 257
A.2 Sediment concentration (g/l) data for Test 2 257
A.3 Sediment concentration (g/l) data for Test 3 258
A.4 Sediment concentration (g/l) data for Test 4 259
A.5 Sediment concentration (g/l) data for Test 5 259
A.6 Sediment concentration (g/l) data for Test 6 260
A.7 Dye concentration (mg/l) data for Test 1 261
A.8 Dye concentration (mg/l) data for Test 2 262
A.9 Dye concentration (mg/l) data for Test 3 263
A.10 Dye concentration (mg/l) data for Test 4 265
A.11 Dye concentration (mg/l) data for Test 5 266
A.12 Dye concentration (mg/l) data for Test 6 267

A.13 Temperature mesurements (°C). 268

LIST OF SYMBOLS

A_e = Empirical coefficient

a_b = Amplitude of near-bed wave-induced horizontal excursion

B = Coefficient in relationship between constituent concentration and light intensity

B', B'' = Characteristic coefficients in relationship between constituent concentration and light intensity

C, C_d = Constituent concentration in water

C_b = Constituent concentration just outside the bottom diffusive layer in water

C_{eq} = Constituent concentration in water at equilibrium

C_{d0} = Initial constituent concentration in water

C_{1d} = Constituent concentration in water layer

C_{2d} = Constituent concentration in pore water in fluid mud

C_{3d} = Constituent concentration in pore water in bed

$C_{d\infty}$ = Final or equilibrium constituent concentration in water

C_F = Consolidation coefficient

C_h = Cohesion

C_r = Shear resistance

C_s = Constituent concentration at mud-water interface

$\hat{C}_i$ = Concentration of component i

$\overline{C}$ = Time-averaged constituent concentration

$\overline{C_A}$ = Depth-averaged dye concentration in water at location A

$\overline{C_B}$ = Depth-averaged dye concentration in water at location B

$\overline{C_C}$ = Depth-averaged dye concentration in water at location C

$\overline{C_D}$ = Depth-averaged dye concentration in water at location D

$\overline{C_E}$ = Depth-averaged dye concentration in water at location E

$\overline{C_m}$ = Depth-average dye concentration in water over mud trench

$\overline{C_O}$ = Depth-averaged dye concentration in water beyond mud trench

$\overline{C_t}$ = Average suspended sediment concentration

$\tilde{C}$ = Wave oscillating part of constituent concentration

C' = Turbulent fluctuation part of constituent concentration

c_e = Equivalent viscous coefficient

c_2 = Equivalent viscous coefficient of fluid mud

c_3 = Equivalent viscous coefficient of bed

$c_{a0.5}$ = Sediment concentration at about one-half water depth at location A

$c_{b0.5}$ = Sediment concentration at about one-half water depth at location B

$c_{c0.5}$ = Sediment concentration at about one-half water depth at location C

$c_{d0.5}$ = Sediment concentration at about one-half water depth at location D

$c_{e0.5}$ = Sediment concentration at about one-half water depth at location E

c_* = Constant coefficient

D = Diameter of particle or floc

D_e = Empirical coefficient

D_f = Wave-induced diffusivity in fluid mud

D_m = Molecular diffusivity

D_i, $\hat{D}_i$ = Diffusion coefficients of component i

D_r = Sediment deposition flux

d = Bed thickness

d_1, d_2 = Empirical coeffcients

d_e = Effective grain size

E_{ij} = Strain tensor

E_r = Sediment entrainment flux

E_* = Non-dimensional entrainment rate

E'_0 = Amplitude of E'_{ij}

E'_{ij} = Deviatoric components of strain

$\hat{E}_w$ = Non-dimensional entrainment rate

e = Void ratio

F = Static force

F_1, F_2, F_3, F_4 = Normal forces from adjacent particles

F_{12m} = Molecular diffusive flux of constituent

F_{12c} = Direct convective flux of constituent

F_{12d} = Indirect convective flux of constituent

F_{12e} = Indirect convective flux of constituent associated with entrainment

F_{12p} = Particle-bound flux of constituent

F_{12s} = Indirect convective flux of constituent associated with settling

F^{s}_{12e} = Particle-bound flux of constituent associated with entrainment

F^{s}_{12s} = Particle-bound flux of constituent associated with settling

F_A = Advective flux

F_D = Diffusive flux

F_d = Sediment diffusive flux in water

F_i = Mass flux of component i

F_p = Sediment deposition flux

F_r = Sediment flux corresponding to the fraction of entrained sediment that is returned to fluid mud by deposition

F'_r = Sediment flux corresponding to the fraction of "settled" sediment that is entrained into water

F_s = Sediment settling flux in water

f = Wave frequency (= $\omega/2\pi$)

f_1, f_2, f_3, f_4 = Shear forces from adjacent particles

fr = Fraction of sediment exchange between water and fluid mud

f_{nc} = Bottom friction coefficient

G = Elastic modulus

G_1, G_2 = Elastic moduli in standard solid model

G_n = Extensional elastic modulus

G^r = Bed rigidity

G' = Elastic energy storage modulus

G'' = Viscous energy dissipation modulus

G^* = Complex shear modulus

g = Gravitational acceleration

g' = Effective gravitational acceleration

H = Wave height

H_s = Significant wave height

H_{rms} = Root mean square wave height

h_1 = Depth of water layer

h_2 = Depth of water and fluid mud

h_3 = Total depth of water, fluid mud and bed layers

h_k = Thickness of clay particles

I = Light intensity through a fluid medium

I_0 = Light intensity through clear water

I_A = Hue value of Erioglaucine A

I_B = Hue value of Rhodamine B

II_D = Second invariant of E'_{ij}

J_0 = Instantaneous compliance

J_i = Diffusive flux of component i

J_{Ma} = Mass flux in fluid mud

J_{Mo} = Momentum flux in fluid mud

J_t = Total mass flux in fluid mud

K = Coefficient in relationship between constituent concentration and light intensity

K_m = Ratio of floc volume concentration to sediment concentration

K_{12c} = Convective mass transfer coefficient

K_d = Constituent distribution coefficient

K_n = Neutral mass diffusivity

K_x = Diffusivity in x-direction

K_y = Diffusivity in y-direction

K_z = Diffusivity in z-direction

K_{z1} = Diffusivity in z-direction in water

K_{z2} = Diffusivity in z-direction in fluid mud

K_{z3} = Diffusivity in z-direction in bed

K', K'' = Characteristic constants in releationship between constituent concentration and light intensity

k = Wave number

k_2 = Equivalent elasticity of fluid mud

k_3 = Equivalent elasticity of bed

k_c = Convective mass transfer coefficient under current

k_e = Equivalent elasticity

k_i = Wave damping coeficient or imaginery part of complex wave number

k_i = Wave number or real part of complex wave number

k_w = Permeability

k_y = Yield strength

$k'_{i(i=1\sim8)}$ = Empirical coefficients

L_A = Length range represented by flume location A

L_B = Length range represented by flume location B

L_C = Length range represented by flume location C

L_c = Cohesive resistance

L_D = Length range represented by flume location D

L_E = Length range represented by flume location E

L_{EA} = Optimal light wave length for Rhodamine B dilution

L_i = Inertial force

L_{mt} = Length of mud trench

L_{RB} = Optimal light wave length for Erioglaucine A dilution

M_f = Empirical coefficient

m_p = Particle mass

m_e = Equivalent mass

m_2 = Equivalent mass of fluid mud

m_3 = Equivalent mass of bed

n = Porosity

n_1 = Porosity in water layer

n_2 = Porosity in fluid mud

n_3 = Porosity in bed

n_m = Manning's bed resistance coefficient

P = Constituent concentration sorbed on sediment

P_0 = Initial constituent concentration sorbed on sediment

P_1 = Constituent concentration sorbed on solids in water

P_2 = Constituent concentration sorbed on solids in fluid mud

P_3 = Constituent concentration sorbed on solids in bed

P_∞ = Final or equilibrium constituent concentration sorbed on sediment

P^m = Maximum concentration of constituent that can be sorbed

p = Deposition probability

p_0 = Amplitude of wave-induced cyclic pressure

p_p = Wave-induced excess pore pressure

p_r = Coefficient related to viscoelastic model

p_w = Wave-induced cyclic pressure

Q = non-dimensional bouyancy flux

q = Bouyancy flux

q_s = Coefficient related to viscoelastic model

R = Radius of clay particle

R^2 = Coefficient of determination

Re_b = Bottom wave Reynolds Number over rigid bed

Re'_b = Bottom wave Reynolds Number over soft bed

Re^*_b = Bottom wave Reynolds Number over soft bed

Re_x = Reynolds Number for current

Re_δ = Reynolds Number of wave boundary layer

Ri = Richardson Number

Ri_g = Global Richardson Number

Ri_w = Wave Richardson Number

Ri_{wc} = Critical wave Richardson Number for entrainment

Ri_* = Critical Richardson Number for entrainment under current

$\hat{R}_i$ = Rate of reaction of component i

R_r = Relative roughness of mud surface

r = First-order rate coefficient of sorption

r_α = Ratio of bottom boundary layer across coefficient, α_{12c}, to this coefficent at static condition, α_{12c0}

S = Sediment concentration

S_1 = Sediment concentration in water

S_2 = Sediment concentration in fluid mud

S_3 = Sediment concentration in bed

Sc = Schmidt Number

Sc_f = Schmidt Number in fluid mud

S_{v2} = Sediment volume fraction in mud

S^*_1 = Upper limit concentration for free settling

S^*_2 = Upper limit concentration for flocculation settling

S^*_3 = Upper limit concentration for hindered settling

S^*_4 = Lower limit concentration for negligible settling

$\overline{S}$ = Depth-averaged sediment concentration

$\overline{S_A}$ = Depth-averaged suspended sediment concentration at location A

$\overline{S_B}$ = Depth-averaged suspended sediment concentration at location B

$\overline{S_C}$ = Depth-averaged suspended sediment concentration at location C

$\overline{S_D}$ = Depth-averaged suspended sediment concentration at location D

$\overline{S_E}$ = Depth-averaged suspended sediment concentration at location E

$\overline{S_m}$ = Depth-average suspended sediment concentration over mud trench

$\overline{S_O}$ = Depth-averaged suspended sediment concentration beyond mud trench

$\overline{S_t}$ = Average suspended sediment concentration

s = Surface renewal factor

$s_{a0.5}$ = Sediment concentration at about one-half water depth at location A

$s_{b0.5}$ = Sediment concentration at about one-half water depth at location B

$s_{c0.5}$ = Sediment concentration at about one-half water depth at location C

$s_{d0.5}$ = Sediment concentration at about one-half water depth at location D

$s_{e0.5}$ = Sediment concentration at about one-half water depth at location E

T = Wave period

TS = Total suspended sediment mass in flume

T_{ij} = Stress tensor

T'_0 = Amplitude of T'_{ij}

T'_{ij} = Deviatoric components of stress

U = Mean mixed layer horizontal velocity

u = Horizontal velocity in x-direction

u_1 = Horizontal velocity in water layer in x-direction

u_2 = Horizontal velocity in fluid mud in x-direction

u_{2max} = Maximum horizontal velocity in fluid mud in x-direction

u_3 = Horizontal velocity in bed in x-direction

u_∞ = Mean longitudinal velocity outside boundary layer

u_b = Maximum wave-induced horizontal velocity just outside wave boundary layer

u_e = Rate of downward propagation of interface

u_w = Pore water pressure

u_* = Bottom friction velocity

u_2^* = Characteristic horizontal momentum velocity

u_2^{**} = Characteristic horizontal energy velocity

$\bar{u}$ = Time-averaged velocity in x-direction

$\tilde{u}$ = Wave oscillating velocity in x-direction

u' = Turbulent fluctuation velocity in x-direction

V = Phase velocity of a high frequency shear wave

v = Horizontal velocity in y-direction

v_1 = Horizontal velocity in water layer in y-direction

v_2 = Horizontal velocity in fluid mud in y-direction

v_3 = Horizontal velocity in bed in y-direction

$\bar{v}$ = Time-averaged velocity in y-direction

$\tilde{v}$ = Wave oscillating velocity in y-direction

v' = Turbulent fluctuation velocity in y-direction

w = Vertical velocity in z-direction

w_1 = Vertical velocity in water layer in z-direction

w_2 = Vertical velocity in fluid mud in z-direction

w_3 = Vertical velocity in bed in in z-direction

w_s = Settling velocity of sediment

w_{sf} = Free settling velocity of fine-grained sediment

$\hat{w}$ = Vertical velocity of flow relative to sediment-water interface

$\overline{w}$ = Time-averaged velocity in x-direction

$\tilde{w}$ = Wave oscillating velocity in x-direction

w' = Turbulent fluctuation velocity in x-direction

z'_c = Fluidization depth

α = Coefficient modulating submerged weight of particle

α_{12c} = Bottom boundary layer constituent transport coefficient

α_{12c0} = Bottom boundary layer constituent transport coefficient in static condition

$\alpha_{i\,(i=1\sim8)}$ = Empirical coefficients

α_f = Empirical coefficient

α_n = Empirical coefficient

α_v = Empirical coefficient

$\beta_{i\,(i=1\sim8)}$ = Empirical coefficients

β_f = Empirical coefficient

β_n = Empirical coefficient

β_v = Empirical coefficient

γ_1 = Empirical coefficient

γ_n = Empirical coefficient

$\dot{\gamma}$ = Shear strain rate

ϵ = Empirical coefficient

ϵ_s = Specific area of particles

ϵ_x = Current-associated momentum diffusion coefficient in x-direction

ϵ_y = Current-associated momentum diffusion coefficient in y-direction

ϵ_z = Current-associated momentum diffusion coefficient in z-direction

$\overline{\epsilon_D}$ = Wave energy dissipation rate per unit area

θ_x = Wave-induced momentum diffusion coefficient in x-direction

θ_y = Wave-induced momentum diffusion coefficient in y-direction

θ_z = Wave-induced momentum diffusion coefficient in z-direction

Δ = Empirical coefficient

Δu = Absolute value of velocity difference across mud-water interface

$(\Delta u)_c$ = Critical value of Δu for bottom mud entrainment

Δu_w = Excess pore water pressure

Δb = Buoyancy jump across mud-water interface

$\Delta \rho$ = Density jump across mud-water interface

δ = Boundary layer thickness

δ_1 = Empirical coefficient

δ_c = Thickness of bottom diffusive layer

δ_f = Thickness of bottom boundary layer for "film theory"

δ_{ij} = Kronecker delta

ϵ = Empirical coefficient

ζ = Vertical visplacement of particle

ζ_1 = Water surface dispalcement

ζ_{01}, ζ_0 = Wave amplitudes

ζ_2 = Vertical fluid mud surface dispalcement

ζ_{02} = Amplitude of fluid mud surface dispalcement

ζ_3 = Vertical bed surface dispalcement

ζ_{03} = Amplitude of bed surface dispalcement

θ = Tortuosity

κ = von Karman constant

μ = Dynamic viscocity

μ_∞ = Constant viscosity at the limit of high (theoretically infinite) shear rate

μ_a = Apparent dynamic viscosity

μ_b = Dynamic viscosity

μ_n = Extensional viscosity

μ_p = Apparent dynamic viscosity

μ' = Dynamic viscosity

μ'' = Second viscosity

μ^* = Complex viscosity

ν = Kinematic viscosity

ν_e = Apparent kinematic viscosity

ρ = Density

ρ_1 = Density of water

ρ_2 = Density of fluid mud

ρ_3 = Density of bed

ρ_f, ρ_w = Density of water

ρ_s = Specific gravity

σ = Total normal stress

σ' = Effective normal stress

τ = Shear stress

τ_b = Applied bed shear stress

τ_{cd} = Critical shear stress for deposition

τ_{cm} = Critical maximum shear stress for deposition of non-uniform sediment

τ_{cn} = Critical minimum shear stress for deposition of non-uniform sediment

τ_s = Shear strength

τ_y = Yield stress

Ψ_a, Ψ_b = Shape functions

Φ = Density stratification correction factor

ϕ = Friction angle of sand

ϕ_1, ϕ_2, ϕ_3 = Phase shifts

ϕ_w = Weighting coefficient for wave diffusivity in combined diffusivity of waves and current

ϕ_c = Weighting coefficient of current diffusivity in combined diffusivity of waves and current

ω = Angular wave frequency

ω_0 = Characteristic resonance frequency

ω_θ = Coefficient related to tortuosity

Abstract of Dissertation Presented to the Graduate School
of the University of Florida in Partial Fulfillment of the
Requirements for the Degree of Doctor of Philosophy

SEDIMENT-ASSOCIATED CONSTITUENT RELEASE AT
THE MUD-WATER INTERFACE DUE TO MONOCHROMATIC WAVES

By

YIGONG LI

May, 1996

Chairperson: Dr. Ashish J. Mehta
Major Department: Coastal and Oceanographic Engineering

Constituent release fluxes across the wave-modulated fluid mud-water interface from bottom sediment into water have been determined through a combination of theoretical analyses and laboratory experiments.

The dependence of the equilibrium fluid mud depth on characteristic wave and bed rheological parameters is examined for water-bed and water-fluid mud-bed systems. Theoretical results are compared with data obtained in a wave flume, and an order of magnitude agreement between measured and predicted fluid mud thicknesses is achieved. A three-layered, water-fluid mud-bed system is set up for modeling vertical fine-grained sediment transport. Model results are shown to be in good agreement with laboratory data, and are also shown to successfully simulate field measurements from two coastal sites.

A vertical constituent transport model, which includes sorption kinetics, is developed and is combined with the sediment transport model. The total constituent release flux from

mud under wave action comprises mainly three sub-fluxes including direct convective flux of the dissolved constituent, indirect convective flux of dissolved constituent and indirect particle-bound constituent flux. The behavior of the mass transfer coefficient of the direct convective flux is examined through dimensional analysis, and a Chilton-Colburn type relation is obtained for determining this coefficient as a function of measurable parameters.

Two clayey sediments are used to prepare bottom mud, and two conservative dyes are used as constituent surrogates. By calibrating the constituent transport model against wave flume data obtained for the rate of release of dyes from bottom mud, release sub-fluxes under wave loading are calculated. The indirect convective sub-flux is found to be an order of magnitude lower than the directive convective and particle-bound sub-fluxes. However, the direct convective sub-flux can be amplified several times due to interfacial oscillation, and the interfacial flux coefficient is found to be related to the Richardson Number. Particle-bound sub-flux can dominate the constituent release process when significant resuspension occurs. However, resettling of the sediment flocs and entrapped water tends to considerably reduce the net release of constituent to the ambient water column. Finally, wave-induced diffusivity in mud, which controls the rate of upward supply of the constituent to the interfacial region, is found to be proportional to wave energy dissipation rate per unit volume of mud, and is shown to be two or three orders of magnitude greater than molecular diffusion.

CHAPTER 1
INTRODUCTION

1.1 Problem Statement

Considerable effort has been made in recent years toward reducing the discharge of contaminants into fresh water and marine systems. However, these systems, which should be the beneficiary of an abatement of contaminants, have not always improved as expected. One reason is that external contaminants have already accumulated in bottom sediments and, as a result, after the external sources have been removed or reduced, bottom sediments have become the main sources of contaminants to the water column. Bottom-contaminated sediments affect the water quality directly via diffusion and convection of the contaminants into water, or indirectly through resuspension of sediment particles (Fig.1.1). From Fig. 1.1 we observe that the bottom contaminant released flux can be divided into two categories: (1) direct flux, due to diffusion and convection and (2) indirect flux, which depends on bottom sediment suspension. The direct flux has two components: molecular diffusion, which always exists but is very small compared with the other three fluxes, and convection, which is due to external wave and/or current action. The sediment suspended-related indirect flux also has two components: particle-bound flux, in which the contaminant sorbs on sediment and is transported together with sediment suspension, and indirect convective flux, which is due to water flow into or out of the bed.

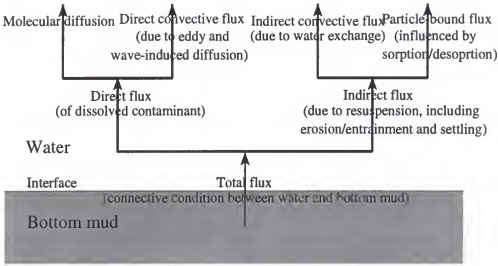
Molecular diffusion
Direct convective flux (due to eddy and wave-induced diffusion)
Indirect convective flux (due to water exchange)
Particle-bound flux (influenced by sorption/desoprtion)
Direct flux (of dissolved contaminant)
Indirect flux (due to resuspension, including erosion/entrainment and settling)
Water
Interface
Total flux
(connective condition between water and bottom mud)
Bottom mud

Figure 1.1 Total contaminant flux and sub-fluxes.

Some examples of bottom contaminated sediment as sources of contaminant to aquatic systems are summarized in Table 1.1. From this table we note that many types of contaminants have already accumulated in bottom sediments. Since these sediments represent an in-place potential contaminant source, quantification of the direct as well as indirect releases of the contaminant is essential for making an assessment of water quality, and for predicting further contamination or recovery of aquatic systems (Eadie and Robbins, 1987; Basmadjian and Quan, 1988; Burton, 1991; Reible and Savant-Malhiet, 1993; and Brownawell and Flood, 1994). For such a quantification, the release fluxes constitute the crucial boundary or connective conditions at the sediment-water interface in water quality and contaminant transport models, such as the hydrodynamic and water quality model WASP5 developed by the Environmental Protection Agency (Ambrose et al., 1991), the Green Bay integrated exposure model GBTOX for the Great Lakes (DePinto, 1994), and the

3-D hydrodynamic, sediment transport and nutrient dynamics models that have been applied to Lake Okeechobee and Tampa Bay, Florida (Chen, 1994).

Table 1.1 Examples where bottom sediment is the main contaminant source.

Location	Contaminants	Source
Detroit River, Michigan	Metals	Theis et al. (1979)
Lake Tarli Karng, Targo Reservoir and East Basin Lake, Australia	Trace metals	Hart and Davies (1981)
Toronto and Hamilton Harbors, Canada	Metals	Nriagu et al. (1983)
Ninigret Pond, New York	Cadmium and Fluoranthene	Di Toro et al. (1989)
Long Island Sound, New York	Cadmium	Di Toro et al. (1989)
Godavari River Basin, India	Heavy metals	Biksham et al. (1991)
Guan-Tin Reservoir, China	Heavy metals	Xian-Chen et al. (1991)
Lake Ontario, Canada	PCBs and Mirex	Brownawell et al. (1994)
Massachusetts Bay and Cape Cod Bay, Massachusetts	Heavy Metals, organic pollutants, and sewage contaminants	Butman (1994)
Lake Okeechobee and Tampa Bay, Florida	Nutrients, e.g., Phosphorus and Nitrogen	Chen (1994)
Mikawa Bay, Japan	Nutrient salts, e.g., inorganic phosphorus (PO_4-P)	Inoue et al. (1994)
Tampa Bay, Florida	Trace metals, PAHs, and PCBs	Long et al. (1994)
Boston Harbor, Massachusetts	Mercury and Lead	Manheim (1994)

Among sediments, fine-grained, especially cohesive, materials play a key role in sediment-associated contaminant transport, because these sediments possess large specific surface areas and net electrical charges on their surfaces and edges that are essential for the sorption of contaminants. A variety of factors can influence the release of contaminants from the bottom sediment to the water column, e.g., hydrodynamic conditions (current velocity, wave height and frequency, water depth, turbulent mixing, etc.), bottom sediment

characteristics (sediment mineral composition, density, rheological properties, cation exchange capacity, organic content, sorptive properties, etc.), suspended sediment characteristics (sediment mineral composition, flocculation and aggregation, sorptive properties, etc.), water-sediment exchange processes (settling, deposition, erosion, entrainment, fluidization, dewatering, etc.), contaminant characteristics (molecular diffusivity, partitioning properties, etc.), and water properties (pH value, salinity, etc.).

Field evidence and model simulations show that, typically, the top 10-30 cm layer of bottom mud in the marine and lacustrine environments is active in storing and releasing contaminants is usually soft and oscillates with water waves (Mehta and Jiang, 1992). Contaminant fluxes across the sediment-water interface are affected considerably by this motion and by the thixotropic changes that ensue within the oscillating bed. As a case in point, Vanderborght et al. (1977) noted that due to bottom stirring the diffusion coefficient of dissolved silica in the pore water within the top 3.5 cm of the shallow North Sea sediment was two orders of magnitude greater than that due to molecular diffusion.

For sorptive contaminants, e.g., hydrophobic organic compounds (DDT, PBCs, PAHs, etc.) or heavy metals (Pb, Cs, etc.), the release flux is also controlled by the reworking of bottom sediment surface due to sediment entrainment and deposition (Reible and Savant-Malhiet, 1993 and Brownawell and Flood, 1994). Since the transport processes--settling, diffusion, deposition and entrainment--are greatly affected by wave loading (Thimakorn, 1983; Maa, 1986; Ross, 1988; Hwang, 1989; Mimura, 1993 and Winterwerp, 1994), waves can also affect the indirect release of contaminants from the bed through resuspending bottom sediment, in addition to direct transfer at the interface.

Thus, it is evident that contaminant transport models must accurately incorporate the physical and the physico-chemical mechanisms that operate in the wave-governed dynamical environment. Typically however, wave-enhanced fluxes are conventionally accounted for merely by calibrating transport models that are only valid for conditions specified by fixed beds having constant (time-independent) properties (Berner, 1980). Therefore, given the considerable importance of properly modeling bottom fluxes for particle-associated contaminant transport in wave-dominated waters, the need for improving the state of the art in prediction of fluxes clearly exists.

1.2 Objective, Tasks and Scope

The primary objective of this research is to investigate the role of water waves in governing the direct and indirect contaminant fluxes across the interface between soft mud and water layers. Specifically, through modeling and laboratory experiments, the inter-relationships between wave parameters, contaminant kinetics and mud properties will be examined for specific contaminant surrogates and bottom muds. This investigation should also provide an accurate mechanistic description of the connective or boundary condition of the contaminant mass transfer flux across the wave-modulated water-mud interface for water quality or contaminant transport models. The specific tasks to accomplish the work were as follows:

1. Since the mud bed may be fluidized under wave motion, and because once the bed is fluidized the rheological properties and mass transport characteristics of fluid mud can be

significantly different from those of the non-fluidized bed, a fluidization model was developed. Using this model, the fluidization depth under wave motion was predicted.

2. Because aquatic contaminant transport is characteristically associated with sediment transport, a sediment transport model was set up in a three-layered water-fluid mud-bed system, which incorporated the effects of fluid mud.

3. Sorption kinetics between sediments and dyes, to be used as contaminant surrogates in experiments, were determined based on sorption experiments.

4. A sediment-associated contaminant transport model was developed in the three-layered system. This model incorporated sorption kinetics and was used in conjunction with the sediment transport model.

5. By calibrating the contaminant transport model against flume experimental data, the total bottom contaminant releasing flux and its sub-fluxes under wave motions were determined for various conditions specified by sediment and contaminant compositions and wave conditions. The relevent coefficients, which determine the magnitudes of the release fluxes, were obtained for the selected sediments and contaminants under wave motion.

6. An effort was made to explain the results in terms of a phenomenological model relating the effect of wave and sediment properties on the release fluxes.

To achieve the above tasks, the scope of this study was defined as follows:

1. In the developement of the mud fluidization model, only normal stresses were considered and shear stresses neglected. Thus, this model is only applicable to short period waves. Also, from this model only the final equilibrium fluidization depth, as would result

from steady and sustained wave action, was obtained. The time-dependent process of fluidization is not predicted by this model.

2. The sediment transport model in the three-layered water-fluid mud-bed system did not consider sediment exchange between fluid mud and bed, because the fluid mud depth was considered to be its equilibrium value.

3. Only sorption experiements were carried out for sediments and dyes. The desorption process were assumed to be the reverse of sorption.

4. Contaminant exchange was studied experimentally by initially inoculating the bottom sediment with dye and tracking dye release in water under wave loading.

5. The contaminant transport model was calibrated only against laboratory data. The contaminant surrogates, i.e., were use in the laboratory experiments because their properties are easily measurable.

1.3 Outline of Presentation

Chapter 2 reviews relevant previous topics and studies on sediment transport, i.e., mud rheology, wave-mud interaction, mud fluidization and resuspension of bottom sediment. Prior investigations on generic sorption models and release of bottom contaminants are also discussed in this chapter. The fluidization model is developed in Chapter 3. It is compared with expeirmental data and applied to field, i.e., Lake Okeechobee, in Florida. In Chapter 4, a sediment transport model in the water-fluid mud-bed system is developed. The model is first calibrated against laboratory data and then applied to field conditions, i.e., the southwest coast of India and the coast of Louisiana. Chapter 5 describes sorption

experiments for dyes, i.e., Rhodamine B and Erioglaucine A, sorbed onto selected sediments, i.e., a kaolinite and a mixture of kaolinite and an attapulgite. The sorptive properties between these dyes and sediments are obtained and incorporated in the transport model described in Chapter 6. In Chapter 6 the sediment-associated contaminant transport model is developed, which includes sorption kinetics in conjunction with the sediment transport model developed in Chapter 4. Chapter 7 describes the flume experimental conditions for bottom contaminant release under wave motion and presents laboratory data for both sediment and contaminant transport under wave action. To obtain the bottom contaminant release flux under wave motion, the contaminant transport model developed in Chapters 4 and 6 was calibrated against the flume data, and the results presented in Chapter 7. In Chapter 8, the release flux and sub-fluxes are compared and correlated to wave conditions and mud rheological properties, and phenomenological explanations are provided for these corrections. Also in this Chapter, overall study conclusions are presented and recommendations for future studies are made.

CHAPTER 2
BACKGROUND INFORMATION

2.1 Introduction

The release of conservative contaminants stored in bottom sediments depends on external hydrodynamic factors, bottom sediment properties and contaminant sorptive properties. Sediment transport characteristics also play an important role in contaminant release of contaminants. Thus, theoretical and modeling studies done in the sediment transport area, i.e., mud rheology, wave-mud interaction, mud fluidization and resuspension of bottom sediment, are reviewed first in this chapter. Following this review, generic sorption models and sorptive properties of the selected dyes, i.e., Rhodamine B, Erioglaucine A, used in this study are described. Field and laboratory experimental observations and previous studies on the release of bottom contaminants are also described in this chapter.

2.2 Mud Rheology and Wave-Mud Interaction Modeling

The interaction between waves and mud beds is an important issue in understanding coastal processes. When waves propagate over a mud bed, wave attenuation, energy dissipation, change in wave kinematics due to corresponding changes in mud properties under oscillatory loading and bed fluidization, mud mass transport etc. are all due to the interactions between the wave and bottom mud. Also, vertical sediment transport, due to

settling, diffusion, erosion, deposition, entrainment, etc., are influenced by wave-mud interactions. For modeling these interactions it is necessary to construct a closed set of equations under wave loading, which include continuity and momentum equations for water and mud motions. These equations must be solved analytically or numerically. A key step in formulating the equations is prescribing the momentum equation for mud motion, which requires a constitutive equation to describe the rheological properties of mud.

In contrast to a sandy bed, the mud bed is almost impermeable. Thus, mud is usually considered as a single-phase continuum. Mud rheology supplies the constitutive equation to relate the applied load with the mud internal response, which thus describes the macro-scale behavior of mud under loads resulting from the micro-scale structure of the mud matrix. Then, substituting the constitutive equation into the equations of motion, the general dynamic equations for a continuum are obtained.

Thus, the important steps for modeling wave-mud interactions are (1) developing a mud rheological model and (2) solving the closure equations for water and mud under wave motion with specific boundary conditions.

2.2.1 Mud Rheology

The importance of rheologic properties of cohesive sediment has been recognized in the coastal seas and estuaries where oscillatory forcing is typically dominant (Mehta, 1991). Natural cohesive sediments are mainly composed of minerals, colloids and organic materials. They settle as mud with density determined by the degree of dewatering or consolidation. The rheological properties of such sediments are quite complicated and depend on the loading shear stress and the reactive shear strain or shear strain rate (Chou,1989) and on the

loading frequency (Jiang, 1993), and may in addition be time-dependant (Williams and Williams, 1992). The general constitutive equation for a continuum is (Malvern, 1969)

$$T'_{ji} = f(E'_{ji}) \tag{2.1}$$

where T'_{ji} are the applied deviatoric stresses, E'_{ji} are the reactive deviatoric strains and subscripts i and j denote directions in conjunction with ji, which implies a second order tensor. Due to the complexity of mud rheology many rheological models have been proposed, as briefly described next.

Linear viscoelastic models

Linear viscoelastic models are widely used at present, and can be generally expressed as:

$$\sum_{r=0}^{M} p_r \frac{\partial^r}{\partial t^r}(T'_{ji}) = \sum_{s=0}^{N} q_s \frac{\partial^s}{\partial t^s}(E'_{ji}) \tag{2.2}$$

where superscripts r and s denote orders of partial differentiation, p_r and q_s are coefficients related to the selected viscoelastic model, and M and N are the specified maximum differential orders of the chosen model. Some special and widely used cases of Eq. 2.2 are as follows:

(1) Elastic material. With $p_0 = 1$, $q_0 = 2G$ and all other p_r and q_r equals to zero, the constitutive equation for an elastic material is (Mallard and Dalrymple, 1977; Dawson, 1978; Foda, 1989)

$$T'_{ji} = 2GE'_{ji} \tag{2.3}$$

where G is the elastic modulus.

(2) Newtonian fluid. With $p_0 = 1$, $q_1 = 2\mu$ and all other p_r and q_s equal to zero, the constitutive equation for a Newtonian fluid is (Dalrymple and Liu, 1978; Shibayama et al., 1986)

$$T'_{ji} = 2\mu \dot{E}'_{ji} \tag{2.4}$$

where μ is the viscosity and $\dot{E}'_{ji}$ is the deviatoric strain rate, i.e., the time derivative of E'_{ji} with the dot denoting a time-derivative.

(3) Voigt model. With $p_0=1$, $q_0=2G$, $q_1=2\mu$ and all other p_r and q_s equal to zero, the constitutive equation for the well known Voigt model is (Fig.2.1a, Carpenter et al., 1973; Hsiao and Shemdin, 1980; McPherson, 1980; Maa, 1986; Sakakiyama and Bijker, 1989)

$$T'_{ji} = 2GE'_{ji} + 2\mu \dot{E}'_{ji} \tag{2.5}$$

(4) Maxwell model. With $p_0 = 1/2\mu$, $p_1 = 1/2G$, $q_1 = 1$ and all other p_r and q_s equal to zero, the constitutive equation for the well known Maxwell model is (Fig. 2.1b)

$$\frac{1}{2\mu} T'_{ji} + \frac{1}{2G} \dot{T}'_{ji} = \dot{E}'_{ji} \tag{2.6}$$

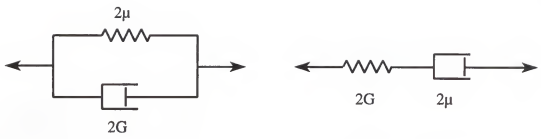

(a) Voigt model (b) Maxwell model

Figure 2.1 Common two-parameter viscoelastic models.

(5) Jeffrey model. The three-parameter Jeffrey model is an extension of the Voigt and Maxwell models. Modulating the Voigt model by an additional elastic modulus, $2G_1$ (Fig. 2.2a), with $p_0 = (G_1+G_2)/\mu_2$, $p_1 = 1$, $q_0 = 2G_1G_2/\mu_2$, $q_1 = 2G_1$ and all other p_r and q_s equal to zero, the constitutive equation for the Standard Solid model is obtained as (Keedwell, 1984; Kolsky, 1992; Jiang, 1993)

$$\frac{G_1+G_2}{\mu_2}T'_{ji} + \dot{T}'_{ji} = \frac{2G_1G_2}{\mu_2}E'_{ji} + 2G_1\dot{E}'_{ji} \tag{2.7}$$

Constraining the Maxwell model by an elastic modulus, $2G_1$ (Fig. 2.2b), with $p_0 = G_2/\mu_2$, $p_1 = 1$, $q_0 = 2G_1G_2/\mu_2$ and $q_1 = 2(G_1+G_2)$ and all other p_r and q_s equal to zero, the resulting Jeffrey-Maxwell constitutive equation is

$$\frac{G_1+G_2}{\mu_2}T'_{ji} + \dot{T}'_{ji} = \frac{2G_1G_2}{\mu_2}E'_{ji} + 2(G_1+G_2)\dot{E}'_{ji} \tag{2.8}$$

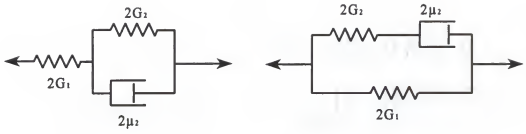

(a) Standard Solid Model (b) Jeffrey-Maxwell Model

Figure 2.2 Jeffrey models.

When the external loading is cyclic, e.g., due to water waves, the general constitutive equation of linear viscoelasticity can be simplified. Assuming that

$$T'_{ji} = T'_0 \exp[-i(\omega t)]$$
$$E'_{ji} = E'_0 \exp[-i(\omega t - \delta)] \tag{2.9}$$

where ω is the angular frequency of loading, δ is the phase shift, T'_0 and E'_0 are the amplitudes of T'_{ji} and E'_{ji}, respectively, and $I = (-1)^{1/2}$, the general relation between the deviatoric stress and the strain is simplified as

$$T'_{ji} = \frac{\sum_{s=0}^{N} q_s(-i\omega)^s}{\sum_{r=0}^{M} p_r(-i\omega)^r} E'_{ji} = 2(G' - iG'')E'_{ji} = 2G^* E'_{ji} \tag{2.10}$$

where G^* is called the complex modulus, G' is the elastic energy storage modulus and G'' is the viscous energy dissipation modulus. As an alternative to Eq. 2.10, the general relation between the deviatoric stress and the strain rate can be obtained as

$$T'_{ji} = \frac{\sum_{s=0}^{N} q_s(-i\omega)^s}{\sum_{r=0}^{M} p_r(-i\omega)^{r+1}} \dot{E}'_{ji} = 2(\mu' + i\mu'')\dot{E}'_{ji} = 2\mu^* \dot{E}'_{ji} \tag{2.11}$$

where μ^* is called the complex dynamic viscosity, μ' is the dynamic viscosity and μ'' is called the second viscosity. Accordingly, the different rheological models described can be obtained as follows:

(1) Elastic material,

$$\mu' = \mu \quad ; \quad \mu'' = 0 \tag{2.12}$$

(2) Newtonian fluid,

$$\mu' = 0 \quad ; \quad \mu'' = \frac{G}{\omega} \tag{2.13}$$

(3) Voigt model:

$$\mu' = \mu \quad ; \quad \mu'' = \frac{G}{\omega} \tag{2.14}$$

(4) Maxwell model,

$$\mu' = \frac{G\left(\frac{G}{\mu}\right)}{\omega^2 + \left(\frac{G}{\mu}\right)^2} \quad ; \quad \mu'' = \frac{G\omega}{\omega^2 + \left(\frac{G}{\mu}\right)^2} \tag{2.15}$$

(5) Standard Solid model,

$$\mu' = \frac{G_1\left(\frac{G_1}{\mu_2}\right)}{\omega^2 + \left(\frac{G_1+G_2}{\mu_2}\right)^2} \quad ; \quad \mu'' = \frac{\frac{G_1\left[(G_1+G_2)G_2}{\omega\left[\frac{}{\mu_2^2} + \omega^2\right]}\right]}{\omega^2 + \left(\frac{G_1+G_2}{\mu_2}\right)^2} \tag{2.16}$$

(6) Jeffery-Maxwell model,

$$\mu' = \frac{G_2\left(\frac{G_2}{\mu_2}\right)}{\omega^2 + \left(\frac{G_2}{\mu_2}\right)^2} \quad ; \quad \mu'' = \frac{\frac{1}{\omega}\left[\frac{G_1 G_2^2}{\mu_2^2} + \omega^2(G_1+G_2)\right]}{\omega^2 + \left(\frac{G_2}{\mu_2}\right)^2} \tag{2.17}$$

As mud rheology is complicated, none of the above models can describe mud response under all types of loading conditions. However, for the case of mud response to cyclic loads (Eqs. 2.10 and 2.11), a practical way to characterize mud rheology is by carrying out a dynamical oscillatory test (Chou, 1989; Jiang, 1993). Through this test the complex modulus, G^*, or the complex dynamic viscosity, μ^*, can be obtained under specific conditions for practical use, without considering a particular model describing mud rheology. Thus, for example, Chou (1989) related the complex modulus, G^*, with strain amplitude by using controlled strain rheometry. Then, he incorporated the resulting strain-dependant rheologic model into his wave-mud interaction model to predict mud response to wave motion. Jiang (1993) related the three parameters of the standard solid model to wave loading frequency and then obtained the complex dynamic viscosity, μ^*, which also therefore depends on the loading frequency, for his wave-mud interaction model. Such

experimentally based relations will continue to play an important role in modeling mud rheology, before a fuller theoretical understanding of mud rheology is obtained.

Theoretically, predictive accuracy can be increased by introducing more and more elastic/viscous elements used for modeling mud rheology. However, the more the elements in a model, the greater the number of coefficients that must be determined. Thus, greater complicated experimental procedures are required, which in turn limit the use of large-element models. On the other hand, some nonlinear properties, e.g., plasticity, time-dependant properties, etc., are often important in mud rheological response to loading. As a result, some nonlinear viscoelastic models have also been proposed for mud rheology.

Nonlinear and Time-Dependent Models

The three-dimensional structure of soft mud beds can resist small shear stresses at rest. To account for this resistance, viscoplastic models have been used (Engelund and Wan, 1984; Suhayda, 1986; Mei and Liu, 1987; Tsuruya, 1987; Liu and Mei, 1989; Shibayama et al., 1990). For small strains, the constitutive equation for a viscoplastic material can be expressed as (Malvern, 1969)

$$T'_{ji} = \left(2\mu_p + \frac{k_y}{\sqrt{\Pi_D}} \right) \dot{E}'_{ji} \tag{2.18}$$

where μ_p is the apparent viscosity, k_y is the yield strength and Π_D is the second invariant of $\dot{E}'_{ji}$. For the one-dimensional condition, Eq.2.18 can be simplified to (Wilkinson, 1960)

$$\tau = \tau_y + \mu_p \dot{\gamma} \tag{2.19}$$

where τ is the applied shear stress, τ_y is the yield stress and $\dot{\gamma} = \partial u/\partial z$. Here u is the velocity in the same direction as τ.

For the commonly found shear-thinning behavior of mud, i.e, one in which the apparent viscosity decreases as the shear strain rate increases under increased shear stress loading, mud can be modeled by a power-law equation (Sisko, 1958; Feng, 1992)

$$\tau = \mu_\infty \dot{\gamma} + c\dot{\gamma}^n \tag{2.20}$$

where the apparent viscosity, $\mu_p = u_\infty + c\dot{\gamma}^{n-1}$, μ_∞ is the constant viscosity at the limit of high (theoretically infinite) shear rate, c is a measure of the consistency of the material and $n < 1$ is a mud-specific parameter.

James et al. (1987) conducted creep-compliance tests for illitic suspensions by using a combination of an applied stress rheometer and a miniature vane geometry. They found the instantaneous compliance, $J_0 = \gamma/\tau$, to be related to the applied shear stress. The material was predominantly elastic at low shear stresses and was essentially viscous at high shear stresses. Chou (1989) measured soft mud rheological properties composed of a kaolinite and a montomorillonite and found that the storage modulus, G′, and the loss modulus, G″, changed with the shear strain amplitude.

By using shear wave rheometry, Williams and Williams (1992) measured the G′ and G″ values of mud under oscillatory loads, and found that G′ and G″ changed with the wave loading time, thus quantitatively demonstrating that mud has a time-dependant rheological response. Mehta et al. (1995) correlated the phase velocity of a high-frequency shear wave in a mud bed with bed rigidity. The fall in the velocity, starting with an undisturbed bed

under monochromatic wave, indicated that the bed rigidity decreased as a result of bed fluidization under wave motion. Thus, the bed had a time-dependant rheological response to wave motion.

2.2.2 Wave-Mud Interaction Modeling

Prior to the late 1950s, wave energy dissipation was mainly considered in connection with bottom friction, percolation, wave refraction and shoaling. Brestschneider and Reid (1954) presented graphic solutions for obtaining wave attenuation by these factors. However, it must be pointed out that a mud bottom is usually not rigid and is almost impermeable to water flow. The dissipation of propagating wave energy over the mud bed is mainly due to internal friction within mud, which is characterized by mud rheology and wave loading.

Based on Biot's (1941) 2-D, nonporous, perfect-elastic soil theory, Mallard and Dalrymple (1977) modeled mud bed as an elastic material to study soil stresses and displacement under wave motion. In their modeling, soil inertia was neglected and there was no energy dissipation since mud viscosity was not included. Taking soil inertia into account, Dawson (1978) also modeled mud as an elastic material. However, wave energy dissipation was not considered.

An early theoretical and laboratory study on the effects of a nonrigid, impermeable bottom on the surface wave was carried out by Gade (1958), who modeled the water layer as an inviscid fluid overlying a viscous fluid layer of greater density. Solution for the shallow water, single harmonic wave indicated that wave height decayed exponentially with distance traveled, and that wave energy dissipation over the soft bottom was substantially

greater than that over a rigid bed. Dalrymple and Liu (1978) developed a theory for a small amplitude linear wave propagating in a two-layered viscous fluid system. Both the governing equations of continuity and motion and the surface, interface and bottom boundary conditions were linearized, and an analytical approach was used for solving the equations. The results showed that most of the energy dissipation was due to internal friction within the soft mud as a result of high viscosity, and that extremely high wave attenuation rates are possible when the thickness of the lower layer is of the same order as the internal boundary layer thickness. Based on Dalrymple and Liu's work and boundary layer approximation, Jiang and Zhao (1989) and Jiang et al. (1990) developed analytical approaches for calculating wave attenuation for viscous mud beds under shallow water solitary and cnoidal waves. These modeling studies included the nonlinear properties of waves in shallow water.

By considering both the viscous and the elastic properties, Hsiao and Shemdin (1980) and McPherson (1980) independently applied the Voigt model to represent mud rheology and used analytical approaches to solve for the assumed inviscid water wave propagating over a linear viscoelastic bed. McPherson introduced a viscoelastic parameter, $\nu_e = \mu^*/\rho$ (see Eq. 2.11), which is essential for the formulation of the problem based on the viscoelastic assumption. For the Voigt model, $\nu_e = \mu/\rho + iG/\omega\rho$ (see Eq. 2.14). McPherson's results showed that depending on the elasticity and the viscosity of the sea bed, wave attenuation can be of the same or a larger order of magnitude than that due to bottom friction or percolation. Hsiao and Shemdin compared their results with field measurement reported by Tubman and Suhayda (1976) in East Bay, Louisiana, and obtained reasonable predictions. Considering mud density increases with depth, a multi-layered Voigt model was used by Mehta and Maa

(1986) to model mud bed motion under a linear wave. The calculated water-mud interfacial bed shear stresses was found to be larger than those obtained by assuming mud to be rigid.

Chou (1989) developed a three-phased viscoelastic model for mud rheology, and under linear water wave motion a four-layered wave-mud interaction model was set up. The depths of the second, viscous layer, and the third, viscoelastic layer, layers were determined as part of the solution through an iterative technique. The model showed that the mud fluidization depth and wave attenuation rate increase with wave height for a partially consolidated mud. Using controlled-stress rheometry, Jiang (1993) modeled mud as a Standard Solid (see Eq. 2.16). An analytical solution and laboratory tests were used to study wave-mud interaction, wave attenuation and mud mass transport. The modeling results compared favorably with laboratory experimental data and with field data from Lake Okeechobee in Florida and the southwest coast of India.

Besides linear viscoelastic models, some nonlinear viscoelastic, viscoplastic and other models have also been used in wave-mud interaction modeling and mud behavior in general. Engelund and Wan (1984) used the viscoplastic model to study the instability of hyperconcentrated flows. They claimed that the Bingham model was valid for the description of the instability of the fluid surface elevation.

Mei and Liu (1987) considered bottom mud to be viscoplastic. The special case of a shallow mud layer under the action of long waves propagating in water was considered. It was found that under certain conditions the dynamics of a plug flow layer, unsheared in the domain with stresses below the yield stress, contributed measurably to wave attenuation

over a long fetch. In particular, as waves propagated mud motion could change from continuous to intermittent.

Tsuruya et al. (1987) extended Dalrymple and Liu's (1978) viscous-fluid model to a Bingham fluid. The equivalent viscosity, μ_a, which takes non-Newtonian mud rheology into account, was defined as

$$\tau = \mu_a \frac{\partial u}{\partial z} = \tau_0 + \mu_b \frac{\partial u}{\partial z} \tag{2.21}$$

where τ_0 is the yield stress, μ_b is the dynamic viscosity and the apparent dynamic viscosity

$$\mu_a = \frac{\tau_0}{\frac{\partial u}{\partial z}} + \mu_b \qquad (\tau > \tau_0) \tag{2.22}$$

Thus, the Bingham fluid was introduced into the Newtonian equation of motion in an approximate fashion. Laboratory tests on wave attenuation and mud mass transport were also conducted.

Using the viscoplastic Bingham model for a thin mud layer under solitary waves, Liu and Mei (1989) analytically solved the wave-mud interaction problem through a boundary layer approximation. They found that wave dissipation is due to the bottom mud shear layer and the turbulent interfacial stress. Continuous to intermittent mud motion could be predicted from this model.

Studying linear wave propagation over a soft mud, Shibayama et al. (1990) modeled mud as a viscoelastic and/or viscoplastic material depending on the loading shear stress. Fluid mud was assumed to be viscoelastic when the stress was less than the yield stress, and

was considered to be viscoplastic when the stress exceeded the yield stress. The resulting numerical model could predict mud mass transport under wave action.

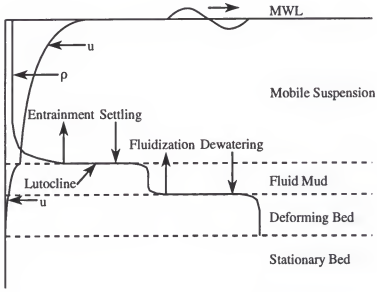

Figure 2.3 A typical wave-mud system (after Hwang, 1989)

2.3 Mud Fluidization and Fluid Mud

The interactions between unsteady flows and soft bottom mud are not well understood at present, especially when a fluid mud occurs at the bottom. Fluid mud is a concentrated sediment slurry having non-Newtonian rheological properties. It may be generated by rapid deposition of suspended sediment or by fluidization of the mud bed by waves (Winterwerp, 1994). In Fig. 2.3, a qualitative description of the mud-water system is given, in which u is the horizontal wave orbital velocity. The bulk density of the water-mud mixture, ρ, varies from the water surface to the bed bottom. A sharp density gradient, or lutocline (Parker and Kirby, 1982), separates the upper column suspension from fluidized

mud below. The bed just below fluid mud tends to undergo deformation. Below the level at which the depth of penetration of the wave orbit ends, the bed remains uninfluenced by wave motion.

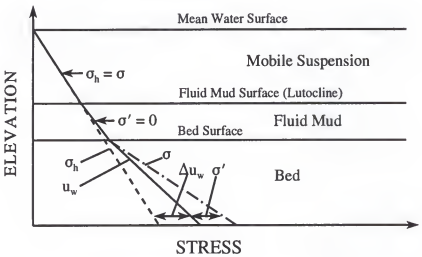

Figure 2.4 Schematic of instantaneous stress profile in a wave-mud system (after Mehta et al., 1994).

An instantaneous view of the stress profiles in the mud-water system is shown schematically in Fig. 2.4, in which σ_h is the hydrostatic pressure, Δu_w is the wave-averaged excess pore pressure, σ' is the wave-averaged effective normal stress, u_w is the pore pressure and the total stress, $\sigma = u_w + \sigma' = \sigma_h + \Delta u_w + \sigma'$. Considering the time-variation of the normal stress in the bed at a given point, as the excess wave-mean pore water pressure builds up gradually under wave motion, the effective stress reduces accordingly. When the pore water pressure equals the total pressure at some elevation, i.e. when the effective normal stress is zero, the bed at and above this elevation is considered to be fluidized (Ross, 1988;

Feng, 1992). Thus, fluid mud is actually supported by water and has fluid-like properties, while the non-fluidized bed retains a structured sedimentary matrix.

Because the rheological properties and the mass transport characteristics of fluid mud can be significantly different from those of the non-fluidized bed, fluid mud must be modeled separately from the bed. Therefore, to investigate water-mud bed interactions, once the bed is fluidized, a three-layered water-fluid mud-bed system must be set up (see Fig. 2.5).

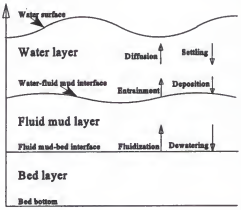

Figure 2.5 Three-layered water-fluid mud-bed system and vertical sediment transport processes under waves.

To investigate vertical mass transport in the three-layered system, several mass flux-associated processes must be determined quantitatively. In the water layer, the sediment settling velocity and the buoyancy-stabilized diffusivity must be specified. The entrainment rate of fluid mud and the deposition rate of sediment onto the surface of fluid mud must be modeled. To determine the fluid mud layer thickness and the mass fluxes of sediment across the fluid mud-bed interface, fluidization characteristics of the bed and dewatering of fluid mud by consolidation must be understood.

Fluid mud thickness can affect both the velocity distribution in the water column through wave-fluid mud interaction (Jiang, 1993), and mass exchange between water and bed. However, a fully operational model to predict fluidization under waves has not yet been developed. Roberts (1993) used the three-layered system to develop a two-dimensional horizontal model to predict fluid mud movement under storm waves in the coastal zone. The thickness of fluid mud was assumed to be equal to the wave boundary layer height by way of the argument that the water-fluid mud interface coincides with the top of the wave boundary layer. However, this assumption is not always appropriate, since in general the interface can rise above the height of the boundary layer or occur below the latter. By measuring the pore and total pressures within the bed under wave motion in a laboratory flume, Feng (1992) developed an empirical formula for determining fluid mud thickness. Combining the experimental data of Feng (1992) and the rheological properties of mud measured by a miniature shearometer (Williams and Williams, 1992), Mehta et al. (1994) also developed an empirical formula to predict time-varying fluid mud thickness during fluidization. These two empirical relations are limited to the types of sediment and wave conditions used in the experiments for which they were derived. Therefore, to determine the necessary coefficients for other sediments or wave conditions, additional experiments must be carried out.

For modeling the depth of fluidization, Foda et al. (1993) applied a wave-bed interaction model incorporating the assumption that the viscoelastic properties of mud are dependent on the wave-induced strains within the bed. This model can only predict the final equilibrium fluidization depth, which is actually a time-dependent process starting with a bed

over which wave motion commences. By using a miniature rheometer to measure the phase velocity, V, of a high-frequency shear wave in a mud bed and then correlating V with bed rigidity, G', Mehta et al. (1995) obtained the empirical relation

$$\frac{G'(t)}{G'(0)} = \left[\frac{V(t)}{V(0)}\right]^2 = \exp(-\alpha_v t^{\beta_v}) \tag{2.23}$$

where α_v and β_v are empirical coefficients dependent on bed rheological properties and the wave characteristics. It was found that the trends of increasing measured fluid mud thickness with time, $d_f(t)$, were quantitatively in agreement with the trend of decreasing V(t) and were empirically expressed as

$$d_f(t) = M_f[1 - \exp(-\alpha_f t^{\beta_f})] \tag{2.24}$$

where M_f, α_f and β_f are empirical coefficients. However, a theoretical explanation for Eq. 2.24 was not provided. In fact, since the fluidization process is not well understood, in the present development the fluid mud layer will be considered to be of the final equilibrium thickness.

Dewatering is the process by which fluid mud consolidates and the bed structure is rebuilt. Experimental measurements of Feng (1992) and de Wit (1994a, 1994b) indicate that, as long as wave motion continues, fluid mud can be maintained and may not dewater. Since in the present case only the equilibrium thickness of fluid mud is to be considered, the dewatering process will not be examined. Thus, no portion of fluid mud will be considered to dewater to become part of the bed layer. For the same reason, no bed sediment will be

fluidized. Therefore, sediment mass transport across the interface between the fluid mud and the bed will be neglected and the fluid mud-bed interface will be considered to be fixed in elevation.

2.4 Processes Governing the Vertical Structure of Suspension

Referring to Fig. 2.5, in the water layer settling and upward diffusion of the suspended sediment determine the vertical distribution of sediment concentration. The entrainment rate of fluid mud or bed and the deposition rate of suspended sediment onto the surface of fluid mud or the bed govern sediment exchange between the water and fluid mud or bed.

2.4.1 Settling

The settling velocity of cohesive sediments strongly varies with the concentration in suspension (Mehta, 1988a). A descriptive plot is shown in Fig. 2.6 for the relationship that is typically found between the settling velocity, w_s, and the suspended sediment concentration, S. Also shown is the variation of the corresponding settling flux, $F_s = w_s S$. The settling velocity regime can be divided into three sub-ranges depending on the concentration and the mode of settling, which can be free settling, flocculation settling or hindered settling.

Free settling occurs in the very low suspension concentration range, when $S < S_1^*$ (see Fig. 2.6). In this range the particles or flocs settle independently and the settling velocity is not a function of suspension concentration. For cohesive sediments, the upper

concentration limit, S_1^*, is considered to be in the range of 0.1 to 0.3 g/l (Mehta, 1988). The settling velocity in the free settling range is usually assumed as a constant, i.e.:

$$w_s = w_{sf} = \alpha_1 S_1^{*\beta_1} = \text{const} \qquad (S < S_1^*) \qquad (2.25)$$

where α_1 and β_1 are coefficients which will be explained next.

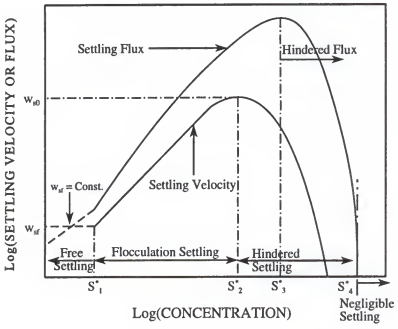

Figure 2.6 A schematic description of settling velocity and flux variation with suspension concentration (after Hwang, 1989).

Flocculation settling occurs in the middle suspension concentration range specified by $S_1^* < S < S_2^*$. In this range increasing concentration leads to increasing interparticle collision and enhanced particle aggregation. Thus, the settling velocity increases with concentration due to the formation of stronger, denser and larger flocs or aggregates. The typical relationship between the settling velocity and suspended sediment concentration is

$$W_s = \alpha_1 S^{\beta_1} \qquad S_1^* < S < S_2^* \tag{2.26}$$

where β_1 is 4/3 theoretically (Krone, 1962), although the actual value typically varies between about 0.8 and 2 (Mehta, 1988a). The proportionality coefficient, b_1, can vary by an order of magnitude depending on sediment composition and the flow environment.

Hindered settling occurs in the high concentration range, when $S > S_2^*$. In this range, the occurrence of an aggregate network hinders the upward transport of interstitial water. Thus, w_s decreases with increasing S (Kynch, 1952). A widely accepted relationship for the settling velocity as a function of concentration was developed by Richardson and Zaki (1954)

$$w_s = w_{s_o}(1 - \alpha_1' S)^{\beta_2} \qquad (S > S_2^*) \tag{2.27}$$

where w_{so} is the initial or reference settling velocity, α_1' is a coefficient depending on the sediment composition and $\beta_2 = 5$. Above the concentration S_4^*, the settling flux is negligible.

Hwang (1989) measured the settling velocity of sediments collected from Lake Okeechobee in Florida, and parameterized the effects of flocculation and hindered settling on the settling velocity by way of a nonlinear formula dependent on the sediment concentration, and expressed as

$$w_s = \frac{\alpha_1 S^{\beta_1}}{(S^2 + \gamma_1^2)^{\delta_1}} \tag{2.28}$$

where α_1, β_1, γ_1 and δ_1 are empirical constants which must be experimentally determined for different sediments.

2.4.2 Diffusion

The rate of upward diffusion of suspended fine-grained sediment is governed by the mass diffusivity determined by hydrodynamic forcing and also by density stratification, which tends to damp diffusion. The diffusivity, K_z, is usually expressed as the product of the neutral mass diffusivity, K_n, and the density stratification correction factor, Φ (Rossby and Montgomery, 1935; Munk and Anderson, 1948; Ross, 1988), i.e.

$$K_z = K_n \Phi \tag{2.29}$$

The most commonly applied expression of the vertical variation of the neutral mass diffusivity for turbulent unidirectional flow was developed by Rouse (Vanoni, 1975). Following von Karman's assumption of a linear shear stress distribution with depth and a logarithmic velocity profile, the neutral diffusivity is expressed as

$$K_n = \kappa u_* z\left(1 - \frac{z}{h}\right) \tag{2.30}$$

where κ is von Karman's constant, u_* is the friction velocity, h is the water depth and the coordinate z is upward originating from bed surface. However, under wave motion, the diffusivity becomes complicated and has not been fully parameterized thus far. By analogy with the mixing length theory in unidirectional flows, Homma et al. (1962) gave a plausible expression for the wave diffusivity. To overcome the shortcomings found in the derived

expression, Homma et al. (1965) modified the expression by introducing a mixing length following the von Karman hypothesis. The resulting neutral wave diffusivity under the linear waves was expressed as

$$K_n = \beta_2 \frac{H\omega}{k \sinh kh} \frac{\sinh^3 k(h+z)}{\cosh^2 k(h+z)} \tag{2.31}$$

where β_2 is a constant, H is the wave height, ω is the wave frequency and k is the wave number.

Hwang and Wang (1982) summarized the models available for the turbulent diffusion coefficient outside the wave boundary layer and indicated that Prandtl's mixing length theory may not be applicable due to the large scale of wave motion. They assumed that the wave diffusivity is proportional to the vertical velocity component and the orbital radius of the water particle in the vertical direction. Using the linear wave theory, the expression for wave diffusivity was obtained as

$$K_n = \alpha_2 H^2 \omega \frac{\sinh^2 kz}{2 \sinh^2 kh} \tag{2.32}$$

where α_2 is a constant. From the concept based on energy in a turbulent field, Thimakorn (1984) expressed the eddy diffusivity as

$$K_n = 0.885 H^2 \omega \frac{\sinh^2 kz}{\sinh^3 kh} \tag{2.33}$$

which is similar to Hwang and Wang's expression, with $\alpha_2 = 1.77/\sinh kh$.

Stratification due to density variation in suspension can measurably alter the vertical momentum and mass mixing characteristics. In the case of stable density stratification in which the density decreases upward, vertical diffusion is impeded by the stabilizing gravitational force of sediment suspension acting against the destabilizing force due to fluid shear. The local gradient Richardson number, Ri, is usually used as a measure of stability, and is defined as

$$Ri = -\frac{g}{\rho}\frac{\frac{\partial \rho}{\partial z}}{\left(\frac{\partial u}{\partial z}\right)^2} \tag{2.34}$$

where g is the gravitational acceleration, ρ is the density and z is positive upward. Positive values of Ri indicate stable stratification, negative values indicate unstable stratification and Ri = 0 implies a neutral condition. The greater of the positive value of Ri, the greater the suppression of vertical diffusion.

A number of models for the density stratification correction factor, Φ, in Eq. 2.27, and therefore for stratified diffusivity, have been proposed. One of the most frequently used expression was developed by Munk and Anderson (1948), which is

$$K_z = K_n(1+\beta_3 Ri)^{\alpha_3} \tag{2.35}$$

where α_3 and β_3 are empirical coefficients and, typically, α_3 varies from -0.5 to -2.0 and β_3 varies from 0.3 to 30 (Rossby and Montgomery, 1934; Holzman, 1943; Munk and Anderson,

1948; Nelson, 1972; French, 1979; French and McCutcheon, 1983) depending on sediment composition and the flow environment. Thus, the diffusive flux, F_d, can be expressed as

$$F_d = -K_z \frac{\partial S}{\partial z} = -K_n (1 + \beta_3 Ri)^{\alpha_3} \frac{\partial S}{\partial z} \qquad (2.36)$$

Without the effect of buoyancy stabilization, Ri = 0 and $K_z = K_n$, so that the diffusive flux is linearly proportional to the vertical concentration gradient, $\partial S/\partial z$. However, since the local gradient Richardson number, Ri, is proportional to $\partial \rho/\partial z \propto \partial S/\partial z$, the stratified diffusivity, K_z, is inversely proportional to the vertical concentration gradient with $\alpha_3 < 0$. Thus, nonlinearity between the diffusive flux, F_d, and $\partial S/\partial z$ develops when gravitational stability is considered. Also, from the theoretical results of Eq. 2.34, the diffusivity flux initially increases with low values of $\partial S/\partial z$, reaches a maximum and then slowly decreases with high values of $\partial S/\partial z$. The formation of the lutocline is strongly related to the nonlinear dependence of F_d on $\partial S/\partial z$ (Eq. 2.34) (Ross, 1988; Hwang, 1989; Costa, 1989; Scarlatos and Mehta, 1990).

Ross (1988) and Hwang (1989) used Eqs. 2.30 and 2.34 in their vertical fine-grained sediment transport modeling. Model results were found to be in agreement with laboratory data, and with field data from the Severn Estuary and tributaries, United Kingdom (Kirby, 1986; Kirby and Parker, 1977) and from Lake Okeechobee in Florida (Hwang, 1989). Also, lutoclines could be simulated with the models.

2.4.3 Deposition Rate

The deposition rate of suspended sediment onto fluid mud surface can be expressed as the product of the settling rate of sediment near the mud surface and the probability of deposition (Krone, 1962; Mehta, 1988b). Thus, deposition rate, F_p, is expressed as

$$F_p = -w_s Sp|_{\text{mud surface}} \tag{2.37}$$

where p is the deposition probability. The concept of this probability implies that deposition occurs through the sorting of suspended sediment aggregates, which in turn occurs because of the high rates of fluid shear near the bottom. When the aggregates are strong enough to withstand the near-bed shear stress, they stick to the bottom mud; if not, they are disrupted and resuspended.

Krone (1962) first related the deposition probability to the relative shear stress as

$$p = \begin{cases} 0 & (\tau_b \geq \tau_{cd}) \\ \left(1 - \dfrac{\tau_b}{\tau_{cd}}\right) & (\tau_b < \tau_{cd}) \end{cases} \tag{2.38}$$

where τ_b is the bed shear stress and τ_{cd} is the critical shear stress above which no deposition occurs. This stress typically varies from 0.04 ~ 0.15 Pa.

Mehta (1986) and Mehta and Lott (1987) studied nonuniform sediment deposition and defined the critical shear stress for deposition of such sediment. With τ_{cm} and τ_{cn} defined as the maximum and minimum values, respectively, of the critical shear stress for deposition, τ_{ci}, for $\tau_b > \tau_{cm}$ no initially suspended sediment can deposit, while for $\tau_b < \tau_{cn}$ the entire of

suspended material will eventually deposit. For $\tau_{cn} < \tau_b < \tau_{cm}$ a fraction of the initially suspended sediment for which $\tau_{ci} < \tau_b$ will not deposit, while the remainder will finally deposit at steady state. Using this approach the instantaneous concentration variation with time can be predicted depending on the initial suspension concentration, settling velocity, sediment size distribution and the flow condition.

Sanford and Halka (1993) investigated sediment resuspension in Chesapeake Bay and found that the resuspension model with the assumption of no critical stress for deposition described the field data better than one including the critical stress. They suggested that deposition always occurs, and is proportional to the near bottom suspension concentration. Thus, even at steady state when the suspended sediment concentration is constant, sediment exchange between the water column and the bed exists. The deposition rate in this case is expressed as

$$F_p = -w_s S|_{\text{mud surface}} \tag{2.39}$$

which is a special case of Eq. 2.37 with the deposition probability equal to one.

2.4.4 Entrainment

The problem of erosion of cohesive sediments has been extensively investigated (Grissinger, 1966; Kelly and Gularte, 1981; Parchure and Mehta, 1985; Sheng, 1986; Maa and Mehta, 1987; Shaikh et al, 1988), with different types of deposited or remolded clay beds under current or wave motion, in fresh or saline water. Erosion of mud bed is due to: (1) frictional, gravitational and cohesive bonding forces of bed being exceeded by the hydrodynamic erosive force, which causes bed surface erosion, and (2) the bed bulk shear

stress being exceeded by the flow-induced shear stress, which causes mass erosion (Mehta, 1986).

In the above context it should be noted that the mechanism by which fluid mud is entrained by shear flow differs from that governing the rate of erosion of the settled mud having a structured matrix (Mehta and Srinivas, 1994 and Kranenburg, 1994). Entrainment is due to the breakup of the fluid mud-water interface, which is characterized by the ratio of the destabilizing factor, the mechanical mixing energy, and the stabilizing factor, the potential energy stored in density stratification (Scarlatos and Mehta, 1993 and Mehta and Srinivas, 1993).

Kato and Phillips (1969) applied a constant shear stress, $\tau = \rho u_*^2$, at the surface of an initially linearly stratified fluid in an annular flume. This resulted in the development of an upper homogeneous layer and a lower stratified fluid with an interfacial buoyancy jump Δb. They arrived at the expression

$$E_* = \frac{u_e}{u_*} = K_1 Ri_*^{-1} \tag{2.40}$$

where E_* is the non-dimensional entrainment rate, u_e is the rate of downward propagation of the interface, u_* is the friction velocity and the Richardson Number, $Ri_* = h\Delta b/u_*^2$, and h is the depth of the upper homogeneous layer. Moore and Long (1971) ran two-layered experiments in a race-track shaped flume with density and velocity profiles being uniform in the longitudinal direction. Over the range of the global/overall Richardson Number, Ri_g,

studied, they found that the non-dimensional buoyancy flux, $Q = q/\Delta b\ (2\Delta U)$, was related to the overall Richardson Number according to

$$Q \sim Ri_g^{-1} \tag{2.41}$$

where q is the buoyancy flux, $2\Delta U$ is the velocity difference between the two layers and $Ri_g = \hat{H}\Delta b/(2\Delta U)$, in which $\hat{H}$ is the total depth.

In the field, Bedford et al. (1987) measured sediment entrainment in Long Island Sound, and examined its dependence on the bed shear stress, the Reynolds stress, and the turbulent and wave kinetic energies. Only the time-patterns of turbulent and wave kinetic energies correlated with the entrainment time pattern.

Scarlatos and Mehta (1993) approximated the mud-water system by a two-layered, slightly viscous, horizontal system with water flowing over fluid mud. By introducing a slight disturbance along the interface, the vortex sheet initially developed a wave-like pattern, typical of Kelvin-Helmholz instability. Then the vortex sheet stretched, folded and eventually caused a thickening and vigorous mixing of the interface. It was demonstrated that the dynamic behavior of the vortex sheet is controlled by the velocity and density gradients across the interface.

Mehta and Srinivas (1993) examined the entrainment behavior of fluid mud subjected to turbulent shear flows based on theoretically analyzing the turbulent kinetic energy equation and using experimental data. A non-dimensional formula for the entrainment rate dependent on the global Richardson Number was obtained as

$$E = A_e Ri_g^{-1} - D_e Ri_g \qquad (2.42)$$

where $E = u_e/U$, $Ri_g = h\Delta b/U^2$, Δb is the buoyancy jump across the water-fluid mud interface, U is the mean mixed layer velocity, h is the mixed layer depth, and A_e and D_e are experimentally determined coefficients. The first term on the right side represents the interaction between mechanical mixing energy and potential energy stored in density stratification. The second term arises from influences of particle settling, cohesion, viscosity difference between mud and water etc. It should be noted that according to Eq. 2.40, at low values of Ri_g the upward flux of sediment mass is proportional to the cube of the mean mixed layer velocity. In contrast, the rate of erosion of cohesive bed depends on U^2 in turbulent flows (Partheniades, 1965; Mehta, 1989).

Winterwerp (1994) carried out experiments on the entrainment of soft mud layers in an annular flume and also found the entrainment rate of fluid mud to be governed by the global Richardson number. The non-dimensional entrainment rate, $E_* = u_e/u_*$, was correlated with $Ri_*^{-1/2}$ for small Ri_* and with Ri_*^{-1} for large Ri_*, where $Ri_* = h\Delta b/u_*^2$.

Kranenburg (1994) derived an entrainment model for fluid mud by integrating the equation for turbulence kinetic energy over the mixed layer and introducing some modeling assumptions. Two basic conditions for entrainment were considered. In case 1, the water layer was selected to be the turbulent mixing layer and fluid mud entrained into water layer. In case 2, turbulence was considered to be produced primarily in the fluid mud layer due to the shear stress at the bottom of the fluid mud layer. Water entrained downward into fluid

mud layer increased the fluid mud depth with time. Such behavior has also been reported in the field by Wolanski et al. (1988) and Le Hir (1994).

2.5 Sorption Models

Sorption processes include adsorption, chemisorption, absorption and ion exchange (Fetter, 1992). Adsorption is the process by which a solute (sorbate) clings the solid (sorbent), i.e., sediment, surface. Chemisorption occurs when the solute is incorporated on a solid surface by a chemical reaction. Absorption describes the process that the solute goes beyond the solid surface and diffuses into the porous interior compartment of the solid. Ion exchange is the process that charged solutes exchanges with ion on solids surface. From a practical point of view the important aspects are the removal of the solute from solution to sorb onto or into solid, or the release of solute from solid into solution, irrespective of the details of process mechanics. If the rate of sorption is much faster than advective-diffusive transport rate of solute, the process can be described by an equilibrium sorption isotherm. If the rate of sorption is slow or of the same order of magnitude as advective-diffusive transport rate of solute, the process must be described by a kinetic sorption model. Some sorption processes may be more complicated and must be described by more complicated models which may include multi-step reaction and/or diffusion steps (Wu and Gschwend, 1986).

2.5.1 Equilibrium Sorption Isotherm

Linear Sorption Isotherm

The simplest and most widely used equilibrium sorption isotherm is the linear sorption isotherm which is given by a linear relationship between the solute concentration in solution, C, and sorbed on solid, P

$$P = K_d C \tag{2.43}$$

where K_d is the distribution coefficient, which is a measure of the retention of solute by the solid.

The linear isotherm model has been used frequently to describe the sorption of radioactive materials by soils (Burkhoider, 1976; Van De Pol et al., 1977). Davison et al. (1968), Scott and Phillips (1972) and Sleim et al. (1977) have employed Eq. 2.43 in studies of the movement of herbicides in the soil column. Lai and Jurinak (1972) and Lai et al. (1978) have used the linear isotherm for the sorption of metals, i.e. Na^+ and Mg^{2+}, on soils in their studies of cation sorption during convective-diffusive flow through soil. Overman et al. (1976) have used this isotherm in their study of phosphorous transport. Since the linear isotherm can be conveniently incorporated into solute transport models and is easily determined, it has also been used in a number of studies to predict the rate of movement of solute fronts (Anderson, 1979; Faust and Mercer, 1980 and Srinivasan and Mercer, 1988). However, a limitation of this isotherm is that it does not include any upper limit to the amount of solute that can be sorbed onto the solid.

Freundlich Sorption Isotherm

A more general equilibrium sorption isotherm is the Freundlich isotherm, which is defined by a nonlinear relationship

$$P = k'_1 C^N \qquad (2.44)$$

where k'_1 and N are constants. When $k'_1 = K_d$ and N = 1, Eq. 2.44 reduces to the linear sorption isotherm (Eq. 2.43).

The Freundlich isotherm has been widely applied to model the sorption of various metals such as copper, zinc and cadmium by Sidle et al. (1977), molybdenum by Jarrell and Sabey (1977) and cadmium by Garcia-Miragaya and Page (1976) and Street et al. (1977). Bowman and Sans (1977), Van Bladel and Moreale (1977) and Yaron (1978) proposed the use of Eq. 2.44 to describe the sorption of herbicides and pesticides on soils. Fitter and Sutton (1975), Harter and Foster (1976) and White and Taylor (1977) fitted data on phosphorous sorption on soil to Freundlich isotherm. Nathwani and Phillips (1977) reported the equilibrium distribution of the hydrocarbons benzene, toluene, o-xylene and n-hexadecane between the liquid and sorbed phase in soil following the Freundlich isotherm. Note however that this sorption isotherm suffers from the same fundamental problem as the linear isotherm, that is, there is no upper limit to the amount of the solute that can be sorbed, so that the solid is never saturated.

Langmuir Sorption Isotherm

The Langmuir isotherm was developed by Langmuir (1918) based on the concept that a solid surface processes a finite number of sorption sites. When all the sorption sites are filled, the surface will no longer sorb the solute. The standard form of this isotherm is

$$\frac{P}{C} = \frac{P^m}{\frac{1}{k'_2} + C} \tag{2.45}$$

where P^m is the maximum amount of solute that can be sorbed and k'_2 is a sorption constant related to the binding energy.

The Langmuir model has been used extensively to describe the sorption of solutes, i.e., metals, phosphorous etc., by soil. Thus, for example copper, lead, cadmium and zinc sorbed to soil were shown to follow the Langmuir isotherm by Singh and Sekhon (1977a and 1977b), Harter (1979) and Shukla and Mittal (1979) in their studies on metals distribution and transport by flow in soil. This isotherm was also used by Enfield and Bledsoe (1975) and Novak et al. (1975) to model the movement of phosphorous in soils resulting from the renovation of waste water by a land application treatment system.

All the equilibrium models assume that the rate of change of concentration due to sorption is much greater than that due to the advective and diffusive transport. If this is not the case, a kinetic model is needed.

2.5.2 Kinetic Sorption Models

Reversible Linear Kinetic Sorption Model

The most frequently used kinetic sorption model is the kinetic form of the linear sorption isotherm, which is called a reversible linear kinetic sorption model,

$$\frac{dP}{dt} = k'_3 C - k'_4 P \tag{2.46}$$

where k'_3 and k'_4 are forward and backward sorption rate coefficients. Equation 2.46 can also be written in a different form (Nielsen et al. 1986)

$$\frac{dP}{dt} = k'_4(K_d C - P) \tag{2.47}$$

where k'_4 is the first-order rate coefficient. If sufficient time is available for the system to reach equilibrium, $dP/dt \rightarrow 0$, so that $P = K_d C$, which is the linear sorption isotherm.

One of the most frequent applications of Eqs. 2.46 or 2.47 is in the description of sorption kinetics of phosphorous in soil. Among those who have used this model to describe the movement of phosphorous through soil are Enfield and Bledsoe (1975), Enfield et al. (1976), Shah et al. (1975) and Novak and Petschauer (1979). Leistra and Dekkers (1977) applied this model to describe simultaneously fast and slow sorption phenomena that occur with the addition of pesticides in solution to soil. Cho (1971) also used Eq. 2.47 for calculations the convective transport of various oxides of Nitrogen in soil.

Reversible Nonlinear Kinetic Sorption Model

Corresponding to Freundlich sorption isotherm, the reversible nonlinear kinetic sorption model is expressed as

$$\frac{dP}{dt} = k'_5 C^N - k'_6 P \tag{2.48}$$

where k'_5 and k'_6 are the forward and backward sorption rate coefficients, respectively, and N is a constant. When N = 1, Eq. 2.48 reduces to the reversible linear kinetic sorption model. If the system reaches equilibrium, $dP/dt \rightarrow 0$, we obtain $P = (k'_5/k'_6)C^N$, which is the Freundlich sorption isotherm.

Hornsby and Davidson (1973) used this model to describe the transport of the organic pesticide fluometuron in soils. The distributions of the sorbed and solution phases of the pesticide were well described at high flow rates. At low flow rates, where equilibrium conditions existed, the kinetics of the sorption was not too important, and the process was described equally well by the Freundlich isotherm. Enfield et al. (1977) and Fiskell et al. (1979) found that phosphorous movement in the soil could be described with the reversible nonlinear kinetic model with the value of N less than unity.

Bilinear Kinetic Sorption Model

The kinetic version of the Langmuir isotherm is given by the bilinear kinetic sorption model:

$$\frac{dP}{dt} = k'_7 C(P^m - P) - k'_8 P \qquad (2.49)$$

where k'_7 and k'_8 are the constant. The theoretical foundation for Eq. 2.49 is the same as that for the Langmuir sorption isotherm. If the time is sufficient, $dP/dt \rightarrow 0$, and Eq. 2.49 is reduced to the Langmuir isotherm.

Gupta and Greenkorn (1973) and Kuo and Loste (1974) have applied the model to the study of sorption of phosphorous on clay minerals. Despite its strong theoretical foundation, Eq. 2.49 has not received widespread application. One reason is that the constituent transport equation coupled with Eq. 2.49 is difficult to solve for.

Mass Transfer Model

If the rate of solute sorption is controlled by the mass transport process from solution to solid surface, the mass transfer model is applied

$$\frac{dP}{dt} = k'_g(C - C^*) \qquad (2.50)$$

where k'_g is a sorption rate parameter that accounts for the diffusive transport of the solute through a liquid layer surrounding the solid, and C^* is the liquid phase concentration of the solute in immediate contact with the solid surface. The mass transfer model has been used by Navok and Pelschauer (1979) to describe orthophosphate sorption and used by Vilker (1980) to describe the capacity of activated sludge to sorb pathogenic viruses.

All the isotherms and kinetic models discussed above are called one-box or one-step models, in which sorption is a function of the solute concentration sorbed on the sorbent (viewed as a completely mixed box) and concentration in solution (Lapidus and Amundson, 1952 and Oddson et al., 1970). However, some sorption processes are complicated, e.g., when a rapid initial intake is followed by a slower approach to equilibrium (Karickhoff, 1980), and for these cases the one-step model is not accurate enough to describe processes kinetics. As a results, advanced model, which typically include more than one step, have been applied.

2.5.3 Advanced Sorption Models

Diffusion-Sorption Model

To describe the sorption of hydrophobic organic chemicals, i.e., chlorobenzene congeners, to and from suspended sediment and soil particles, Wu and Gschwend (1986) combined diffusive penetration and the linear isotherm to develop their two-step sorption model. The model is based on the following assumptions

(1) The ambient fluid is sufficiently turbulent that an exterior boundary layer does not limit sorptive exchange.

(2) The porous sorbent, i.e., suspended sediment and soil particles, is spherical and homogeneous. The rate at which the sorbate molecules diffuse through the pore fluids held in the interstices of the porous sorbent is expressed as

$$\frac{\partial[(1-n)\rho_s P'(r) + nC'(r)]}{\partial t} = D_m n\left[\frac{\partial^2 C'(r)}{\partial r^2} + \frac{2}{r}\frac{\partial C'(r)}{\partial r}\right] \qquad (2.51)$$

where C′ is the solute concentration in the pore fluid, P' is the solid bound solute concentration, n is the porosity of the sorbent, r is radial distance, ρ_s is the specific gravity of the sorbent, D_m is the molecular diffusion coefficient and $(1-n)\rho_s P'(r) + nC'(r)$ is the local total volumetric concentration in the sorbent.

(3) The solute concentrations in pore fluid and that bounded by solid are locally in equilibrium and are described by linear isotherm

$$P' = K_d C' \qquad (2.52)$$

By incorporating Eqs. 2.51 and 2.52 into the convective-diffusive transport equation, Wu and Gschwend (1988) simulated the sorption of nonpolar organic chemicals transported in an aqueous system containing a spectrum of particle sizes.

ME-SORB Model

For assessments of the impact of bottom sediment resuspension events on an aquatic ecosystem, DePinto et al. (1994) developed the ME-SORB model. This model is intended

to be used in formulating a mechanistic description of metal ion sorption onto and/or desorption from sediments. The following five steps are examined and included in the model.

(1) Bulk transport--transfer of material from liquid bulk solution to the liquid surface film surrounding the particle. In a well mixed suspension, this step is normally rapid and not rate limiting.

(2) Film transport--transfer of the material through the surface film, which usually is a thin layer of quiescent liquid lying between the bulk solution and the sorbent particle surface.

(3) Surface sorption--sorption of the material on to the surface of sorbent.

(4) Pore diffusion--transport of the sorbate radially between the particle surface and the center of the particle through the intra-particle pore space.

(5) Pore sorption--sorption of diffused material on to the walls of the pores.

Each of these steps can occur in either the forward or reverse direction depending on the sorbate gradient at a particular point. One or more steps may be insignificant compared to others at a particular condition. The model was calibrated by resuspension experiments carried in the Trenton Channel (Theis, 1988), and was applied to predict bulk solution concentration versus time relations for lead, nickel and cobalt desorption from sediment during a resuspension event.

Since the advanced sorption models include more transport and sorption processes, they are usually more accurate in simulating the real process. However, the calibration procedure for these models becomes more difficult and complicated than for simpler but less accurate models. That is the reason why simpler sorption models are still widely used.

2.6 Sediment-Associated Contaminant Transport

The transport of contaminant in the three-layered water - fluid mud - bed system shown in Fig. 2.7 must include dissolved contaminant transport, particle-bound contaminant transport (related to sediment transport) and sediment-contaminant interaction, i.e., sorption/desorption. In this system, contaminant transport exhibits different characteristics within each of the three layers. Contaminant fluxes across the water-fluid mud interface and the fluid mud-bed interface represent the connective conditions for each of the two adjacent layers and control the rates of contaminant exchange between them. The fluxes across the water surface and bed bottom represent the boundary conditions.

2.6.1 Contaminant Transport in Water

In the water layer under wave motion, dissolved contaminant transport is governed by the diffusion process, which includes molecular diffusion and wave-induced diffusion, and also by sorption/desorption kinetics. Since particle-bound contaminant transport occurs together with the sediment to which the contaminant is sorbed, the transport of particle-bound contaminant is determined by sediment transport and the kinetics of sorption/ desorption. Sorption/desorption of contaminants onto/from the sediment is dependent on contaminant (sorbate) characteristics, sediment (sorbent) characteristics and on water quality (pH value, salinity, temperature, etc.).

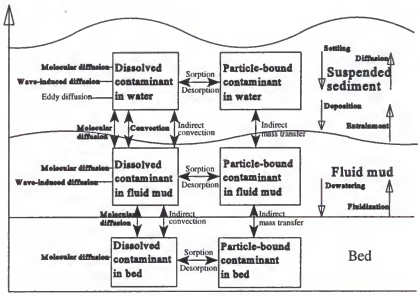

Figure 2.7 Sediment-associated contaminant transport processes.

Considering the water layer as a well mixed layer and ignoring the vertical transport and distribution in water, Onishi (1982), O'Connor (1988a, 1988b and 1988c), Basmadjian and Quan (1988) and Wang et al. (1991) used the depth-averaged contaminant concentration of water layer in their transport models. Onishi (1982) formulated a horizontal two-dimensional sediment and contaminant transport model named FETRA, by coupled a sediment transport sub-model, a dissolved contaminant transport sub-model and a particulate contaminant transport sub-model. The dissolved contaminant transport sub-model includes (1) advection and diffusion/dispersion of dissolved contaminants; (2) sorption (uptake) of dissolved contaminants by both moving and stationary sediment or desorption from sediment into water; and (3) chemical and biological degradation, or radio nuclide decay of contaminants. The particulate contaminant transport sub-model includes (1) advection and

diffusion/dispersion of particulate contaminants; (2) sorption (uptake) of dissolved contaminants by sediments or desorption from sediments into water; (3) chemical and biological degradation, or radio nuclide decay of contaminants; and (4) deposition of particulate contaminants onto the river bed or erosion from the river bed. The sorption of contaminant between the water and solid phases is described by the linear sorption isotherm. The model was applied to the James River estuary to simulate the transport of sediment and the pesticide Ketone.

O'Connor (1988a) has developed the equations that define the steady state distribution of solids and sorptive chemicals in fresh water systems. The dissolved and particulate phases of chemicals, as well as the sediment, are considered and yield a series of six simultaneous equations for depth-averaged values in the water and bed layers considered to be totally mixed. Instantaneous equilibrium is applied to the chemical sorption between the dissolved and particulate states. The solution of the equations is applied to steady state and time-variable conditions in (1) lakes and reservoirs (O'Connor, 1988b) and (2) streams and rivers (O'Connor, 1988c) under different flow and wastewater discharge conditions.

Basmadjian and Quan (1988) developed the differential equations that describe the fate of chemicals in rivers as they transfer, react and volatilize, both during contamination and recovery. The sorption reaction in the water layer is given by linear isotherm. The water column is assumed to be well-mixed and vertical and lateral concentration changes in the water layer are neglected. Diffusive transport in the direction of flow is neglected compared to advective transport in this direction. An explicit analytical solution is obtained for the 1-D unsteady distribution of chemicals in both the aqueous and sediment phases.

Considering the vertical transport and distribution of contaminants in the water layer, Hayter and Pakala (1989), Huber and Dickinson (1992), Sheng (1993) and Chen (1994) used 3-D models to simulate the contaminant transport in water column. The diffusion coefficients of dissolved contaminants in water are same as the eddy diffusivity. The particulate part of contaminants transports together with the sorbent, i.e. sediment, which can be obtained by the coupled 3-D hydrodynamic and sediment transport models. The first-order reversible kinetic model is used in these models to describe the sorption process. Hayter and Pakala (1989) applied their CONTAM-3D model to a partially stratified tidal river, Sampit River, South Carolina, to predict the lead transport and distribution in this river. Huber and Dickinson (1988) used their water quality model for simulating various phosphorus component distributions in Lake Okeechobee, Florida. Sheng (1993) and Chen (1994) applied his model to Lake Okeechobee and Tampa Bay for prediction of phosphorus and nitrogen transport transformation and distributions in both water and bottom sediments.

2.6.2 Contaminant Transport in Bottom Sediment

Compared to the movement in water, the movement of interstitial water in the bottom layer tends to be considered slower. Thus, Onishi (1982) neglected contaminant transport and sorption within the bottom layer. In his FETRA model only sorption/desorption between water and bottom sediment surface is considered. However, since bottom sediment may be an important sink and/or source of contaminants, contaminant transport and transformation within the bottom layer must be taken into account. Contaminant transport in bottom sediment includes dissolved contaminants transport, particulate contaminant transport and sorption.

For modeling the vertical movements of pore water and dissolved constituents in the bottom sediment layer, Berner (1980) gave the general diagenetic equation, which is expressed as

$$\frac{\partial \hat{C}_i}{\partial t} = \frac{\partial\left(\hat{D}_i \frac{\partial \hat{C}_i}{\partial z}\right)}{\partial z} - \frac{\partial(\hat{w}\hat{C}_i)}{\partial z} + \Sigma \hat{R}_i \qquad (2.53)$$

where $\hat{C}_i$ is the concentration of component i in terms of mass per unit volume of total sediment (solids plus water), $\hat{D}_i$ is the diffusion coefficient of component i, $\hat{w}$ is the velocity of flow relative to sediment-water interface, $\hat{R}_i$ is the rate of reaction and z is the coordinate with origin at the sediment-water interface and directing vertical downward. The first term on the right side of Eq. 2.53 is the diffusion term, the second term is the advection term and the third one is the term for chemical, biological and radiogenic reactions. The relative flow velocity and diffusion coefficient depend on bottom sediment characteristics, overlying water motion and contaminant properties, etc. and are site-specific. To solve Eq. 2.53, $\hat{w}$, $\hat{D}_i$, as well as $\hat{R}_i$, must be provided.

For a mud bed, the self-weight consolidation is an important way by which advective transport of water and its dissolved constituents is produced. A series of studies for one-dimensional consolidation of saturated clays was carried out by Gibson et al. (1967, 1981), Znidarcic et al. (1984) and Schiffman et al. (1984). Base on these studies, the general consolidation equation in term of the void ratio, e, is expressed as:

$$\left(\frac{\rho_s}{\rho_f} - 1\right)\frac{d}{de}\left[\frac{k_w(e)}{1+e}\right]\frac{\partial e}{\partial z} + \frac{\partial}{\partial z}\left[\frac{k_w(e)}{\rho_f(1+e)}\frac{d\sigma'}{de}\frac{\partial e}{\partial z}\right] + \frac{\partial e}{\partial t} = 0 \qquad (2.54)$$

where k_w is the permeability which is a function of void ratio e, σ' is the effective normal stress and ρ_f is the pore water density.

To solve Eq. 2.54 requires the effective stress/void ratio, $\sigma'(e)$, and the permeability/void ratio, $k_w(e)$, relationships. By introducing the assumption that the effective stress/void ratio and permeability/void ratio are relationships linear and that the consolidation coefficient, $C_F = [-k(e)/\rho_f(1+e)]\ d\sigma'/de$, is a constant, Lee and Sills (1981) solved Eq. 2.54 analytically. It should be noted, however, that the $\sigma'(e)$ and k(e) relationships are in general nonlinear functions for real soils and are also site-specific. Furthermore, the consolidation coefficient, C_F, is usually not a constant. Thus, numerical modeling is generally needed for solving Eq. 2.54. In that connection, Gibson et al. (1967 and 1981) have developed the theory and solutions for the finite nonlinear consolidation of both thin and thick homogeneous layers. Macay et al. (1986) applied the theory to quiescent consolidation of phosphatic waste clays. Since the $\sigma'(e)$ and k(e) relationships are site-specific, experiments are required to supply these relationships for numerical modeling. Znidarcic et al. (1984) has summarized existed testing procedures for laboratory consolidation experiments and found that the current laboratory methods are restricted in their applicability and only give approximate soil properties for theoretical calculation and numerical modeling.

In the vicinity of the sediment-water interface, advective transport of pore water and dissolved constituents is affected by the overlying water motion and thus is enhanced. Savant et al. (1987) carried out laboratory experiments and numerical simulations to investigate the transport of chemically inert, non-sorbed contaminants in a river sediment and showed that interstitial fluid advection controlled contaminant transport within the stable sediment bed with an in-bed Peclet number on the order of 100~1,000. These high Peclet numbers indicated the negligible influence of molecular diffusion under the conditions examined. Through an analytical solution of the two-dimensional Navier-Stokes equation for oscillatory flow over a rippled bed, it was examined the transport of reactive solutes (governed by a first-order kinetic model below the rippled bed) under wave motion and the enhanced exchange of non-reactive solutes across the water-sediment interface. Shum concluded that the wave-induced pore water circulation below the rippled bed and the total wave-induced exchange across the water-sediment interface increased with the wave height and decreased with the wave period.

For the mud bed, the permeability is much lower than that of sand bed, so that the bed is typically considered to be impermeable over comparatively short time-scales, e.g., of the order of wave motion. However, the mud bed may be fluidized under wave motion and form a fluid mud layer. Thus, although advective transport may be negligible in the fluid mud layer, the mixing process will be obviously enhanced because of its slurry-like properties and oscillation under wave motion.

Contaminant diffusion in the interstitial water takes place in accordance with Fick's laws of diffusion (Crank, 1975), which are

(1) first law:

$$J_i = -D_i \frac{\partial \hat{C}_i}{\partial z} \tag{2.55}$$

(2) second law:

$$\frac{\partial \hat{C}_i}{\partial t} = -\frac{\partial J_i}{\partial z} = \frac{\partial \left(D_i \frac{\partial \hat{C}_i}{\partial z} \right)}{\partial z} \tag{2.56}$$

where J_i is the diffusion flux of component i.

Within the undisturbed sediment that is relatively far below the sediment-water interface and is not affected by the overlying water motion, diffusion can be only due to molecular diffusion. Due to the presence of particles, it is not easy for dissolved contaminants to diffuse in any direction within the sediment as they do in the overlying water layer. Instead, diffusion is hindered by the solid particles and follows tortuous paths of fluid flowing between and around particles. Mathematically, tortuosity, θ, is defined as (Fetter, 1981)

$$\theta = \frac{dl}{dz} \tag{2.57}$$

where dl is the length of the actual sinuous path over a depth interval dz. The diffusion coefficient of component i, in terms of tortuosity, is expressed as

$$D_i = \frac{D_m}{\theta^2} = \omega_\theta D_m \tag{2.58}$$

where ω_θ is a coefficient that is related to the tortuosity (Bear, 1972). Perkins and Johnson (1963) found that ω_θ was equal to 0.7 in sand columns studies using a uniform sand. In laboratory studies for geologic materials, Freeze and Cherry (1979) found that ω_θ ranged from 0.5 to 0.01. Also, according to Li and Gregory (1974) and McDuff and Ellis (1979), an average θ value for deep sea clays is 1.8. The molecular diffusion coefficients of some ionic constituents in typical muds with porosity, n, are listed in table 2.1.

The typical molecular diffusion coefficient is seen to be in the range of $10^{-10} \sim 10^{-9}$ m^2/s, while the kinematic viscosity, ν, of water is around 10^{-6} m^2/s. Thus, the Schmidt Number, Sc, which is the ratio of mass transfer rate to momentum transfer rate, i.e., $Sc = \nu/D_m$, in the nonturbulent environment is about 1/1,000 ~ 1/10,000, an extremely low range.

Table 2.1 Diffusion coefficients for some tracers in some typical marine mud beds.

Component	Porosity, n	D_m (10^{-10} m^2/s)
Na^+	0.71	7.4
Ca^{++}	0.71	7.4
Cl^-	0.71	10.2
SO_4^-	0.71	5.0
SO_4^-	0.772	5.0
SO_4^-	0.64	4.0
NH_4^+	0.72	9.8
HPO_4^-	0.72	3.6

Near the sediment-water interface, due to the effect of overlying water motion, diffusion is not solely due to molecular diffusion. Vanderborght et al. (1977) analyzed the

vertical transport of dissolved constituents in a large muddy zone along the Belgian North Sea coast. They selected a diffusion coefficient that was 100 times larger than that for molecular diffusion down to 3.5 cm depth from the sediment-water interface. In the lower compact layer diffusion was only due to molecular movement. This two-layered model of bottom sediments was applied to simulate the vertical transport and profile of dissolved silica, oxygen, sulfate, nitrate and ammonium.

DePinto (1994) in his Green Bay study classified the range of 0 ~ 4 cm depth below bottom sediment surface as surface-mixed sediment layer, and the lower layer as subsurface-mixed sediment layer. The fate and transport properties of contaminants in these two layers were recognized and modeled separately in his GBTOX model. Berger and Heath (1968) used an "box-model" approach to represent the active surfacial sediment layer in which a fast rate of mixing occurs over a certain depth over which sediment properties are uniform.

In the three-layered system shown in Fig. 2.6, the fluid mud oscillates under wave motion. In this layer, contaminant diffusion will include the molecular diffusion and wave-induced diffusion as a result of the effect from overlying water motion. Therefore, the production, decay and transport of fluid mud can be expected greatly affect contaminant transport between water and bottom sediment.

2.6.3 Fluxes Across the Sediment-Water Interface

Contaminant flux across the water-fluid or bed interface controls the rate of contaminant mass transfer between water and bottom sediment. The accumulation of contaminants in bottom sediments and the release of bottom contaminant are both controlled by this flux. Generally, this flux is composed of dissolved and particulate contaminant

subfluxes. The dissolved part is transported by diffusion and advection, whereas the particulate part is transported together with the sorbent, i.e., sediment. Thus, resuspension and deposition of sediment can strongly influence the particulate contaminant flux across the interface.

The transport of materials across a solid boundary surface and a moving fluid or a interface between two relatively immiscible moving fluids is defined as convection (Welty, et al., 1969). The flux of convective mass transfer is expressed in the form

$$F_i = k_c \Delta C_i \tag{2.59}$$

where F_i is the mass flux of component i across the interface, ΔC_i is the concentration difference of constituent i across the interface and k_c is the convective mass-transfer coefficient.

The so called film theory for mass transfer is based on the assumption of the presence of a fictitious film at the interface that offer the same resistance to mass transfer as actually exists in the entire field. Accordingly, the convective mass transfer coefficient is modeled as

$$k_c = \frac{D_i}{\delta_f} \tag{2.60}$$

where D_i is the molecular diffusion coefficient of component i and δ_f is the film thickness. Thus, the mass transfer coefficient, k_c, is a function of molecular diffusion coefficient D_m and the chemical and hydrodynamic parameters that determine the film thickness, namely, water

viscosity, ν, bottom friction velocity, u_*, and the Schmidt number, Sc (Boudreau and Guinasso, 1982). Expressions for k_c are generally expressed as

$$k_c = \alpha_{12c} u_* Sc^{-\beta_{12c}} \tag{2.61}$$

where coefficient α_{12c} is in the range of 0.04 ~ 1.0 and β_{12c} is in the range of 2/3 ~ 1.

The so-called penetration theory was first proposed by Higbie (1935) based on the idea that the diffusive component only penetrates a short distance into the phase of interest. This theory has been subsequently applied to turbulent flow by Danckwerts (1951). The convective mass-transfer coefficient based on this theory is expressed as

$$k_c = \sqrt{D_i s} \tag{2.62}$$

where s is the surface-renewal factor. Toor and Marchello (1958) have pointed out that the penetration concept is valid only when surface renewal is relatively rapid, in which case $k_c \sim \sqrt{D_i}$. For relatively slow surface renewal, the film theory is valid in which $k_c \sim D_i$. In reality the convective mass-transfer coefficient is proportional to a power of the molecular mass diffusivity, D_i, between 0.5 and 1.0.

In studying diffusive fluxes across the sediment interface, Morse (1974) considered that there exists a stagnant benthic boundary layer just over the sediment-water interface. The transport of dissolved constituents across this layer is purely by molecular diffusion, while the transport in the main water column overlying the boundary layer is by turbulent mixing. The maximum possible thickness of the stagnant layer is on the order of 1 cm, which is within the limit of the calculations of Wimbush (1970) for the South Pacific.

Santschi et al. (1983) investigated the resistance of chemical transport within the deep-sea boundary layer and concluded that the equivalent stagnant boundary film thickness is about 0.47 mm. The result is based on the directly measurements of $CaCO_3$ dissolution and Mn^{++} released from bottom sediment at a site in the eastern Pacific.

Under wave motion the exchange of water and dissolved constituents between water and bottom sediments is evidently enhanced due to wave-induced diffusion and advection in the near interface layer. Savant et al. (1987) and Shum (1992,1993) examined contaminant release from sandy beds under wave motion. They found that wave-induced advection, which causes a flux across the interface, is so great that molecular diffusion can be neglected.

In contaminant transport modeling, DePinto (1994) used a diffusion process which included the effects of diffusion and advection induced by external hydrodynamics to describe contaminant transport across the sediment-water interface. Hayter and Pakala (1989) considered contaminant sorption/desorption onto/from the bottom sediment surface and advection due to bottom sediment consolidation in their CONTAM-3D model. Chen (1994) only included advective transport due to the hydrodynamic effect on the bottom but neglected the effect of diffusion in his three-dimensional contaminant transport model.

Particle-bound contaminant flux has been shown to be related to the sediment entrainment and deposition rates and to contaminant sorptive properties in water and fluid mud or bed (Onishi, 1981; O'Connor, 1988; Hayter and Pakala, 1989, DePinto, 1994 and Chen, 1994). However, one issue that has not always been fully accounted for by most investigators is that together with the entrainment and deposition of sediment, water is also

entrained and deposited. Thus, sediment mass transfer between the water and fluid mud or bed layers can not only induce particle-bound contaminant transfer between the two layers, but also enhance dissolved contaminant transfer. This is the dissolved contaminant mass transfer through water exchange induced by sediment entrainment and deposition, which must be considered when entrainment and/or deposition take place.

2.6.4 Fluxes Across the Fluid Mud-Bed Interface

Contaminant transfer across the fluid mud -bed interface can also be divided into two parts: dissolved part and particulate part. When the bed is fluidized or fluid mud dewaters to become part of bed, the particle-bound contaminants will be effectively transported across the interface. However, under those situations in which only an equilibrium fluidization depth occurs, as in the present case, there will be no sediment mass transfer is considered across the interface and also no particulate contaminant transport across the interface.

For dissolved contaminants, since around the fluid mud-bed interface there is typically no disturbance from the overlying water motion, molecular diffusion may be the only diffusion process across the interface. In the GBTOX model (DePinto, 1994), the transfer of unbounded PCB between the surface-mixed and the subsurface-mixed sediment layers is only by molecular diffusion. Vanderborght et al. (1977) also considered only the molecular diffusion to describe dissolved silica flux across the interface between the top 3.5 cm bed layer and the more compact lower layer of the bed.

Consolidation may be the main advective process for dissolved contaminants across the fluid mud-bed interface. However, typically consolidation is a slow process, in

comparison with wave-induced transport. Thus, for example for an episodic event, consolidation is usually neglected.

CHAPTER 3
MUD FLUIDIZATION BY WAVES

3.1 Introduction

The rheological and mass transport characteristics of fluid mud can be significantly different from those of the non-fluidized bed. Thus, once fluid mud develops, it must be considered separately from the non-fluidized bed, as noted in Section 2.3.

The main step for setting up the three-layered water-fluid mud-bed system is the determination of the thickness of the fluid mud layer. Fluidization is a time-dependent process starting with a bed over which wave motion commences initially in clear water. Thus, it is a function of the wave characteristics and bottom mud properties. In this chapter, by assuming the mud bed to be a single-phase continuum, fluidization is considered in terms of forcing due to cyclic normal pressure loading and the horizontal pressure gradient. First, the mechanism of fluidization of mud beds by waves is examined. The bed is considered to fluidize when the effective submerged weight of the particle or floc is exceeded by the upward inertia force due to bed vibration. Then, by characterizing the bed as a uniaxial extensional-Voigt solid, it is represented in terms of an equivalent spring-dashpot-mass system. The dependence of the fluidization depth on characteristic wave and bed rheological parameters is examined for a water-bed and a water-fluid mud-bed system represented, respectively, as one-degree and two-degrees of freedom analogs. Theoretical results obtained

are compared wave flume data obtained by Ross (1988), Lindenberg et al. (1989) and Feng (1992) on fluid mud thickness. Finally the model is applied to lake Okeechobee in Florida, where fluid mud thicknesses were measured previously.

3.2 Mechanics of Fluidization

3.2.1 Vertical and Horizontal Motions of Bed under Waves

For a mud bed under waves, two aspects of wave motion can be distinguished (Ross, 1988): "pumping" due to cyclic normal stress on bed surface and "shaking"due to cyclic shear stress on bed surface. Pumping is responsible for bed motion in the vertical direction, while shaking may cause bed motion in the horizontal direction.

The gradients of pressure and shear stress on the bed provide the forcing for the horizontal motion of the bed. Dalrymple and Liu (1978) compared results on water wave attenuation from their wave-soft bed interaction model with results from Gade's (1957) inviscid, shallow water model, and found that despite Gade's neglect of viscosity in the upper fluid, and therefore absence of shear stress at the interface, both solutions agreed reasonably well with the laboratory data collected by Gade. A conclusion can therefore be drawn that the principal mode of energy transfer to the mud is the normal stress rather than the shear stress, due to wave-induced work on the lower medium. Isobe et al. (1992) carried out experiments to check the predominance of forces for mud bed horizontal motion. In one experiment, the bed was covered with a nylon sheet which transferred the pressure and but not the shear stress. A second experiment was done without cover. The results showed that wave height decay with and without the cover were almost same over a wide range of

incident wave heights. This also implies that the pressure gradient due to wave motion is the dominant external force for the mud horizontal motion and wave energy dissipation.

Under wave motion mud beds are known to fluidize, and a fluid mud layer of equilibrium thickness is observed to occur after a certain elapsed time depending on the initial conditions with respect to the mud-water system and the forcing wave characteristics. Thus, a mechanistic framework for explaining mud bed fluidization must be based on a consideration of forces required to cause particle-particle separation, hence a loss of effective stress. These forces can be considered in three ways: (1) forces in the vertical direction, (2) forces in the horizontal direction and (3) combination of vertical and horizontal forces.

3.2.2 Bed Failure by Horizontal Forces

Madsen (1974) hypothesized that a large horizontal pressure gradient can cause bed failure. The criterion for failure was expressed in a non-dimensional form:

$$-\frac{1}{\rho_w g}\left(\frac{\partial p_p}{\partial x}\right)_{crit} = \frac{\rho_3 - \rho_w}{\rho_w}\tan\phi \qquad (3.1)$$

where p_p is the wave-induced pore pressure in excess of the hydrostatic pressure, ρ_w is the water density, g is the gravitational acceleration, ρ_3 is the bed density and ϕ is the friction angle. This shear failure criterion is applicable only to non-cohesive sediment, because the effects of cohesion and rheology are not included. Modifying Eq. 3.1 by introducing cohesion, C_h, and the multiplying factor $\rho_w gD$ for both sides of the equation, we obtain a more general, stress-form, criterion

$$-\left(\frac{\partial p}{\partial x}\right)_{crit} D = \rho_w g' D \tan\phi + C_h \qquad (3.2)$$

where the effective gravitational acceleration, $g' = g(\rho_3 - \rho_w)/\rho_w$ and D is the diameter of the particle or floc. By using the definition of the effective stress $\sigma' = \rho_w g' D$ and referring to the well-known Coulomb equation for shear strength, $\tau_s = \sigma' \tan\phi + C_h$, Eq. 3.2 can be expressed as

$$\begin{aligned} -\left(\frac{\partial p_p}{\partial x}\right)_{crit} D &= \rho_w g' D \tan\phi + C_h \\ &= \sigma' \tan\phi + C_h = \tau_s \end{aligned} \qquad (3.3)$$

Thus, when the horizontal pressure difference equals the bed shear strength, the mud bed fails. The inter-connections between the particles or flocs are cut off at that level where Eq.3.3 is satisfied and the bed above that level is fluidized at that instant.

Although Madsen (1974) successfully used the criterion, $-(\partial p_p/\partial x)_{crit}/\rho_w g = 0.5$, for loose sand liquefaction, the use of Eq. 3.3 for the mud bed may lead to an underestimation of fluidization. The reason is that Eqs. 3.1, 3.2 and 3.3 are obtained by considering forces in the horizontal direction only. For sandy beds this may be acceptable because there may be practically no vertical motion of the bed under waves. However, for the mud bed, oscillations under wave action are typically significant and cannot be neglected.

In the following development, we show that a vertical oscillation of the mud bed produces an upward inertia stress, σ_i, that can greatly reduce the effective stress. Also, the

buildup of the excessive pore pressure, Δu_w, will reduce the effective stress. Thus, Eq. 3.2 can be applied for the mud bed under long wave action, in which motion in the vertical direction is negligible and the excessive pore pressure buildup is minor.

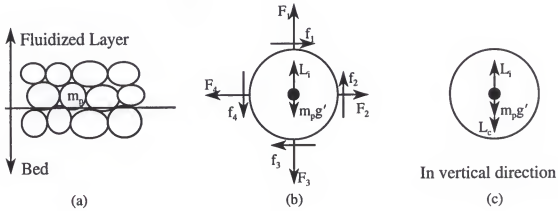

Figure 3.1 Forces on a particle or floc. F_1, F_2, F_3 and F_4 = normal forces from adjacent particles; f_1, f_2, f_3 and f_4 = shear forces from adjacent particles; L_i = inertia force; L_c = cohesive resistance; m_p = particle mass and g' = effective gravity: a) Bed and fluidized mud with tagged particle forming a part of the lower boundary of fluid mud; b) forces on tagged particle; c) forces in the vertical direction.

3.2.3 Bed Fluidization by Vertical Forces

Consider a particle (or a cohesive floc treated as an integral particle) mass m_p in the mud bed under wave motion as shown in Fig. 3.1. Four types of forces acting on this particle must be recognized: (1) effective gravity or buoyancy in water, (2) inter-particle cohesive forces, (3) normal and shear forces due to contacts between adjacent particles, and (4) inertia force due to vibration, $L_i(t)$, under wave loading. Considering the forces in the vertical direction, the normal and shear forces (F_1, F_2, F_3, F_4, f_1, f_2, f_3, and f_4) due to contacts between adjacent, almost randomly positioned, particles can be represented together as a

downward cohesive resistance (force), $L_c(t)$, as a first order approximation. Thus, the L_c can be expressed as

$$L_c(t) = \begin{cases} 0 & (L_{imax} - m_p g' \leq 0) \\ L_i(t) - m_p g' & (0 < L_{imax} - m_p g' < L_{cmax}) \\ 0 & (L_{imax} - m_p g' \geq L_{cmax}) \end{cases} \quad (3.4)$$

where L_{cmax} is the maximum value of $L_c(t)$ and L_{imax} is the maximum value of $L_i(t)$.

While the bed can sustain great pressure, it cannot withstand significant stretching. Thus, in the vertical direction, when the sum of the upward forces, L_{imax}, equals (or just exceeds) the sum of the downward forces, $m_p g' + L_{cmax}$, the bed is critically stretched, the connections between particles are broken and incipient bed fluidization occurs. We therefore select the criterion for fluidization at any point to be that instant when the effective submerged weight of the particle in water plus cohesive resistance, $m_p g' + L_{cmax}$, is exceeded by the maximum upward inertia force, L_{imax}, due to wave-induced vibration. Thus,

$$L_{imax} \geq m_p g' + L_{cmax} \quad (3.5)$$

Eq. 3.5 can be written in a stress form for the zero excess pore pressure condition, $\Delta u = 0$, (Fig. 2.4) as

$$\sigma_{imax} = \rho_w g' D + C_r = \sigma' + C_r \quad (3.6)$$

where $\sigma_i(t)$ is the inertia stress induced by the vertical vibration of the bed, σ_{imax} is the maximum value of $\sigma_i(t)$, and C_r is the cohesive resistance stress, which is different from C_h in Eq. 3.3. Note that C_h is the shear resistance when the normal stress is zero and its magnitude depends on the interparticle cohesion and interlocking of particles, whereas C_r is the resistance to normal stress due to the interparticle cohesion.

Eq. 3.6 is the required criterion for fluidization, which has been obtained by only considering motion in the vertical direction under zero excess pore pressure condition. However, for a typical wave, neglecting motion in the horizontal direction may cause an underestimation of fluidization, because the effect of horizontal pressure gradient is not considered. Also, the excess pore pressure build-up is an important feature for mud fluidization which cannot be neglected (Ross, 1988; Feng, 1992).

3.2.4 A Heuristic Criterion for Bed Fluidization Under Waves

In a mud bed under wave action, at a level where the inertia force, L_i, equals the effective weight, $m_p g'$, the bed is critically stretched at that level. Since the wave-induced inertia force is periodic, the bed is stretched and compressed periodically. Water is sucked in during stretching and is squeezed out during compression. There exist three cases with respect to water flow: (1) Bed permeability is zero, i.e., the bed is over-consolidated and bed density is high. In this case, there will be no water flow. (2) Bed permeability is quite low but not zero, with relatively low density (1,050 ~ 1,300 kg/m^3). In this case, water will flow in and out of the bed very slowly and restrictively. (3) Bed permeability is high, i.e., the bed is sand-like. In this case, water can flow in and out of the bed fast and freely under a pressure gradient.

In case (1) excess pore pressure cannot build up under periodic stretching and compression due to the absence of water entrainment into the bed. In case (2), since the permeability is quite low, its value is affected by the wave-induced vibration. Thus, it becomes higher when the bed is stretched and lower when the bed is compressed. As a result, more water flows into and less water flows out of the bed during the periodic stretching and compressing. Also, water in bed is not drained under compression. Thus, excess pore water pressure is built up (Ross, 1988; Feng, 1992). In case (3), because the permeability is high, stretching and compression of the bed have a negligible effect on bed permeability, and water entering the bed during stretching is drained during compression. Thus, excess pore pressure cannot build up.

For case (2) as the excess pore pressure, Δu_w, increases, the effective stress, $\sigma' = \rho_w g' D - \Delta u_w$, drops. Ultimately, when σ' approaches zero, from Eq. 3.6 only cohesive resistance, C_r, causes the particles to remain together to resist fluidization. At the present stage of knowledge, parameterization of cohesive resistance is not well defined. Cohesion depends on the type of sediment and increases with the consolidation time and bed density and therefore its resistive influence is strongly dependent on mud bed properties and state. Thus, as an approximation for partially consolidated, low density mud beds for which resistance against fluidization due to cohesion is of the same order of magnitude or less than that due to particle weight in water, we will select the criterion for fluidization at any point to be that instant when the effective submerged weight of the particle in water, $m_p g'$ modified by cohesion, equals the maximum upward force, L_{imax}, due to wave-induced vibration, i.e.

$$L_{imax} = \alpha m_p g' \tag{3.7}$$

where the cohesion dependent parameter α (≥ 1) must be determined experimentally. We will now assume that this criterion, based on forces on a single particle, reflects the corresponding condition causing the separation of the fluidized mud layer from the bed layer (Fig. 3.1). Using ζ as the displacement of the particle and $\ddot{\zeta}$ as the acceleration, Eq. 3.7 can be expressed as the following form:

$$\ddot{\zeta}_{max} = \alpha g' \tag{3.8}$$

The criterion, Eq. 3.8, which can be used to determine the depth of fluidization, is applicable to partially consolidated, low density mud beds under typical short period waves. For long waves, the horizontal pressure gradient can be the dominant force for fluidization. For fully consolidated beds with a high bulk density, cohesion may be much stronger and resist horizontal and/or vertical forces and thus prohibit fluidization. In the following, we will first use Eq. 3.8 by considering the bed to be a linear viscoelastic medium.

3.3 Voigt and Extensional-Voigt Models

For the commonly used (Maa, 1986; Chou, 1989) Voigt model representing bed viscoelasticity the shear stress-strain relationship is

$$T'_{ij} = 2GE'_{ij} + 2\mu \dot{E}'_{ij} \tag{3.9}$$

where T_{ij}' = stress deviator, E_{ij}' = strain deviator, subscripts i and j indicate directions, ij indicates a second order tensor, G = elastic modulus, μ = viscous coefficient, and the dot denotes derivative with respect to time. For examing bed response to wave-induced periodic normal stress, we are interested in the corresponding extensional stress-strain relationship. Assuming the bed's shear viscoelasticity to be represented by Eq. 3.9, its extensional viscoelasticity is characterized as follows:

The volumetric relationship between the mean normal stress and the mean normal strain of the bed material is usually assumed to be elastic (Malvern, 1969):

$$tr[T_{ij}] = 3Ktr[E_{ij}] \tag{3.10}$$

where T_{ij} = stress, E_{ij} = strain, K = bulk modulus and tr = trace, i.e., the summation of the three diagonal elements a tensor. Assuming the dynamic external pressure to be important only in the vertical (z or I = j = 3) direction, Eq. 3.10 reduces to

$$T_{33} = 3Ktr[E_{ij}] \tag{3.11}$$

Next, the deviators of stress and strain are expressed as

$$E_{ij}' = E_{ij} - \frac{1}{3}tr[E_{ij}]\delta_{ij} \quad ; \quad T_{ij}' = T_{ij} - \frac{1}{3}tr[T_{ij}]\delta_{ij} \tag{3.12}$$

where δ_{ij} = kronecker delta such that when i = j, δ_{ij} = 1 and when i $\neq$ j, δ_{ij} = 0. Then, inserting Eq. 3.12 into Eq. 3.9 and setting ij = 33 we obtain the isothermal uniaxial stress, $T_{33}(t)$, versus tensile strain, $E_{33}(t)$, relation for a material which is described by the equation

$$T_{33} - \frac{1}{3}T_{33} = 2G\left(E_{33} - \frac{1}{3}tr[E_{ij}]\right) + 2\mu\left(\dot{E}_{33} - \frac{1}{3}tr[\dot{E}_{ij}]\right) \tag{3.13}$$

Inserting Eq. 3.11 into Eq. 3.13 then yields

$$\frac{2\mu}{9K}\dot{T}_{33}+\left(\frac{2G}{9K}+\frac{2}{3}\right)T_{33} = 2GE_{33}+2\mu\dot{E}_{33} \qquad (3.14)$$

Since mud in the saturated condition is incompressible, $K \to +\infty$ (Das, 1983). Therefore, Eq.3.14 becomes

$$T_{33} = 3GE_{33}+3\mu\dot{E}_{33} = G_nE_{33}+\mu_n\dot{E}_{33} \qquad (3.15)$$

where G_n = extensional elastic modulus and μ_n = extensional viscous coefficient. Hence, the bed viscoelasticity in the normal direction is described under the given assumptions by the extensional-Voigt model (Eq. 3.15) in which the parameters are, $G_n = 3G$ and $\mu_n = 3\mu$, provided the shear viscoelasticity is characterized by Eq. 3.9. When $G = 0$, Eq. 3.15 satisfies the uniaxial extensional relationship for a Newtonian fluid developed by Petrie (1978).

3.4 Bed as a Spring-Dashpot-Mass System

Given the bed to be an almost impermeable continuum, we can choose to represent it as a mechanical, spring-dashpot-mass (S-D-M) analog. The essential aspect of this approach is to find the equivalent elastic and viscous coefficients and the equivalent mass of the entire bed. To obtain these quantities the application of a constant stress, F, to the bed surface is considered first. We will assume that the vertical distributions of the bed density, $\rho(z)$, the elastic modulus, $G_n(z)$, and the extensional viscous coefficient, $\mu_n(z)$, are known, as shown schematically in Fig. 3.2. Unfortunately, arbitrary distributions of these parameters are not amenable to an analytical solution of Eq. 3.15. Two specific cases are therefore considered next.

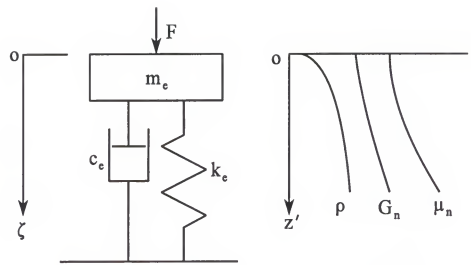

Figure 3.2 Bed simulated as a S-D-M system with known vertical distributions of bed density, ρ, extensional elastic modulus, G_n, and extensional viscous coefficient, μ_n. m_e = equivalent mass, k_e = equivalent elasticity, and c_e = equivalent viscous coefficient.

3.4.1 Case 1: G_n and μ_n Independent of Depth

Given d = bottom sediment thickness, k_e = equivalent elastic coefficient, c_e = equivalent viscous coefficient and m_e = equivalent mass (Fig. 3.2), from Eq. 3.15 we have

$$F = G_n \frac{d\zeta}{dz'} + \mu_n \frac{d\dot{\zeta}}{dz'} \tag{3.16}$$

where $F = T_{33}$ is the normal stress, $d\zeta(z,t)/dz' = E_{33}$ is the normal strain and $\zeta(z, t)$ = vertical displacement within the bed. Since F is independent of time, the solution of Eq. 3.16 is

$$\frac{d\zeta}{dz'} = \frac{F}{G_n}\left(1-e^{-\frac{G_n}{\mu_n}t}\right) \tag{3.17}$$

Further, integrating Eq. 3.17 from z to d we obtain

$$\zeta(z',t) = \int_{z'}^{d}\frac{F}{G_n}\left(1-e^{-\frac{G_n}{\mu_n}t}\right)dz' = \frac{F}{G_n/d}\left(1-e^{-\frac{G_n/d}{\mu_n/d}t}\right)\left(1-\frac{z'}{d}\right) \tag{3.18}$$

At the bottom sediment surface, $z' = 0$, we have

$$\zeta(0,t) = \frac{F}{G_n/d}\left(1-e^{-\frac{G_n/d}{\mu_n/d}t}\right) \tag{3.19}$$

Eq. 3.19 in fact represents the surface response of a Voigt solid to loading by F, with a retardation time-constant, $\left(G_n/d\right)/\left(\mu_n/d\right)$. For the equivalent S-D-M system shown in Fig. 3.2, we have

$$\zeta(0,t) = \frac{F}{k_e}\left(1-e^{-\frac{k_e}{c_e}t}\right) \tag{3.20}$$

Thus, the extensional stress-strain relationship for the bed satisfies the Voigt model relationship with $k_e = G_n/d$ and $c_e = \mu_n/d$. Therefore, the bed can be simply represented as a S-D-M system with equivalent coefficients k_e and c_e.

From Eqs. 3.18 and 3.19 we obtain

$$\zeta(z',t) = \zeta(0,t)\left(1-\frac{z'}{h_3}\right) = \zeta(0,t)\ \Psi_a \tag{3.21}$$

where $\Psi_a = (1-z'/h_3)$ is a shape function which relates the displacement at any depth, z', to the displacement at the bed surface, $z' = 0$.

The equivalent mass is in general obtained from

$$m_e\ddot{\zeta}(0) = \int_0^d \rho(z')\ddot{\zeta}(z')dz' \tag{3.22}$$

where $\ddot{\zeta}(z')$ = vertical acceleration profile. Thus, from Eq. 3.22,

$$m_e = \int_0^d \rho_3(z')\left(1-\frac{z'}{d}\right)dz' = \int_0^d \rho_3(z')\Psi_a dz' \tag{3.23}$$

3.4.2 Case 2: G_n, and μ_n Increase with Depth

Here we present a case in which G_n and μ_n increase with depth according to

$$G_n = \alpha_n e^{\gamma_n z'} \quad ; \quad \mu_n = \beta_n e^{\gamma_n z'} \tag{3.24}$$

where α_n, β_n and γ_n are mud-specific coefficients. Since the bed is assumed to be a Voigt solid, the solution steps are the same as in Case 1. By substituting Eq. 3.24 into Eq. 3.16, we obtain

$$\frac{d\zeta}{dz} = \frac{F}{G_n}\left(1-e^{-\frac{G_n}{\mu_n}t}\right) = \frac{F}{\alpha_n e^{\gamma_n z}}\left(1-e^{-\frac{\alpha_n}{\beta_n}t}\right) \tag{3.25}$$

Integrating Eq. 3.24 from 0 to d we next obtain

$$\zeta(z',t) = \int_{z'}^{d}\frac{F}{\alpha_n e^{\gamma_n z'}}(1-e^{-\frac{\alpha_n}{\beta_n}t})dz' = \frac{F}{\alpha_n\gamma_n}(1-e^{-\frac{\alpha_n\gamma_n}{\beta_n\gamma_n}t})(e^{-\gamma_n z'}-e^{-\gamma_n d}) \tag{3.26}$$

At the bed surface, $\zeta(0,t)$ is given by

$$\zeta(0,t) = \frac{F}{\alpha_n\gamma_n}(1-e^{-\frac{\alpha_n\gamma_n}{\beta_n\gamma_n}t})(1-e^{-\gamma_n d}) \tag{3.27}$$

Comparing with Eq. 3.20, for the equivalent S-D-M system shown in Fig. 3.2, the equivalent S-D-M coefficients for bed are: $k_e = \alpha_n \gamma_n$ and $c_e = \beta_n \gamma_n$. The relationship between the displacement of the bed surface and that at any depth in the bed is obtained as

$$\zeta(z',t) = \zeta(0,t) \frac{(e^{-\gamma_n z'} - e^{-\gamma_n d})}{(1 - e^{-\gamma_n d})} = \zeta(0,t)\Psi_b \tag{3.28}$$

where $\Psi_b = (e^{-\gamma_n z'} - e^{-\gamma_n d})/(1 - e^{-\gamma_n d})$ is a shape function. Finally, the equivalent mass is obtained in the same general way as in Case 1 (Eq. 3.22), which is

$$m = \int_0^d \rho(z') \frac{(e^{-\gamma_n z} - e^{-\gamma_n d})}{(1 - e^{-\gamma_n d})} \, dz' = \int_0^d \rho(z')\Psi_b \, dz' \tag{3.29}$$

Since $\lim_{d \to +\infty} e^{-\gamma_n d} = 0$, the shape function can be simplified as $\Psi_b = e^{-\gamma_n z'}$ when $d \to +\infty$.

Thus far, we have considered two representations of the bed by an equivalent S-D-M system. Once $\zeta(0, t)$ is obtained, the response at any depth within the bed can be determined through the appropriate shape function. For Case 1 representing a uniform bed, the bed depth, d, must be specified, because of the assumptions of uniform distribution of G and μ. G_n and μ_n can be determined through rheometry from which G and μ are obtained. Then $G_n = 3G$ and $\mu_n = 3\mu$. In the more common situation of a stratified bed (Case 2), it is necessary to determine $G_n(z)$ and $\mu_n(z)$. For this case the bed depth can be finite or it may extend to infinity. We will next examine the response of the bed to wave motion. In the following, subscript 1 is used to denote the water layer, 2 indicates fluid mud layer, and 3 is for the bed.

3.5 Dynamic Response of Bed

3.5.1 Wave over Bed: One-Degree of Freedom

In Fig. 3.3, the wave-induced cyclic normal pressure, p_w (with an angular wave frequency, ω), acting on the bed can be expressed as (Dean and Dalrymple, 1993)

$$p_w = p_0 \sin\omega t = \frac{\rho_1 g \zeta_{01}}{\cosh k_{w1} h_1} \sin\omega t \tag{3.30}$$

where p_0 = pressure amplitude, ζ_{01} = wave amplitude, k_{w1} = wave number and h_1 = water depth. The dynamic equation for this case is (Fertis, 1973)

$$m_3 \ddot{\zeta}_3(0,t) + c_3 \dot{\zeta}_3(0,t) + k_3 \zeta_3(0,t) = p_0 \sin\omega t \tag{3.31}$$

where c_3, k_3 and m_3 are defined in Fig. 3.3. Denoting the characteristic resonance frequency, $\omega_0 = (k_3/m_3)^{1/2}$, and also $\beta = \omega/\omega_o$, $\xi = c_3/2m_3\omega$, and $\omega_D = \omega\sqrt{1-\xi^2}$ we obtain the solution

$$\zeta_3(0,t) = e^{-\xi t}(A\sin\omega_D t + B\cos\omega_D t) + \frac{\frac{p_0}{k_3}[(1-\beta^2)\sin\omega t - 2\xi\beta\cos\omega t]}{[(1-\beta^2)^2 + (2\xi\beta)^2]} \tag{3.32}$$

where A, B are coefficients that are dependent on the initial conditions. Since the first term decays exponentially with time and the second term is the harmonic response sought, for $t \to +\infty$ the solution is

$$\zeta_3(0,t)\big|_{t\to+\infty} = \frac{p_0}{k} \frac{1}{[(1-\beta^2)^2 + (2\xi\beta)^2]^{1/2}} \sin(\omega t - \phi_1) \tag{3.33}$$

where $\phi_1 = \tan^{-1}[c_3\omega/(k_3 - m_3\omega^2)] = \tan^{-1}[2\xi\beta\omega/(1-\beta^2)]$. The amplitude, ζ_{03}, of ζ_3 is

$$\zeta_{03} = \frac{p_0}{k_3} \frac{1}{[(1-\beta^2)^2+(2\xi\beta)^2]^{1/2}} \tag{3.34}$$

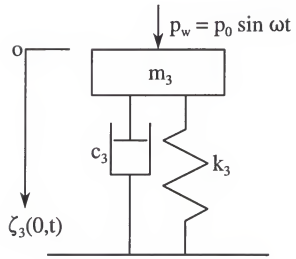

Figure 3.3 Bed layer represented by a one-degree of freedom system. m_3 = equivalent mass; k_3 = equivalent elasticity and c_3 = equivalent viscosity.

3.5.2 Wave over Fluid Mud above Bed: Two-Degrees of Freedom

Quite often a layer of fluid mud is initially present on the bed. Because the rheological properties of fluid mud and the bed from which it is derived are different, the two layers of continua must be represented by two equivalent S-D-M systems in series, constituting the two-degrees of freedom system shown in Fig. 3.4. In this case, whether or not the bed is fluidized will depend on the wave parameters, fluid mud properties and layer thickness, and bed properties. The governing equations of motion for this are

$$m_2\ddot{\zeta}_2+c_2(\dot{\zeta}_2-\dot{\zeta}_3)+k_2(\zeta_2-\zeta_3) = p_0e^{i\omega t} \tag{3.35}$$

$$c_2(\dot{\zeta}_2-\dot{\zeta}_3)+k_2(\zeta_2-\zeta_3) = m_3\ddot{\zeta}_3+c_3\dot{\zeta}_3+k_3\zeta_3 \tag{3.36}$$

where $i=\sqrt{-1}$, ζ_2 and ζ_3 are displacements of the fluid mud surface and the bed surface, respectively, and the coefficients m_2, m_3, k_2, k_3, c_2 and c_3 are noted in Fig. 3.4.

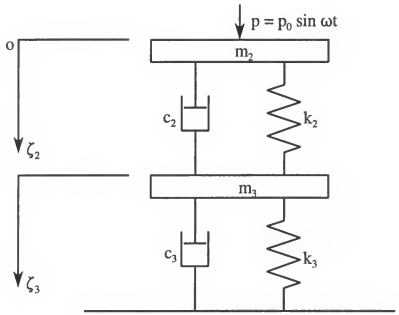

Figure 3.4 Fluid mud and bed layers represented by a two-degrees of freedom system. m_2, m_3 = equivalent masses; k_2, k_3 = equivalent elasticities and c_2, c_3 = equivalent viscosities.

As in Eqs. 3.31 and 3.32, the dynamic response sought is represented by the steady (harmonic) term. Thus, we will express $\zeta_2=\zeta_{02}\exp[i(\omega t-\phi_2)]$ and $\zeta_3=\zeta_{03}\exp[i(\omega t-\phi_3)]$, where ϕ_2 and ϕ_3 are the respective phase shifts of fluid mud and bed displacements relative to ζ_1, and ζ_{02}, ζ_{03} are the corresponding amplitudes. Then, solving Eqs. 3.34 and 3.35 we obtain the harmonic solution

$$\zeta_2(0,t)\,|_{t\to+\infty} = p_0\,\frac{(k_3+k_2-m_3\omega^2) + i(c_3\omega+c_2\omega)}{Z_3 + iZ_2} \tag{3.37}$$

$$\zeta_3(0,t)\,|_{t\to+\infty} = p_0\,\frac{(k_2) + i(c_2\omega)}{Z_3 + iZ_2} \tag{3.38}$$

where $Z_2=c_3\omega(k_2-m_2\omega^2)+c_2\omega[k_3-(m_3+m_2)]\omega^2$, $Z_3=(k_3-m_3\omega^2)(k_2-m_2\omega^2)-(k_2m_2+c_3c_2)\omega^2$.

Thus, the amplitude, ζ_{02} and ζ_{03}, are

$$\zeta_{02} = p_0\left[\frac{(k_3+k_2-m_3\omega^2)^2+(c_3\omega+c_2\omega)^2}{Z_3^2+Z_2^2}\right]^{1/2} \tag{3.39}$$

$$\zeta_{03} = p_0\left[\frac{(k_2)^2+(c_2\omega)^2}{Z_3^2+Z_2^2}\right]^{1/2} \tag{3.40}$$

Next, note that for $k_2 = 0$, fluid mud becomes a viscous Newtonian fluid, a common assumption. In this case the solution is simplified as

$$\zeta_{02} = p_0\left[\frac{(k_3-m_3\omega^2)^2+(c_3\omega+c_2\omega)^2}{Z_{3v}^2+Z_{2v}^2}\right]^{1/2} \tag{3.41}$$

$$\zeta_{03} = p_0\left[\frac{(c_2\omega)^2}{Z_{3v}^2+Z_{2v}^2}\right]^{1/2} \tag{3.42}$$

where $Z_{2v}=-c_3\omega m_2\omega^2+c_2\omega[k_3-(m_3+m_2)]\omega^2$ and $Z_{3v}=-(k_3-m_3\omega^2)m_2\omega^2-c_3c_2\omega^2$.

If $c_2\to+\infty$ or $k_2\to+\infty$ and m_2 is set equal to zero, we recover the solution for the one-degree of freedom system (Eq. 3.32), which is

$$\zeta_2(0,t)\,|_{t\to+\infty} = \zeta_3(0,t)\,|_{t\to+\infty} = \frac{p_0}{k_3}\frac{1}{[(1-\beta^2)^2+(2\xi\beta)^2]^{1/2}}\sin(\omega t-\phi) \tag{3.43}$$

3.6 Fluidization Depth

3.6.1 Model Results

From Eqs. 3.21 and 3.28, we recognize that the vibratory displacement and acceleration decrease from the bed surface downward. Therefore, the inertia force decreases downward while the resistance force either remains constant (uniform bottom) or increases (stratified bottom). Thus, there must exist an equilibrium depth, z'_c, down to which the bed is fluidized, as schematized in Fig. 3.5.

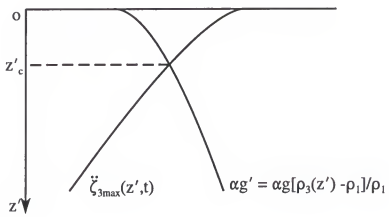

Figure 3.5 A schematic description of the criterion for equilibrium fluidization depth, z'_c.

For the water-bed (one-degree of freedom) or the water-fluid mud-bed (two-degrees of freedom) system, z'_c can be obtained through Eq. 3.33 or Eqs. 3.37 and 3.38, respectively, and the criterion

$$\alpha g' = \ddot{\zeta}_{3max}(z'_c,t) \tag{3.44}$$

in which mud cohesion and viscoelasticity are characteristically included via α and $\ddot{\zeta}_3$, respectively.

Since $\ddot{\zeta}_3 = \omega^2 \zeta_3$, the criterion of Eq. 3.43 can be expressed as

$$\alpha g \frac{\rho_3(z'_c) - \rho_1}{\rho_1} = \omega^2 \zeta_{03} \Psi(z'_c) \tag{3.45}$$

where $\Psi(z'_c)$ is the value of shape function at $z' = z'_c$ with $\Psi = \Psi_a$ for case 1 and $\Psi = \Psi_b$ for case 2. Thus, z'_c can be obtained by solving Eq. 3.44 through iteration. We will consider three examples here.

Example 1: Initial water-bed system with negligible cohesion without considering effects from initial fluid mud.

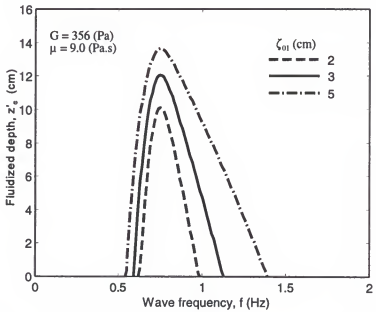

Figure 3.6 Fluidization depth variation with wave frequency and amplitude with negligible cohesion and without considering initial fluid mud effects.

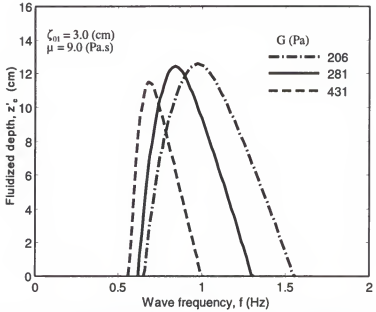

Figure 3.7 Fluidization depth variation with wave frequency and bed elastic modulus with negligible cohesion and without considering initial fluid mud effects.

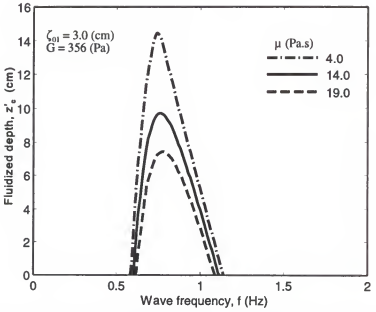

Figure 3.8 Fluidization depth variation with wave frequency and bed viscous coefficient with negligible cohesion and without considering initial fluid mud effects.

Figures 3.6, 3.7 and 3.8 are results for z'_e based on the criterion of Eq. 3.44 for a bed - water system initially without the presence of fluid mud, with $\alpha = 1$ (i.e. negligible cohesion); $h_1 = 19$ cm; $h_3 = 16$ cm; $\rho_1 = 1{,}000$ kg/m^3; $\rho_3 = 1{,}170$ kg/m^3; $\zeta_{01} = 2$, 3, and 5 cm; wave frequency, $f(=\omega/2\pi)$ range 0.4 to 4.0 Hz; G = 206, 281, 356 and 431 Pa and μ = 4.0, 9.0, 14.0 and 19.0 Pa.s. These parameters are representative of the laboratory experiments of Feng (1992) described later.

In Fig. 3.6, z'_e is observed to increase with the wave amplitude. For a given amplitude, z'_e attains a maximum, z'_{cmax}, at the characteristic resonance frequency, $\omega_0 = (k_3/m_3)^{1/2}$. In Fig. 3.7, z'_{cmax} is observed to occur at increasing ω_0 as G increases. Also, the greater the value of μ, the smaller the z'_e (Fig.3.8). It is noteworthy that for high frequency waves, wave-induced cyclic normal pressure tends to zero (Eq. 3.29), while for low frequency waves, the inertia force, L_i, due to bed vibration becomes very small. Thus for both high and low frequency waves, the bed is not fluidized. The bed reaches its maximum fluidization depth at a characteristic wave frequency which depends on the bed rheological properties and density. It must also be noted that for low frequency waves the horizontal pressure gradient can be the dominant cause of bed fluidization, for which Eq. 3.3 should be used as the fluidization criterion (which is not considered in the above derivation). Therefore, the above results, which are based on the criterion of Eq. 3.45, are only valid for short period wave action. The effect of long wave action in causing bed fluidization needs further studies.

Example 2: Initial water-bed system with negligible cohesion by considering the initial fluid mud effects on fluidization depth.

In case a layer of fluid mud is initially present on the bed the water-fluid mud-bed three layered system must be considered. Thus, the two - degree free system will be used to determine the fluidization depth in the three-layered system. Also from experimental observations (Ross, 1988 and Feng, 1992) we note that once the bed is fluidized, the broken inter-particle bonds apparently do not reform as long as wave motion continues. Therefore, the calculated fluidization depth represents the maximum fluid mud layer thickness for the one-and the two-degrees of freedom systems. The procedure involves calculation of z'_c at first for the one-degree of freedom system. Then with this value of z'_{c1}, a second z'_c is calculated for the two-degree of freedom system. Finally, the value of z'_c represented in the figures (Figs. 3.9, 3.10 and 3.11) is the layer of the two fluid mud thickness.

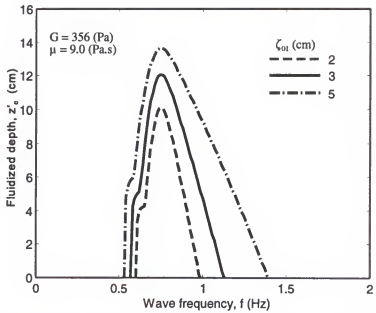

Figure 3.9 Fluidization depth variation with wave frequency and amplitude with negligible cohesion, but including initial fluid mud effects.

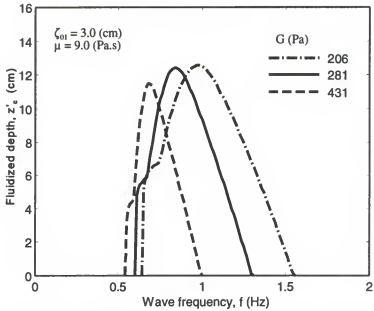

Figure 3.10 Fluidization depth variation with wave frequency and bed elastic modulus with negligible cohesion, but including initial fluid mud effects.

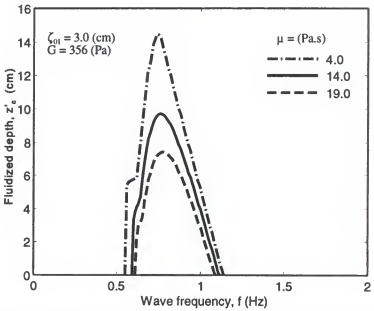

Figure 3.11 Fluidization depth variation with wave frequency and bed viscous coefficient with negligible cohesion, but including initial fluid mud effects.

Comparing Figs. 3.9, 3.10 and 3.11 with Figs. 3.6, 3.7 and 3.8 it is found that only considering water - bed two - layered system may under predict the fluidization depth at relatively low frequencies. At these frequencies the presence of fluid mud layer apparently helps the fluidization of the deeper bed layer.

Example 3: Effect of cohesion on z'_c starting with a water - bed system.

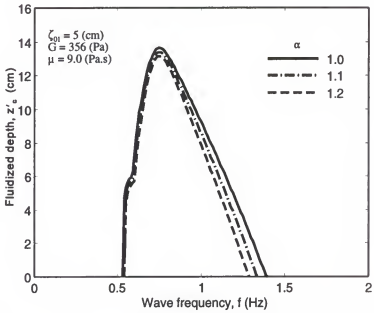

Figure 3.12 Fluidization depth variation with wave frequency and cohesion parameter.

In this example we will select the parameters from Example 1, and also G = 295 Pa and μ = 6.1 Pa.s. To incorporate cohesion, the parameter α will be selected as 1.1 and 1.2. For a wave amplitude ζ_{01} = 5 cm, we will examine the variation of z'_c with α and wave frequency, f. The final fluidization depth is the larger of the calculated values for water-bed and water-fluid mud-bed systems. It is observed from Fig. 3.12 that the effect of cohesion

on fluidization depth only slightly changes the value of fluidization depth but does not affect the shape and phase of the fluidization depth variation with frequency.

3.6.2 Comparison with Data

The mud bed fluidization experiments of Feng (1992) were conducted in a wave flume in which the water level was maintained at 35 cm elevation above the bottom and the wave frequency was 1 Hz. The nominally 16 cm thick initial bed was composed of an aqueous mixture of attapulgite and kaolinite clays in equal proportion by weight and with an initial depth-average density $\rho_3 = 1{,}150$ kg/m^3. For each setting of the wave amplitude the pore and total pressures were measured at different depths within the bed. The maximum depth below mud surface at which the effective stress (total pressure minus pore pressure; see Section 2.3) was equal to zero was considered to be fluid mud thickness. In each test, this thickness increased with time from zero at the beginning as wave motion continued and seemingly approached an equilibrium value, z'_e.

From the work of Mehta and Jiang (1993) involving the use of a Carri-Med CSL applied stress rheometer to determine the mud rheological properties, the muds are represented as a Standard Solid with three parameters, i.e., G_1, G_2 and μ_2. These parameters were determined for the mud used by Feng (1992) as functions of mud density and forcing wave frequency (in the 0.01 to 10 Hz range). The equivalent parameters, G and μ, of the Voigt model can be obtained from Eq. 2.16

$$\mu = \mu' = \frac{G_1\left(\frac{G_1}{\mu_2}\right)}{\omega^2 + \left(\frac{G_1+G_2}{\mu_2}\right)^2} \quad ; \quad G = \mu''\omega = \frac{G_1\left[\frac{(G_1+G_2)G_2}{\mu_2^2} + \omega^2\right]}{\omega^2 + \left(\frac{G_1+G_2}{\mu_2}\right)^2} \tag{3.46}$$

At $\omega = 2\pi$ rad/s, the data of Mehta and Jiang (1993) give $G_1 = 300$ Pa, $G_2 = 1.65$ Pa and $\mu = 365$ Pa.s. Therefore, we obtain $G = 295$ Pa and $\mu = 6.1$ Pa.s from Eq. 3.46. Results are compared with measurements in Table 3.1 in which $\alpha = 1.05$ has been selected to obtain minimal error.

Table 3.1 Wave and bed conditions and calculated and measured fluidization depths.

Test no.	Wave amplitude (cm)	Water depth (cm)	Initial bed thickness (cm)	Fluid mud thickness, z_c		
				Measured (cm)	Calculation (cm)	Error (%)
8	2.0	18.4	16.6	3.5	4.6	+7
9	2.8	19.3	15.7	8.4	8.0	-1
10	4.0	20.3	14.7	7.0	8.1	4
11	1.9	20.2	14.8	2.0	1.2	-12

Table 3.2 Summary of selected fluid mud generation experiments in flumes from Ross(1988) and Lindenberg et al. (1989).

Source	Mud	h_1 (cm)	h_2 (cm)	ρ_1 (kg/m^3)	ρ_2 (kg/m^3)	ζ_{01} (cm)	f (Hz)	μ (Pa.s)	G (Pa)
Ross (1988)	Tampa Bay	31.4-31.7	11.8-13.0	1,000	1,080	3.1-3.6	1.0-1.1	25.0	100
Lindenberg et al. (1989)	Kaolin	25	4.8-4.9	1,000	1,300	2.4-3.6	0.4-0.7	3.0	5

[a]A 50/50 (by weight) clayey mixture of an attapulgite and a kaolinite

In addition to Feng's data, flume data on the thickness of fluid mud generated by wave action over mud beds are selected from Ross (1988) and Lindenberg et al. (1989) to

illustrate the applicability of the method developed. Test conditions for data from these two selected sources are summarized in Table 3.2, and the works of Maa (1986) and Jiang (1993) were consulted for obtaining the parameters μ and G.

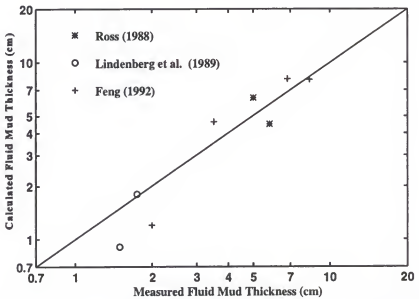

Figure 3.13 Comparison between calculated and flume-measured fluidization depths.

The plot of measured versus calculated values of z'_c given in Fig. 3.13 indicates a generally acceptable degree of overall agreement between theory and data, although at the lower end two values, one of Lindenberg et al. (1989) and the other obtained by Feng (1992), are notably under predicted. A likely reason is that because the mud-water interface tends to be indistinct in flume experiments, small fluid mud thicknesses are not always measured accurately. It is conceivable that in the two cases cited, the reported thicknesses included a thin surfacial layer that was actually a comparatively low density suspension above the fluid mud surface.

For the purpose of calculation, it was found that the value of 1.05 for the resistance modifying parameter α in Eq. 3.8 was generally applicable to all the data. The fact that this was so and that this value is close to unity is commensurate with the relatively low cohesion of all the muds listed in Tables 3.1 and 3.2.

In two of the tests of Lindenberg et al. (1989) for which experimental conditions are given in Table 3.3, no fluid mud formation could be detected due to low wave heights. This condition can be further examined by referring to Eq. 3.5. Thus, it can be shown that in Test T3-3 at the surface ζ_{max} was equal to 2.5 m/s^2, which was smaller than $\alpha g'$=3.1 m/s^2. In Test T4-4 the two respective values were 3.4 m/s^2 and 3.1 m/s^2. Thus, in test T3-3 the threshold condition for fluid mud generation was not reached, and in T4-4 it was barely exceeded. We will illustrate this point further by considering fluid mud generation in Lake Okeechobee.

Table 3.3 Flume tests of Lindenberg et al. (1989) without fluid mud generation

Test No.	Mud	h_1 (cm)	h_2 (cm)	ρ_1 (kg/m^3)	ρ_2 (kg/m^3)	ζ_{01} (cm)	f (Hz)	μ (Pa.s)	G (Pa)
T3-3	Kaolin	25	4.9	1,000	1,300	4.8	2.5	3	5
T4-4	Kaolin	25	4.8	1,000	1,300	4.7	1.5	3	5

3.7 Application to Field Data

3.7.1 Field Conditions

Lake Okeechobee, Florida (Fig. 3.14), is the largest freshwater lake in the United States, exclusive of the Great Lakes. It provides many functions for south-central Florida including drainage, water supply, flood relief and recreation. The lake is shallow with maximum depths of 4 ~ 5 m. Along the western margin of the lake, emergent and

submerged vegetation cover more than a third of the lake area. Toward the eastern part of the lake the bed is covered with dark grey mud with a characteristic granular density of 2,140 kg/m^3. This mud has about 40% organic material by weight of mud. Bottom mud thickness generally ranges from 10 to 80 cm (see Fig. 3.15) and the very soft top 0.05 to 0.2 m of mud has negligible vane shear strength (Kirby et al., 1989). The original source of this mud is believed to be the Kissimmee River, whose waters enter the lake near its northern end.

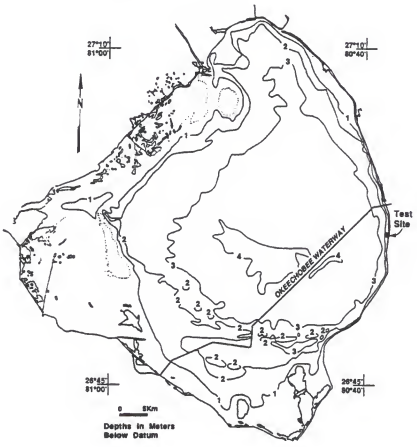

Figure 3.14 Bathymetric map of Lake Okeechobee. Depth are relative to a datum which is 3.81 m above msl (after Mehta and Jiang, 1990).

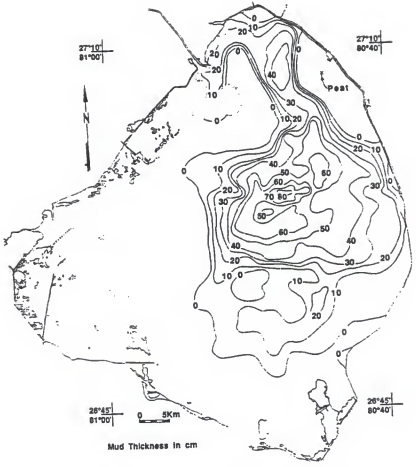

Figure 3.15 Mud thickness contour map of Lake Okeechobee (after Kirby et al., 1989).

A sedimentological investigation, which included vibracoring, acoustical sub-bottom profiling and sidescan imaging of the lake bed, was carried out to characterize mud properties and state (Kirby et al., 1994). In a complementary study, wave spectra were measured as a part of an assessment to determine the erodibility of bottom mud (Jiang and Mehta, 1992). From these studies it was determined that, most of the time, typical wind-generated waves are able to maintain the top 5-20 cm thick layer of the soft organic-rich mud in a fluid-like state. Characteristic bottom density data and a representative equation fit are

shown in Fig. 3.16. This profile as such does not distinguish between fluid mud and bed, and for the present purpose we will consider the equation to represent mud bed in the lake.

3.7.2 Model Application

It is of interest to determine what portion of the density profile in Fig. 3.16 is fluid mud. For that purpose the following characteristic parameters are selected: a representative mean mud thickness over the entire mud bottom, h_2=0.55 m; water density, ρ_1=1,000 kg/m^3; a representative significant wave height, ζ_{0i}=0.08 m and wave frequency, f=0.4 Hz (Jiang and Mehta, 1992). The mud density is empirically expressed as

$$\rho_m = \rho_{m0} + \alpha_m z'^{\beta_m} \tag{3.47}$$

where the empirical coefficients ρ_{m0} = 1,000 kg/m^3, α_m = 280 and β_m = 0.3 with z′ in units of meter obtained by fitting the measurements, shown in Fig. 3.16.

Mud rheology was measured by Jiang (1993) using controlled-stress rheometry, and was represented by the standard solid model (see Fig. 2.2 and Eqs. 2.7 and 2.16) with the three parameters expressed as

$$\mu_2,\ G_1 \text{ or } G_2 = \exp(\epsilon) \bullet f^{\Delta} \tag{3.48}$$

where f is the wave frequency and ϵ and Δ are empirical coefficients obtained from experiments with ϵ = 5.548 and Δ = 0.127 for μ_2, ϵ = 0.318 and Δ = -0.687 for G_2 and ϵ = 5.290 and Δ = -0.687 for G_1 at the mud density of 1,125 kg/m^3 (Jiang, 1993). As a result, the equivalent parameters were obtained (Eq. 2.16) as μ=21 Pa.s and G=216 Pa. In addition, the resistance modifying coefficient α=1.05 is selected following the earlier examples and

considering the weakly cohesive nature of lake mud. The water depth h_1 is varied from 0.5 m to 4 m.

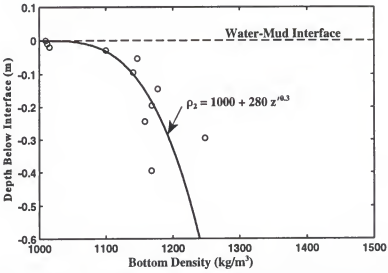

Figure 3.16 A representative bottom mud density profile in Lake Okeechobee.

As observed in Fig. 3.17, the calculated fluid mud thickness decreases from a value that is a little over 0.3 m in the vicinity the shallow littoral zone of the lake where the effect of wave action can be expected to be comparatively strong, to practically nil in the deepest part near the center, where waves would be considerably less effective in liquefying mud. Despite the very approximate nature of this calculation, it is seen to be illustrative of the actual range of fluid mud found in the lake. Since, however, the measured thicknesses were not resolved of a site-specific basis, it is not possible to glean the dependence of measured fluid mud generation on water depth. In any event, the generation of fluid mud by wind waves, and the fact that in this lake episodic wind-driven currents on the order of 10 cm/s occur, may explain the mode by which mud from the mouth of Kissimmee River was eventually transported to the center of the lake.

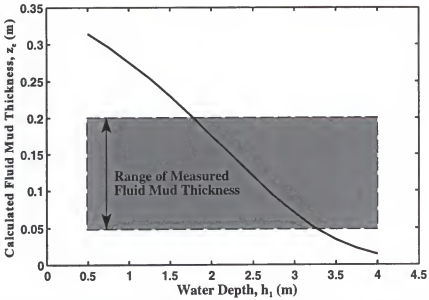

Figure 3.17 Calculated fluidization depth as a function of water depth in Lake Okeechobee and band of measured values.

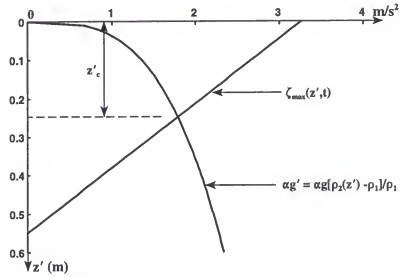

Figure 3.18 An example of fluidization depth calculation for Lake Okeechobee at a site where water depth was 1.43 m.

It is instructive to qualitatively examine the sensitivity of bottom mud conditions on the potential for generation of fluid mud with respect to conditions during an experimental

study on mud resuspension close to the eastern bank of Lake Okeechobee (Jiang and Mehta, 1992). At this site all the above selected parameters are applicable, except the water depth, h_1, which was 1.43 m. The criterion of Eq. 3.8 is plotted in Fig. 3.18, in which the fluid mud thickness is seen to be about 25 cm. Observe that z'_e is seemingly sensitive to the shapes of the two intersecting curves, and consideration of depth-dependent rheological parameters would tend to make z'_e further sensitive to the depth-varying profile of particle acceleration, because in that case the shape of that profile would become qualitatively akin to that shown in Fig. 3.5. Thus, assuming that the method considered here is realistic, it is seen that for given a forcing, fluid mud generation can be expected to be very sensitive to mud properties. The experiments of Lindenberg et al. (1989) seem to corroborate this assertion based on their finding that fluid mud development in some of their tests was highly sensitive to small fractions of organic matter and fine sand.

3.8 Conclusions

The main observations from this chapter are as follows:

(1) The continuum bed, assumed to be characterized as a uniaxial extensional-Voigt solid, can be represented simply an one-degree of freedom S-D-M system, whereby the displacement at any point in the bed is related to the bed surface displacement by an appropriate shape function. When fluid mud is present over the bed, a two-degree of freedom representation is appropriate.

(2) The thickness of the fluidized mud layer at equilibrium under period short wave action can be estimated by considering the balance of vertical forces on a particle (or floc) within the bed.

(3) Comparison between theoretically calculated and measured fluidization depths indicates an order of magnitude agreement. This agreement implies that shear rheometry can be used to determine mud-specific viscoelastic coefficients required to estimate the depth of fluidization.

(4) The effect of cohesion from partially consolidated bed on fluidization depth is comparatively much smaller than that due to the change of bed viscoelasticity and/or bulk density.

The limitations and required further studies for fluidization are as follows:

(1) The criterion, Eq. 3.8, is only suitable for partially consolidated, low density mud beds under short period waves. For long waves, horizontal motion may have a dominant role. For consolidated, high density mud beds, the strong cohesion between particles must be determined independently. For highly permeable sand-like beds, fluidization occurs mainly due to the relative motion between pore water and the particle in the horizontal or the vertical direction (Madson, 1974 and Selly, 1988), which is a different from the mechanism considered here.

(2) To represent bed and fluid mud as an equivalent S-D-M system, only two special cases are derived. More theoretical work and, perhaps, numerical models will be required for representing the bed with arbitrary depth - distributions of elasticity and viscosity.

(3) Only equilibrium fluidization depth is treated in this study. However, during fluidization the rate of excess pore pressure buildup and effective stress decrease depending on mud permeability and its change by stretching and compression, which in turn depend on the time-varying mud bed properties and on wave characteristics. The transient processes leading to the equilibrium depth of fluidization need to be studied further.

CHAPTER 4
SEDIMENT TRANSPORT MODELING

4.1 Introduction

To investigate contaminant release across the wave-modulated mud-water interface, a vertical sediment-associated contaminant transport model is required for the three-layered system (Figs. 2.5 and 2.7). For that purpose, a vertical sediment transport model must be coupled with a vertical contaminant transport model to include sediment resuspension effects. This sediment model is developed in this Chapter.

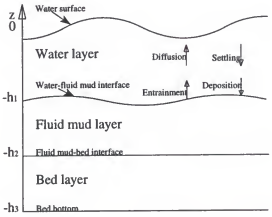

Figure 4.1 Three-layered system and vertical sediment transport processes considered.

4.2 Three-Layered System

By using the equilibrium fluidization depth as the requisite fluid mud depth, Fig. 2.5 can be modified for the proposed study, since fluid mud dewatering is not involved and no

bed sediment is fluidized in this case. Therefore, sediment mass transport across the interface between the fluid mud and the bed is neglected and the fluid mud-bed interface is considered to be fixed in elevation. In addition, since changes in the thickness of water and fluid mud layers due to sediment entrainment and deposition are typically small, they can be neglected. Thus, the water-fluid mud interface is also considered to be fixed in elevation.

In Fig. 4.1, the three-layered system is considered to have fixed interfaces/boundaries on a wave-average basis. The z-axis is vertically upward, originating from the water surface. The elevation of the water-fluid mud interface is $z=-h_1$ and that of the fluid mud-bed interface is at $z=-h_2$. The bed bottom is specified at $z=-h_3$. In the following development, subscript "1" will be used to denote the water layer, "2" the fluid mud layer and "3" the bed layer. Within the water column, vertical sediment transport will be considered to be governed by sediment settling, upward diffusion, entrainment and deposition.

4.3 Wave-Averaged Transport Equation for Constituent Transport

Due to the characteristics of boundary layer turbulence and wave motion, and the difficulty of tracking individual particle movement, wave-averaged governing equations will be obtained with suitable diffusion coefficients to incorporate the effects of turbulent diffusion, wave-induced diffusion and molecular diffusion. The equations will be derived starting from the global advection-diffusion equation for any conservative constituent. Characterized by different transport properties within each of the three layers and for different constituents, i.e. sediment and contaminant, the equations will describe vertical sediment transport and contaminant transport within each layer.

The temporal change of concentration of a conservative constituent at a point is equal to the gradient of the mass flux of the constituent at that point, i.e.

$$\frac{\partial C}{\partial t} = \nabla \cdot \vec{F} \tag{4.1}$$

where C is the constituent concentration and $\vec{F}$ is the mass flux of the constituent. $\vec{F}$ can be decomposed into an advective component, $\vec{F}_A$, a diffusion component, $\vec{F}_D$, and a settling component, $\vec{F}_s$:

$$\vec{F}_A = \bar{u}C \; ; \; \vec{F}_D = D_m \nabla C \; ; \; \vec{F}_s = -w_s C \vec{k} \tag{4.2}$$

where $\bar{u}$ is the instantaneous flow velocity, D_m is the molecular diffusion coefficient, $\vec{k}$ is a unit vector in the vertical z-direction and w_s is the settling velocity of the constituent.

Inserting Eq. 4.2 into Eq. 4.1 and expanding it,

$$\begin{aligned} &\frac{\partial C}{\partial t} + \frac{\partial (uC)}{\partial x} + \frac{\partial (vC)}{\partial y} + \frac{\partial (wC)}{\partial z} \\ &= \frac{\partial}{\partial x}\left(D_m \frac{\partial C}{\partial x} \right) + \frac{\partial}{\partial y}\left(D_m \frac{\partial C}{\partial y} \right) + \frac{\partial}{\partial z}\left(D_m \frac{\partial C}{\partial z} \right) + \frac{\partial}{\partial z}(w_s C) \end{aligned} \tag{4.3}$$

where u, v and w are the instantaneous flow velocities in the x, y and z directions, respectively.

Considering that the time-scale of the turbulent fluctuation (about 0.0001 ~ 1 s; see Hinze, 1959) and the wave period (about 1 ~ 10 s) are usually orders of magnitude smaller than the time-scales of characteristic natural flows, i.e. tidal current, river flow etc., the flow

velocity components and the constituent concentration can be decomposed into three parts, i.e., a wave-averaged part, a wave oscillating part and a turbulent fluctuation part. Thus,

$$u = \bar{u} + \tilde{u} + u', \quad v = \bar{v} + \tilde{v} + v', \quad w = \bar{w} + \tilde{w} + w', \quad C = \bar{C} + \tilde{C} + C'$$

where $\bar{u}$, $\bar{v}$, $\bar{w}$, and $\bar{C}$ are time-averaged values over the wave period, $\tilde{u}$, $\tilde{v}$, $\tilde{w}$ and $\tilde{C}$ are the wave oscillating parts and u', v', w', and C' are the turbulent fluctuation parts.

Substituting u, v and w components in Eq. 4.3 and time-averaging over one wave period, we obtain

$$\begin{aligned}\frac{\partial \bar{C}}{\partial t} + \frac{\partial (u\bar{C})}{\partial x} + \frac{\partial (v\bar{C})}{\partial y} + \frac{\partial (w\bar{C})}{\partial z} &= \frac{\partial}{\partial x}\left(D_m \frac{\partial \bar{C}}{\partial x}\right) + \frac{\partial}{\partial y}\left(D_m \frac{\partial \bar{C}}{\partial y}\right) + \frac{\partial}{\partial z}\left(D_m \frac{\partial \bar{C}}{\partial z}\right) \\ &+ \frac{\partial}{\partial z}(w_s \bar{C}) - \frac{\partial}{\partial x}(\overline{\tilde{u}\tilde{C}}) - \frac{\partial}{\partial y}(\overline{\tilde{v}\tilde{C}}) - \frac{\partial}{\partial z}(\overline{\tilde{w}\tilde{C}}) - \frac{\partial}{\partial x}(\overline{u'C'}) - \frac{\partial}{\partial y}(\overline{v'C'}) - \frac{\partial}{\partial z}(\overline{w'C'})\end{aligned} \tag{4.4}$$

where the over bar implies time-averaging.

The last six terms in Eq. 4.4 correspond to the gradients of wave and current diffusion fluxes and are commonly modeled, by analogy with the molecular diffusion, as

$$-\overline{\hat{u}\hat{C}} - \overline{u'C'} - \overline{\hat{v}\hat{C}} - \overline{v'C'} - \overline{\hat{w}\hat{C}} - \overline{w'C'} = \epsilon_x \frac{\partial \bar{C}}{\partial x} + \epsilon_y \frac{\partial \bar{C}}{\partial y} + \epsilon_z \frac{\partial \bar{C}}{\partial z} \tag{4.5}$$

where ϵ_x, ϵ_y and ϵ_z are the diffusion coefficients due to wave-induced and turbulent current-induced diffusion.

Using the combined diffusive coefficients, K_x, K_y and K_z which incorporate molecular diffusion, wave-induced diffusion and turbulent diffusion, the general wave-averaged transport equation for the conservative constituent is

$$\frac{\partial \bar{C}}{\partial t}+\frac{\partial(u\bar{C})}{\partial x}+\frac{\partial(v\bar{C})}{\partial y}+\frac{\partial(w\bar{C})}{\partial z}=\frac{\partial}{\partial x}\left(K_x\frac{\partial \bar{C}}{\partial x}\right)+\frac{\partial}{\partial y}\left(K_y\frac{\partial \bar{C}}{\partial y}\right)+\frac{\partial}{\partial z}\left(K_z\frac{\partial \bar{C}}{\partial z}\right)+\frac{\partial}{\partial z}(w_s\bar{C}) \quad (4.6)$$

where $K_x = D_m + \epsilon_x$, $K_y = D_m + \epsilon_y$, $K_z = D_m + \epsilon_z$.

The horizontal gradients in concentration are typically three to four orders of magnitude smaller than the corresponding vertical gradients in the coastal zone, estuaries and shallow lakes (Ross, 1988). Therefore, for simplicity, changes in the two horizonal directions can be neglected, and all the variables considered uniform in the horizontal plane. Also, as a special case, for linear waves considered here, $\bar{u} = \bar{v} = \bar{w} = 0$. Thus, Eq. 4.6 can be simplified as a one-dimensional problem, in which only the vertical z-direction is considered, i.e.,

$$\frac{\partial \bar{C}}{\partial t} = \frac{\partial}{\partial z}\left(K_z\frac{\partial \bar{C}}{\partial z}\right) + \frac{\partial}{\partial z}(w_s\bar{C}) \quad (4.7)$$

Equation 4.7 can be used for sediment transport, for which $\bar{C}$ would represent the sediment concentration and K_z and w_s the vertical diffusion coefficient and the sediment settling velocity, respectively. Eq. 4.7 can also be used for the transport of any conservative contaminant, for which $\bar{C}$ would represent contaminant concentration, K_z the vertical

contaminant diffusion coefficient and w_s the contaminant settling velocity, which is zero for dissolved constituents considered here.

In the above derivation, since no layering has been specified, Eq. 4.7 is suitable for all the three layers. However, the vertical diffusion coefficient and the settling velocity need to be specified depending on wave loading, on the dynamic response of the bed to loading, and on the layer, i.e., water, fluid mud or bed.

In the following, the over bar over C is dropped for convenience. However, the variable will continue to represent a wave-averaged value.

4.4 Sediment Transport Model

4.4.1 Vertical Fine-grained Sediment Transport Equation

Referring to Fig. 4.1, within the water column vertical sediment transport is governed by settling and upward diffusion. In Eq. 4.7, choosing S_1 to represent suspended sediment concentration (or the dry density), K_{z1} the vertical diffusion coefficient of sediment, and w_s the sediment settling velocity, the vertical suspended sediment transport equation for the water layer becomes

$$\frac{\partial S_1}{\partial t} = \frac{\partial}{\partial z}(w_s S_1 + K_{z1}\frac{\partial S_1}{\partial z}) \tag{4.8}$$

In Eq. 4.8, the settling velocity is strongly dependent on the sediment concentration (Wolanski et al., 1989; Hwang, 1989). This dependence can be expressed as (see Eqs. 2.25 and 2.28)

$$w_s = \begin{cases} \dfrac{\alpha_1 S_1^{\beta_1}}{(S_1^2 + \gamma_1^2)^{\delta_1}} & S_1 > S_1^* \\ \dfrac{\alpha_1 S_1^{*\beta_1}}{(S_1^{*2} + \gamma_1^2)^{\delta_1}} = w_{sf} & S_1 \le S_1^* \end{cases} \tag{4.9}$$

where α_1, β_1, γ_1, and δ_1 are empirical constants which depend on sediment properties and on the rate of shearing due to turbulence (Wolanski et al, 1992). The concentration, S_1^*, defines the limit below which w_s remains practically constant, equal to w_{sf}.

The mass diffusivity of the suspended sediment, K_{z1}, depends on the flow field and its modulation by density stratification. Given the diffusivity, K_n, under non-stratified or neutral flow conditions, we specify

$$K_{z1} = K_n \Phi \tag{4.10}$$

where Φ is the Monin-Obukov correction for stratification, which increasingly reduces the ratio, K_{z1}/K_n, below unity with increasing concentration gradient in the water column, or decreasing flow energy required for entrainment (Dyer, 1986). Thus, Φ characterizes the degree of damping of neutral diffusion due to a stably stratified concentration gradient. When the wave field is modulated by a weak current, often a noteworthy effect on sediment transport is that material eroded from the bottom tends to be entrained upward into the water column at a measurably faster rate than when only waves are present. To simulate this effect in an approximate way in terms of the effect of the wave-weak current boundary layer on the

vertical diffusion of suspended sediment, we will introduce the following assumed form of the neutral diffusion coefficient

$$K_n = \phi_w K_{nw} + \phi_c K_{nc} \tag{4.11}$$

in which it remains to specify the wave and diffusion coefficients, K_{nw} and K_{nc}, respectively, and the corresponding weighting coefficients, ϕ_w and ϕ_c. For the neutral diffusivity coefficient under wave motion we will select the expression proposed by Hwang and Wang (1982)

$$K_{nw} = \alpha_2 \frac{\omega \zeta_{01}^2}{8} \frac{\sinh^2 k(h_1 + z)}{\sinh^2 k h_1} \tag{4.12}$$

in which $\omega = 2\pi/T$ is the angular wave frequency, T is the wave period, ζ_{01} is the wave amplitude, i.e., one-half wave height, k is the wave number and α_2 is a scaling coefficient, which for a given sediment depends on the flow field. For diffusion due to the current-induced boundary layer the well known Prandtl-von Karman expression is selected, i.e.,

$$K_{nc} = \frac{\kappa n_m g^{1/2}}{h_1^{1/6}} U(h_1 - z)\left(1 - \frac{h_1 - z}{z}\right) \tag{4.13}$$

where κ is the Karman constant, n_m is the Manning's the bed resistance coefficient, g is the acceleration due to gravity and U is the mean current velocity. For turbulent, open channel flows devoid of sediment, $\kappa = 0.4$ (Dyer, 1986). This value will be used consistently in the analysis given here, ignoring the variability in κ is comparison with the uncertainties

involved in selecting the values of the several other parameters required for concentration profile simulation. In the absence of site-specific data on bed resistance, it is acceptable to assume the bottom to be smooth, and represent its resistance to flow by selecting Manning coefficient $n_m = 0.011$ (Mehta et al., 1982). Finally, for the stratification factor, Φ, we will select the expression of Munk and Anderson (1948), which has also been used by Hwang (1989) for simulating the influence of stratification under wave motion, and by Ross (1988) for sediment-induced stratification under a tidal current. This expression is

$$\Phi = (1+\alpha_3 Ri)^{-\beta_3} \tag{4.14}$$

where the coefficients α_3 and β_3 depend on the effect of suspended sediment on the turbulent mixing length. The gradient Richardson Number, Ri(z), which embodies the influence of stratification on the turbulent mixing energy, is defined as

$$Ri = - \frac{\frac{g}{\rho_1}\frac{d\rho_1}{dz}}{\left(\frac{du_1}{dz}\right)^2} \tag{4.15}$$

where ρ_1 is the density of water and $u_1(z)$ is the horizontal velocity amplitude. A restriction on the application of Eq. 4.15 is that it is not valid where and when the velocity is uniform, since in that case $Ri \rightarrow \infty$ by virtue of Eq. 4.15.

4.4.2 Boundary Conditions

The boundary condition at the water surface, z=0, is that the net flux of sediment across the water surface is zero, i.e.,

$$w_s S_1|_{z=0} + K_{z1}\left.\frac{\partial S_1}{\partial z}\right|_{z=0} = 0 \qquad (4.16)$$

For the water layer, the water-fluid mud interfacial condition is that the net flux of sediment into the water column across the interface is equal to the net flux of sediment entrainment, E_r, and deposition, D_r, i.e.,

$$w_s S_1|_{z=-h_1} + K_{z1}\left.\frac{\partial S_1}{\partial z}\right|_{z=-h_1} = E_r - D_r \qquad (4.17)$$

The entrainment flux of sediment from fluid mud will be determined in the next section. The deposition flux can be expressed as (Krone, 1962; Ross, 1988 and Hwang, 1989)

$$D_r = p w_s S_1|_{z=-h_1} \qquad (4.18)$$

where p is the probability of deposition of the sediment onto the fluid mud surface. According to Krone (1993), $p = (\tau_{cr}-\tau_b)/\tau_{cr}$, where τ_b is the shear stress at the interface and τ_{cr} is defined as the critical shear stress for deposition. By this definition, deposition is permissible when $\tau_b < \tau_{cr}$. The critical shear stress depends on the properties of the flocs in the flow field to which they are subjected, and has been found to depend on the size distribution of the suspended sediment suspended (Mehta, 1988a). We note that $p = 0$ corresponds to the condition when no deposition can occur, and $p = 1$ denotes the condition of complete deposition of all suspended sediment. Since a restriction on the ability of the sediment to deposit can only be modeled when the dependence of τ_{cr} on sediment properties

is known, for the solution of many practical problems for which such information is not available it is best to set $\tau_b / \tau_{cr} = 0$, i.e., $p = 1$, which means that deposition is permitted under any flow condition, as long as there is sediment in suspension, with the rate of deposition equal to the product of the settling velocity and the suspension concentration at the bottom per Eq. 4.18.

Thus, the governing equation, Eq. 4.8, together with boundary conditions, Eqs.4.16 and 4.17, constitute the necessary expressions for defining the vertical sediment transport in the water layer.

4.5 Fluid Mud Entrainment Rate

4.5.1 Entrainment Rate Formulation

The entrainment of sediment due to hydrodynamic instabilities at the interface resulting in the generation and breakup of sediment billows by shear flow (Scarlatos and Mehta, 1993) has been described in terms of the balance between the production of turbulent kinetic energy, buoyancy work in entraining the sediment and viscous energy dissipation (Kranenburg, 1994; Winterwerp et al., 1993; Mehta and Srinivas, 1993). This process is distinct from surface erosion of sediment flocs, which occurs over typically harder cohesive beds (Taki, 1990; Parchure and Mehta, 1985). Mud bottom hardness as defined here depends on the density as well as the dynamic state of mud. Thus, at a given density, a stationary bottom subjected to a current may erode by floc erosion, whereas the same bed can be liquefied by waves without a measurable decrease in density (Ross, 1988). This is because in this case liquefaction amounts to a loss of effective stress, which occurs as the inter-

particle bonds are broken under cyclic loading. The resulting fluidized bottom is prone to destabilization and entrainment in bulk. In Lake Okeechobee in south-central Florida, for instance, comparatively dense bottom mud indefinitely remains fluidized by wind generated waves (Kirby et al., 1994).

By analyzing the turbulence kinetic energy equation and experimental data, Mehta and Srinivas (1993) obtained the non-dimensional entrainment rate expression given in Eq. 2.42 as

$$E = \alpha_4 Ri_g^{-1} - \beta_4 Ri_g \tag{4.19}$$

where the global Richardson Number $Ri_g = h\Delta b/U^2$, U is the depth averaged current velocity, h is the water depth, $\Delta b = g(\rho_2 - \rho_1)/\rho_1$, α_4 depends on sediment composition and β_4 depends on the settling and cohesive behaviors of the sediment. Here, ρ_2 is the density of the fluid mud layer. Under wave motion the mean velocity in the upper layer is zero or negligible, and the boundary layer thickness is on the order of $\sqrt{\nu/\omega}$ in contrast to that for steady current, which is usually much greater. Here, ν is the water kinematic viscosity and ω is the wave frequency. Thus, the global Richardson Number must be modified for using it under wave motion.

Wave-induced entrainment of sediment from fluid mud into the water layer can also be looked upon as the result of the breakup of the water-fluid mud interface as under unidirectional flow. Thus, entrainment is controlled by the velocity difference across the interface which acts as the destabilizing factor, while the density gradient across the interface is the stabilizing factor (Scarlatos and Mehta, 1993). Then, in analogy with the

unidirectional current case we can redefine the global Richardson Number for wave motion as

$$Ri_w = \frac{\delta g \frac{\Delta \rho_b}{\rho_1}}{(\Delta u)^2} \tag{4.20}$$

where $\delta = \sqrt{\nu T}$ is the wave boundary layer thickness near the water bottom, T = wave period, $\Delta\rho = \rho_2 - \rho_1$ and Δu is the magnitude (absolute value) of the maximum difference between the velocities across the water-fluid mud interface. Δu must be obtained from measurements or by using a wave-mud interaction model.

We will further introduce a critical value of $Ri_w = Ri_{wc}$ above which entrainment can occur, ignoring molecular diffusion. Then, in analogy with and following Mehta and Srinivas (1993), the non-dimensional entrainment rate, $\hat{E}_w$, can be expressed as

$$\hat{E}_w = \begin{cases} \alpha_4 Ri_w^{-1} - \beta_4 Ri_w = \alpha_4 \left(\frac{Ri_{wc}^2}{Ri_w} - Ri_w \right) & Ri_w < Ri_{wc} \\ 0 & Ri_w \geq Ri_{wc} \end{cases} \tag{4.21}$$

where the condition for entrainment is defined according to

$$\begin{cases} Ri_w \leq Ri_{wc} & \text{Entrainment occurs} \\ Ri_w > Ri_{wc} & \text{No entrainment occurs} \end{cases} \tag{4.22}$$

Based on this expression for $\hat{E}_w$, the entrainment flux of sediment, E_r, in Eq. 4.17 can be expressed as

$$E_r = \rho_2 u_b \hat{E}_W = \alpha_4 \rho_2 u_b (Ri_{wc}^2 Ri_w^{-1} - Ri_w) \qquad (4.23)$$

where u_b is the maximum wave-induced horizontal velocity just outside the bottom wave boundary layer. Also note that α_4 is a constant and Ri_{wc} depends on sediment composition, as discussed next.

4.5.2 Laboratory Experiment

To determine Ri_{wc}, experiments were carried out in a wave flume at the Coastal and Ocean Engineering Research Institute of the Hohai University, Nanjing, China. When entrainment occurred, the suspended sediment concentration in the upper layer was also measured until an equilibrium concentration was reached.

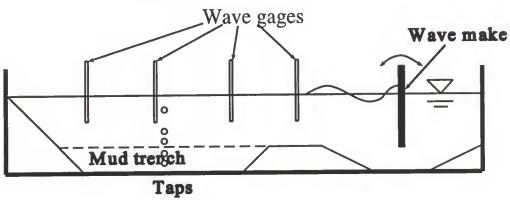

Figure 4.2 Side view of wave flume used in entrainment experiments.

Experimental Equipment

Shown schematically in Fig. 4.2, the flume was 30 m long, 50 cm wide and 60 cm deep. In the middle of the flume a 10 m long, 50 cm wide and 15 cm deep flat bottom trench served as the container of the test mud. In the section where the mud trench lay the sidewall

was made of plexiglass for observation and the others were made of concrete. A flap-type wave-maker was located near one end of the flume. Wave height and period could be adjusted by a controller in the ranges of about 0 ~ 9 cm and 0.5~1.6 Hz, respectively. At both ends of the flume, there were 1:3 slopes covered by a wave-absorbing material to minimize wave reflection.

Four capacitance-type gages were used to measure the wave height and period. One was located at the wave-maker end of the trench along the centerline of the flume for measuring the incident wave characteristics, and the other three were near the front, the mid-point and the end of the trench along the flume centerline. Signals corresponding to surface water oscillations were recorded by a light oscillograph which was analyzed later.

The suspended sediment concentration was measured by using a pycnometer with 100 ml volume. Samples (each about 120 ml) were taken from the water column at four elevations through taps on the sidewall near the mid-point of the trench.

Experimental Procedure

The experimental procedure was as follows:

(1) Specified amounts of fine-grained sediment and water were mixed to prepare muds with densities of 1,100 kg/m^3, 1,150 kg/m^3, 1,200 kg/m^3 and 1,250 kg/m^3. The sediment was taken from the Changjiang River estuary and sieved through a 50 μm sieve to remove the coarser portion. The sediment was mainly composed of illite, kaolinite , montmorillonite and quartz, with a mean diameter of 8 μm.

(2) The mud slurry was placed in the flume trench to a height of 13 cm to form a fluid mud layer.

(3) Water was pumped into the flume slowly from one end of flume to a depth of 20 cm over the mud layer carefully in such a way that the fluid mud was not disturbed.

(4) The wave-maker was started to produce the specified wave height and period and the water-fluid mud interface was observed visually.

(5) The wave height was increased beginning from 1 cm in steps of 0.5 ~ 1.0 cm until entrainment occurred.

(6) Using different wave periods, step (5) was repeated.

(7) Using muds of different densities, steps (5) and (6) were then repeated.

Five different wave periods, i.e., 0.8 s, 0.9 s, 1.0 s, 1.2 s and 1.6 s, were tested with wave heights ranging from 1 cm ~ 8 cm. Altogether, 19 tests were carried out.

Experimental Results

For determining the critical entrainment condition, the wave heights when entrainment occurred for a specific wave period and mud density are listed in Table 4.1. The equilibrium suspended sediment concentration for a specific wave condition after entrainment occurred is listed in Table 4.2.

Table 4.1 Experimental results for determination of the critical entrainment condition.

Wave period (s)	Mud bulk density (kg/m^3)			
	1,110	1,150	1,200	1,250
0.8	6.4 cm	6.4 cm	5.6 cm	7.5 cm
0.9	N.O.[a]	6.5 cm	7.1 cm	6.2 cm
1.0	6.5 cm	N.O.	N.O.	N.O.
1.0	5.6 cm	N.O.	5.6 cm	6.4 cm
1.2	6.3 cm	5.3 cm	6.0 cm	5.9 cm
1.6	5.5 cm	5.1 cm	5.0 cm	5.0 cm

[a]: No observation made.

4.5.3 Critical Global Richardson Number for Entrainment

From the experimental data of Table 4.1, the critical global Richardson Number, R_{wc}, can be calculated from

$$Ri_{wc} = \frac{\delta g \frac{\Delta \rho}{\rho_1}}{(\Delta u_c)^2} \tag{4.24}$$

where the boundary layer thickness $\delta = \sqrt{\nu T}$ (Dean and Dalrymple, 1991; Jiang, 1993) and Δu_c is the critical value of Δu which can be obtained from a wave-mud interaction model for the critical condition. In the present study, the model of Jiang (1993) was used. In this model, bottom mud is assumed to be a viscous fluid with viscosity depending on mud density. The viscosity is empirically expressed as

$$\mu_2 = d_1 \exp(d_2 K S_{v2}) \tag{4.25}$$

where μ_2 is the dynamic viscosity of mud, S_{v2} is the sediment volume fraction of mud, K is the sediment volume expansion coefficient due to flocculation and/or aggregation, and d_1 and d_2 are empirical constants. For the sediment from the Changjiang River, K = 3.0 and d_1 = 33.5 and d_2 = 2.1 in the experimental range of ρ_2 = 1,030 ~ 1,210 kg/m^3 (Ren and Zheng, 1986; Li, 1989). This empirical formula may be extended to ρ_2 = 1,250 kg/m^3 as an approximation for calculating the dynamic viscosity at this density. The calculated critical global Richardson Numbers are plotted against the corresponding wave boundary layer Reynolds Numbers, Re_δ, in Fig. 4.3.

Table 4.2 Equilibrium depth-averaged suspended sediment concentrations for specified wave conditions.

Mud density (kg/m^3)	Wave period (s)	Wave height (cm)	Equilibrium concentration (kg/m^3)
1,100	1.6	6.0	1.10
		9.5	1.35
		7.3	1.73
		8.1	0.64
	1.2	8.3	1.23
		9.5	1.49
	1.0	7.2	1.23
		7.9	1.49
	1.0	8.3	1.49
		9.3	1.15
	0.8	6.9	0.35
		7.9	0.56
1,150	1.6	5.0	0.63
		6.0	1.15
	1.2	6.6	0.64
		6.6	0.96
	1.0	8.1	1.49
		9.5	1.49
	0.9	8.9	0.52
		9.8	0.74
	0.8	7.9	0.47
		8.9	0.64

Table 4.2(continued).

Mud density (kg/m^3)	Wave period (s)	Wave height (cm)	Equilibrium concentration (kg/m^3)
1,200	1.6	6.0	0.76
		7.5	0.30
	1.2	6.6	0.30
		8.0	0.30
	1.0	6.7	0.57
		7.5	1.27
	0.9	8.9	0.34
	0.8	6.7	0.19
		7.9	0.32
1,250	1.6	6.0	1.13
		7.5	1.33
		8.7	1.33
	1.2	7.3	0.79
		8.0	1.33
	1.0	8.7	0.68
		9.5	1.36
	0.9	8.0	0.21
		10.7	0.90
	0.8	7.9	0.15
		8.9	0.82

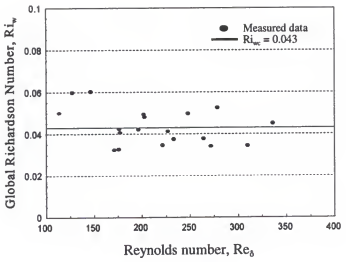

Figure 4.3 Critical Richardson Number for entrainment by waves.

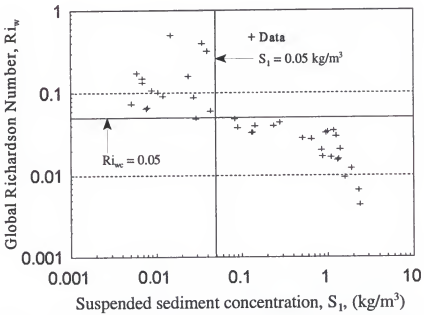

Figure 4.4 Critical Richardson Number estimated from the experiments of Maa (1986).

Under wave motion in water, viscous effects can become important only within the bottom boundary layer, and the entrainment can be looked on as the result of the shear effect

from wave boundary layer upon bottom sediment surface. Thus, the wave boundary layer Reynolds Number is selected as the parameter for entrainment, in analogy with the Reynolds Number, selected by Keulegon (1953) and Ippen and Harleman (1951) for entrainment under current. The Reynolds Number of wave boundary layer is expressed as

$$Re_\delta = \frac{\Delta u \delta}{\nu_1} \tag{4.26}$$

It is observed that not withstanding data scatter, the critical Richardson number can be represented in the mean as a constant equal to 0.043 within the experimental range of the Reynolds Number of 100 ~ 350.

For a further examination of the entrainment behavior we next note Maa's (1986) wave-induced mud erosion experiments. These experiments were carried out in a wave flume, which will be described in details in Chapter 7, by using a commercial kaolinite and an estuarine mud. Sediment concentration response in the water column with elapsed time under different wave loading were measured (see Section 4.6.1). Additional tests were conducted to evaluate the viscoelastic properties of the selected sediment using a Brookfield viscometer. The condition that the final depth-averaged suspended sediment concentration less than 0.04 kg/m^3 can be interpreted to mean no entrainment, and the final depth-averaged suspended concentration greater than 0.06 kg/m^3 can be considered to indicate that entrainment occurred. The low suspended sediment concentration in the absence of entrainment may be attribute to molecular level diffusion, which is usually neglected in the entrainment process during which considerably greater quantities of sediment are

resuspended due to causes other than molecular diffusion (Mehta and Srinivas, 1993). It can be shown that the critical Richardson Number in Maa's (1986) experiments corresponding to a concentration of 0.05 kg/m^3 was about 0.05 (see Fig. 4.3). In calculating the Richardson Number, the mud bed density was considered to be uniform by using the depth average density calculated from the measured mud density profiles. The viscoelastic parameters as functions of bed density were calculated from the empirical formulae obtained from experiments by using controlled-strain rheometry.

Finally, we note the laboratory experiments of Mimura (1993), which were carried out in a wave flume that was 13 m long and 0.3 m wide. Two types of clays, namely kaolinite and bentonite, and a natural mud taken on the Fukushima Coast, Japan, were used as sediments. The wave height was varied from 1.2 to 13.7 cm and the period from 0.77 to 1.3 s. A mud bed of 2 m length and 0.1 m depth was placed in the middle portion of the flume, and then waves were generated. As erosion proceeded to establish a vertical distribution of the concentration of suspended sediment, the sediment profiles and the amount of resettled sediment were measured at 10 sections along the flume repeatedly with an interval of 20, 40 or 80 minutes. The critical bottom shear stress, τ_{cr}, for mud bed erosion was found to vary from 0.12 to 0.3 Pa. Using the formula $\tau = 0.5 \rho_1 f_{ric} u_b^2$ (Johnson, 1966) and assuming the friction coefficient $f_{ric} = 0.02$ as a typical value for mud beds, the amplitude of horizontal orbital velocity at the water bottom, u_b, can be shown to range from 0.11 to 0.27 m/s, with an average value of 0.19 m/s. Since the rheology of the muds used was unknown, the wave-mud interaction model cannot be used to calculate Δu_c. Here, by assuming the mud bed to be motionless, Δu_c is set equal to u_{1m}.

Since the wave period in Mimura's (1993) experiments varied from 0.77 to 1.3 s, the Reynolds Number is obtained from Eq. 4.23 in the range from about 100 to 310. Also, in these experiments the fluid-like mud bed with a water content > 180 % had densities in the range of about 1,100 ~ 1,250 kg/m^3. Thus, the critical Richardson Number can be calculated from Eq. 4.21 to be in the range of 0.024 ~ 0.082 with an average value of 0.053, which is in agreement with the earlier values.

4.5.4 Comparison with Experimental Data

In Eq. 4.20, the two parameters, α_4 and Ri_{wc}, must be determined from experimental data. Under the wave condition when entrainment occurs, i.e., $Ri_w < Ri_{wc}$, the sediment concentration in the water column increases with time. With increasing concentration the settling flux, D_r, increases for typical concentrations (< 3~ 10 kg/m^3) according to Eq. 4.15, and when $E_r = D_r$, the concentration reaches an equilibrium value. Note that because E is equal to S at equilibrium, $E_r = D_r = w_s\bar{S}$, where $\bar{S}$ is the depth-averaged concentration, which, as an approximation, can be considered to be the concentration of a uniform, mixed layer of suspension above the bottom. The settling velocity, w_s, can be obtained from Eq. 4.9 using $\bar{C}$ and sediment-specific values of the coefficients in that equation. To calculate the corresponding values of Ri_w, the velocity difference, Δu, in Eq. 20 was calculated by using the first order solutions of a second order analytic model developed by Jiang (1993) and Jiang and Mehta (1996). In this approach, water is treated as a viscid fluid that is free of sediment. The rheometry required for this application has been prescribed by Jiang and Mehta (1995) for determining the viscosities and the shear moduli. Note that to simplify the method of analysis for determining the entrainment rate function, u_b in Eq. 10 was calculated

from the analytic model by considering the bottom mud to have an arbitrarily high value of the shear modulus of elasticity. This assumption essentially means that u_b was determined from the linear wave theory assuming a hard bottom.

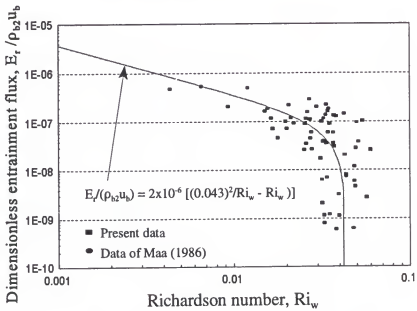

Figure 4.5 Dimensionless entrainment rate as a function of Richardson Number.

From the experiments described earlier and those of Maa (1986), the final concentration in water can be considered as the equilibrium concentration because of the long duration (about 2 ~ 7 hrs) of wave action and the small changes in concentration measured at later times. Since the settling velocities were not measured, the four parameters in settling velocity formula for calculating D_r will be selected to be $\alpha_1 = 0.01$, $\beta_1 = 1.33$, $\gamma_1 = 1.5$ and $\delta_1 = 9.0$, with the upper limit concentration for free settling, $S_1^* = 0.1$ kg/m^3, from the data of Hwang (1989). The critical Richardson Number will be selected as 0.043 from Fig. 4.3. The plot of the dimensionless entrainment flux, $E_r/\rho_2 u_b$, versus Ri_w in terms of the

data points derived from the above analysis is shown in Fig. 4.5, in which Eq. 4.20 has also been plotted, with the best-fit value of $\alpha_4 = 2x10^{-6}$.

Notwithstanding the evident paucity of data points as well as clustering and smear, the trend of Eq. 4.23 in Fig. 4.5 is seen to be in agreement with the data points, and is analogous to the trend found for the entrainment fluid-like mud under steady shear flows (Mehta and Srinivas, 1993). In consonance with the entrainment of a salt water layer into fresh water, at low values of Ri_w, E varies with Ri_w^{-1}, which in turn can be shown to mean that the rate of entrainment is proportional to the rate of change of potential energy of the suspension. As Ri_w increases, it becomes increasingly difficult for the flow to lift the sediment, with the result that E_r begins to decrease rapidly when Ri_w exceeds about 0.030, and a cutoff of entrainment occurs at $Ri_w = 0.043$, assuming molecular diffusion to be negligible.

It must be pointed out the application of Eq. 4.23 to field data may not be straightforward, because of the scaling effects represented by the Reynolds Number, Re_w, which is characteristically higher in the field than in flume experiments. On the other hand, we must note that the data points of Fig. 4.5 collectively cover a wide range of Re_w. Thus, defining $Re_w = a_b\omega/\nu$, where $a_b = u_b\omega$is the near-bottom amplitude of wave-induced horizontal excursion, the ranges of Re_w in the experiments of Maa (1986) and Li (1996) approximately were $3.1x10^3$ to $7.8x10^3$ and $1.3x10^5$ to $1.0x10^6$, respectively. Therefore, the overall range of Re_w represented in Fig. 4.5 is fairly wide, encompassing incipient turbulent to fully turbulent flow conditions. In turn, the observation that the two sets of data are affine, when plotted in terms of the dimensionless groups in Fig. 4.5, suggests that scaling may have

been at least partly accounted for in Eq. 4.23. In any event, it is believed that the main parameter to be scaled is α_4, which must be determined by calibration for each site-specific case.

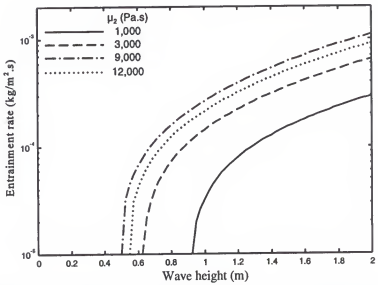

Figure 4.6 Entrainment flux as a function of wave height and mud viscosity.

The sensitivity of E_r to Δu is indirectly illustrated in Fig. 4.6 in terms of the dependence of E on the wave height, $2\zeta_0$, and mud viscosity, μ_2. For each wave height and mud viscosity, E_r was calculated by using the following parameters applicable to a "typical" nearshore conditions: water depth, $h_1 = 3.0$ m, mud thickness, $h_2 = 2.0$ m, wave period, T = 8.5 s, mud density, $\rho_2 = 1{,}270$ kg/m^3, entrainment coefficient, $\alpha_4 = 2\text{x}10^{-5}$ and mud shear modulus, $G_2 = 2{,}000$ Pa. In Fig. 4.6, observe the dependence of the entrainment flux on wave height. Thus, for example, selecting a characteristic value of the viscosity, μ_2, of 7,000 Pa.s, there will be practically very little turbidity when the waves are lower than about 0.5 m in height. On the other hand, as the height increases above around 0.5 m, entrainment is

observed to increase logarithmically, in qualitative agreement with the typically found episodic increases in turbidity levels in the nearshore areas under inclement sea conditions. The influence of viscosity at a given wave height is seen to be non-monotonic. Thus, as μ_{m2} increases, entrainment increases at first because Δu increases. However, as μ_{m2} increases from 9,000 to 12,000 Pa.s, the entrainment flux decreases because the mud becomes less responsive to wave motion than at 9,000 Pa.s.

4.6 Laboratory Simulations

Laboratory data were selected to be flume experimental Runs 4, 5 and 6 conducted by Maa (1986), as described briefly in Section 4.5.3. In these experiments Cedar Key (Florida) mud was entrained by changing the wave conditions in steps so as to increase the applied bottom shear stress in steps. Starting with a water column of known residual or initial concentration distribution, C(z,t), the first (monochromatic) wave loading was maintained for 3 to 7 hours, then it was increased and continued for another 3 to 7 hours. In Run 6, a third wave loading, increased from the second one, was maintained for 4 hours. Suspended sediment samples were taken for each wave loading at variable time intervals, e.g., 15, 30, 60, 120, 180 and 240 minutes, at three selected elevations. Wave height, period and crude density profiles of bottom mud were also measured. Mud rheology was characterized in terms of Voigt viscoelastic solid, for which the viscosity, μ_m, and the shear modulus of elasticity, G (Jiang and Mehta, 1995), were determined in separate rheometric tests as functions of mud density.

Relevant parameters for settling and entrainment were derived from the study of Maa (1986) as well as from the wave-induced resuspension study of Hwang (1989) and Ross (1989), and current-induced resuspension simulations of Ross (1989). Accordingly, the settling velocity related parameters in Eq. 4.9 were selected to be: $w_{sf} = 6.37 \times 10^{-7}$ m/s, $S_1^* = 0.1$ kg/m^3, $\alpha_1 = 0.01$, $\beta_1 = 1.33$, $\gamma_1 = 1.5$ and $\delta_1 = 9$. Since a current was not externally generated in the experiments, it is appropriate to set $\phi_w = 1$ and $\phi_c = 0$ in Eq. 4.11. Values of the wave diffusion parameter, α_2, in Eq. 4.23, given in Table 4.3 are seen to range from 0.19 to 0.60. These values are considerably larger than $\alpha_2 = 0.0008$ used by Ross (1988), signifying a much greater upward diffusion in the tests of Maa(1986). For resuspension of 0.2 mm sand, Hwang and Wang (1982) found α_4 to range from 0.13 to 0.20 for non-breaking waves, which are comparable with those in Table 4.3. The stratification parameter, Φ, in Eq. 4.10 was characterized by $\alpha_3 = 0.5$ and $\beta_3 = 0.5$. These values are well within the ranges of the two parameters used in previous studies on stratified flows. Thus, we note that from a compilation of such studies Ross (1988) found α_3 to range from 0.062 to 180 and β_3 from -0.75 to 0.50. The entrainment proportionality coefficient, α_4, in Eq. 10 was selected to be 2.5×10^{-5} for the three runs. This value is higher than $\alpha_4 = 2 \times 10^{-6}$ in Fig. 4.5 because the latter value is inclusive of the influence of settling in the experiments, whereas, since in Eq. 4.9 settling is considered to be separate and distinct from entrainment, a higher value of α_4 must be chosen to simulate the concentration profiles. The critical global Richardson Number, Ri_w, was assumed to be 0.043, as in Fig. 4.5. Input parameters required for simulations of Runs 4, 5 and 6, other than those already prescribed, are listed in Table 4.3.

The simulated variations of suspension concentrations at the three elevations are shown along with the data points in Figs. 4.7, 4.8 and 4.9.

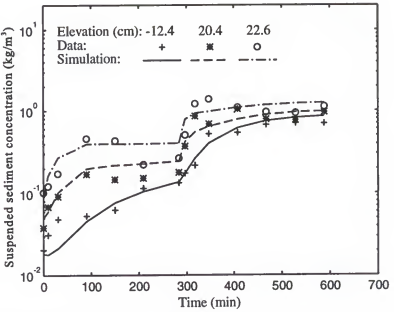

Figure 4.7 Comparison between simulated and measured data for Run 4 of Maa (1986).

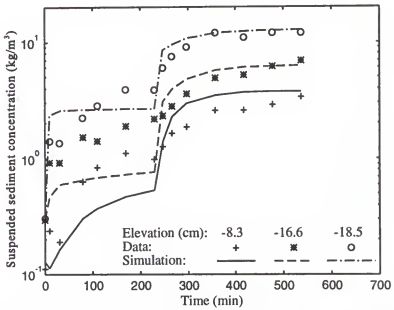

Figure 4.8 Comparison between simulated and measured data for Run 5 of Maa (1986).

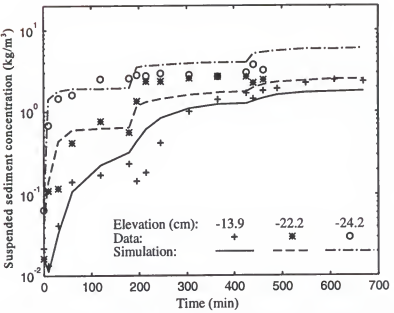

Figure 4.9 Comparison between simulated and measured data for Run 6 of Maa (1986).

Figure 4.7 shows the time-variation of the simulated suspended sediment concentration for Run 4 (Maa, 1986). From the time of commencement of wave motion the concentrations increase and approach equilibrium values by the end of the duration over which constant wave conditions were maintained. The equilibrium condition is defined by the equality between the upward diffusive and settling fluxes at all levels including the interface, where the rate of sediment entrainment equals the rate of deposition. When the wave height was increased, the concentrations increased again to approach higher equilibrium values. The model results approximately mimic the trends of the data points over the entire test time range, with the possible exception of the initial part of the first phase (step) at the highest elevation (-12.4 cm), during which the model slightly underpredicted the concentration. For results of Run 5 are shown in Fig. 4.8, the simulations measurably under-

predict the concentrations at the two upper elevations during the first step of the test. Since, however, during the second step the agreements are better, one is led to suggest that at the beginning of Run 5 the bottom material was considerably looser than assumed in the model. This situation probably arose because the bottom mud was stratified with respect to the density, whereas in the simulation a uniform bottom of constant density, ρ_m, was assumed. Since ρ_m was obtained by vertically averaging the bottom mud density profile, ρ_m was greater than the actual density at the time of initiation of entrainment. Unfortunately, this explanation is not entirely consistent with the trends for the lowest elevation at -18.5 cm, where there seems to be over-prediction followed by under-prediction during the first step. One would suspect that experimental errors are at least in part responsible for the observed differences between the data points and simulation. Finally, note that in Run 6 (Fig. 4.9), in which entrainment was carried out in three steps, the simulated and data trends generally are agreement, although in this case the lack of data points at the two lower elevations during the third step precludes a fuller comparison between the model results and the measurements.

4.7 Model Application to Field Data

Field data previously obtained from the Louisiana coast and the southwest coast of India, where muddy bottom sediments occur, are chosen for application of the sediment transport model.

Field experiments conducted along the Louisiana coast by Kemp (1986) sought, in part, to quantify the relationship between the wave characteristics and the suspended sediment distribution. The study was aimed at providing data during the passage of a winter

cold front, which induced a strong wind field and then, severe wave conditions to resuspend bottom sediments. Suspended sediment concentrations from a multi-level sampler were measured for the pre-frontal, frontal and post-frontal periods together with the wave conditions at the same time.

The active mudbanks along the southwest coast of India were investigated by Mathew (1992) in terms of their formation, movement and dissipation. The study area was dominated by waves with relatively weak currents. Suspended sediment concentration profiles before and during the presence of the mudbank were measured.

4.7.1 Coast of Louisiana

Field Conditions

The 30 km section of coast selected for study lies west of the Southwest Pass of Vermilion Bay on the eastern margin of the Louisiana Chenier plain (Fig. 4.9). Presently, this area receives an influx of mud from the Atchafalaya River, a Mississippi distributary having a delta lobe in a bay 100 km to the east of the study area. Atchafalaya River discharge, comprising roughly a third of the combined Mississippi and Red River flows at Simmesport, Louisiana, average 5126 m^3/s. It is dispersed onto the shelf mainly through a dredged navigation channel. The most significant influx of low salinity, sediment-laden waters from the bay occurs during the spring flood typically from December to April. At several locations, fine-grained sediments accumulate near the shore by deposition from highly concentrated mud-water suspension or fluid mud.

Table 4.3 Parameters for simulating Runs 4, 5 and 6 of Maa (1986).

		Run 4	Run 5	Run 6
Wave period (s), height (cm), and duration (min)		1.6; 3.4; 0 ~ 285	1.7; 3.2; 0 ~ 230	1.8; 3.5; 0 ~ 180
		1.1; 5.5; 285 ~ 588	1.2; 5.2; 230 ~ 537	1.4; 4.5; 180 ~ 425
				1.0; 5.3; 425 ~ 670
Water depth (cm)		26.4	19.7	27.4
Mud depth (cm)		9.3	16.0	10.5
Mud density (kg/m^3)		1,080	1,080	1,100
Settling velocity parameters	S_1^*	0.1	0.1	0.1
	w_{sf}	6.37×10^{-7}	6.37×10^{-7}	6.37×10^{-7}
	δ_1	0.01	0.01	0.01
	$\hat{\delta}_1$	1.33	1.33	1.33
	$\hat{\bullet}_1$	9.0	9.0	9.0
	δ_1	0.5	0.5	1.5
Wave diffusion coefficient, α_2		0.19	0.5	0.6
Stratified damping coefficients	α_3	0.5	0.5	0.5
	β_3	0.5	0.5	0.5
Critical Richardson Number, Ri_{wc}		0.043	0.043	0.043
Entrainment coefficient, α_4		2.5×10^{-5}	2.5×10^{-5}	2.5×10^{-5}
Mud rheological parameters	G_2 (Pa)	168.2	168.2	122.8
	μ_2 (Pa.s)	15.4	20.9	63.7
Elevation of sediment sample below water surface (cm)	#1	-12.4	-8.3	-13.9
	#2	-20.7	-16.6	-22.2
	#3	-22.6	-18.5	-24.2

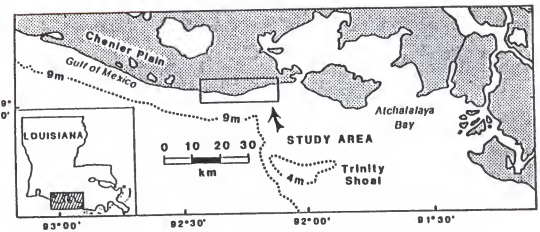

Figure 4.10 Location map of the study area of Kemp (1986).

Tidal and wind-driven currents control the mixing of Atchafalaya and Gulf waters and the dispersal of river sediments on the inner continental shelf. Mixed diurnal and semi-diurnal tides in the study area have a mean amplitude of 60 cm. Currents associated with these tides have average speeds less than 10 cm/s. However, the wind-driven currents usually have speeds up to 50 cm/s and play a significant role in the shelf sediment transport. High winds are the main factor promoting vertical mixing of the water column and developing waves which suspend bottom sediment into the water column. Barring hurricanes and tropical storms, sustained high winds are common between September and April when tropical cyclone or cold fronts cross the coast every 5 to 10 days.

The density of deposited mud ranges from 1,200 kg/m^3 at the surface to 1,400 kg/m^3 a meter below. The fraction of sand-size particles in the mud samples are from zero to 14 percent, while silt content varied from 20 to 50 percent. Clay make up the remainder, between 50 and 80 percent of total. The major clay mineral groups were smectite (37%), illite (30%) and kaolinite (18%).

Model Application

During the period of 10 through 13 December 1982, a cold front traversed the study area. Data on wave conditions and suspended sediment concentration were collected in this area corresponding to the pre-frontal, frontal, and post-frontal periods.

Table 4.4 Measured wave and suspended sediment data from Louisiana coast (based on Kemp, 1986).

Time	Wave height H_{rms} (cm)	Wave period T (s)	Suspended sediment concentration (g/l)			
			-1 cm	-25 cm	-55 cm	-80 cm
Frontal, Dec. 11, 1982						
13:07	Average 11.7	Average 6.6	0.205	0.256	0.350	3.213
13:38			0.304	0.355	0.634	4.650
14:23			0.360	0.341	0.362	5.666
15:09			-	0.341	0.515	1.155
Post-Frontal, Dec. 13, 1982						
10:51	Average 5.2	Average 6.9	-	0.820	0.301	1.355
11:30			-	0.582	0.618	1.131
12:34			0.413	0.426	0.439	0.732
13:01			0.431	0.477	0.466	0773

The water depth at the experiment site ranged from 85 to 105 cm. During the pre-frontal period arriving, waves formed spilling breakers near the shoreline. In subsequent periods, i.e., frontal period and post-frontal period, waves were largely attenuated before reaching the shoreline. This suggests that during the pre-frontal period fluid mud had not been formed and therefore the wave energy was mainly dissipated by breaking, while during the frontal and post-frontal periods the wave energy was dissipated by the motion of the newly formed bottom fluid mud. Wave data were obtained from representative 20 minute pressure records acquired before, during and after frontal passage. Wave spectra computed

from these data showed that energy density peaks appeared at two frequencies in the gravity wave range. These peaks defined distinct wave trains: swell with an average period of 6.8 s and locally generated seas of about 3.1 s period. The average ratio of H_{rms} (root-mean-square wave height) of sea to that of swell was about 0.7 during the experiment. Thus, swell were considered to be the main factor for wave-mud interaction and sediment resuspension. Wave data based on swell activity are given in Table 4.4.

Suspended sediment concentrations ranged from 0.2 g/l to 5.7 g/l and decreased with elevation above the bottom. The highest concentrations were monitored at 10 cm above the mud bottom during the frontal period. These measurements are given in Table 4.4.

Mud thickness or its properties were not measured. As an approximation, the thickness of fluid mud is assumed to be 0.18 cm. Mud rheology is modeled as a Voigt solid with the dynamical viscosity to be 50 Pa.s and elasticity to be 100 Pa. Since the settling velocity of the sediment was not measured, three of the four coefficients for the settling velocity formula are taken from Hwang (1989), with $\beta_1 = 1.33$, $\gamma_1 = 1.5$ and $\delta_1 = 9.0$. The four coefficients and wave diffusive coefficient, α_2, are determined by fitting the model results to data. The parameters for the entrainment rate equation, i.e., the critical Richardson Number, Ri_{wc}, and entrainment rate coefficient, α_4, are selected as $Ri_{wc} = 0.063$ for the frontal period and 0.060 for the post-frontal period, and $\alpha_4 = 1 \times 10^{-4}$ obtained by fitting the simulated results to data. The choice of slightly smaller critical Richardson Number for the post-frontal period than that for the frontal period is attributed to increased stratification of mud bed with time and the entrainment of the weaker surface layer of fluid mud by frontal waves, exposing a more resistant layer below.

Table 4.5 Parameters for simulating data from the Louisiana coast.

		Frontal	Post-Frontal
Wave period (s), height (cm), and duration (min)		6.6; 11.7; 76	6.9; 5.2; 190
		5.9; 10.2; 46	
Water depth (cm)		0.9	0.3
Mud depth (cm)		0.03	0.18
Settling velocity parameters	S_1^*	0.3	0.3
	w_{sf}	1.9×10^{-6}	1.0×10^{-4}
	α_3	0.03	0.03
	β_1	1.33	1.33
	α_3	9.0	0.3
	δ_1	0.9	1.5
Wave diffusion coefficient, α_2		0.3	0.3
Stratified damping coefficients	α_3	0.9	0.5
	β_3	0.33	0.03
Critical Richardson Number, R_{wc}		0.063	0.06
Entrainment coefficient, α_4		1.0×10^{-4}	1.0×10^{-4}
Mud rheological parameters	G_2 (Pa)	100	100
	μ_2 (Pa.s)	50	50
Elevations of sediment samples below water surface (cm)	#1	-0.5	-0.5
	#2	-25.0	-25.0
	#3	-55.0	-55.0
	#4	-80.0	-80.0

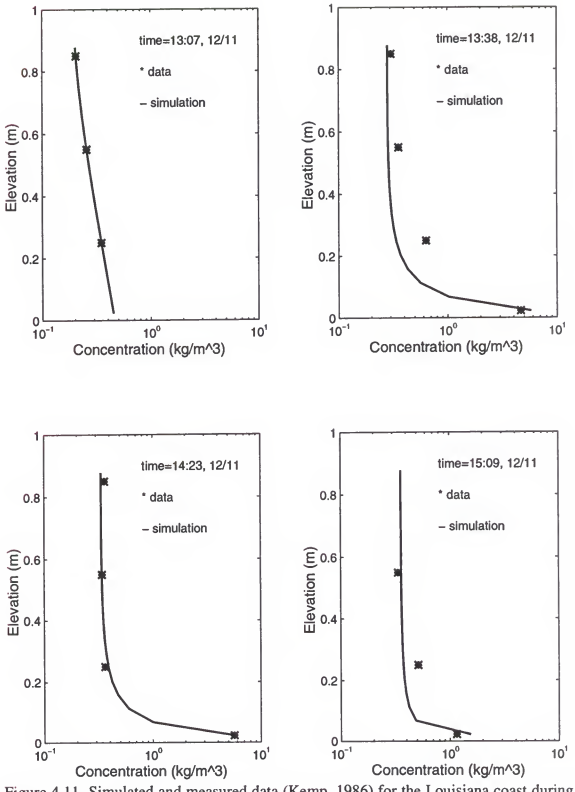

Figure 4.11 Simulated and measured data (Kemp, 1986) for the Louisiana coast during frontal passage.

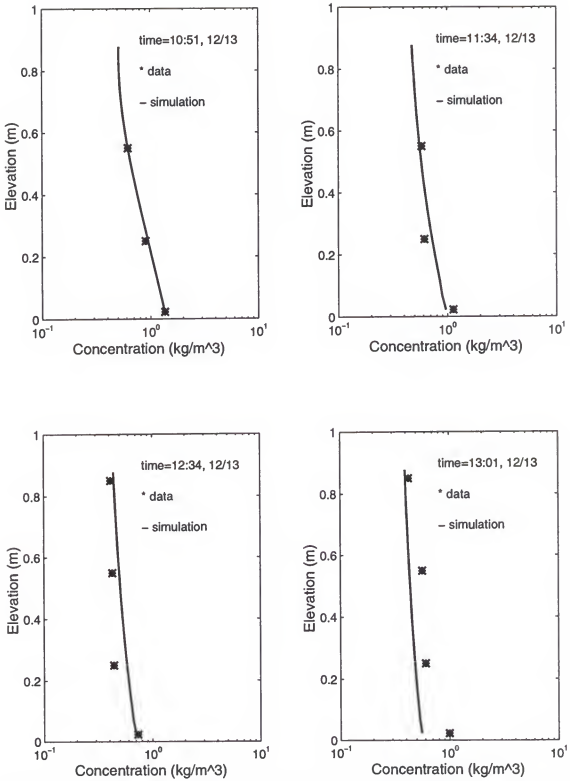

Figure 4.12 Simulated and measured data (Kemp, 1986) for the Louisiana coast during the post-frontal period.

Suspended sediment concentration profile for both the frontal and the post-frontal periods are simulated. The initial sediment concentration in water is obtained from data at 13:07 on 12/11/1982 for the frontal period and at 10:51 on 12/13/1982 for the post-frontal period. The input parameters are summarized in Table 4.5, and the model results and data are shown in Fig. 4.11 for the frontal period and Fig. 4.12 for the post-frontal period.

During the frontal period, due to the resuspension of bottom sediment by wave motion caused by the front, the suspended sediment concentration in water increased from the initial assumed background sediment concentration at 13:07 on 12/11/1982. Initially, the concentration increased faster near the water bottom than that in the upper water layer, i.e, at 13:38, because of the resuspension of bottom sediment and a lack of significant diffusion to transport the near bottom sediment into the upper water layer. Then, as wave action continued the sediment concentration in the upper water layer increased, i.e., at 14:23, while the near-bottom suspension did not increase as much as before because the accumulation of suspension near the bottom enhanced the deposition flux. Till time 15:09, the concentration in the upper layer increased and the near-bottom suspension concentration decreased due to diffusion. Thus, under wave motion the suspended sediment concentrations in water lag wave action. This lag shift depends on wave characteristics and sediment properties. This is why the suspended sediment concentrations are not directly related to wave energy, as found by Kemp (1986) in his field survey. The model can successfully simulate the resuspension process including the lag and agree with the field data during the frontal period.

For the post-frontal period, since the wave energy decreases, the suspended sediment concentration decreases with time. The model simulates the suspended sediment

concentration decrease with the same parameters used for the frontal period except for the wave conditions, and are in good agreement with data.

4.7.2 Southwest Coast of India

Field Conditions

The study area selected by Mathew (1992) was located on the southeast coast of India off the city of Alleppey, in the State of Kerala (Fig. 4.13). A mudbank is formed almost every year in this area, composed principally of montmorillonite and kaolinite with small amounts of illite and gibbsite. The main sediment source of the mudbank is from the offshore (inner shelf) area and is transitory in nature depending on the season. It is believed that mass transport mechanisms in the cross-shore direction primarily control the response of the mudbank to wave forcing (Jiang, 1993). The mudbank propagates shoreward and arrives at the shore from deeper offshore waters of about 20 m depth under intense wave action at the onset of monsoon during May and June. During the middle part of the monsoon in July, the mudbank tends to remain attached to the shore and extends to about 10 m depth at the offshore end, and eventually returns to the deeper waters due to the slope-driven gravity effect as the monsoon wanes in August and September.

Wave recording in the nearshore was made using a pressure-type wave and tide gage and a telemetering system. Wave measurements 1.1 km offshore were made using a waverider buoy (Fig. 4.13). Synchronous wave data from outside and inside the mudbank were collected and used for understanding the behavior of waves during their propagation over mudbanks and the process of wave energy dissipation. Water and sediment sampling

and field measurements of currents, salinities and temperature were carried out in the mudbank area.

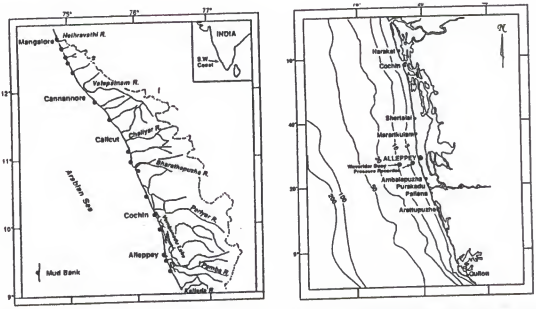

Figure 4.13 Location map of the study area of Mathew (1992) off Alleppey in the State of Kerala, India.

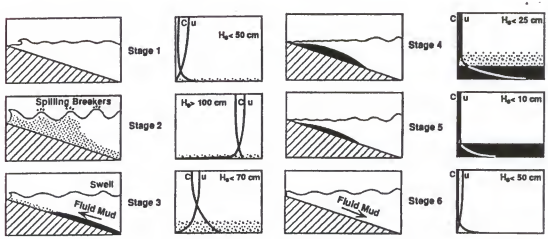

Figure 4.14 A conceptual model of mudbank evolution, C: suspended concentration, u: wave orbital velocity; H_s: significant wave height (after Mathew, 1992).

Based on the above mentioned field observations, Mathew (1992) proposed a conceptual model to qualitatively describe the development and dissipation of the mudbank (Fig. 4.14). In stage-1, the pre-monsoon condition, a homogeneous water column with negligible suspended sediment concentration and relatively low wave activity occurs. By the start of storm wave activity with the onset of monsoon, in stage-2, the bottom sediment is stirred up and suspended, causing a high suspended sediment concentration in the nearshore region. At about the same time, in the offshore region, continuously high wave action on the mud bottom tends to fluidize the bed. Thus, fluid mud is formed in the offshore region first and is transported to the nearshore region by waves and currents as schematized in stage-3. Since the fluid mud absorbs most of the wave energy, a calm situation in the nearshore region develops (stage-4), although there continues to be a high wave activity in the offshore region. The suspended sediment settles over the fluid mud in the nearshore region due to the low wave activity there, which in turn results in a relatively low suspended sediment concentration in this area. Toward the end of the monsoon, as the wave height decreases, onshore transport due to wave action also decreases, and gravity-driven downslope transport of fluid mud leads to the dissipation of the mud bank (stage-5). When the monsoon is over, the mudbank slides back to offshore region and the waves are again able to reach the shoreline (stage-6).

Model Application

Based on the work of Mathew (1992) conducted during the 1986-89 period, and later reported by Mathew et al. (1995), the following characteristic wave conditions can be derived for the nearshore region off Alleppey. The significant wave height, H_s, during the fair

weather period from October to April was less than 0.75 m for most of the time with no significant inter-annual variability. During the monsoon period, from about May to September, H_s reached 2~3 m maximum. The wave period ranged between 10~18 s for the fair weather period and 7~10 s in the monsoon, signifying a greater contribution to wave energy from the shorter period sea in the monsoon in contrast with the fair weather condition when the wave energy is mainly imparted by the longer period swell activity. In the monsoon, most of the wave spectra were found to be single-peaked and the energy was confined to the 0.05~0.5 Hz frequency ($\omega/2\pi$) range. The spectral peaks, which were mostly observed at 0.09~0.1 Hz (10~11 s) before the mudbank period shifted to about 0.11~0.13 Hz (8~9 s) upon the formation of the mudbank. Overall, 10.5 s can be chosen as a representative wave period for the pre-mudbank condition, and 8.5 s for all subsequent states of the mudbank.

A bottom-mounted pressure recorder installed at the end of the Alleppey Pier (Fig. 4.13), yielded wave information necessary to simulate the suspended sediment profiles, which were obtained by lowering samplers from a boat in the same general area. As for the bottom mud, it is believed that the damping of the waves provides a net forward thrust which pushes mud from deeper (~20 m) offshore waters toward the shore. At the same time, wave refraction effects cause this mud to accumulate where the wave energy is focussed. The thickness of the fluid-like mud was about 2 m during the formation phase of the mudbank and in the period immediately after formation.

Characteristically, the wave height inside the mudbank area decreases once the bottom mud is in place, as does the turbidity, due to its correlation with the wave height.

Eventually, toward the end of the monsoon, as the incoming energy decreases, the wave-induced forward thrust is no longer sufficient to hold the mud against the shoreline. As a result the mud slides back into the deeper offshore region. At Alleppey, as the wave action decreases, the mudbank has been observed to begin to dissipate initially through shore-normal as well as lateral spreading, aided by very weak currents. At this stage its average thickness decreases to about 1 m. At the end of the monsoon, during the later stage of dissipation, wave height and turbidity drop further, before the offshore slide causes the mud layer to reduce to just a few centimeters in thickness (Mathew et al, 1995).

For a characteristic Alleppey mud density of 1,270 kg/m^3 in native salt water 1,030 kg/m^3 density, mud rheology was found to be best described by the standard solid model (Eq. 2.16), in which the three parameters, G_1 (Pa), G_2 (Pa) and μ_2 (Pa.s), were found to be frequency dependant and expressed as:

$$\begin{aligned} G_1 &= \exp(9.160) \times f^{0.257} \\ G_2 &= \exp(3.843) \times f^{-0.405} \\ \mu_2 &= \exp(9.292) \times f^{-0.405} \end{aligned} \tag{4.27}$$

where f is the frequency in Hertz.

In the fair weather period, the suspended sediment concentration near the surface was less than 0.007 kg/m^3, while in the lower part of the water column it reached a maximum of 0.064 kg/m^3. However, with the onset of monsoonal waves but before the mudbank was formed, the concentration in the upper half of the water column was observed to increase to 0.6~0.9 kg/m^3. Following mudbank formation a few days after the arrival of the monsoon,

the concentration reduced to less than 0.1 kg/m^3, due to a decrease in the wave height by damping.

Table 4.6 Parameters for simulating field data of Mathew (1992) from the southwest coast of India.

State of mudbank		Before formation	During formation	Formed	During dissipation	During dissipation
Wave height (m)		1.23	0.77	0.31	0.50	0.45
Wave period (s)		10.5	8.5	8.5	8.5	8.5
Mean current velocity (m/s)		0.0	0.0	0.01	0.04	0.05
Manning Coefficient		0.011	0.011	0.011	0.011	0.011
Water depth (m)		5.0	3.0	3.0	4.0	4.0
Mud depth (m)		0.05	2.0	2.0	4.0	4.0
Settling velocity parameters	S_1^* (kg/m^3)	0.1	0.1	0.1	0.1	0.1
	w_{sf} (m/s)	2.16×10^{-5}	2.16×10^{-5}	2.16×10^{-5}	2.16×10^{-5}	2.16×10^{-5}
	α_1	0.16	0.16	0.16	0.16	0.16
	β_1	1.3	1.3	1.3	1.3	1.3
	α_1	7.0	1.5	1.5	7.0	7.0
	δ_1	7.0	7.0	7.0	7.0	7.0
Wave diffusion coefficient, α_2		0.19	0.02	0.02	0.02	0.02
Stratified damping coefficients	α_3	0.5	0.5	0.5	0.5	0.5
	β_3	0.33	0.33	0.33	0.33	0.33
Critical Richardson Number, Ri_{wc}		0.043	0.043	0.043	0.043	0.043
Entrainment coefficient, α_4		2×10^{-5}	2×10^{-5}	2×10^{-5}	2×10^{-5}	2×10^{-5}

For purposes of simulation, the settling velocity data and relationships shown in Fig. 6 will be used, based on information provided by Mathew (1992). We will select the parameters, $\phi_w = \phi_c = 1$, assuming equally weighted neutral wave and current diffusion coefficients in Eq. 4.11. Selected values of α_4 characterizing wave diffusion (Eq. 4.23) are given in Table 4.5, which also lists other relevant parameters for the five characteristic phases or states of the Alleppey mudbank identified by Mathew (1992). Before the formation of the mudbank, the diffusion parameter was relatively large (0.19) because of spilling breakers in the nearshore region, and became smaller (0.02) when the mudbank was formed, as wave breaking became comparatively minor due to energy absorption. Note that for simulating the resuspension of mud in Lake Okeechobee in Florida, Hwang (1989) found $\alpha_4 = 0.016$ as the best-fit value, which is in agreement with 0.02 selected here.

The parameters characterizing stratification, α_5 and β_2, were selected to be 0.5 and 0.33, which are close to those selected by Hwang (1989). For all simulations, the entrainment coefficient, α_4, was chosen as 2×10^{-5}, obtained as the best value through calibration, while the critical gradient Richardson Number, $Ri_{wc} = 0.043$ was selected in the absence of relevant data for the Alleppey mud. The relevant range of the wave Reynolds Number, Re_w, was 1.1×10^6 to 1.3×10^6, which is comparable with the upper limit of Ri_w in the earlier described entrainment tests.

As observed in Fig. 4.15a, before the mudbank was formed, high wave energy and vertical mass diffusion led to relatively high suspended sediment concentration. This plot and others in Fig. 4.15 show the formation of a sediment-induced pycnocline or lutocline, although this lutocline was not detected in the measurements, because sampling was limited

to the top half of the water column. On the other hand, careful near-bottom measurements elsewhere have shown the way in which the lutocline rises and falls under wave forcing (Kemp and Wells, 1987). During mudbank formation, the reduction in the wave energy caused the concentration to decrease by an order of magnitude, and at the same time the lutocline fell closer to the bottom (Fig. 4.15b). Mathew (1992) noted that once the mudbank was fully formed, a weak current appeared; however, no measurements were reported. It is therefore interesting to note that for the simulation of the suspended sediment profile for the formed mudbank condition (Fig. 4.15c) as well as during the stages of dissipation, a small current velocity, U, ranging from 0.01 to 0.05 m/s was required for matching the measured and simulated concentrations. In general, the effect of current is to lift the lutocline and enhance the upward diffusion of the entrained material. This effect is evident in Fig. 4.15c, in which the profile without current (dashed line) is observed to shift to the profile with current (0.01 m/s) with a greater concentration and elevated lutocline. This example demonstrates the degree of sensitivity of the current-induced boundary layer in influencing wave-induced sediment resuspension. Furthermore, despite the significant degree of empiricism inherent in the method for simulation presented here, this example highlights the difficulty that characteristically occurs in predicting fine-grained sediment resuspension. At the same time, note that the simulation method emphasizes the significance of vertical transport mechanisms in determining the structure and the dynamics of the suspended sediment concentration profiles in the mudbank area. While the process equations for entrainment and deposition are limited by the fact that their use requires the selection of several empirical coefficients, it is also observed that when properly calibrated, these

equations can qualitatively account for the measured variability in the turbidity in the mudbank area.

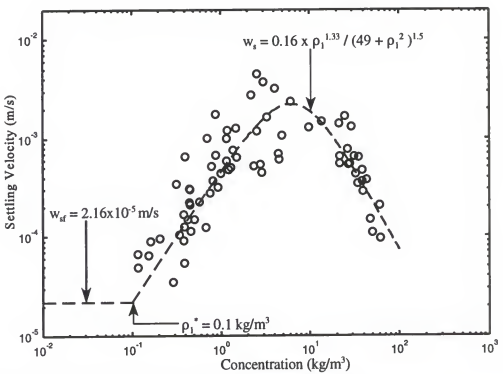

Figure 4.15 Settling velocity data used for mudbank turbidity simulation.

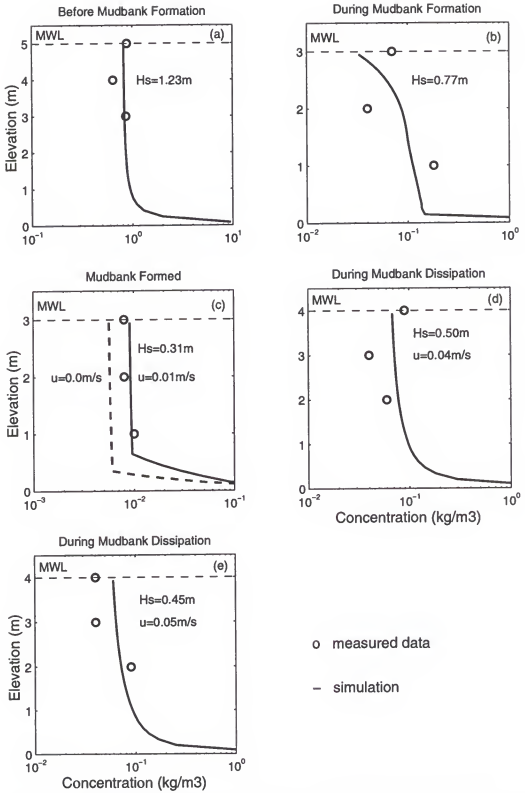

Figure 4.16 Simulated suspended sediment concentration profiles and data of Mathew (1992) in the vicinity of Alleppey Pier.

CHAPTER 5
SORPTION KINETICS

5.1 Introduction

The sorptive properties of contaminants onto sediments can greatly affect their transport characteristics. The concentration of any contaminant in a water-sediment mixture can in general be divided into two parts, namely the dissolved part in water, C_d, and the partitioned part sorbed on sediment, P. The general partitioning relationship for contaminant concentration between the dissolved phase and the sorbed phase is

$$f(C_d, P) = 0 \tag{5.1}$$

Thus, a non-sorptive contaminant is as a special case in which $P = 0$.

In this chapter, the sorptive properties of selected dyes used to represent the contaminant in the flume experiments are determined. Two dyes--Rhodamine B and Erioglaucine A, are tested with two sediments--kaolinite and AK mud. A photographic method, which has advantages for the flume experiments because of its non-intrusive and space-continuous measuring capability, is developed to measure the concentration of the sampled dye solutions in test tubes. The sorption kinetics of the dyes is then incorporated into modeling for simulation of flume experiments.

5.2 Dyes, Sediments and Fluid Characteristics

Rhodamine B and Erioglaucine A were purchased from Fluka Chemical Corp. Inc., New York. Table 5.1 gives some physical and chemical properties of these two dyes. Rhodamine B is an orange fluorescent dye tracer in water. It is readily adsorbed by most sediments, because Rhodamine B is cationic in water while sediment, especially clay, particles are negatively charged in water. Erioglaucine A is a blue dye tracer, which is not strongly adsorbed by the negatively charged clay particles because it is anionic in water. The reason to select these two dyes as contaminant surrogates is that Rhodamine B is a commonly available dye used in laboratory and field studies and Erioglaucine A was chosen as a less sorptive constituent.

Table 5.1 Physical and chemical properties of Rhodamine B and Erioglaucine A.

Properties	Rhodamine B	Erioglaucine A
Alternative Name	Tetraethylrhodamine	Brilliant Blue FCF
Color Index	45170	42090
Sum Formula	$C_{28}H_{31}ClN_2O_3$	$C_{37}H_{38}N_3Na_2O_9S_3$
Appearance	Green Powder	Purple powder
Melting Point	211° C	283° C
Molar mass	479	787
Ions in Water	Cation	Anion

Kaolinite (pulverized kaolin), a light beige color clay, is purchased from the EPK Division of Feldspar Corporation in Elgar, Florida. Its Cation Exchange Capacity (CEC) was in the range of 5.2 - 6.5 milliequivalent per 100 grams. AK mud consists of (by weight) 50% attapulgite and 50% kaolinite. Attapulgite (palygorkite), a greenish-white color clay, was

purchased from Floridin in Quincy, Florida. Its Cation Exchange Capacity (CEC) is 28 milliequivalent per 100 grams. Table 5.2 gives the chemical compositions of the two clays. The reason for using these two types of sediments for experimental studies is that both of them are available in Florida and their properties, i.e., erodibility and rheology have been characterized by previous investigators, i.e., Maa (1986), Ross (1988), Feng (1992), Jiang (1993) and Lee (1995).

Table 5.2 Chemical compositions of kaolinite and attapulgite (%).

Composition	Kaolinite	Attapulgite
SiO_2	46.50	55.20
Al_2O_3	37.62	9.48
Fe_2O_3	0.51	8.92
MgO	0.16	8.92
Na_2O	0.02	9.48
K_2O	0.40	9.48
CaO	0.25	0.65
FeO	-	9.48
TiO_2	0.36	-
H_2O	-	10.03
P_2O_5	0.40	-
NH_2O^-	-	9.48
SO_3	0.21	-
V_2O_5	<0.001	-

Particle size distributions of kaolinite and attapulgite were obtained by Feng (1992). The median dispersed particle sizes of kaolinite and attapulgite are 1.10 μm and 0.86 μm, respectively. These clays readily flocculate tap in water. Scanning Electron Microscope

(SEM) photographs of the dry particles of these two clays show kaolinite to be platy and attapulgite to be tube- or needle-like.

The chemical composition of tap water used to prepare the mud is given in table 5.3. Its pH value was 8 and conductivity 0.284 millimhos.

Table 5.3 Chemical composition of tap water.

Parameter	Tap water
Ca	24.4 ppm
Mg	16.2 ppm
Si	11.4 ppm
Na	9.6 ppm
Al	1.2 ppm
Fe	1.2 ppm
Total salts	278 ppm

5.3 Sorption Test Procedure

5.3.1 Sampling of Sediment-Dye-Water Mixture

As depicted in Fig. 5.3, one liter solution of water with a known concentration of dye was prepared in a 1,100 ml conical flask. After a specified amount of sediment was mixed with the solution, samples of the solution are taken at 0.5, 1, 2, 5, 10, 30, 60, 120 and 1,440 minutes. The sampling system consisted of an adjustable-speed two-directional peristaltic pump, Teflon fluorocarbon resin tubes of 3.2 mm diameter and a 2µm stainless-steel filter (Upchurch Scientific Solvent Inlet Filter Kit, Fisher Scientific, Pittsburgh, PA). The pump was controlled by a Solid State Speed Control, which could change the flow direction and the pump motor speed in the range of 1 - 100 RPM (Cole-Parmer Instrument Co., Chicago).

The filter was used to eliminate the flocs and obtain a residual dye solution. To keep the sediment suspended during the sorption experiments, the solution was continuously agitated with a magnetic stirrer within the conical flask (Fisher Scientific, Pittsburgh, PA). The mixing process lasted for two hours until the last but one samples was taken.

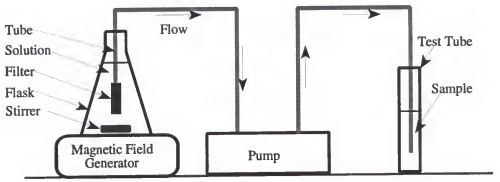

Figure 5.1 Schematic diagram of the sorption procedure.

5.3.2 Photographic Method for Dye Concentration Determination in Water

The concentrations of the sampled dye solutions in test tubes were measured by a photographic method. The basic principle is that different concentration dye solutions show different color intensities, which can be quantified by taking color photos of the solutions, scanning the developed color prints into the computer as image figures, and then obtaining digitized data of the images. As schematized in Fig. 5.4, photographs of the dye solution were taken in a dark room by a Quantaray D2-RZ camera at a distance of 0.6 m with Aperture 11. A Vivitar Auto 2600 flash was used as the light source, which was attached at the bottom of a 1 m long, 0.4 m wide and 0.4 m high black foamboard box with a light scattering board at the front to make the light source uniform. A Reala film was used and developed without adjustments for color or density.

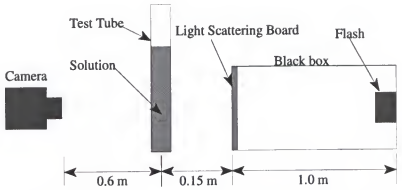

Figure 5.2 Schematic diagram for photography in sorption tests.

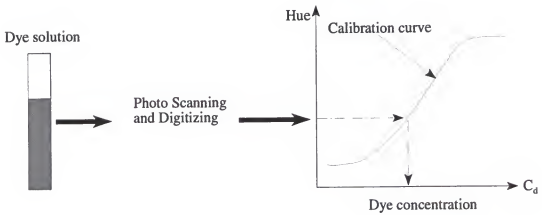

Figure 5.3 Procedure for determining dye concentration.

The color prints were scanned by an HP ScanJet IIC/ADF scanner into a 24-bits tif (Tagged Image Format) file with brightness 125, contrast 131 and 300x300 dpi (dots per inch) resolution. The tiff file was then read-in by using the Image Toolbox of Matlab as an RGB (Red, Green and Blue) file. The RGB file was then converted to the NTSC (National Television System Committee) format composed of Luminance, Hue and Saturation. Hue represents color intensity while luminance represents the gray scale of a color image.

To obtain the absolute value of the dye concentration in solution, calibration curves were obtained by developing empirical relationships between the digitized hue data and the dye concentrations. For an unknown concentration of the dye solution, by photographing the solution, obtaining the digitized data and using the calibration curve, the dye concentration of this solution could be obtained, as schematized in Fig. 5.5

5.3.3 Calibration Experiments

The calibration experiments were carried out under the same conditions as those for the sorption experiments except that the dye concentration was known *a priori*. The selected concentration ranges were 0.01 ~ 500 mg/l for Rhodamine B and 0.01 ~ 100 mg/l for Erioglaucine A. Experimental data and the corresponding best-fit curves are shown in Figs. 5.6 and 5.7. The relationships between the hue (I_B or I_A) and concentration, C_d (mg/l) can be expressed for Rhodamine B as

$$I_B = 0.22 \times \mathrm{erf}\left[\log_{10}\left(\frac{C_d}{16.5}\right)^{0.962}\right] + 0.25 \qquad (5.2)$$

and for Erioglaucine A as

$$I_A = 0.24 \times \mathrm{erfc}\left[\log_{10}\left(\frac{C_d}{12.1}\right)^{1.370}\right] - 0.45 \qquad (5.3)$$

The NTSC hue ranges from -0.596 to +0.596 from blue to red (high to low frequency light). Since Rhodamine B is a red dye, the higher the concentration of the Rhodamine B solution, the higher the hue. For Erioglaucine A, which is a blue dye, the higher the solution

concentration, the lower the hue. Thus, the calibration curve begins from the background hue value, which is 0.03 corresponding to zero concentration of Rhodamine B or Erioglaucine A, and increases/decreases when the dye concentration of Rhodamine B/Erioglaucine A increases. However, it was found that for high dye concentrations, i.e., > 500 mg/l for Rhodamine B and > 100 mg/l for Erioglaucine A, due to light being blocked by the high concentrated solution, the images tended to become dark and thus, the hue decreased/increased again for Rhodamine B/Erioglaucine A, resulting in dual-values of concentration at a given hue. To avoid this problem, an upper limit was found to exist for the applicability of the calibration curves for Rhodamine B (500 mg/l) and Erioglaucine A (100 mg/l).

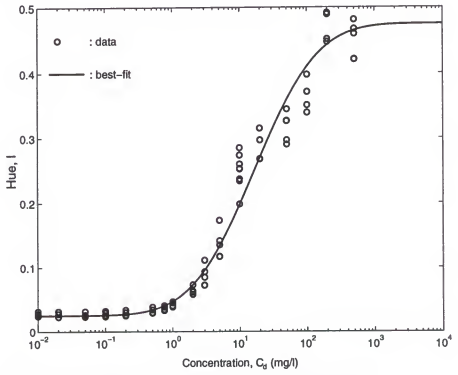

Figure 5.4 Calibration curve for Rhodamine B solutions.

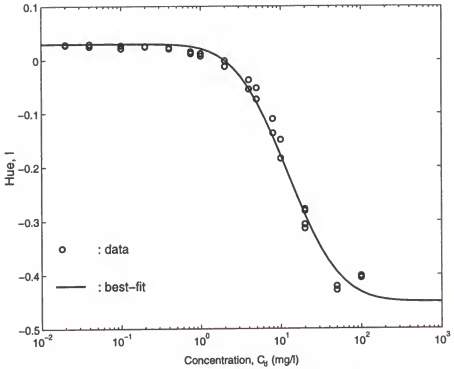

Figure 5.5 Calibration curve for Erioglaucine A solutions.

5.4 Results and Discussion

5.4.1 Sorption Isotherms

The simplest and most widely used sorption relationship is the linear reversible isotherm, which assumes that the sorption/desorption rate is so fast that sorption occurs instantaneously. Thus, only the relationship between the dye concentration in water, C_{eq}, and that sorbed on sediment, P, at equilibrium are considered according to

$$P = K_d C_{eq} \tag{5.4}$$

where K_d is the equilibrium sorption distribution coefficient. The C_{eq} value was obtained by measuring the dye concentration at 24 hours, which was found to be a sufficiently long

duration for attainment of equilibrium. The experimental data thus obtained and the corresponding best-fit curves for Rhodamine B and Erioglaucine A sorbed onto kaolinite and AK mud are shown in Figs, 5.8, 5.9, 5.10 and 5.11, respectively. It is observed that the concentration of dye sorbed onto sediment was proportional to the dissolved dye concentration in solution. Rhodamine B was more sorptive than Erioglaucine A, and AK mud was more easily be sorbed onto than kaolinite. The corresponding distribution coefficients are given in Table 5.4.

Table 5.4 Equilibrium sorption distribution coefficient, K_d (l/g)

Sediment	Rhodamine B	Erioglaucine A
Kaolinite	0.083	0.032
AK mud	0.158	0.039

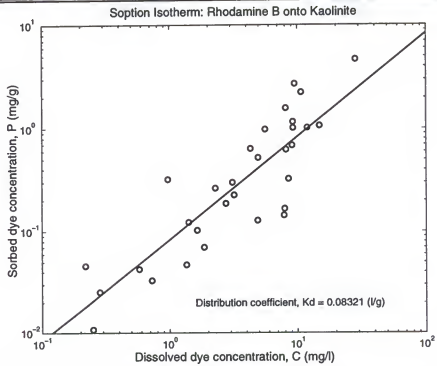

Figure 5.6 Linear isotherm of Rhodamine B sorbed onto kaolinite.

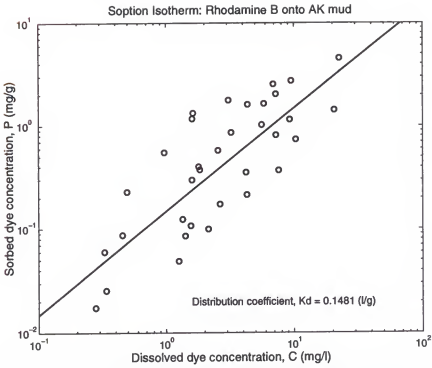
Soption Isotherm: Rhodamine B onto AK mud
Sorbed dye concentration, P (mg/g)
Dissolved dye concentration, C (mg/l)
Distribution coefficient, Kd = 0.1481 (l/g)

Figure 5.7 Linear isotherm of Rhodamine B sorbed onto AK mud.

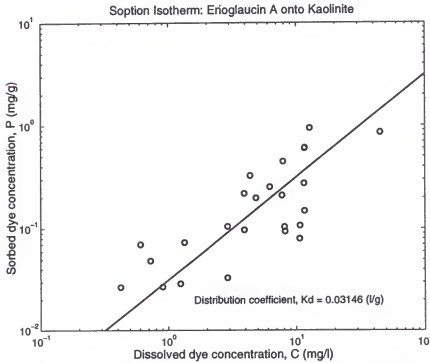
Soption Isotherm: Erioglaucin A onto Kaolinite
Sorbed dye concentration, P (mg/g)
Dissolved dye concentration, C (mg/l)
Distribution coefficient, Kd = 0.03146 (l/g)

Figure 5.8 Linear isotherm of Erioglaucine A sorbed onto kaolinite.

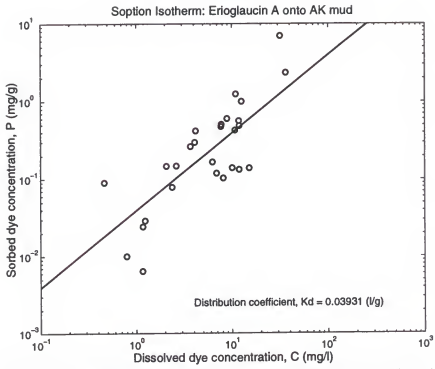
Soption Isotherm: Erioglaucin A onto AK mud
Sorbed dye concentration, P (mg/g)
Distribution coefficient, Kd = 0.03931 (l/g)
Dissolved dye concentration, C (mg/l)

Figure 5.9 Linear isotherm of Erioglaucine A sorbed onto AK mud.

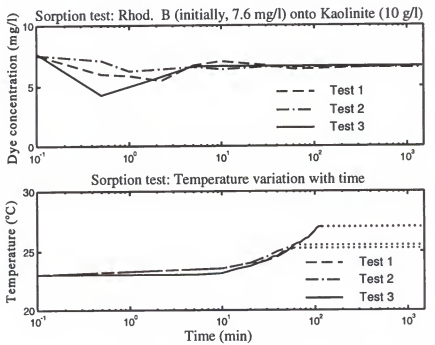

Figure 5.10 Effect of temperature on sorption of Rhodamine B on kaolinite:
(1) Upper figure shows the variation of dye concentration in solution with time;
(2) Lower figure shows temperature changes in solution during the experiments.

During the experiments it was also found that the temperature of the solution increased due to the energy imparted by the magnetic stirrer used for mixing the solution to keep the sediment suspended. Thus, some experiments were carried out to ascertain the temperature effect on sorption, with an initial Rhodamine B concentration of 7.6 mg/l added to kaolinite of 10 g/l concentration. The temperature was measured every 5 minutes. For the first two experiments, stirring were stopped at 1 hour and for the third it was stopped at 2 hours. The second test was a repeat of the first one. Variations of the dye concentration and temperature with time for all three experiments are shown in Figure 10. The maximum increase in temperature in the experiments was 4°C, from 23°C to 27°C. The final temperature difference between the first two and the third experiment was 2°C, because the stirring time in Test 3 was 2 hr as opposed to 1 hr for Tests 1 and 2. The final dye concentrations were 6.59 mg/l and 6.50 mg/l for the first two experiments and 6.64 mg/l for the third one. Note that the maximum change in concentration due to temperature effect was 2.1% for a 2°C rise in temperature, which is small enough to be considered negligible. Thus, for the maximum 4 °C temperature difference in the experiments, the error in dye concentration measurement may also be considered negligible.

5.4.2 Sorption Kinetics

To consider the sorption/desorption rate, the linear, first-order model that is the kinetic version of the linear reversible sorption isotherm is commonly used

$$\frac{dP}{dt} = r(K_d C_d - P) \qquad (5.5)$$

where r is the first-order rate coefficient, which depends on the properties of the sorbent and the sorbate, on the mixing process and, under certain conditions, on the initial concentrations of the sorbent and the sorbate. For a conservative dye in the water-sediment mixture, the total dye mass, composed of the dissolved and sorbed components should be a constant, equal to the initial mass of dye dissolved in water. Thus, we have

$$SP + nC_d = SP_0 + nC_{d0} \tag{5.6}$$

where C_{do} (mg/l) and P_0 are the initial dye concentration dissolved in water and sorbed on sediment, respectively, S (g/l) is the sediment concentration or dry density and n is porosity. Substituting Eq. 5.6 into Eq. 5.5, we obtain

$$\frac{dC_d}{dt} = -\frac{Sr}{n}\left[K_d C_d - \left(P_0 + \frac{nC_{do} - nC_d}{S}\right)\right] \tag{5.7}$$

and we note that at $t = 0$, $C_d = C_{do}$. Then, by solving the ordinary differential equation, i.e., Eq. 5.7 we get

$$C_d = \frac{1}{n}\frac{nC_{d0} + SP_0}{1 + SK_d/n} + \frac{1}{n}\frac{S(K_d C_{d0} - P_0)/n}{1 + SK_d/n}\exp[-r(1 + SK_d/n)t] \tag{5.8}$$

and, according the conservation of dye mass in solution, Eq. 5.6, we also obtain

$$P = \frac{(nC_{d0} + SP_0)K_d/n}{1 + SK_d/n} - \frac{(K_d C_{d0} - P_0)}{1 + SK_d/n}\exp[-r(1 + SK_d/n)t] \tag{5.9}$$

For the present experiments, $n \approx 1$, $P_0 = 0$. Thus, we have

$$C_d = \frac{C_{d0}}{1 + SK_d} + \frac{SK_dC_{d0}}{1 + SK_d} \exp[-r(1 + SK_d)t] \tag{5.10}$$

$$P = \frac{K_dC_{d0}}{1 + SK_d} - \frac{K_dC_{d0}}{1 + SK_d} \exp[-r(1 + SK_d)t] \tag{5.11}$$

At $t \rightarrow \infty$, the equilibrium dissolved and sorbed dye concentrations are

$$C_{d\infty} = \frac{C_{d0}}{1 + SK_d} \quad \& \quad P_\infty = \frac{K_dC_{d0}}{1 + SK_d} \tag{5.12}$$

Comparisons between Eq. 5.8 and selected experimental results are shown in Figures 11 through 15. It must be noted that the time-scale in these figures is logarithm, i.e., in terms of the actual time-scale, the dye concentration in water dropped rapidly at the beginning and then slowed down exponentially, as expressed by Eq. 5.10. The first-order rate coefficient, r, was obtained by best-fitting Eq. 5.10 to the experimental data and is given in Table 5.5. The range of r is observed to be from 0.1 to 10.0. At r = 0.1, corresponding to the slowest rate of approach to equilibrium, equilibrium was attained within 8 minutes. Thus, comparing this time-scale with those for sediment diffusion and settling processes, for typical settling velocity of 0.2 mm/s and a water depth of 15 cm in laboratory, the time-scale for sediment diffusion and settling are on the order of 12 minutes, which means that sorption can be of the same time-scale or smaller than those for diffusion and settling.

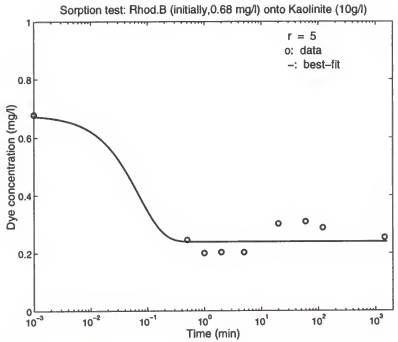

Figure 5.11 Comparison between kinetic sorption model and experimental data.

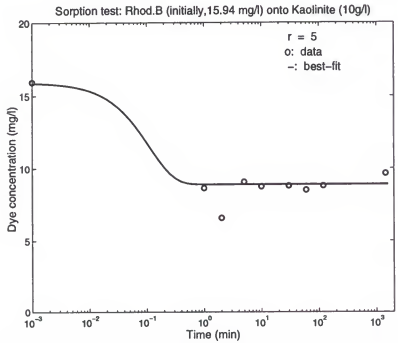

Figure 5.12 Comparison between kinetic sorption model and experimental data.

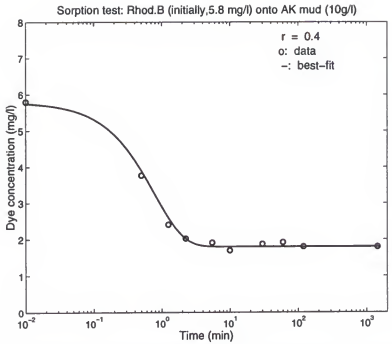

Figure 5.13 Comparison between kinetic sorption model and experimental data.

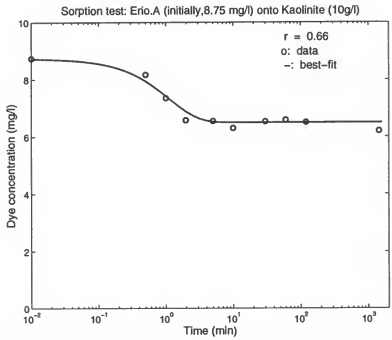

Figure 5.14 Comparison between kinetic model and experimental results.

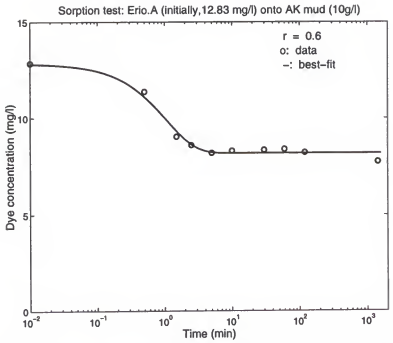

Figure 5.15 Comparison between kinetic sorption model and experimental data.

5.4.3 Discussion

From Table 5.4, Rhodamine B is seen to be more sorptive than Erioglaucine A. The molecular structures of Rhodamine B and Erioglaucine A are shown in Fig. 5.10. Note also that Rhodamine B in water is cationic, whereas Erioglaucine A is anionic. The surfaces of clay particles, i.e., kaolinite and attapulgite, are generally negatively charged when they are mixed in water (van Olphen, 1963). As a result, the positively charged Rhodamine B ion is easier to be sorbed onto the negatively charged sediment particles than the negatively charged Erioglaucine A ion.

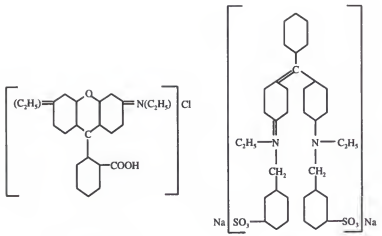

Rhodamine B Erioglaucine A

Figure 5.16 Chemical structures of Rhodamine B and Erioglaucine A.

As noted from the experimental results, we find that AK mud is easier to be sorbed onto than kaolinite. This is in turn means that attapulgite is a stronger sorbent than kaolinite for these two dyes. According to Grim (1968), kaolinite particles are flake-like and attapulgite particles are tube-like. Thus, the representative specific area, ϵ_s, i.e., surface area per unit volume, or $(2h_k + 2R)/Rh_k$, is on the order of 1 μm^{-1} for kaolinite and is 100 μm^{-1} for attapulgite. As a result, attapulgite has about 100 times more specific area than kaolinite for sorption, which may well explain why attapulgite is easier to be sorbed onto than kaolinite.

Kaolinite
h_k: 0.05 ~ 2 μm, 2R: 0.3 ~ 4 μm

Attapulgite
h_k: 5 ~ 50 μm, 2R: 0.005 ~ 0.01 μm

Figure 5.17 Idealized clay geometries of kaolinite and attapulgite.

Many observation have been made showing that fine-divide powder, e.g., charcoal or sediment particles, are able to take up dyes from solution by sorption. Sorption may be considered from two aspects: it may be regarded as molecular attraction by chemical forces, as sorption of gas onto a solid surface, or it may be looked on as a lowering of interfacial tension when sorbed. According to Glasstone (1962), in the sorption of dyes by finely divided powder, the formation of a single molecular sorbed layer is not exceeded. Thus, the sorption procedure should follow Langmuir Sorption Isotherm (Eq. 2.45). However, for relatively dilute dye solutions or highly concentrationed sediments, the linear isotherm is accurate enough for simulating sorption. Another reason for not using the Langmuir Sorption Isotherm is because of its nonlinear properties, which can mean much additional work for solving the model using this isotherm.

Whatever the mechanism of sorption from solution, it is certain that the extent depends mainly on the available surface of the sorbent, especially with colloidal particles (Glasstone, 1962). This is evidenced by the experimental observation that attapulgite is easier to be sorbed onto than kaolinite.

Also, according to Glasstone (1962) sorption is almost invariably reversible, and a definite equilibrium is reached in a short time dependent on the concentration of the solution and the quantity of sorbent. Therefore, desorption can be assumed to be the reverse of sorption without carrying out desorption tests. Note also that, in general, desorption tests are much more difficult to carry out than the sorption tests.

Table 5.5 First order rate coefficient for sorption kinetics.

Dye (C_o, mg/l)	Sediment (S, g/l)	r (1/s)
Rhodamine B (0.68)	Kaolinite (10)	5.0
Rhodamine B (2.56)	Kaolinite (10)	3.0
Rhodamine B (5.45)	Kaolinite (10)	9.0
Rhodamine B (12.96)	Kaolinite (1)	10.0
Rhodamine B (15.94)	Kaolinite (10)	5.0
Rhodamine B (19.40)	Kaolinite (10)	5.0
Rhodamine B (33.25)	Kaolinite (1)	9.0
Rhodamine B (0.59)	AK mud (10)	9.0
Rhodamine B (2.27)	AK mud (10)	9.0
Rhodamine B (5.59)	AK mud (10)	3.0
Rhodamine B (13.27)	AK mud (10)	3.0
Rhodamine B (14.89)	AK mud (10)	0.18
Rhodamine B (17.72)	AK mud (1)	0.46
Rhodamine B (22.29)	AK mud (10)	0.1
Rhodamine B (27.14)	AK mud (1)	4.2
Rhodamine B (34.83)	AK mud (10)	0.1
Erioglaucine A (1.53)	Kaolinite (10)	2.0
Erioglaucine A (3.23)	Kaolinite (10)	0.8
Erioglaucine A (8.75)	Kaolinite (10)	9.0
Erioglaucine A (9.14)	Kaolinite (10)	9.0
Erioglaucine A (1.36)	AK mud (10)	3.0
Erioglaucine A (3.17)	AK mud (10)	2.0
Erioglaucine A (8.55)	AK mud (10)	9.0
Erioglaucine A (12.83)	AK mud (10)	0.6
Erioglaucine A (16.45)	AK mud (10)	9.0

From the experimental results on sorption, the first order rate coefficient, r, is in the range of 0.1 ~ 10.0, which corresponding to the time of approach to equilibrium in the range of 0.5 ~ 8.0 min. If we define a time-scale, Ts, of sediment settling as h_1/w_s, where h_1 is the characteristic water depth and w_s is the sediment settling velocity, then Ts will be on the order of 4 hours, assuming h_1 = 15 cm and $w_s = 1 \times 10^{-5}$ m/s corresponding to experimental conditions described in Chapters 7 and 8. Therefore, the time-scale which in turn means that equilibrium is reached rapidly and that an instantaneous equilibrium condition can be assumed. Note, however, that for generality of model application, the kinetic relationship is in fact used for modeling in Chapter 6. It should also be pointed out that for the cases of r ranging between 0.1 ~ 10.0, model results are found to be almost same as those when the instantaneous equilibrium relationship is used.

CHAPTER 6
CONSTITUENT TRANSPORT MODELING

6.1 Introduction

The transport of constituents in the sediment-water mixture includes dissolved contaminant transport, particle-bound contaminant transport and sediment-contaminant interaction, i.e. the sorption/desorption process. In the system shown in Fig. 2.7, contaminant transport has different characteristics within each of the three layers. The contaminant fluxes across the water-fluid mud interface and the fluid mud-bed interface represent the connective conditions for each of the two adjacent layers, and control the rate of contaminant transfer between them. In this chapter, a vertical contaminant transport model will be set up for the three-layered system modified from Fig. 2.7. In Chapter 8, the model is calibrated against experimental results given in Chapter 7 to determine the contaminant release fluxes from bottom sediment. These fluxes are then correlated with wave loading, contaminant properties and sediment characteristics.

6.2 Constituent Transport Model

6.2.1 Formulation

The contaminant transport processes considered are described in Fig. 6.1, as modified from Fig. 2.7. In this figure, dissolved contaminant transport having different characteristics

due to the different dynamical responses of each layer under wave loading is shown. Because of the assumed absence of transport of sediment within the fluid mud and the bed layers, there is no particle-bound contaminant transport in, or across these two layers. Within the water layer, particle-bound contaminant transport are considered to occur together with sediment transport.

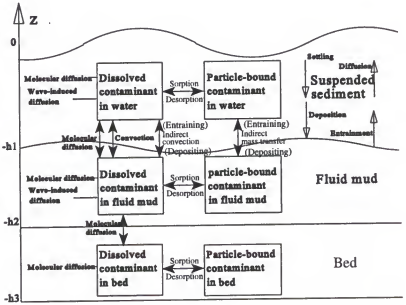

Figure 6.1 Sediment-associated contaminant transport processes considered.

The total contaminant flux across the water-fluid mud interface is composed of the molecular diffusion, direct convection of dissolved contaminant due to water exchange caused by wave-induced diffusion, indirect convection of dissolved contaminant due to water exchange caused by sediment entrainment and/or deposition, and the particle-bound contaminant flux, which also depends on sediment deposition and/or entrainment rates. The

dissolved contaminant flux across the fluid mud-bed interface in the absence of waves is by molecular diffusion only.

6.2.2 Governing Equations

Considering that at any point in a layer (using subscript j = 1, 2 or 3 to indicate the water layer, the fluid mud layer and the bed layer, respectively), the dissolved contaminant concentration in water is denoted C_{jd}, the particle-bound contaminant concentration is P_j, the sediment concentration (or dry density) is S_j, and the porosity is n_j. Then, the total contaminant concentration at that point, C_j, can be expressed as

$$C_j = n_j C_{jd} + P_j S_j \tag{6.1}$$

The general partitioning relationship for contaminant concentration between the dissolved and sorbed phases is

$$f(C_d, P) = 0 \tag{6.2}$$

This relation is determined by experimental results described in Chapter 5. A first-order kinetic relationship, Eq. 5.5, which relates the dissolved and sorbed phases of dyes, is used in modeling dye transport described in Chapter 8.

Inserting Eq. 6.1 into Eq. 4.7 and noting that the settling velocity of the dissolved contaminant is zero, we obtain

$$\frac{\partial}{\partial t}(n_j C_{jd} + P_j S_j) = \frac{\partial}{\partial z}\left[K_{zj}\frac{\partial(n_j C_{jd})}{\partial z} + K_{zj}\frac{\partial(P_j S_j)}{\partial z}\right] + \frac{\partial}{\partial z}(w_s P_j S_j) \tag{6.3}$$

In the water layer, since the volume occupied by suspended sediment is typically very small compared with the volume of water, sediment volume can be neglected. Thus, the porosity in the water layer, $n_1 = 1$. Therefore, the transport equation becomes

$$\frac{\partial}{\partial t}(C_{1d} + P_1 S_1) = \frac{\partial}{\partial z}\left[K_{z1}\frac{\partial(C_{1d})}{\partial z} + K_{z1}\frac{\partial(P_1 S_1)}{\partial z}\right] + \frac{\partial}{\partial z}(w_s P_1 S_1) \qquad (6.4)$$

where K_{z1} is the buoyancy-stabilized diffusivity in the water layer that in general includes the effects of molecular diffusion, wave-induced diffusion, eddy diffusion and sediment-induced density stratification.

In the fluid mud layer, there is no transport of sediment as noted earlier. Thus, the settling velocity, w_s, is assumed to be zero. Also, the dry density of fluid mud, S_2, is assumed to be uniform. Thus, the porosity n_2 is a constant in the fluid mud layer. Therefore, the contaminant transport equation in the fluid mud layer, simplified from Eq.6.3, becomes

$$\frac{\partial}{\partial t}(n_2 C_{2d} + P_2 S_2) = \frac{\partial}{\partial z}\left[K_{z2}\frac{\partial(n_2 C_{2d})}{\partial z}\right] \qquad (6.5)$$

where K_{z2} is the diffusion coefficient in the fluid mud layer, which depends on wave loading, mud rheological properties and sediment characteristics. At present, wave-induced diffusion in fluid mud is not well understood and no theory has been developed to predict it. A preliminary examination for the diffusion mechanism is be carried out in next section.

In the bed layer, the soil frame is considered to be immobile and sediment settling and diffusion are ignored. Furthermore, the transport of dissolved contaminant is by molecular diffusion only. Thus,

$$\frac{\partial}{\partial t}\left(n_3 C_{3d} + P_3 S_3\right) = \frac{\partial}{\partial z}\left[D_m \frac{\partial (n_3 C_{3d})}{\partial z}\right] \tag{6.6}$$

where D_m is the molecular diffusion coefficient.

6.2.3 Boundary and Interfacial Connective Conditions

At the water surface at z=0, contaminant evaporation rate is neglected, so that the flux of contaminant is zero, i.e.,

$$\left[K_{z1}\frac{\partial (C_{1d})}{\partial z} + K_{z1}\frac{\partial (P_1 S_1)}{\partial z}\right]\Bigg|_{z=0} + (w_s P_1 S_1)|_{z=0} = 0 \tag{6.7}$$

At $z=-h_1$, the water-fluid mud interfacial condition expresses the equality between contaminant flux toward the interface from the fluid mud layer, flux across the interface and flux out of the interface. This condition is expressed as

$$\left[-K_{z1}\frac{\partial C_{1d}}{\partial z} - W_s P_1 S_1 - K_{z1}\frac{\partial (P_1 S_1)}{\partial z}\right]\Bigg|_{z=-h_1} = \left[-K_{z2}\frac{\partial (n_2 C_{2d})}{\partial z} + F_{12d} + F_{12p}\right]\Bigg|_{z=-h_1} \tag{6.8}$$

$$= (F_{12m} + F_{12c} + F_{12e} + F_{12s} + F^{s}_{12e} + F^{s}_{12s})|_{z=-h_1} = (F_{12m} + F_{12c} + F_{12d} + F_{12p})|_{z=-h_1}$$

where F_{12m} is the molecular diffusion sub-flux of the dissolved contaminant, which will be neglected, F_{12c} is the direct convective sub-flux of the dissolved contaminant between water and fluid mud, F_{12e} is the indirect sub-flux of the dissolved contaminant associated with sediment entrainment, F_{12s} is the indirect sub-flux of the dissolved contaminant associated with sediment deposition, F^{s}_{12s} is the sub-flux of the particle-bound contaminant transported

together with the depositing sediment, F^s_{12e} is the sub-flux of the particle-bound contaminant transported together with the entraining sediment, $F_{12d} = F_{12e} + F_{12s}$, is the indirect subflux of the dissolved contaminant, and $F_{12p} = F^s_{12e} + F^s_{12s}$, is the particle-bound sub-flux (see Fig. 6.2). Here, subscript "m" denotes molecular diffusion, "c" convective diffusion, "e" entrainment, "s" settling, "d" dissolved, "p" particle-bound and "s" means sorbed onto sediment.

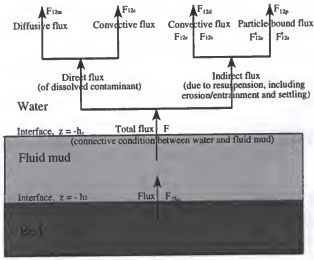

Figure 6.2 Contaminant fluxes across the water-fluid mud and fluid mud-bed interfaces.

The direct convective flux across the interface is proportional to the concentration difference between the surface of the fluid mud layer and the bottom of the water layer, i.e.,

$$F_{12c} = -K_{12c}(C_1|_{z=-h_1} - C_2|_{z=-h_1}) \tag{6.9}$$

where subscript "c" denotes convection and K_{12c} is the convective mass transfer coefficient, which is described in detail in the next section.

The flux associated with sediment entrainment is

$$F_{12e} = \frac{n_2}{(1-n_2)\rho_s}(E_r - F_r)C_{d2}\Big|_{z=-h_1} \tag{6.10}$$

where n_2 is the porosity of fluid mud, ρ_s is the particle density, subscript "e" denotes entrainment and F_r is the sediment flux corresponding to the fraction of entrained sediment that is brought back to the fluid mud layer by deposition. The flux associated with sediment deposition over the fluid mud surface is

$$F_{12s} = \frac{n_2}{(1-n_2)\rho_s}(-D_r + F_r')C_{d1}\Big|_{z=-h_1} \tag{6.11}$$

where F_r' is the sediment flux corresponding to the portion of the "settled" sediment that is entrained into the water layer. Note that under equilibrium condition, $F_r = F_r'$.

For sorptive contaminants, besides the fluxes F_{12e}, F_{12e} and F_{12s}, the sorbed contaminant is transported together with the entrained and/or deposited sediment across the interface. The flux, F_{12e}^s, of the contaminant across the water-fluid mud interface from the fluid mud layer into the water layer due to sediment entrainment can be expressed as

$$F_{12e}^s = (E_r - F_r)P_2|_{z=-h_1} \tag{6.12}$$

where superscript "s" denotes sorption. Similarly, the flux, F_{12s}^s, of the contaminant across the water-fluid mud interface from water into fluid mud due to sediment deposition can be expressed as

$$F_{12s}^{s} = (-D_r + F_r')P_1|_{z=-h_1} \tag{6.13}$$

The Fr and Fr′ values for Eqs. 6.10, 6.11 and Eqs. 6.12 and 6.13, respectively, can be generally expressed as

$$F_r = F_r' = fr \cdot \min[D_r, E_r] \tag{6.14}$$

where fr denotes fraction and $\min[D_r, E_r]$ implies the smaller of the two sediment fluxes, D_r and E_r, of deposition and entrainment, respectively.

At this point, it is necessary to comment on resuspension and deposition fluxes of sediment and associated water transport. Typically, the release/entrapment of pore water in mud during erosion/deposition is not considered when modeling sediment transport, because only particulate fluxes are matters of common concern. For contaminant transport, when sediment resuspension occurs, significant water exchange can also occur through gross entrainment of bottom sediment and settling of the suspended water-sediment mixture. In turn, there can be significant associated fluxes of dissolved contaminant in the interfacial region. Note further that gross resuspension and settling fluxes of sediments need to be considered for contaminant transport modeling, because even when the net sediment flux is zero, e.g., at equilibrium, significant sediment exchange may still exist (Cervantes et al., 1995). In that case, significant associated particulate contaminant fluxes may occurs if the concentrations of particulate contaminant are different in water and fluid mud.

Not all the resuspended sediment and associated pore water contribute to the indirect contaminant release. In fact, typically, much of the resuspended sediment and pore water is

brought back into fluid mud by settling before a significant contaminant transfer takes place with the ambient water (see Fig. 6.3). Unfortunately, we cannot track every sediment particle or pore water package to determine what net fraction of contaminant has actually been released. Therefore, we must assume that only a certain part of the resuspended sediment and associated pore water will cause contaminant transfer from fluid mud into water, and therefore the indirect contaminant release flux at the interface must be determined by calibrating the model against experimental data. To accomplish this task, we will also assume that the fractions of resuspended sediment and associate pore water, which take part in exchange, are equal.

Between the fluid mud and the bed at $z=-h_2$, the interfacial condition must specify that contaminant flux to the interface from the bed layer is equal to the flux from the interface to the fluid mud layer, i.e.,

$$-K_{z2}\frac{\partial(n_2C_{2d})}{\partial z}\bigg|_{z=-h_2} = F_{23m} = -K_{z3}\frac{\partial(n_3C_{3d})}{\partial z}\bigg|_{z=-h_2} \tag{6.15}$$

The boundary condition at the bed bottom at $z=-h_3$ is that the contaminant flux is zero, i.e.,

$$\frac{\partial C_{3d}}{\partial z}\bigg|_{z=-h_3} = 0 \tag{6.16}$$

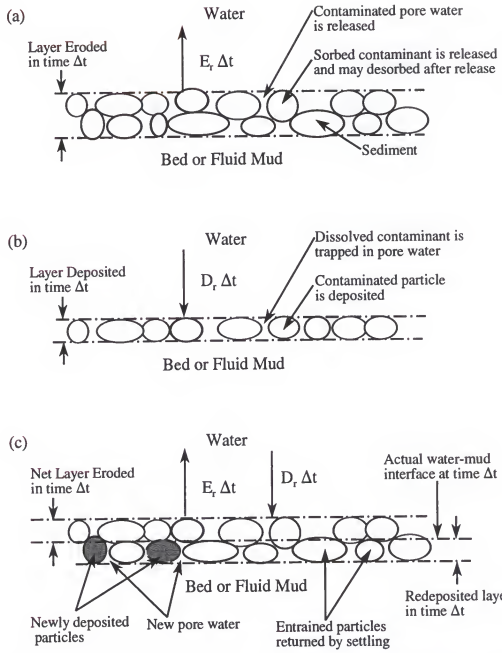

Figure 6.3 Schematic representation of the mode of indirect dissolved and particulate contaminant transport across the water-mud interface: (a) Gross entrainment of sediment and pore from fluid mud into water; (b) Gross deposition of sediment and associated water onto fluid mud from water; and (c) Sediment and water exchange between water and fluid mud under net conditions.

6.3 Wave-Induced Diffusivity in Fluid Mud, K_{z2}

For an undisturbed bed, the molecular diffusivity, D_m, of the constituent in water is characteristically on the order of $10^{-10} \sim 10^{-9}$ (m^2/s) (Li and Gregory, 1974; McDuff and Ellis, 1979). In laboratory studies by Freeze and Chery (1979), the coefficient for diffusivity in porous media related to tortuosity, ω_θ, was found to range from 0.01 to 0.1. Thus, the effective diffusivity in an undisturbed bed, which is equal to $\omega_\theta D_m$, is on the order of $10^{-12} \sim 10^{-10}$ (m^2/s). However, from the experimental results analyzed in Chapter 8, the diffusivity, K_{z2}, under wave motion is found to be on the order of 10^{-8} m^2/s, which is 100 to 10,000 times higher than $\omega_\theta D_m$ in undisturbed beds. The following is a preliminary examination to explain this difference.

For sandy beds under wave motion, Shum (1992, 1993) and Savant et al. (1987) found that the relative movement of pore water to sediment particles, termed convective transport, dominated the overall transport process. Molecular diffusion was orders of magnitude lower than this convective transport. Thus, diffusion in sandy beds, which characteristically possess higher permeabilities than mud beds, can obviously be enhanced by wave action. In fact, for mud beds the permeability can be practically zero (Das, 1983), and there is very little relative movement of pore water in mud over wave time-scales. Thus, the increased wave-enhanced diffusivity in mud beds cannot be due to enhanced convective transport.

According to Harrison et al. (1983), the relative importance of wave-induced convective motion and molecular diffusion can be expressed by the Peclet Number, Pe, defined as

$$Pe = \frac{c_* d_e^3}{D_m} e^{-k(z+h_1)} \frac{kH}{2\cosh kh_1} \tag{6.17}$$

where c_* is a constant equal to 1.84×10^4 $(ms)^{-1}$ according to Krumbein and Munk (1942), d_e is the effective grain size, k is the wave number, H is the wave height and the z-axis originates from water surface, as shown in Fig. 6.1. For a mud bed, if we choose the diameter of flocs (on the order of 10^{-6} m) as the effective grain size, which is much greater than the dispersed particle size, the Peclet number would be less than order of 10^{-5}. This means that according to this mechanism the contribution of wave-induced relative movement of pore water to constituent diffusion in mud beds is negligible compared with molecular diffusion. Thus, the theory developed for convective transport in sandy bed under wave motion does not appear to be suitable for mud beds.

For mud beds, especially when it is fluidized the oscillation and movement of mud can be significant. Due to the high viscosity of fluid mud, which is typically 100 to 10,000 times higher than that for water (Jiang, 1993), the boundary layer is typically on the order of 0.01 to 1 m, which is much thicker than that in water and, therefore, wave motion in fluid mud cannot be represented by potential flow. Thus, momentum transport in fluid mud must exist. Note also that wave energy is strongly dissipated in mud due to its high viscosity., and in fact the majority of wave energy dissipation occurs within mud. Since the main difference

between fluid mud and the undisturbed mud bed is that energy dissipation and momentum transport occur significantly in fluid mud, it can be concluded that the enhanced diffusion must be related to energy dissipation and momentum transport.

For wave transport over mud, due energy dissipation the wave height, H, decay is exponential (Gade, 1958, Dalrymple and Liu, 1978, McPherson, 1980), i.e.,

$$H(x) = H_0 e^{-k_i x} \tag{6.18}$$

where x is positive in the wave transport direction, k_i is the wave damping coefficient and H_0 is the incident wave height at x = 0. The wave-mean rate of energy dissipation per unit area, $\overline{\epsilon_D}$, can be expressed as (Lee, 1995)

$$\overline{\epsilon_D} = E\sigma \frac{2k_i}{k_r} \tag{6.19}$$

where $E = \frac{1}{8}\rho g H^2$ is the wave energy, σ is the wave frequency and k_r is the wave number. For simplicity it can be assumed that all the energy is lost in mud and that dissipation is uniform over the fluid mud depth, $h_2 - h_1$. Thus, the energy dissipation rate per unit area due to internal friction in mud can be expressed as

$$\overline{\epsilon_D} = (h_2 - h_1)\mu_2 \left(\frac{\partial u_2}{\partial z} + \frac{\partial u_2}{\partial x} \right)^2 + (h_2 - h_1)\mu_2 \left(\frac{\partial w_2}{\partial z} + \frac{\partial w_2}{\partial x} \right)^2 \tag{6.20}$$

where u_2 and w_2 are the velocity components in the x and z-directions in fluid mud, respectively, and μ_2 is mud viscosity. Since characteristically $\frac{\partial u_2}{\partial z} >> \frac{\partial u_2}{\partial x}, \frac{\partial w_2}{\partial z}, \frac{\partial w_2}{\partial x}$, Eq. 6.20 can be simplified as

$$\overline{\epsilon_D} = (h_2 - h_1)\mu_2 \overline{\left(\frac{\partial u_2}{\partial z}\right)^2} = (h_2 - h_1)\mu_2 \left(\frac{\partial u_2^*}{\partial z}\right)^2 \tag{6.21}$$

where $u_2^* = \frac{u_{2max}}{\pi}\int_0^{\pi} \sin^2 x dx = \frac{1}{2}u_{2max}$ is the characteristic energy dissipation velocity, and u_{2max} is the maximum wave-induced horizontal velocity in mud. Next, the wave-averaged momentum transfer flux, J_{Mo}, in fluid mud can be expressed as

$$J_{Mo} = \mu_2 \overline{\left(\frac{\partial u_2}{\partial z}\right)} = \mu_2 \left(\frac{\partial u_2^{**}}{\partial z}\right) \tag{6.22}$$

where $u_2^{**} = \frac{u_{2max}}{\pi}\int_0^{\pi} \sin x dx = \frac{2}{\pi}u_{2max}$ is the characteristic horizontal velocity due to wave-induced in mud. By substituting Eqs 6.20 and 6.22 into Eq. 6.23, we obtain

$$J_{Mo} = \sqrt{\frac{\pi}{4}\frac{\mu_2 \overline{\epsilon_D}}{(h_2 - h_1)}} = \sqrt{\frac{\pi}{2}\frac{\mu_2 E \sigma k_i}{(h_2 - h_1)k_r}} \tag{6.23}$$

By way of the analogy between mass transfer and momentum transfer, the corresponding mass transfer flux due to wave disturbance in fluid mud, J_{Ma}, is

$$J_{Ma} = D_f \frac{\partial C}{\partial z} = f(J_{Mo})\frac{\partial C}{\partial z} \tag{6.24}$$

where $D_f \propto J_{Mo}$ is the wave-induced mass diffusivity in mud. A schematic representation of energy dissipation and transport, velocity distribution and the corresponding momentum transport and constituent concentration distribution and analogous constituent mass transport is shown in Fig. 6.3. Note that the assumed uniform rate of energy dissipation over the fluid mud depth implies a linear velocity distribution, which in turn means a constant momentum flux. Analogous to momentum transport, the normalized constituent mass transport also has a similar formulation, and the constituent mass transport rate is proportional to momentum transport in fluid mud.

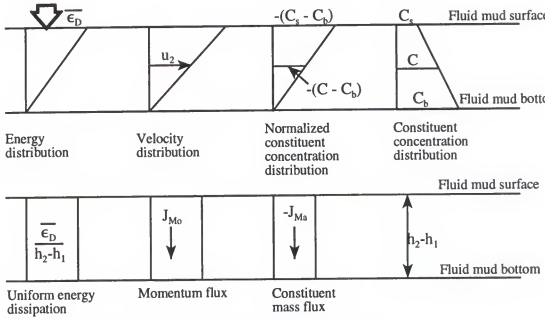

Figure 6.4 Schematic of energy transport and dissipation, velocity distribution and momentum transport, and constituent concentration distribution and momentum-analogous constituent mass transport. C_s and C_b are the surface and bottom values of constituent concentration, C.

Defining the Schmidt Number in fluid mud, $Sc_f = \nu_l/D_f$, which represents the ratio of wave-induced mass transport to momentum transport, since D_f is a function of J_{Mo}, Sc_f should also be a function of J_{Mo}, the fluid mud parameters, i.e., ρ_2, μ_2, G_2, h_2, and wave frequency, σ. This functional dependence can be expressed as

$$\frac{D_f}{\nu_l} = \frac{1}{Sc_f} = f(J_{Mo},\ \rho_2,\ h_2,\ \mu_2,\ G_2,\ \sigma,\ g) \tag{6.25}$$

where g is the gravitational constant. Non-dimensionizing Eq. 6.25, we obtain

$$\frac{D_f}{\nu_l} = f\left[\frac{J_{Mo}}{\rho_2 g(h_2-h_1)},\ \frac{\mu_2\sigma}{G_2}\right] \tag{6.26}$$

Since according to Eq. 6.23, $J_{MO} = \left\{\frac{H^2k_i}{(h_2-h_1)}\frac{\rho_1 g\mu_2\sigma}{k_r}\frac{1}{[\rho_2 g(h_2-h_1)]^2}\right\}^{1/2}$, Eq. 6.26 can be restated as

$$\frac{D_f}{\nu_l} = f\left[\frac{H^2k_i}{(h_2-h_1)},\ \frac{1}{\rho_2 g(h_2-h_1)}\sqrt{\frac{\rho_1 g\mu_2\sigma}{k_r}},\ \frac{\mu_2\sigma}{G_2}\right] \tag{6.27}$$

Because the wave damping coefficient, k_i, in the first dimensionless group on the right hand side of Eq. 6.27 includes the effects of fluid mud density, ρ_2, thickness, h_2, mud rheological parameters, μ_2, G_2, and wave parameters, σ, k_r, ρ_1 (Jiang, 1993, Lee, 1995), the last two dimensionless groups on the right hand side are not independent and can be incorporated within the first dimensionless group. Thus, Eq. 6.27 can be simplified as

$$\frac{D_f}{\nu_l} = f\left(\frac{H^2 k_i}{h_2 - h_1}\right) \tag{6.28}$$

Since molecular diffusion always exists, the total mass transfer flux, $J_t = K_{z2}\partial C/\partial z$, should be the sum of J_{Ma} and molecular diffusion flux, i.e., $\omega_\theta D_m \partial C/\partial z$. Thus, K_{z2} can be expressed as

$$K_{z2} = D_f + \omega_\theta D_m = \nu_l\left(\frac{1}{Sc_f} + \frac{\omega_\theta}{Sc}\right) \tag{6.29}$$

Here $Sc = \nu_l/D_m$ is the Schmidt Number for the constituent in water, while Sc_f represents the Schmidt Number of constituent transport in fluid mud.

From Eq. 6.29, D_f is observed to be proportional to wave energy dissipation rate per area, and inversely proportional to fluid mud depth, h_2, because the thicker the fluid mud the lesser the energy dissipation rate per unit volume of mud.

6.4 Mass Transfer Coefficient, K_{12c}

In water layer near the sediment-water interface, there exists a thin wave boundary layer, commonly called as the diffusive sublayer (Boudreau and Guinasso, 1982). Because the concentration gradient is mainly confined to a this layer when constituent transport across this layer is occurs, a simple model for constituent mass flux across the wave boundary layer can be constructed by assuming that the constituent flux in the diffusive sublayer is described by Fick's first law of diffusion (Fick, 1885). Also, because of the thinness of this layer, the

concentration gradient can be considered to be uniform in this layer, which in turn means that the diffusive flux is constant across this layer. Therefore, the convective flux can be expressed as

$$F_{12c} = K_{12c}(C_s - C_c) = D_m \frac{\partial C}{\partial z} = \frac{D_m}{\delta_c}(C_s - C_c) \qquad (6.30)$$

where $C_s = C_2|_{z=-h_1}$ is the constituent concentration at the mud-water interface, and the constituent concentration just outside the bottom wave boundary layer, $C_c = C_1|_{z=-h_1+\delta_c}$, where δ_c is the diffusive sub-layer thickness (see Fig. 6.5).

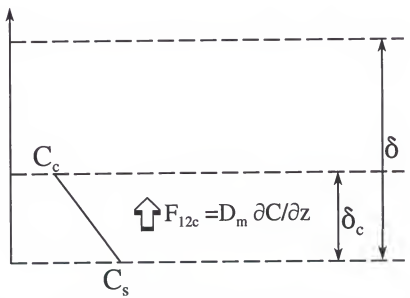

Figure 6.5 Schematic shown of bottom diffusive sub-layer and wave boundary layer in water, and direct convective flux.

The thickness δ_c is directly proportional to the bottom boundary layer thickness, and the ratio of δ_c to δ is related to the Schmidt Number, $Sc = \nu_1/D_m$, the bottom wave Reynolds Number, $Re_b' = u_b' a_b'/\nu_1$ and the relative interfacial roughness, R_r, (Welty, et al., 1969). Here u'_b is the bottom velocity outside the boundary layer, and $a'_b = u'_b\sigma$ is the corresponding maximum horizonal excursion. The relative roughness is defined as, $R_r = a'_b/d_{90,}$ for flat mud-water interface and must also include the interfacial oscillation effect (IOE). Thus, the diffusive layer thickness can be expressed functionally as

$$\frac{\delta_c}{\delta} = f_1(Sc,\ Re_b',\ R_r,\ IOE) \tag{6.31}$$

In general, IOE can be described in terms of its dependence of wave parameters and fluid mud parameters, which is expressed as

$$IOE = f_2(H,\ \sigma,\ h_1,\ \nu,\ \rho_1,\ h_2,\ \mu_2,\ G_2,\ \rho_2,\ g) \tag{6.32}$$

where H is the wave height, σ is the wave frequency, h_1 is the water depth, ν is the water viscosity, ρ_1 is the water density, h_2 is the fluid mud depth, μ_2 is the fluid mud viscosity, G_2 is the fluid mud elasticity, ρ_2 is the mud density and g is the gravitational acceleration. Since IOE is only related to interfacial characteristics, the water wave-related parameters, i.e., H, σ, h_1 and ν_1, can be characteristically represented by the mud-water interface-related velocity difference, Δu and the boundary layer thickness, δ, can be obtained from a wave-mud interaction model. Then by non-dimensionizing the right hand side of Eq. 6.32, we obtain

$$IOE = f_3\left(Ri_w, \frac{h_2}{h_1}, \frac{\rho_2}{\rho_1}, \frac{\sigma\mu_2}{G_2}\right) \tag{6.33}$$

where $Ri_w = \Delta\rho g\delta/\rho_1(\Delta u)^2$, is the wave boundary layer Richardson Number over fluid mud as defined in Chapter 4. Here $\Delta\rho = \rho_2 - \rho_1$. Since in Eq. 6.33 the last three dimensionless groups on the right hand side are representative fluid mud parameters, which can be conveniently incorporated into the first dimensionless group, Eq. 6.33 can be restated as

$$IOE = f_2(Ri_\delta) \tag{6.34}$$

Therefore, inserting Eqs. 6.31 and 6.34 into Eq. 6.30, the dimensionless mass transfer coefficient, K_{12c}/u_b, can be expressed as

$$\frac{K_{12c}}{u_b'} = \frac{D}{u_b'\delta_c} = \frac{\nu_1}{Sc\,u_b'\,\delta\, f_1[Sc,\ Re_b',\ R_r,\ f_2(Ri_\delta)]} \tag{6.35}$$

Incorporating the Reynolds Number, $Re_b^* = u_b'\delta/\nu_1$, into the function f_2, Eq. 6.35 can be rewritten as

$$\frac{K_{12c}}{u_b'} = f'(Sc,\ Re_b',\ R_r)\ f''(Ri_\delta,\ Re_b^*) \tag{6.36}$$

Since the Richardson Number, Ri_w, includes the effects of wave parameters as well as mud parameters, which in turn determine the components of Re_b^*, i.e., u_b, ν_1 and δ, Eq. 6.36 can be simplified as

$$\frac{K_{12c}}{u_b'} = f'(Sc,\ Re_b',\ R_r)\ f''(Ri_\delta) = \alpha_{12c}\, f'(Sc,\ Re_b',\ R_r) \tag{6.37}$$

where $\alpha_{12c} = f''(Ri_w)$ is a diffusion characterizing coefficient. In Eq. 6.37, the first function, f', incorporates the effects of bottom boundary layer on the mass transfer coefficient with an assumed flat mud-water interface, whereas the second function, f'', is for the interfacial oscillation effect.

Two other effects need to be considered for contaminant release across the bottom diffusive layer over the mud-water interface. First, Equation 6.30 was originally shown to be applicable to mass transfer between two immiscible fluids of different densities and with a relative velocity, or to fluid flow over a rigid surface (Welty et al., 1969), in which the interfacial area is the effective area over which diffusive exchange takes place. However, as noted, for water over bottom sediment-water mixture the effective area for constituent transport between water and pore water in fluid mud is much smaller than that between a fluid and a solid or between two immiscible fluids, because only part of the area is occupied by interstitial water for convective transport, the remainder being sediment particles or flocs. Thus, the effective area for direct convection is reduced, and this reduction depends on the type of sediment and its flocculation behavior.

Secondly, under wave motion, mud-water interface oscillation actually enlarges the total interfacial area between mud and water, with the results that the effective area for convection is also enlarged. The greater the interfacial wave slope, i.e., the ratio of interfacial wave height to wave length, the larger the effective area for convection. At the same time, because of the periodic distortion of the mud surface and rotational motion within fluid mud, the rate of replenishment of mud surface is thus enhanced. Therefore, both effective area enlargement and its replenishment rate, are proportional to mud-water interfacial oscillation. As a result, the mass transfer coefficient, K_{12c}, increases with increasing of mud-water interfacial slope, which is determined by wave forcing and mud properties.

The above two effects can in general be expressed as functions of H, σ, h_1, ν_1, ρ_1, h_2, μ_2, G_2, ρ_2 and g, which can be eventually included within the function $f''(Ri_w)$ in Eq. 6.37, based on Eqs. 6.32, 6.33 and 6.34.

When the wave boundary layer is viscous, by the analogy of mass transfer across the diffusive layer to momentum transfer across the boundary layer for an assumed flat mud-water interface (Welty et al., 1969), the diffusive sub-layer can be considered to be related to the hydrodynamic boundary layer by

$$\frac{\delta_c}{\delta} = f'(Sc,\ Re_b',\ R_r) = \text{Const. } Sc^{-1/3} Re_b'^{-1/2} \qquad (6.38)$$

where Const. denotes a constant coefficient. Equation 6.38 is a special case of function f′ in Eq. 6.37. Therefore, mass transfer across the water-mud interface under the waves is given by

$$K_{12c} = \alpha_{12c} S_c^{-2/3} Re_b^{\prime -1/2} u_b^{\prime} \tag{6.39}$$

in which the constant coefficient in Eq. 6.38 has been incorporated in to $f''(Ri_w)$. By neglecting the effects from mud-water interfacial oscillation, which incorporated into $f''(Ri_w)$, Eq. 6.39 cab be shown to be similar to the well known Chilton-Colburn relationship for mass transfer across a boundary layer (Welty, et al., 1969). The function $\alpha_{12c} = f''(Ri_w)$ will be determined by calibrating the model against experiment data in Chapter 8.

6.5 Solution Technique

The model comprises of two parts: (1) the vertical fine-grained sediment transport sub-model developed in Chapter 4, and (2) the vertical sediment-associated contaminant transport sub-model developed in this chapter. The results of the sediment sub-model are inter-linked with those of the contaminant sub-model with a synchronous finite difference scheme. The sediment sub-model supplies the sediment concentration, settling velocity, entrainment and deposition rate at each time step for the contaminant model consisting of Eqs. 6.4 6.7 and 6.8.

Eqs. 6.4, 6.5 and 6.6, together with Eq. 6.2, which relates the particle-bound part and dissolved part of the contaminant, form the governing equations for sediment-associated contaminant transport. The related boundary and connective conditions are represented by

Eqs. 6.7, 6.8, 6.9 and 6.10. Sediment transport in the water layer and the entrainment and deposition fluxes across the fluid mud-water interface are provided by the sediment sub-model. Entrainment and/or deposition fluxes induce particle-bound contaminant transport in the water layer. They also induce particle-bound contaminant flux of the sorptive contaminant and the indirect convective flux of both non-sorptive and sorptive contaminants across the fluid mud-water interface.

CHAPTER 7
FLUME EXPERIMENTS

7.1 Introduction

The laboratory flume experiments were carried out at the Coastal Engineering Laboratory of the University of Florida. The aim was to obtain dye and sediment concentration profiles in water under wave loading. These experimental data will be used to determine the total contaminant release flux and sub-flux from bottom sediment by calibrating the contaminant transport model (see Chapter 6). The experimental set-up, test conditions, data obtained and analysis are given in this chapter. Model calibration and simulation, and analysis of results and discussion are presented in Chapter 8.

7.2 Experimental Equipment

7.2.1 Wave Flume

A 20 m long, 46 cm wide and 45 cm deep wave flume with plexiglass walls was used for the experiments (see Fig. 7.1). A programmable wave maker was located near one end of the flume. Wave height and the period could be adjusted by a DC motor controller in the ranges of 1~8 cm for height and 0.5~2.0 Hz for frequency. In the middle portion of the flume, a segment that was a 10 m long, 46 cm wide and 6 cm deep flat bottom trench served as the container of the test mud. Astroturf mats, which consisted of miniature, tree-like

roughness elements of thickness of about 1 cm in a dense pattern affixed to a rubber base, were nailed to the sloping ends of the flume bed to absorb wave energy in order to minimize wave reflections.

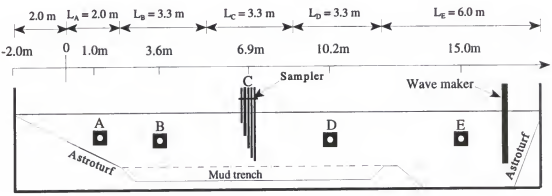

Figure 7.1 Wave flume used in experiments.

7.2.2 Colorimeter

The instrument used to measure dye concentrations was Spectronic 20 Colorimeter made by Analytical System Division, Bausch & Lomb, Rochester, New York. The principle of this device is that when a ray of incident monochromatic light of intensity, I_0, enters an absorbing medium its intensity, I, decreases exponentially with concentration, C_d, of the absorbing material. This decrease is expressed as (Brewer et al., 1974):

$$\log_e \frac{I_0}{I} = 2.303 \log_{10} \frac{I_0}{I} = K' C_d \qquad (7.1)$$

where K' is a characteristic constant. Defining absorbance $A = \log_{10}(I_0/I)$, a linear relationship exists between the concentration, C, and the absorbance, A,

$$A = K'' C_d \qquad (7.2)$$

where K'' is a proportionality coefficient to be determine by calibration. Given that the tap water used in the experiments was not pure and had background absorbance, Eq. 6.2 must be revised according to

$$A = K_d C + B'' \tag{7.3}$$

where B'' is the background absorbance to be determined by calibration. For convenience, Eq. 6.3 can be rewritten as:

$$C_d = K A + B \tag{7.4}$$

in which coefficients K and B were obtained by calibration.

A fluid medium can have different absorbances for different incident light wave lengths. Usually, the wave length at which absorbance is maximum (or transmittance is minimum) is selected, because maximum sensitivity and minimum deviation between the measured and the true absorbance due to incident wave length shift can be obtained at this wave length. Experiments for selecting the optimal wave length were carried out with 0.2 mg/l and 2 mg/l of Rhodamine B within the wave length range of 520 nm to 580 nm, and 1 mg/l and 5 mg/l of Erioglaucine A within the range of 560 nm to 660 nm. The measured relationships between transmittance and the wave length are given in Figs. 7.2 and 7.3 for the two dyes, respectively. Based on these results, the selected optimal light wave lengths are: L_{RB} = 550 nm for Rhodamine B and L_{EA} = 625 nm for Erioglaucine A.

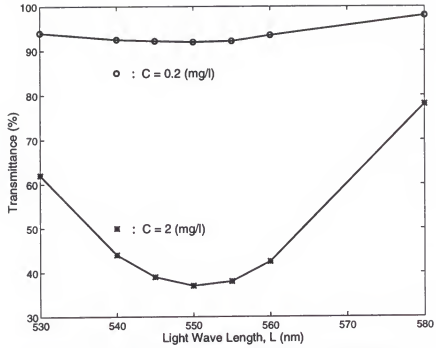

Figure 7.2 Relationship between incident wave length and transmittance for Rhodamine B.

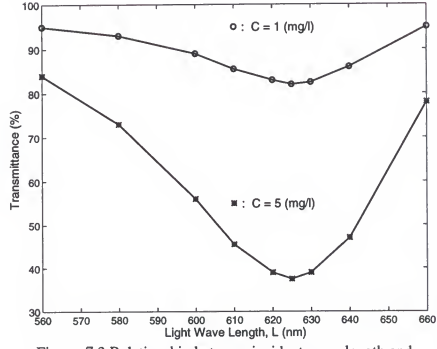

Figure 7.3 Relationship between incident wave length and transmittance for Erioglaucine A.

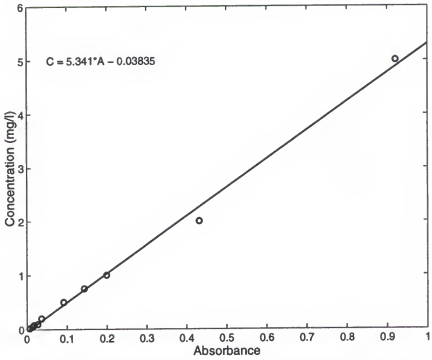

Figure 7.4 Calibration of Rhodamine B concentration with selected light wave length, L_{RB} = 550 nm.

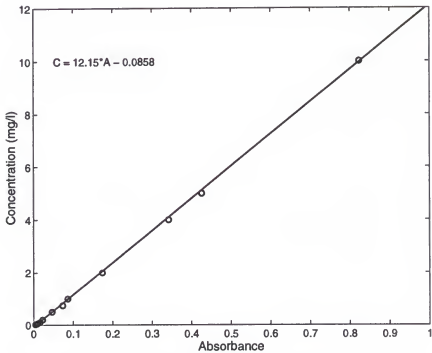

Figure 7.5 Calibration of Erioglaucine A concentration with selected light wave length, L_{EA} = 625 nm.

Table 7.1 Tests Conditions

Test No.	Water depth (cm)	Fluid mud/bed depth (cm)	Fluid mud/ bed density (kg/m^3)	Wave height /frequency (cm)/(Hz)	Loading duration (hr)	Resuspension	Sediment	Dye / pre-mixed mass (g)
1-1	15	2.3/0.0	1,220/-	1.5/0.8	4	No	Kaolinite	E. A[a] / 5
1-2				2.5/1.0	4	No		
2-1	15	2.4/1.8	1,090/1,110	1.0/1.0	4	No	Kaolinite	E. A / 25
2-2				3.5/1.0	4	Yes		
2-3				5.5/1.2	2	Yes		
2-4				0.0/--	2	No		
3-1	15	2.4/2.7	1,220/1,250	1.0/1.0	4	No	Kaolinite	R. B[b] / 35
3-2				4.5/1.0	4	Yes		
3-3				0.0/--	4	No		
4	15	2.8/2.8	1,250/1,280	5.0/1.0	11	Yes	Kaolinite	R. B / 45
5-1	15	2.8/2.8	1,200/1,250	2.0/1.0	4	Yes	AK mud	R. B / 60
5-2				6.0/1.0	4	Yes		
5-3				0.0/--	4	No		
6-1	15	2.8/2.8	1,200/1,250	5.5/1.0	4	Yes	AK mud	E. A / 60
6-2				0.0/--	4	No		
6-3				5.5/1.0	4	Yes		

Note: [a]: Erioglaucine A, [b]: Rhodamine B.

Calibrations were then carried out to determine the proportionality coefficient, K (Eq. 7.4), and the background-related coefficient, B, at the selected light wave lengths. The concentrations of dyes for calibration were varied from 0.02 mg/l to 5 mg/l for Rhodamine B and 0.02 mg/l to 10 mg/l for Erioglaucine A, respectively. As shown in Figs. 7.4 and 7.5, linear relationships between the concentration and absorbance occur over the tested concentration ranges. By using the least-squares method for linear regression, the calibration coefficients are obtained as: (1) K = 5.341 and B = -0.03835 for Rhodamine B with the

coefficient of determination, $R^2 = 0.998$; and (2) K = 12.15 and B = -0.0858 for Erioglaucine A with $R^2 = 0.999$.

7.3 Test Conditions and Procedure

7.3.1 Test Conditions

In all tests the depth of water was maintained at 15 cm, while the bottom mud (fluid mud + bed) depth was varied from 2.2 cm to 5.6 cm. Kaolinite and AK mud were subjected to wave frequencies ranging from 0.8 to 1.2 Hz and wave heights from 1.0 to 6.0 cm. These muds were initially inoculated separately with Rhodamine B and Erioglaucine A. Tap water was used both in preparing the muds and in the flume. The chemical compositions of tap water and sediments (kaolinite and attapulgite), and some physical and chemical properties of Rhodamine B and Erioglaucine A are given in Chapter 5. All the test conditions are summarized in Table 7.1.

7.3.2 Procedure

Mud Preparation

Specific amounts of kaolinite or 50% : 50% by weight of attapulgite and kaolinite (AK mud) were added to plastic containers (about 0.14 m^3 volume each), and were throughly mixed with tap water to make a slurry. Then, a specified amount of Erioglaucine A or Rhodamine B was added to the slurry to inoculate the mud. The mixing process was maintained for about a week to attain an equilibrium state between the pore water and the eroding fluid, and between the dissolved and the particulate phases of the dyes.

The slurry was placed into the test section of the flume a day before the experiment. Tap water was added slowly and carefully by using a pump without significantly disturbing the mud layer until the water surface reached the desired level. The thickness of the fluid mud was estimated later during each experiment by observing bottom mud motion under wave loading. The average fluid mud thicknesses are given in Table 7.1, along with approximate densities. Also given are bed thickness and bed densities.

Suspension Samples

Suspension samples were taken along the flume-centerline at a single elevation at positions A, B, D and E, and at four or five elevations at position C for Tests 1, 2, 4, 5 and 6, as shown in Fig.7.1. In Test 3 suspension samples were taken at four elevations at A, B, C, D, and E for an accurate measurements of the total masses of suspended sediment and dye released from bottom at different times. Over each duration of constant wave loading, suspension samples were taken at 15, 30, 60, 120, 180, 240 minutes and beyond as needed. Each sample was about 80 ml, which was divided into 60 ml and 20 ml parts. Water volume removed due to sampling was replenished by adding tap water to flume.

The 60 ml part of the sample was analyzed gravimetrically for suspended sediment concentration by using a filtration unit, which included a Millipore vacuum pump, 1000 ml beakers, a pipette, a filter holder, filter papers with a pore size of 0.45 micron, a Mettler balance with 0.1 mg accuracy and a sample drying oven.

The 20 ml part was placed in a test tube for at least four days to allow the suspended sediment to settle out. Then, the sediment-free supernatant solution was poured into the colorimeter to obtain the dissolved dye concentration in water.

All the measured suspended sediment and dye concentrations are listed in Tables A.1, A.2, A.3, A.4, A.5, A.6, A.7, A.8, A.9, A.10, A.11, and A.12 in Appendix A.

Water Temperature

Water temperature was monitored by a thermometer during the experiments, and the measurement are listed in the Table A.13 in Appendix A. The maximum change of temperature for each experiment was found to be 3°C and the temperature difference between experiments was equal to or less than 7 °C, which did not cause significant differences in the sorption characteristics according to the results of Chapter 5.

7.4 Data Analysis

In Test 3, suspended sediment and dye concentration profile variations with time were obtained for each of the five positions, A, B, C, D and E. By analyzing these data of Test 3, we will obtain a simplified method for calculating the total suspended sediment and dye masses in water from single-point data obtained in all other tests at locations A, B, D, and E and profiles at location C. Thus, by using this simplified method for Tests 1, 2, 4, 5, and 6, the single-point measurements of sediment and dye each time at A, B, D, and E along with sediment and dye profiles at C will be used to calculate the instantaneous releases of total sediment and dye masses in the water column.

7.4.1 Suspended Sediment

In stage 3-1 (0 ~ 240 minutes) of Test 3, the suspended sediment concentration was zero, because there was no resuspension. Suspended sediment profile variations with time at B, C and D and at A and E are shown in Figs. 7.6 and 7.7, respectively, for the time range

of 240 ~ 480 minutes, during which bottom sediment was suspended. In Figs. 7.8 and 7.9, respectively, corresponding data are given for the time range of 480 ~ 720 minutes, during which suspended sediment settled under no wave action.

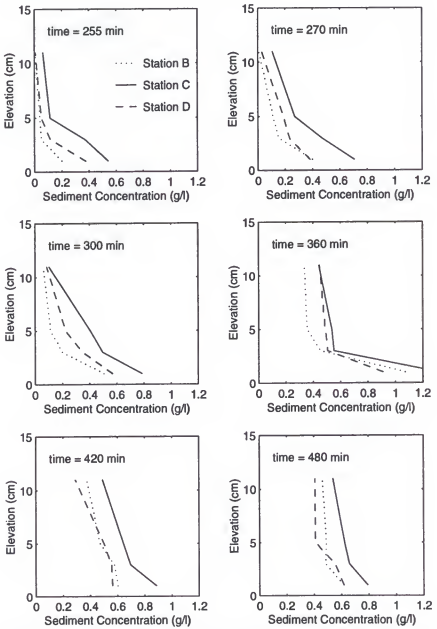

Figure 7.6 Suspended sediment concentration profile variations with time at B, C and D in the duration range of 240 ~ 480 minutes.

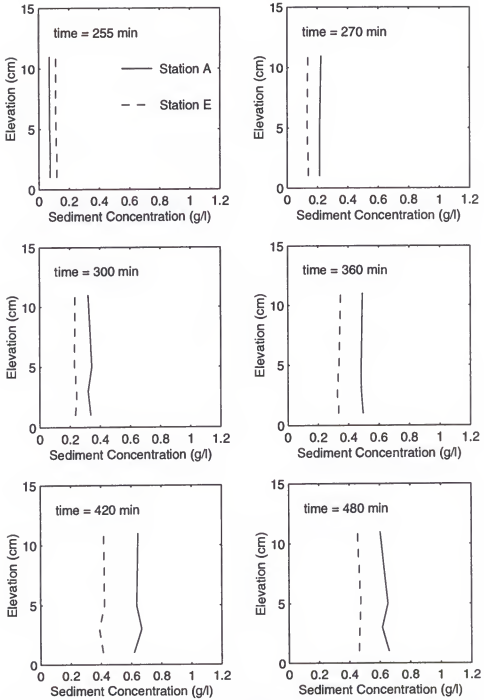

Figure 7.7 Suspended sediment concentration profile variations with time at A and E in the duration range of 240 ~ 480 minutes.

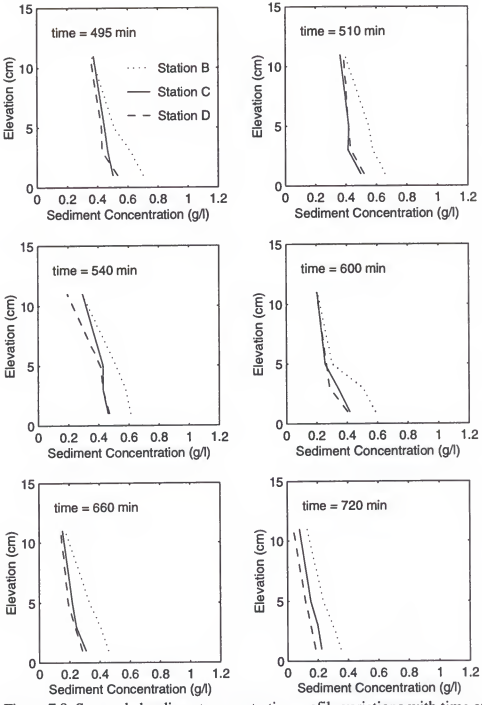

Figure 7.8 Suspended sediment concentration profile variations with time at B, C and D in the duration range of 480 ~ 720 minutes.

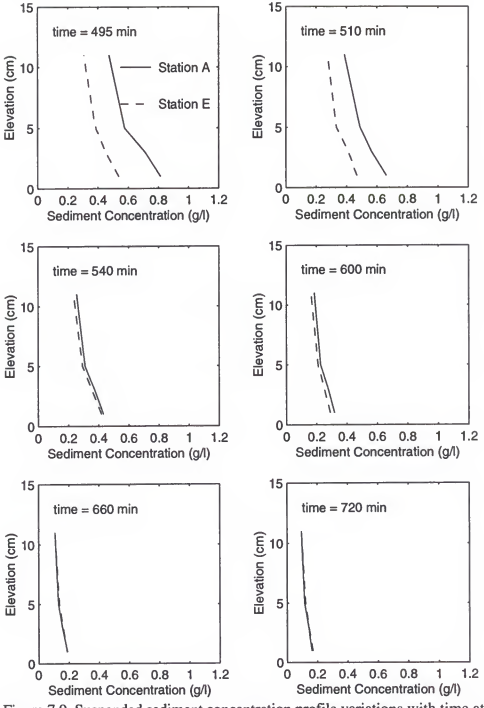

Figure 7.9 Suspended sediment concentration profile variations with time at A and E in the duration range of 480 ~ 720 minutes.

Locations B, C and D were in the range of the mud trench. The suspended sediment at these positions was mainly derived from local bottom sediment suspension. A and D were beyond the mud trench, where the bottom was made of plexiglass. Thus, the suspended sediment at A and E were derived from advection of sediment from the mud trench region. Thus, to obtain the total suspended sediment over the mud trench, sediment outside the mud trench had to be considered as follows:

The total suspended sediment mass, TS, can be expressed as:

$$TS = h_1 (\overline{S_A} L_A + \overline{S_B} L_B + \overline{S_C} L_C + \overline{S_D} L_D + \overline{S_E} L_E) \tag{7.5}$$

where h_1 is the water depth, $\overline{S_A}$, $\overline{S_B}$, $\overline{S_C}$, $\overline{S_D}$ and $\overline{S_E}$ are the depth-averaged suspended sediment concentrations at A, B, C, D, and E, respectively, and L_A, L_B, L_C, L_D, and L_E are the length ranges represented by sections A, B, C, D, and E, respectively, shown in Fig. 7.1. It must be noted that the length of the segment at the flume end opposite to the wave generator, outside the mud trench, was 4.0 m. However, half of the volume of this segment was occupied by a sloping bottom. Thus the effective length of this part should be half of its actual length (see Fig. 7.1).

By including the contributions from beyond the mud trench, the average suspended sediment concentration, $\overline{S_t}$, over the mud trench can be expressed as:

$$\overline{S_t} = \frac{TS}{L_{mt} h_1} = \frac{(\overline{S_A} L_A + \overline{S_B} L_B + \overline{S_C} L_C + \overline{S_D} L_D + \overline{S_E} L_E)}{L_{mt}} \tag{7.6}$$

where $L_{mt} = L_B + L_C + L_D$, is the length of the mud trench. Since $L_A = 2.0$ m, $L_B = 3.3$ m, $L_C = 3.3$ m, $L_D = 3.3$ m, $L_E = 6.0$ m, and $L_{mt} = 10.0$ m,

$$\overline{S_t} = 0.33(\overline{S_B} + \overline{S_C} + \overline{S_D}) + 0.2\overline{S_A} + 0.6\overline{S_E} \tag{7.7}$$

Eq. 7.7 is composed two parts: (1) the average sediment concentration over the mud trench, $\overline{S_m} = 0.33(\overline{S_B} + \overline{S_C} + \overline{S_D})$, and (2) the contribution from beyond the mud trench, $\overline{S_O} = 0.2\overline{S_A} + 0.6\overline{S_E}$. For Test 3 the depth-averaged sediment concentration at each position, $\overline{S_A}$, $\overline{S_B}$, $\overline{S_C}$, $\overline{S_D}$ and $\overline{S_E}$, can be obtained from the measured vertical sediment concentration profiles at these positions. However, for Tests 1, 2, 4, 5 and 6, only single-point measurements were made at A, B, D and E. Therefore, the following method is developed to convert these single-point data to obtain the corresponding average suspended sediment concentration, $\overline{S}$, which should have the same value as would be obtained from measuring complete profiles at these positions.

From Figs. 7.6 and 7.8, it is observed that the shapes of suspended sediment concentration profiles at B, C and D are similar for both the resuspension process, in which a lotucline is also observed, and for the quiescent settling process, in which the profiles are much less stratified. Thus, by assuming that the normalized vertical distribution of suspended sediment concentration at B, C and D are the same, the average sediment concentration over the mud trench, $\overline{S_m}$, can be obtained from

$$\overline{S_m} = 0.33\ \overline{S_C}\left[1 + \frac{S_{b0.5}}{S_{c0.5}} + \frac{S_{d0.5}}{S_{c0.5}}\right] \tag{7.8}$$

where $s_{b0.5}$, $s_{c0.5}$ and $s_{d0.5}$ are the measured suspended sediment concentrations at about one-half the water depth above the mud surface at B, C and D, respectively.

From Figs. 7.7 and 7.9, we find that the vertical distributions of suspended sediment concentration at A and E during the resuspension phase (240 ~ 480 minutes) are almost uniform. During the quiescent settling phase (480 ~ 720 minutes) the vertical distributions are much less stratified than those at B, C and D during the resuspension phase and can be approximately represented in terms of a linear relation with water depth. Thus, the depth-averaged sediment concentration at A and E can also be represented by the single-point concentration at one-half water depth above the mud surface. Thus for both stages:

$$\overline{S_O} = 0.2 s_{a0.5} + 0.6 s_{e0.5} \tag{7.9}$$

where $s_{a0.5}$ and $s_{e0.5}$ are the measured suspended sediment concentrations at about one-half water depth above the mud surface at A and E, respectively. Therefore, the equation for calculating the average suspended sediment concentration over the mud trench using single-point measurements at A, B, D and E can be expressed as

$$\overline{S_t} = 0.33\ \overline{S_C} \left[1 + \frac{s_{b0.5}}{s_{c0.5}} + \frac{s_{d0.5}}{s_{c0.5}} \right] + 0.2 s_{a0.5} + 0.6 s_{e0.5} \tag{7.10}$$

A comparison between the calculated result from Eq. 7.10 and from Eq. 7.7 with measured suspended sediment concentrations from Test 3 is shown in Fig. 7.10. Under wave motion in the flume, suspended sediment is advected from the mud trench to the outside regions. The effects of advection on suspended sediment concentration at B and D is greater

than that at C. Thus, if we only use the sediment concentration measured at C to represent the mean concentration over the mud trench, an inaccuracy would result (Fig. 7.10). For comparison, calculated result is displayed in Fig. 7.10 using

$$\overline{S_t} = \overline{S_C} + 0.2\overline{S_A} + 0.6\overline{S_E} \tag{7.11}$$

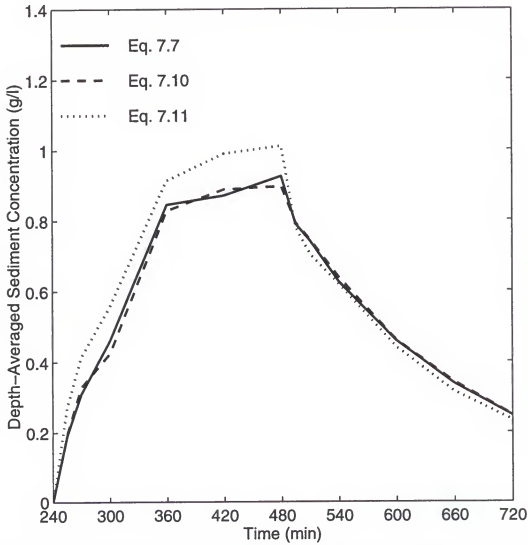

Figure 7.10 Comparison between the calculated suspended sediment concentration using three methods (Eqs. 7.7, 7.10 and 7.11). The resuspension phase is during 240 ~ 480 minutes, while the quiescent settling phase is during 480 ~ 720 min..

It is seen that Eq. 7.10 can yield almost same the suspended sediment concentration as that from Eq. 7.7. However, from Eq. 7.11 the calculated concentration values are generally greater than those from Eq. 7.7 during the resuspension phase, when advection was significant. On the other hand, during quiescent settling, the result from Eq. 7.11 agrees with that from Eq. 7.7 and Eq. 7.10 well, when significant advection did not occur.

In summary, (1) Eq. 7.10, can yield approximately the same suspended sediment concentration as that from Eq. 7.7, and (2) Eq. 7.11 is only valid for the case of no or weak advection.

7.4.2 Dye Release in Water

Analogous to the analysis for suspended sediment, the average dye concentration over the mud trench, $\overline{C_t}$, including the contribution of dye from outside mud trench region can be calculated from

$$\overline{C_t} = 0.33(\overline{C_B} + \overline{C_C} + \overline{C_D}) + 0.2\overline{C_A} + 0.6\overline{C_D} \qquad (7.12)$$

where $\overline{C_A}$, $\overline{C_B}$, $\overline{C_C}$, $\overline{C_D}$ and $\overline{C_E}$ are the depth-averaged dye concentrations at locations A, B, C, D and E, respectively.

Dye concentration profile variations with time at B, C and D, and at A and E are shown in Figs. 7.11 and 7.12, respectively, for Test 3-1 during 0 ~ 240 minutes. For Test 3-2, in the duration range of 240 ~ 480 minutes, the concentrations are shown in Figs. 7.13 and 7.14, respectively, and for Test 3-3, during 480 ~ 720 minutes, in Figs. 7.15 and 7.16, respectively.

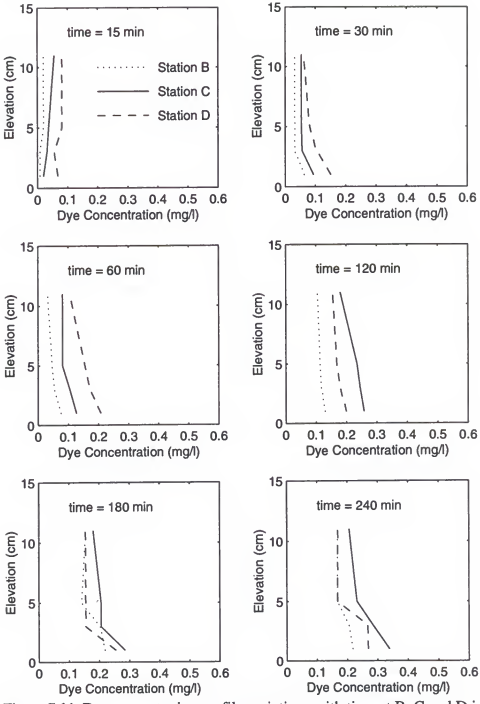

Figure 7.11 Dye concentration profile variations with time at B, C and D in the duration range of 0 ~ 240 minutes.

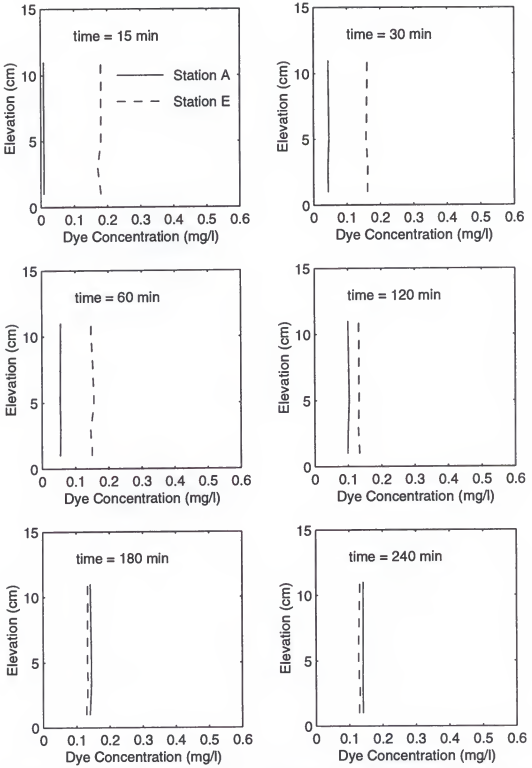

Figure 7.12 Dye concentration profile variations with time at A and E in the duration range of 0 ~ 240 minutes.

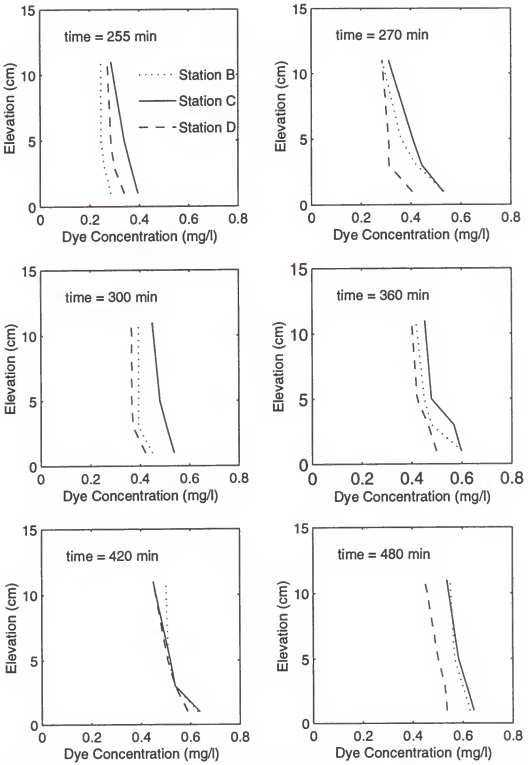

Figure 7.13 Dye concentration profile variations with time at B, C and D in the duration range of 240 ~ 480 minutes.

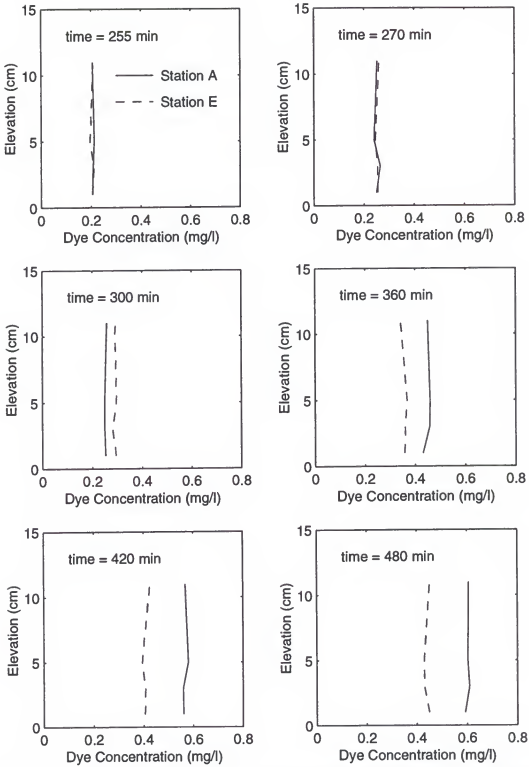

Figure 7.14 Dye concentration profile variation with time at A and E in the duration range of 240 ~ 480 minutes.

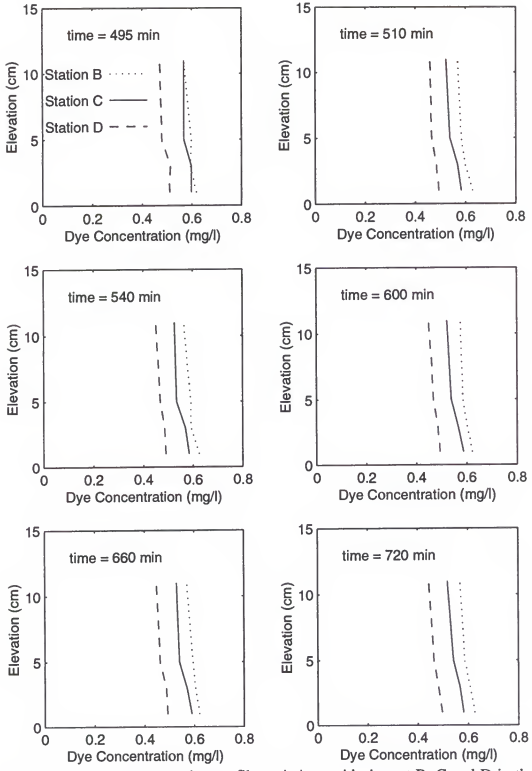

Figure 7.15 Dye concentration profile variations with time at B, C and D in the duration range of 480 ~ 720 minutes.

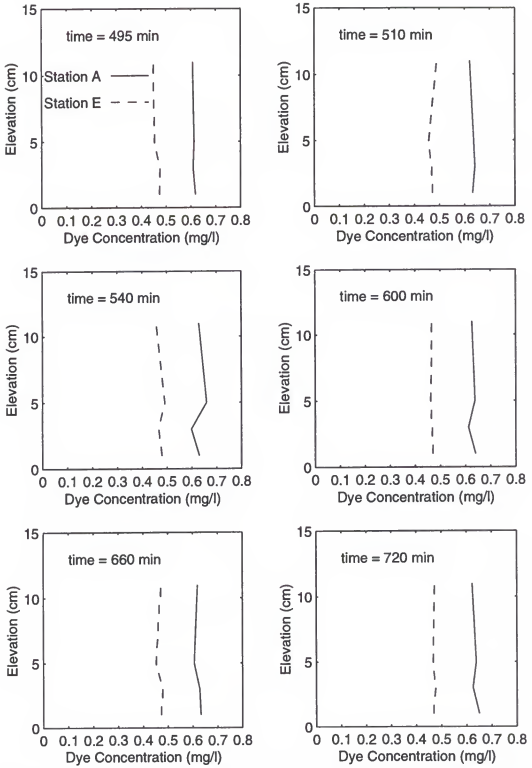

Figure 7.16 Dye concentration profile variations with time at B, C and D in the duration range of 480 ~ 720 minutes.

From Figs. 7.11, 7.13 and 7.15, the shapes of dye concentration profiles at B, C and D are seen to be similar during all three test phases, i.e., no sediment resuspension, sediment resuspension and quiescent settling. Thus, by assuming that the normalized vertical distributions of dye concentration at B, C and D are same, the average dye concentration over the mud trench, $\overline{C_m}$, can be expressed as

$$\overline{C_m} = 0.33\ \overline{C_C}\left[\ 1 + \frac{c_{b0.5}}{c_{c0.5}} + \frac{c_{d0.5}}{c_{c0.5}}\ \right] \tag{7.13}$$

where $c_{b0.5}$, $c_{c0.5}$ and $c_{d0.5}$ are the measured dye concentrations at about one-half water depth above the mud surface at B, C and D, respectively.

From Figs. 7.7 and 7.9, we find that the vertical distributions of dye concentration at A and E during the all three phases (0 ~ 720 minutes) are almost uniform. Thus, the depth-averaged dye concentration at A and E can be represented by the single-point concentration at one-half water depth above the mud surface. Then, the average dye concentration outside mud trench, $\overline{C_O}$, is given by:

$$\overline{C_O} = 0.2c_{a0.5} + 0.6c_{e0.5} \tag{7.14}$$

where $c_{a0.5}$ and $c_{e0.5}$ are the measured dye concentrations at one-half water depth above bottom at A and E, respectively. Therefore, the equation for obtaining the average dye concentration over mud trench with single-point measurement at A, B, D and E, becomes

$$\overline{C_t} = 0.33\ \overline{C_C}\left[1 + \frac{c_{b0.5}}{c_{c0.5}} + \frac{c_{d0.5}}{c_{c0.5}}\right] + 0.2c_{a0.5} + 0.6c_{e0.5} \qquad (7.15)$$

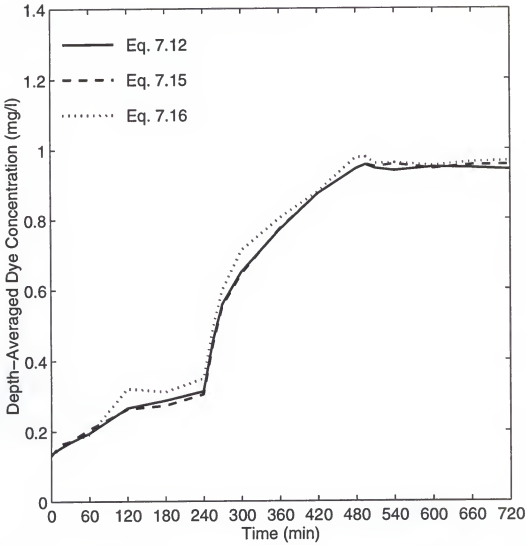

Figure 7.17 Comparison between calculated dye concentration using three methods (Eqs. 7.12, 7.15 and 7.16).

A comparison between the calculated results from Eq. 7.15, and from Eq. 7.12 is shown in Fig. 7.17. Similar to the analysis for suspended sediment, the calculated result

using depth-averaged dye concentration at C to represent the dye concentration over the mud trench is also displayed in Fig. 7.10. The calculation is expressed as:

$$\overline{C_t} = \overline{C_C} + 0.2\overline{C_A} + 0.6\overline{C_E} \tag{7.16}$$

From Fig. 7.17, we obtain the same result as that for suspended sediment, that is: (1) Eq. 7.15 is valid for all three phases, i.e., no sediment resuspension, sediment resuspension, and quiescent settling, and (2) Eq. 7.16 is only valid for phase 3, when no advection occurred.

For data analysis of Tests 1, 2, 4, 5 and 6, Eqs. 7.10 and 7.15 are used for suspended sediment and dye, respectively. On the other hand, for Test 3, Eqs. 7.7 and 7.12 are used for suspended sediment and dye, respectively.

CHAPTER 8
RESULTS, DISCUSSION AND CONCLUSIONS

8.1 Introduction

In this chapter the contaminant transport model developed in Chapter 6 is calibrated against experimental data given in Chapter 7. The wave-enhanced diffusion coefficient in fluid mud, K_{z2} (Eq. 6.5), the relationship between bottom diffusive sub-layer coefficient, α_{12c} and bottom Richardson Number, Ri_w, (Eqs. 6.37 and 6.39), and the fraction of redeposition of entrained sediment and associated pore water, fr (Eq. 6.14), are determined by best-fitting the modeling results to the measured dye profiles in water. Release fluxes and influential factors are then discussed. This is followed by overall conclusions derived from this study and recommendations for further investigations.

8.2 Results of Model Simulations and Calibrations

8.2.1 Model Conditions

For the conditions of the flume experiments described in the Chapter 7, time-simulations were run for both sediment and dye concentration profiles. For that purpose, input data required for modeling were divided into two categories (1) parameters corresponding to the test conditions, which were pre-set or were measured in the tests, and (2) characteristic modeling parameters. The pre-set test parameters including depths of

water, fluid mud and bed, densities of fluid mud and bed, wave height, frequency and loading durations and amount of dye pre-mixed in mud, are given in Table 7.1. The constituent distribution coefficient, K_d, and the first-order reaction rate, r, of dye sorption used in the model are given in Tables 5.4 and 5.5. The molecular diffusivity is selected as $1x10^{-9}$ (m^2/s) according to the previous investigations on diffusion of dissolved constituents (see Table 2.1).

For characteristic modeling parameters, mud rheology was specified in terms of the Voigt viscoelastic solid, for which the viscosity, μ_2, and the shear modulus of elasticity, G_2, were determined in separate rheometric tests by Maa (1986) for kaolinite, and by Jiang and Mehta (1995) for AK mud. Relevant parameters for settling and entrainment were derived from the study of Maa (1986), from the wave-induced resuspension study of Hwang (1989) and Ross (1989), and from the current-induced resuspension simulations of Ross (1989). Accordingly, the settling velocity related coefficients in Eq. 4.9 were selected to be: w_{sf} = $6.37x10^{-7}$ m/s, $S_1^* = 0.1$ kg/m^3, $\alpha_1 = 0.01$, $\beta_1 = 1.33$, $\gamma_1 = 1.5$ and $\delta_1 = 9$ for kaolinite in Tests 1, 2, 3 and 4 and $w_{sf} = 9.7x10^{-7}$ m/s, $S_1^* = 0.1$ kg/m^3, $\alpha_1 = 0.015$, $\beta_1 = 1.33$, $\gamma_1 = 1.5$ and $\delta_1 = 9$ for AK mud in Tests 5 and 6. Values of the wave diffusion parameter, α_2, in Eq. 4.23 and given in Table 8.1 vary from 0.002 to 0.33, which is consistent with the range discussed in Chapter 4. The stratification parameter, Φ, in Eq. 4.10 was characterized by α_3 = 0.5 and $\beta_3 = 0.5$. These values are the same as those used in Chapter 4 for sediment transport modeling. The entrainment proportionality coefficient, α_4 (Eq. 4.21), and the critical global Richardson Number, Ri_w, were selected for kaolinite to be $2.5x10^{-5}$ and 0.043 as in Chapter 4 for Tests 1, 2, 3 and 4, and $2.5x10^{-5}$ and 0.053, respectively, for AK mud, by

best-fitting the model results to experimental data in Tests 5 and 6. Input parameters required for simulations are listed in Table 8.1 for Tests 1 and 2, in Table 8.2 for Tests 3 and 4 and in Table 8.3 for Tests 5 and 6.

Table 8.1 Characteristic parameters for modeling of Tests 1 and 2.

		Test 1		Test 2			
		1-1	1-2	2-1	2-2	2-3	2-4 [a]
Settling velocity parameters	S_1^*	0.1		0.1			
	w_{sf}	6.37×10^{-7}		6.37×10^{-7}			
	γ_1	0.01		0.01			
	β_1	1.33		1.33			
	γ_1	9.0		9.0			
	γ_1	1.5		1.5			
Wave diffusion coefficient, α_2		0.0025	0.005	0.01	0.1	0.038	-
Stratified damping coefficients	α_3	0.5		0.5			
	β_3	0.5		0.5			
Critical Richardson Number, Ri_{wc}		0.043		0.043			
Entrainment coefficient, α_4		2.5×10^{-5}		2.5×10^{-5}			
Mud rheological coefficients	G_2 (Pa)	120		100			
	μ_2 (Pa.s)	80		64			
Equilibrium sorption distribution coefficient, K_d (l/g)		0.032		0.032			
First order rate coefficient for kinetic sorption, r (1/s)		0.1		0.1			
Molecular diffusivity, D_m (m^2/s)		1×10^{-9}		1×10^{-9}			
Tortuosity-related coefficient, ω		0.05		0.05			
Convection coefficient, α_{12c}		0.01	0.07	0.01	0.02	0.03	-
Fluid mud diffusivity, k_{x2} (m^2/s)		1×10^{-8}	2.5×10^{-8}	1×10^{-8}	3×10^{-8}	5×10^{-8}	5×10^{-11}
Fraction, fr (%)		98		98			

[a]: No wave condition.

Table 8.2 Characteristic parameters for modeling of Tests 3 and 4.

		Test 3			Test 4
		3-2	3-2	3-3 [a]	
Settling velocity parameters	S_1^*	9.0			0.1
	w_{sf}	6.37×10^{-7}			6.37×10^{-7}
	δ_1	0.01			0.01
	β_3	1.33			1.33
	γ_1	9.0			9.0
	δ_1	9.0			1.5
Wave diffusion coefficient, α_2		0.03	0.012	-	0.02
Stratified damping coefficients	δ_1	0.5			0.5
	β_3	0.5			0.5
Critical Richardson Number, Ri_{wc}		0.043			0.043
Entrainment coefficient, α_4		2.5×10^{-3}			2.5×10^{-3}
Mud rheological coefficients	G_2 (Pa)	120			120
	μ_2 (Pa.s)	80			80
Equilibrium sorption distribution coefficient, K_d (l/g)		0.083			0.083
First order rate coefficient for kinetic sorption, r (1/s)		0.1			0.1
Molecular diffusivity, D_m (m^2/s)		1×10^{-9}			1×10^{-9}
Tortuosity-related coefficient, ω		0.05			0.05
Convection coefficient, α_{12c}		0.02	0.04	-	0.025
Fluid mud diffusivity, k_{z2} (m^2/s)		1×10^{-8}	3×10^{-8}	5×10^{-11}	5×10^{-8}
Fraction, fr (%)		94			94

*: No wave condition.

Table 8.3 Characteristic parameters for modeling for Tests 5 and 6.

		Test 5			Test 6		
		6-1	5-2	5-3 [a]	6-1	6-2 [a]	6-3
Settling velocity parameters	S_1^*	0.0			0.1		
	w_{sf}	9.7×10^{-7}			9.7×10^{-7}		
	α_1	0.015			0.015		
	β_1	1.33			1.33		
	γ_1	9.0			0.5		
	β_1	1.5			1.5		
Wave diffusion coefficient, α_2		0.03	0.25	-	0.3	-	0.33
Stratified damping coefficients	α_1	0.5			0.5		
	β_3	0.5			0.5		
Critical Richardson Number, Ri_{wc}		0.053			0.053		
Entrainment coefficient, α_4		2.5×10^{-5}			2.5×10^{-5}		
Mud rheological coefficients	G_2 (Pa)	3075			3075		
	μ_2 (Pa.s)	66			66		
Equilibrium sorption distribution coefficient, K_d (l/g)		0.158			0.039		
First order rate coefficient for kinetic sorption, r (1/s)		0.1			0.1		
Molecular diffusivity, D_m (m^2/s)		1×10^{-9}			1×10^{-9}		
Tortuosity-related coefficient, ω		0.05			0.05		
Convection coefficient, α_{12c}		0.01	0.06	-	0.05	-	0.05
Fluid mud diffusivity, k_{z2} (m^2/s)		1.5×10^{-8}	4×10^{-8}	5×10^{-11}	4×10^{-8}	5×10^{-11}	4×10^{-8}
Fraction, fr (%)		98			98		

*: No wave condition.

The dye transport-related coefficients, i.e., the diffusivity in fluid mud, K_{z2} (Eq. 6.5), the interfacial flux coefficient, α_{12c} (Eqs. 6.37 and 6.39) and the fraction, fr (Eq. 6.14), were obtained by calibration of the model against experimental data for best-fit and are also listed in Tables 8.1 through 8.3.

8.2.2 Suspended Sediment Concentrations

No significant resuspension took place in Test 1, which was of a preliminary nature. For resuspension of kaolinite or AK mud in Tests 2, 3, 4, 5 and 6, comparisons between modeling results and experimental data for the depth-averaged sediment concentration are shown in Figs. 8.1, 8.2, 8.3, 8.4 and 8.5, respectively. Comparisons between calculated and measured suspended sediment vertical profiles are shown in Appendix B for Tests 2, 3, 4, 5 and 6.

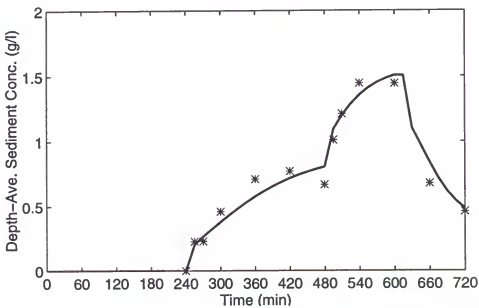

Figure 8.1 Comparison between simulated and measured depth-averaged suspended sediment concentrations in Test 2. Solid line represents model simulation results and the asterisks are measured data.

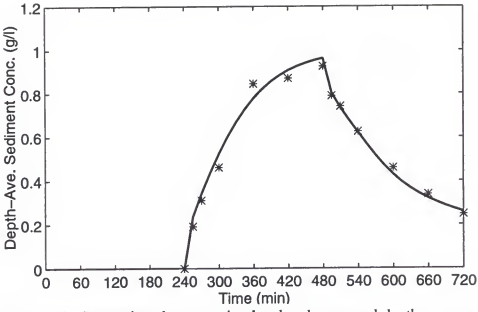

Figure 8.2 Comparison between simulated and measured depth-averaged suspended sediment concentrations in Test 3. Solid line represents model simulation results and the asterisks are measured data.

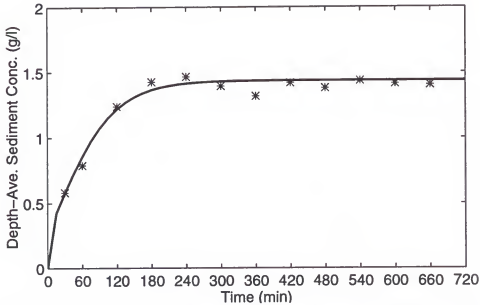

Figure 8.3 Comparison between simulated and measured depth-averaged suspended sediment concentrations in Test 4. Solid line represents model simulation results and the asterisks are measured data.

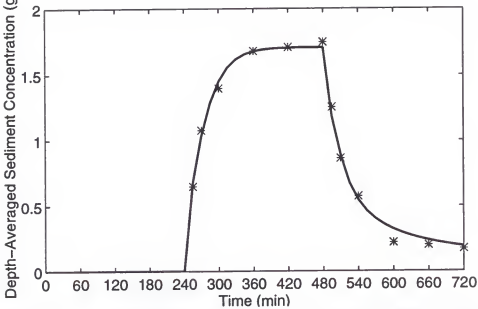

Figure 8.4 Comparison between simulated and measured depth-averaged suspended sediment concentrations in Test 5. Solid line represents model simulation results and the asterisks are measured data.

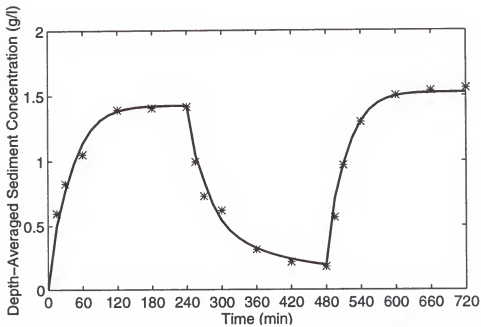

Figure 8.5 Comparison between simulated and measured depth-averaged suspended sediment concentrations in Test 6. Solid line represents model simulation results and the asterisks are measured data.

From Figs. 8.1, 8.2, 8.3, 8.4 and 8.5 it is observed that there exists a threshold for suspension of bottom sediment, which has been described in detail in Chapter 4. Furthermore, the suspended sediment concentration exhibits a tendency to reach an equilibrium value, due to a balance between gravitational settling and wave-induced diffusion. In Test 4 (Fig. 8.3) the equilibrium value was reached after about 4 hours continuous wave motion. In general, however, the time to attain equilibrium varied with wave conditions and sediment properties. Generally, the greater the sediment entrainment flux, the faster the attainment of the equilibrium state. Once wave loading was removed, e.g., in Tests 2-4, 3-3, 5-3 and 6-2, suspended sediment settled to bottom.

8.2.3 Dye Concentrations

Dye release from bottom sediment is characterized by direct flux due to wave-enhanced diffusion and indirect flux due to sediment resuspension. Under wave motion the direct flux always exists, whereas the indirect flux occurs only when the bottom sediment is suspended. In Tests 1, 2-1, 3-1 and 5-1, since no sediment resuspension occurred, dye release can be attributed solely to the direct convective flux (see Fig. 7.2). The magnitude of this flux is determined by the water-fluid mud interfacial coefficient, α_{12c} (Eqs. 6.37 and 6.39) and the diffusion coefficients in water and mud, K_{z1} (Eq. 6.4) and K_{z2} (Eq. 6.5), respectively. The wave-induced diffusion coefficient of dye in water, k_{z1}, can be considered to be the same as that for sediment diffusion in water. Then, α_{12c} and K_{z2} can be obtained by best-fitting model results against experimental data. The values of these coefficients thus obtained are given in Tables 8.1, 8.2 and 8.3.

When resuspension occurs, dye release is affected by sediment entrainment and associated pore water release. The fraction of entrained sediment and released pore water that is exchanged, fr, is obtained by calibrating the modeling results against data from Tests 2-2, 2-3, 3-2, 4, 5-1, 6-1 and 6-3.

Comparisons between model results and experimental data for depth-averaged dye concentration variation with time are shown in Figs. 8.6 through 8.11. Model simulated dye profiles and measurements are shown in Appendix B.

From Figs. 8.6 through 8.11 it is seen that, in contrast with suspended sediment, the depth-averaged dye concentrations in water are generally far from attaining equilibrium values, because the settling rate of dye is zero. Thus, for example, comparing Fig. 8.3 and Fig. 8.9, suspended sediment reaches an equilibrium value after about 4 hours of wave action, whereas after 11 hours of wave action the dye concentration is still far from its equilibrium value, as observed from the tendency of continued increase of dye concentration. Note that for the dye, an equilibrium state can only be reached when the concentrations in water and mud are equal, which may occur over a time-scale that is considerably greater than that over which sediment equilibrium occurs.

From Tests 2-4, 3-3, 5-3 and 6-2 it is observed that when there was no wave loading the dye concentration did not decrease unlike sediment, but remained practically constant. This was because the settling velocity of dye was zero, and dye release flux from the bottom sediment was practically arrested with negligible molecular diffusion, once wave motion stopped.

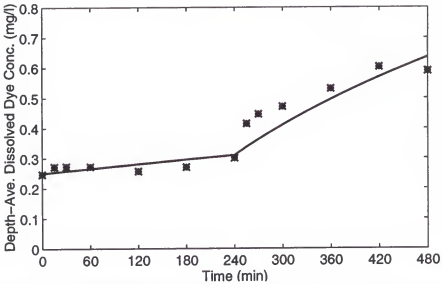

Figure 8.6 Comparison between simulated and measured depth-averaged dye concentrations in Test 1. Solid line represents model simulation results and asterisks are measured data.

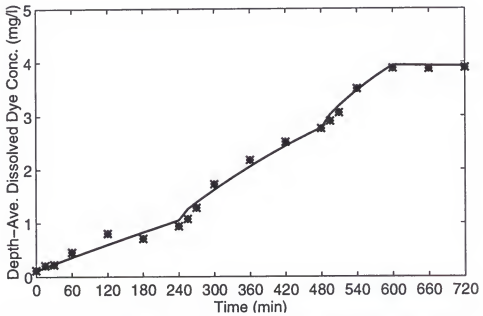

Figure 8.7 Comparison between simulated and measured depth-averaged dye concentrations in Test 2. Solid line represents model simulation results and asterisks are measured data.

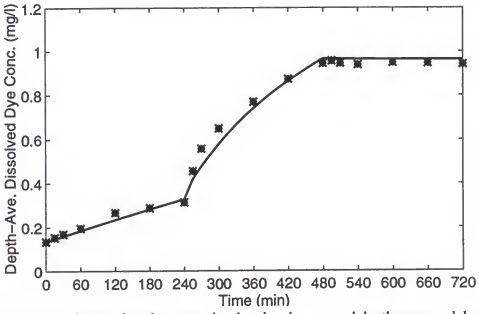

Figure 8.8 Comparison between simulated and measured depth-averaged dye concentrations in Test 3. Solid line represents model simulation results and asterisks are measured data.

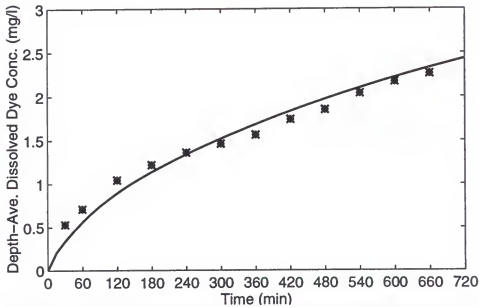

Figure 8.9 Comparison between simulated and measured depth-averaged dye concentrations in Test 4. Solid line represents model simulation results and asterisks are measured data.

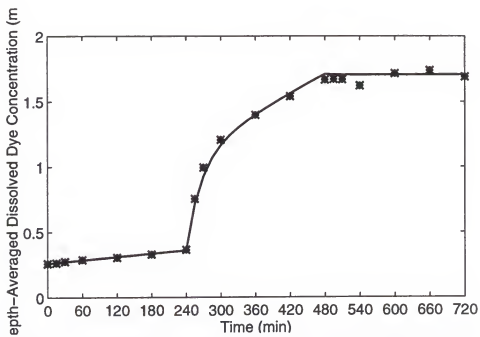

Figure 8.10 Comparison between simulated and measured depth-averaged dye concentrations in Test 5. Solid line represents model simulation results and asterisks are measured data.

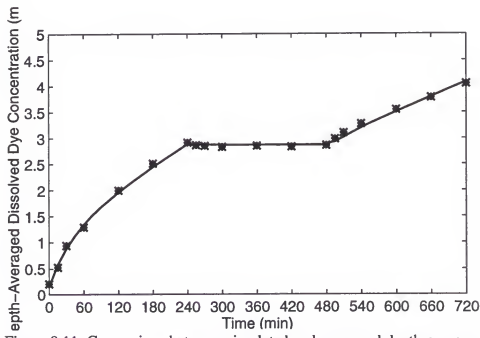

Figure 8.11 Comparison between simulated and measured depth-averaged dye concentrations in Test 6. Solid line represents model simulation results and asterisks are measured data.

8.3 Analysis and Discussion

8.3.1 Release Flux and Sub-fluxes

By calibrating the contaminant transport model developed in Chapter 6 against the experimental data, the bottom dye release flux and its components, i.e., the sub-fluxes, can be obtained. The total release flux, F, and sub-flux variations with time during the experiments are shown in Figs. 8.12, 8.13, 8.14, 8.15, 8.16 and 8.17 for Tests 1, 2, 3, 4, 5 and 6, respectively. Since during the static settling stage, i.e., in Tests 2-4, 3-3, 5-3 and 6-2, the release flux is only due to molecular diffusion that can be neglected for the time-scale of the experiments, these stages have not been plotted.

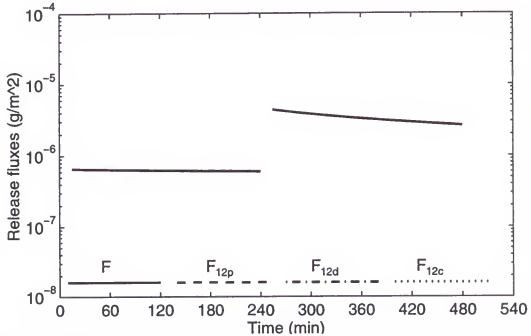

Figure 8.12 Dye release flux and sub-fluxes in Tests 1-1 (0~240 min) and 1-2 (240~480 min).

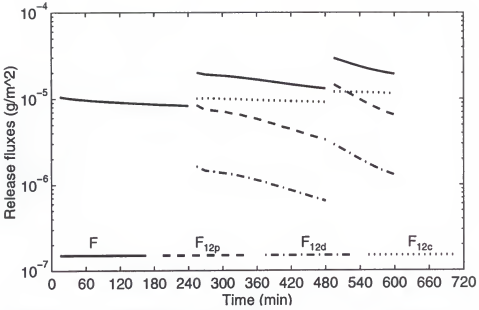

Figure 8.13 Dye release flux and sub-fluxes in Tests 2-1(0~240 min), 2-2 (240~480 min) and 2-3 (480~600 min).

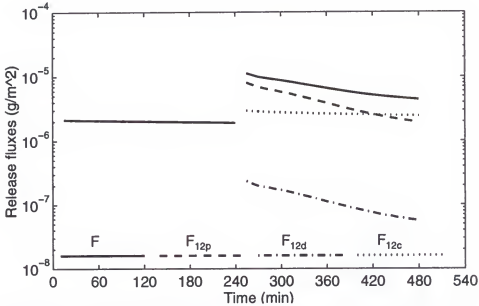

Figure 8.14 Dye release flux and sub-fluxes in Tests 3-1 (0~240 min) and 3-2 (240~480 min).

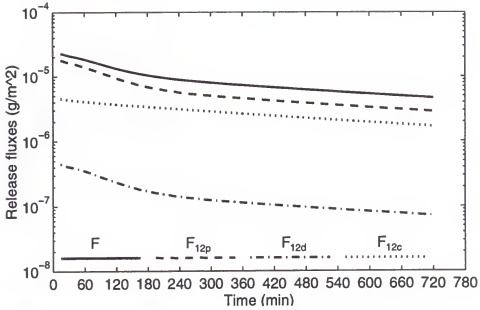

Figure 8.15 Dye release flux and sub-fluxes in Test 4 (0~720 min).

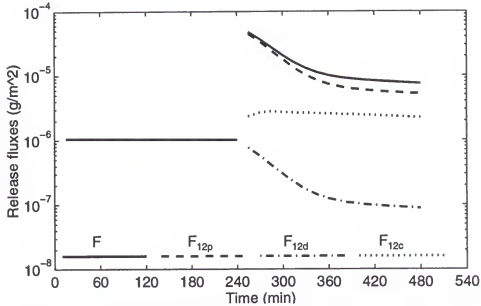

Figure 8.16 Dye release flux and sub-fluxes in Tests 5-1(0~240 min), 5-2 (240~480 min) and 5-3 (480~600 min).

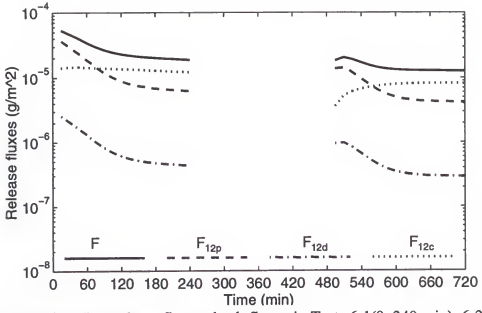

Figure 8.17 Dye release flux and sub-fluxes in Tests 6-1(0~240 min), 6-2 (240~480 min) and 6-3 (480~600 min).

Since in Tests 1-1, 1-2, 2-1, 3-1 and 5-1 there was no significant sediment resuspension, the total dye releasing flux, F, was equal to the direct convection flux, F_{12c}, neglecting molecular diffusion. On the other hand, during Tests 2-2, 2-3, 3-2, 4, 5-2, 6-1 and 6-3, in which bottom sediment was resuspended by waves, F was equal to the sum of the direct convective flux, F_{12c}, the indirect convective flux, F_{12d}, and the particle-bound flux, F_{12p}.

In Figs. 8.13 through 8.17, the indirect convective flux is seen to be an order of magnitude less than the particle-bound flux, F_{12p}, and the direct convective flux, F_{12c}. The difference between the F_{12d} and F_{12p} depends on the rates of sediment resuspension and pore water release, and also on the constituent sorptive capacity of the sediment. The greater the sorption, the larger the difference between F_{12d} and F_{12p}. Thus, for example, the order from high to low for the distribution coefficient, K_d, is: Rhodamine B onto AK mud 0.159,

Rhodamine B onto kaolinite 0.083, Erioglaucine A onto AK mud 0.039, and finally Erioglaucine A onto kaolinite 0.032. As a result, the difference between F_{12d} and F_{12p} for Test 5 (Fig. 8.16) is greatest, in which Rhodamine B and AK mud were used. The second highest difference is that for Tests 3 and 4 (Fig. 8.14 and 8.15) is, in which Rhodamine B and kaolinite were used. Test 6 (Figs. 8.17) is the third, in which Erioglaucine A and AK mud were used, and the least difference is that in Test 2 (Fig. 8.9), in which Erioglaucine A and kaolinite were used.

Comparing the direct convective flux, F_{12c}, with the particle-bound flux, F_{12p}, it must be noted that F_{12p} can become dominant when the rate of sediment resuspension is high and/or the constituent is significantly sorbed onto sediment. On the other hand, F_{12c} may be dominant when the rate of sediment resuspension is low, and/or there is less sorption of the constituent onto sediment. Thus, in general, the relative degree of importance of F_{12p} is of the same order as the sorptive tendency of the constituent onto sediment. For example, the order from high to low significance of F_{12p} in the total flux, F, is Test 5 (Fig. 8.16), Tests 3 and 4 (Figs. 8.14 and 8.15), Test 6 (Fig. 8.17) and finally Test 2 (Fig. 8.13). By comparing Test 2-2 with Test 2-3 (Fig. 8.13) and Test 3-1 (Fig. 8.14) with Test 4 (Fig. 8.15), we find that for the same constituent and sediment, the more the sediment is resuspended, the more the dominance of F_{12p}, e.g., F_{12p} is more dominant in Test 2-3 than in Test 2-2, and also in Test 4 than in Test 3-2. It must be noted that the relative importance of F_{12p} and F_{12c} shown above is based on the experimental results in laboratory. In the field, their relative importance will depend on the site-specific hydrodynamic conditions and sediment and contaminant properties.

From Figs. 8.12 through 8.17, we note that all the release fluxes decreased in each phase under waves, because the concentration difference between water and fluid mud decreased with release. Eventually, as can be expected, the release flux would become zero when the dye concentrations in water and in fluid mud become equal at equilibrium. The only exception to the above trend is Test 6-3, in which the fluxes increased at the beginning and then decreased. The reason is that in Test 6-2, sediment that settled onto fluid mud had a relatively low particulate constituent concentration. Thus, the relatively highly contaminated fluid mud was covered by a thin, about 0.01 mm, sediment layer of low dye concentration. The dye release process was delayed by this thin layer, which caused the initially relatively low release fluxes.

8.3.2 Effects on Release Sub-fluxes

The characteristic coefficients related to the direct convection flux, F_{12c}, are: (1) diffusivity in water, K_{z1} (Eq. 6.7), (2) wave bottom boundary coefficient, α_{12c}, (Eqs. 6.37 and 6.39) and (3) mud diffusivity, K_{z2} (Eq. 6.8). The characteristic coefficients related to the indirect convective and particle-bound fluxes are: (1) diffusivity in water, K_{z1}, (2) mud diffusivity, K_{z2}, and (3) the sediment and pore water entrainment rate, E_r, and exchange fraction, fr (Eq. 6.14). A schematic representation of these coefficients is given in Fig. 8.18.

Diffusivity in water, K_{z1}.

The role of K_{z1} is related to the transport of upward released constituent from the near-bottom region. Therefore, the greater the magnitude of K_{z1}, the faster the rate at which the constituent will be transported away from the near-bottom region, and therefore the greater will be the bottom release fluxes, F_{12c}, F_{12d}, and F_{12p}, because these fluxes are

proportional to the concentration difference across the mud-water interface according to Eqs. 6.9 and 6.30.

The constituent diffusivity in water is assumed to be the same as that for suspended sediment, because wave-induced diffusion in water is basically a characteristic of eddy diffusion due to turbulence, for which the mass diffusivities of constituent and sediment are commonly assumed to be equal to the momentum diffusivity. The diffusivity, K_{z1}, is affected by wave characteristics and mud rheological properties as discussed in Chapter 4, and is determined by best-fitting measured suspended sediment data.

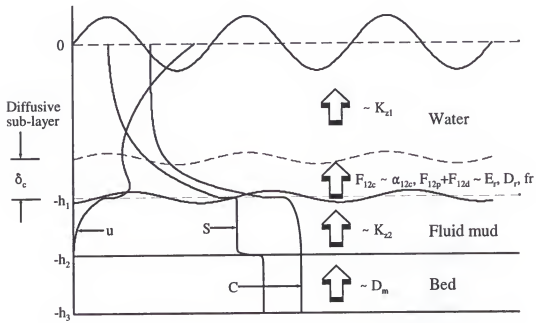

Figure 8.18 Schematic shown characteristic profiles and coefficients related to release fluxes. u is the particle velocity under wave motion, S is sediment concentration, C is constituent concentration, δ_c is the diffusive sub-layer thickness at water bottom, E_r and S_r are entrainment and deposition rate of sediment and D_m is the molecular diffusivity. Arrows indicate directions of constituent release.

Bottom diffusive coefficient, α_{12c}.

From Eqs. 6.37 or 6.39, it is seen that the direct convective flux, F_{12c}, is proportional to α_{12c}, which thus controls the convective flux across the mud-water interface. In the experiments, the bottom Reynolds Number, $Re_b = u_b a_b / \nu_1$, was in the range of 100 ~ 3,600, where u_b is the maximum wave-induced horizontal velocity just outside the bottom boundary layer for wave over a rigid bottom, and a_b is the corresponding amplitude of wave-induced horizontal excursion. Considering the median particle size of bottom sediment, 1.10 μm and 0.86 μm for kaolinite and attapulgite (Feng, 1992), respectively, and according to Dean and Dalrymple (1991), it can be shown that the bottom boundary layer was viscous throughout. Thus, Eq. 6.39 can be used as a special case of Eq. 6.37 for viscous boundary layer condition. For Eq. 6.39, the Schmidt Number is taken to be 1,000, a characteristic value for the sublayer (Berner, 1980).

The Reynolds Numbers for determining the bottom boundary layer condition were calculated by assuming a rigid bottom. This was the case because although, in general, soft bottom amplitudes of the horizontal velocity and excursion just outside the boundary layer can be different from those obtained by assuming a rigid bottom, the actual differences were found to be small according to calculations using the wave-mud interaction model of Jiang (1993). Another reason for using Re_b was that the criterion to assess the bottom wave boundary layer is based on rigid bottom calculations and relative bottom roughness by previous investigators, e.g., Kamphuis (1975).

As a result of the occurrence of a viscous boundary layer, Eq. 6.39 is used in the model to calculate the convective flux, F_{12c}. By best-fitting the model results against the experimental data, the relationship between α_{12c} and Ri_w was obtained as

$$\alpha_{12c} = 0.008 + 0.0017 Ri_\delta^{-0.75} \tag{8.1}$$

which is plotted in Fig. 8.19. Noted that Test 1 was a preliminary experiment, data from this test have not been included.

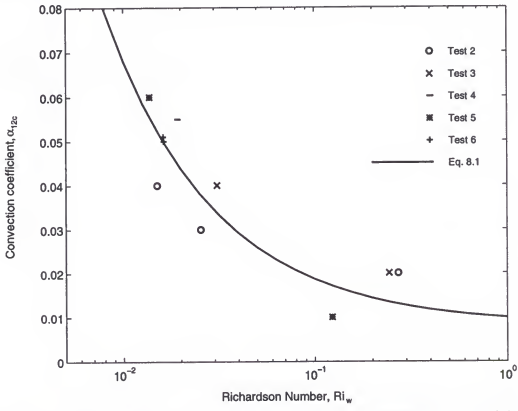

Figure 8.19 Relationship between the direct convective flux coefficient, α_{12c}, and the bottom boundary layer Richardson Number, Ri_w.

At $Ri_w \to \infty$, $\Delta u = 0$, and $\alpha_{12c0} = \alpha_{12c}|_{\Delta u = 0} = 0.008$ is obtained from Eq. 8.1. α_{12c0} is the constant mass transfer coefficient excluding the effects of surface enlargement and

replenishment due to wave action. Therefore, the ratio of $r_\alpha = \alpha_{12c}/\alpha_{12c0}$ can be defined as the effect of surface enlargement and replenishment on mass transfer across the boundary layer. Thus, for example, from Test 5-2 under wave height of H = 6 cm and period T = 1 s we obtain r_α = 7.5, which means that the release flux across the mud-water interface was amplified by 7.5 times due to wave-induced disturbance.

It must noted that Eq. 6.39 is a special case of Eq. 6.37, and is obtained based on the assumption that the bottom boundary layer is viscous. Also, in Eq. 8.1, obtained from calibrating the model against experimental data, should be considered as only suitable for the viscous boundary layer condition

However, in the derivation of Eq. 6.37, no boundary layer condition was specified, so that this equation is suitable for all boundary layers, i.e., viscous, transitional and fully turbulent. For the turbulent and transitional boundary layers, the Prandtl and von Karman analogies (Welty et al., 1969) are needed to specify the relationship such as Eq. 6.39. Also, further larger scale experimental studies with turbulent and transitional bottom boundary layers are required to obtain the relation $\alpha_{12c} = f''(Ri_w)$.

Diffusivity, K_{z2}, in fluid mud

The magnitude of K_{z2} determines the transport rate of the constituent in fluid mud toward the mud-water interface (Fig. 8.18). The greater the K_{z2}, the faster the rate at which the constituent is transported toward mud-water interface, and therefore the greater the bottom release fluxes, F_{12c}, F_{12d}, and F_{12p}, because as noted earlier these fluxes are proportional to the concentration difference across the mud-water interface according to Eqs. 6.9 through 6.14.

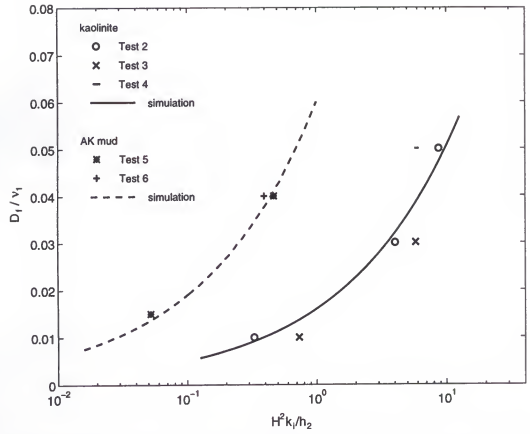

Figure 8.20 Relationship between dimensionless diffusivity in fluid mud, D_f/v_1, and the dimensionless wave damping parameter, $H^2k_i/(h_2-h_1)$.

According to the derivation in Chapter 6, K_{z2} is expressed by Eq. 6.30, in which the dimensionless wave-induced diffusion in fluid mud, D_f/v_1, is be a function of $H^2k_i/(h_2-h_1)$. From the experimental results, this relationship can be expressed as

$$\frac{D_f}{v_1} = \alpha_{z2}\sqrt{\frac{H^2k_i}{h_2-h_1}} \tag{8.2}$$

where the coefficient $\alpha_{z2} = 0.016$ for kaolinite and $\alpha_{z2} = 0.06$ for AK mud, as shown in Fig. 8.20. Here, the wave height, H, and fluid mud depth, h_2, are obtained from observations

during the experiments. The wave damping coefficient, k_i, was obtained from the wave-mud interaction model of by Jiang (1993), while the wave-induced diffusivity, D_f, was obtained by best-fitting the model simulation results against experimental data.

From Fig. 8.20, note that since the wave-induced diffusivity in fluid mud, D_f/v_1, is observed to be proportional to $[H^2k_i/(h_2-h_1)]^{1/2}$, D_f is proportional to the momentum transport rate in fluid mud, which in turn is proportional to the square root of the energy dissipation rate per unit mud volume, $[\overline{\epsilon_D}/(h_2-h_1)]^{1/2}$, as noted in Chapter 6. Due to the gelling property of the thixotropic AK mud, and possibly because of increased turtuosity of the plate-and-needle particle mixture of AK mud relative to plates alone in kaolinite, diffusion through AK mud is seen to be considerably lower than in kaolinite.

Since D_f is on the order of 10^{-8} (m^2/s), which is 100 ~ 1,000 times greater than effective molecular diffusivity, $\omega_0 D_m$, molecular diffusion can be negligible in fluid mud. As a result, the Schmidt Number of fluid mud, Sc_f, is on the order of 100, while the Schmidt Number of constituent in water, Sc, is usually on the order of 1,000 for most constituents (Boudreau and Guinasso, 1982).

E_r and f_r.

The entrainment flux of sediment, E_r, directly affects the particle-bound flux of the constituent. The greater the bottom sediment resuspension, the greater the particulate constituent release by its transport together with the suspended sediment. Once the suspended sediment in water reaches its equilibrium state, which means that the net resuspension flux is zero, as noted in Chapter 6, particle-bound flux continues to occur

because significant exchange of sediment continues, as reflected by $fr \cdot \min[E_r, D_r]$. Therefore, the greater the fraction, fr, the greater the particle-bound flux.

Since pore water is entrained together with sediment, the greater the E_r, the greater the indirect convective flux. The greater the fraction, fr, the greater the exchange of water between pore water and water layer, and therefore, the greater the indirect convective flux.

Due to the partial return of entrained sediment and water in the interfacial zone, the net release of the constituent to the ambient water column tends to be a comparatively very small fraction of the gross rate of entrainment. The ratio of net to gross entrainment, 1-fr, was found to range from 0.02 to 0.06.

Finally, it should be noted that the return fraction of entrained sediment in the interfacial zone should also depend on the wave conditions. In the field situation, since waves are usually more severe and the bottom wave boundary layer is characteristically turbulent, more entrained sediment is likely to be ejected into water column. Thus, the return fraction of entrained sediment in the field may be much lower than that in the laboratory.

8.4 Summary and Conclusions

Contaminant release from bottom mud under wave loading has been investigated through laboratory experiments and mathematical modeling. Since constituent release is significantly related to sediment transport, a mud bed fluidization model under wave loading and a sediment transport model were developed. Both the bed fluidization model and the sediment transport model have been used to simulate laboratory results, and have also been applied to field data. Laboratory experiments were carried out to determine the sorption

kinetics of dyes used as contaminant surrogates in the experiments, and flume experiments for dye release under wave loading were carried out and the results were used to calibrate the developed constituent transport model to obtain the wave-modulated release fluxes. In general, the total release flux was found to be greatly enhanced by waves.

For calculating the equilibrium fluid mud thickness, the bed, assumed to be a single-phase continuum characterized as a uniaxial extentional-Voigt model, is represented by an equivalent spring-dashpot-mass system. The necessary bed rheological parameters are obtained from shear rheometry. The thickness of the fluidized mud layer at equilibrium is determined by considering the balance of vertical forces, i.e., inertia force due to bed vibration under wave action and the effective weight of a cohesive particle (or floc). Comparison between calculated and laboratory measured mud fluidization thicknesses indicates an order of magnitude agreement. The application of this model to Lake Okeechobee, Florida, gives a reasonable estimate of fluid mud thickness found in that lake.

The sediment model derived in Chapter 4 incorporates the effect of wave-mud interaction by characterizing sediment exchange between water and bottom sediment through appropriate entrainment and settling functions. The formula for the rate of entrainment under waves is determined from experimental results. The model successfully simulates laboratory experimental results of Maa (1986) for bottom sediment resuspension. With reference to application to field, i.e., coast of Louisiana, the model simulates suspended sediment concentrations during the frontal and post-frontal periods of a winter cold front. For the southwest coast of India, where transitory mudbank occurs, suspended sediment

concentrations in the coastal area before mudbank formation, during mudbank formation and at the time of mudbank dissipation are well simulated by the model.

In Chapter 5, a contaminant (constituent) transport model is developed in the three-layered water-fluid mud-bed system. By considering fluid mud separated from the bed layer, wave-fluid mud interactions and the rheological and transport properties of fluid mud are incorporated distinctly from those for the bed. Constituent release fluxes from bottom are categorized as direct flux, including molecular and convection fluxes, and indirect fluxes, including indirect convective flux and particle-bound flux.

Molecular diffusion always occurs, while the other three fluxes only occur under external forcing, e.g., waves. The expression for the mass transfer coefficient, K_{12c}, of the direct convective flux is obtained through a dimensional analysis. When the bottom boundary layer is viscous, this expression can be simplified to a Chilton-Colburn type relationship for constituent mass transport. The interfacial coefficient, α_{12c}, is found to be related to the interfacial Richardson Number, Ri_w. The indirect convective and particle-bound fluxes are related to the sediment entrainment and deposition fluxes, which are obtained from the sediment transport model. Due to the partial return of entrained sediment and water in the interfacial zone, only part of the gross entrained sediment and associated water enter the water column. The ratio of net to gross entrainment can greatly affect both particle-bound and dissolved constituents released from mud. The wave-induced diffusivity in fluid mud, D_f, which determines the rate of supply of the constituent toward the interface, is assumed to be proportional to momentum transport flux, and in turn is related to wave

dissipation in fluid mud due to internal friction. Through a dimensional analysis, D_f, is found to be a function of wave dissipation rate per unit volume of fluid mud.

Sorptive properties of the dyes, i.e., Rhodamine B and Erioglaucine A, onto kaolinite and AK mud are obtained from laboratory experiments. It is found that Rhodamine B is more sorptive than Erioglaucine A, and that AK mud is easier to be sorbed onto than kaolinite. The reasons for these differences have been explained qualitatively in terms of the clay structures and dye molecular structures. The resulting sorption kinetic relationships are incorporated into the contaminant transport model developed in Chapter 5.

In order to obtain the release fluxes, a series of experiments were carried out for four combinations of the dyes and sediments, i.e., Erioglaucine A and kaolinite, Rhodamine B and kaolinite, Erioglaucine A and AK mud, and Rhodamine B and AK mud, under quiescent condition, no sediment resuspension condition and with sediment resuspension.

Finally, by calibrating the contaminant transport model against experimental data the dye release sub-fluxes are obtained for the above dye and sediment combinations. Various effects on release fluxes and their correlations with wave characteristics and mud rheological properties are investigated. The main finding are as follows:

(1) The indirect convective flux, F_{12d}, is generally an order of magnitude less than the convective flux, F_{12c}, and the particle-bound flux, F_{12p}. Both the direct convective flux and the particle-bound flux play important roles for bottom constituent release, and which of the two becomes dominant depends on the sediment entrainment rate and the sorptive property of the constituent.

(2) The wave-induced diffusivity in fluid mud, D_f, is found to be proportional to $[H^2k/(h_2-h_1)]^{4/3}$ (Eq. 8.2) and the coefficient, α_{z2}, is found to vary with sediment composition. In the experimental range considered, D_f is found to be 100 ~ 1,000 times higher than the effective molecular diffusivity, $\omega_b D_m$, which means that in this situation molecular diffusion is negligible.

(3) The mass transfer coefficient, K_{12c}, of the convective flux, F_{12c}, is expressed by Eq. 6.37. For the viscous wave boundary layer, which occurred over the entire range of experimental conditions, Eq. 6.39 can be applied. The mud-water interfacial coefficient, α_{12c}, in Eq. 6.39 is related to the interfacial Richardson Number, Ri_w, according to Eq. 8.2.

(4) The entrainment flux of sediment, E_r, directly affects the particle-bound flux. The fraction of entrained sediment which resettled, fr, also determines the particle-bound and indirect convection flux when the condition of equilibrium of suspended sediment in water is reached. The fraction, fr, was found to be in the range of 0.94 to 0.98, which means that most of the entrained sediment and water did not exchange with ambient water.

8.5 Recommendations for Future Studies

To better understand wave-mud interaction and wave modulation of mud beds, the fluidization mechanism needs to be further investigated. The fluidization model developed in Chapter 3 can only predict the equilibrium fluidization depth. However, fluidization is actually a time-dependant process, and the rheological properties of mud tend to change during this process (Feng, 1992). Also, at present, experimental data on soft bed fluidization are sparse. Thus, further investigations will require accurate experiments with measurements

of pore pressure and mud rheological properties over the mud depth throughout the fluidization process, and a more advanced fluidization model to predict the time-dependent process, including pore pressure build up and mud rheological property variations.

For sediment exchange between water and fluid mud, sediment entrainment has been investigated under waves and currents (Srinivas, 1989) separately. In reality, waves and currents tend to occur together and their interaction is nonlinear (Grant and Madson, 1978). Thus, entrainment under the combined action of waves and currents needs to be studied.

The wave-induced diffusivity in fluid mud, K_{z2}, plays a key role in enhancing bottom contaminant release. However, the present analysis for the mechanism that determines K_{z2} is quite preliminary. Further theoretical and laboratory studies are necessary for characterizing K_{z2}, which must include analyses without the simplifying assumptions made in Chapter 6, and direct measurements of the diffusion in fluid mud.

The mass transfer coefficient, K_{12c}, for the direct convective flux, F_{12c}, and the return fraction of entrained sediment, fr, are only studied for the viscous bottom wave boundary layer. For the transitional and turbulent boundary conditions, further theoretical, laboratory and field scale studies are required. The expression for K_{12c} in the transitional and turbulent regions should include the effects of mud surface roughness, interfacial shape and eddy diffusivity in the boundary layer. The return fraction, fr, may be much lower in the field than that in the laboratory due to the different boundary conditions.

Since currents and waves occur simultaneously very frequently, the effects from current and combinations of current and waves on the mass transfer coefficient, K_{12c}, the diffusivity in fluid mud, K_{z2}, and the return fraction, fr, need to be studied. Also, because

even a weak current can cause relatively strong advective transport compared with waves, the horizontal transport process must be included. Thus, two-dimensional and three-dimensional modeling studies will be necessary.

Contaminant release fluxes have been only calibrated against laboratory data. To apply the modeling effort to the field will require considerable further effort. Firstly, as noted advection of water and fluid mud need to be considered. This is because in the field the horizontal scale is usually quite large or practically unlimited, and advection is often significant for contaminant transport. For example, when the released contaminant in water is removed by advection rapidly, the release flux is greatly enhanced because it is proportional to the concentration difference between water and in the bottom. Also, fluid mud may be transport advectively. Thus, bottom contaminant can be transported from one place to another together with fluid mud. As a result, for field calibration, three-dimensional models may be required, and fluid mud movement under waves and current need to be incorporated in the model. Secondly, in the field there may exist contaminants that react with each other, and sometimes these reactions play significant roles in the release process. Thus, chemical and biochemical reactions need to be considered and included in modeling for field applications. Finally, site-specific sediments must be considered, because different types of sediments and their organic content can affect contaminant release in significant ways.

APPENDIX A
FLUME EXPERIMENTAL DATA

Table A.1 Sediment concentration (g/l) data for Test 1.

Time (min)	Station C (elevation, cm)					Station A	Station B	Station D	Station E
	1.5	3.0	5.0	8.0	13.0				
480	0.000	0.000	0.000	0.000	0.000	0.000	0.000	0.000	0.000
495	1.764	0.524	0.186	0.118	0.068	0.218	0.028	0.218	0.112
510	1.878	1.460	0.664	0.346	0.236	0.984	0.726	0.452	0.132
540	2.318	1.710	1.314	0.998	0.554	1.040	1.052	0.914	0.152
600	2.474	2.186	1.506	1.084	0.800	1.640	1.230	1.144	0.318
660	2.340	1.892	1.378	0.928	0.538	1.506	1.256	1.206	0.442
720	2.166	1.994	1.416	1.050	0.818	1.784	1.308	1.102	0.596

Table A.2 Sediment concentration (g/l) data for Test 2.

Time (min)	Station C (elevation, cm)				Station A	Station B	Station D	Station E
	0.5	2.5	5.5	10.5				
240	0.000	0.000	0.000	0.000	0.000	0.000	0.000	0.000
255	6.636	0.486	0.008	0.000	0.624	0.100	0.236	0.272
270	7.420	0.326	0.044	0.010	8.514	0.122	0.310	0.210
300	7.449	0.520	0.312	0.236	7.200	0.416	0.554	0.276
360	9.581	0.936	0.486	0.380	2.302	0.422	0.456	0.292
420	8.208	0.986	0.502	0.560	1.308	0.352	0.156	0.070
480	9.405	0.866	0.394	0.412	1.476	0.542	0.378	0.302
495	9.970	1.290	0.786	0.646	1.532	0.748	0.684	0.400
510	9.928	1.452	1.004	0.862	1.480	0.932	1.052	0.526
540	9.936	1.682	1.292	1.054	2.468	1.190	1.102	0.674
600	9.928	1.682	1.292	1.054	2.468	1.190	1.102	0.674

Table A.3 Sediment concentration (g/l) data for Test 3, Stations A and B.

Time (min)	Station A (elevation, cm)				Station B (elevation, cm)			
	1.0	3.0	5.0	11.0	1.0	3.0	5.0	11.0
240	0.000	0.000	0.000	0.000	0.000	0.000	0.000	0.000
255	0.074	0.075	0.071	0.070	0.200	0.050	0.040	0.004
270	0.214	0.215	0.214	0.225	0.400	0.154	0.112	0.008
300	0.338	0.320	0.345	0.320	0.508	0.202	0.114	0.060
360	0.495	0.484	0.483	0.492	1.074	0.454	0.356	0.336
420	0.619	0.669	0.636	0.645	0.604	0.578	0.472	0.374
480	0.660	0.616	0.653	0.602	0.614	0.484	0.490	0.462
495	0.814	0.713	0.576	0.473	0.702	0.620	0.510	0.362
510	0.662	0.565	0.490	0.387	0.658	0.575	0.550	0.393
540	0.432	0.375	0.310	0.256	0.613	0.579	0.517	0.293
600	0.317	0.276	0.226	0.185	0.587	0.503	0.302	0.206
660	0.189	0.157	0.130	0.108	0.457	0.404	0.333	0.173
720	0.162	0.142	0.115	0.095	0.352	0.300	0.236	0.130

Table A.3 Sediment concentration (g/l) data for Test 3 (continued), Station C, D and E

Time (min)	Station C (elevation, cm)				Station D (elevation, cm)				Station E (elevation, cm)			
	1.0	3.0	5.0	11.0	1.0	3.0	5.0	11.0	1.0	3.0	5.0	11.0
240	0.000	0.000	0.000	0.000	0.000	0.000	0.000	0.000	0.000	0.000	0.000	0.000
255	0.542	0.370	0.114	0.062	0.376	0.116	0.050	0.008	0.119	0.120	0.113	0.113
270	0.708	0.468	0.270	0.106	0.384	0.230	0.188	0.028	0.139	0.139	0.132	0.139
300	0.786	0.496	0.406	0.102	0.570	0.348	0.224	0.086	0.236	0.248	0.230	0.235
360	1.312	0.552	0.536	0.442	0.912	0.506	0.490	0.446	0.337	0.326	0.336	0.349
420	0.888	0.696	0.644	0.490	0.564	0.556	0.500	0.290	0.413	0.389	0.424	0.418
480	0.792	0.658	0.624	0.540	0.618	0.554	0.410	0.408	0.464	0.468	0.476	0.452
495	0.502	0.468	0.446	0.374	0.534	0.430	0.426	0.352	0.537	0.451	0.386	0.307
510	0.498	0.413	0.419	0.363	0.520	0.430	0.417	0.385	0.468	0.412	0.334	0.276
540	0.463	0.429	0.430	0.295	0.472	0.429	0.412	0.194	0.419	0.358	0.293	0.236
600	0.418	0.339	0.255	0.203	0.404	0.284	0.264	0.200	0.290	0.251	0.209	0.163
660	0.309	0.245	0.219	0.155	0.286	0.236	0.191	0.143	0.188	0.163	0.137	0.108
720	0.224	0.199	0.153	0.079	0.184	0.153	0.119	0.039	0.171	0.144	0.123	0.096

Table A.4 Sediment concentration (g/l) data for Test 4.

Time (min)	Station C (elevation, cm)					Station A	Station B	Station D	Station E
	1.0	2.5	4.5	7.5	12.5				
0	0.000	0.000	0.000	0.000	0.000	0.000	0.000	0.000	0.000
30	2.118	0.164	0.164	0.152	0.150	0.230	0.134	0.410	0.166
60	3.284	0.324	0.296	0.288	0.138	0.308	0.250	0.518	0.318
120	4.490	0.624	0.664	0.594	0.488	0.566	0.382	0.672	0.596
180	2.968	0.836	0.812	0.734	0.646	0.698	0.540	0.760	0.794
240	2.044	0.902	0.882	0.790	0.696	0.710	0.696	0.856	0.774
300	1.732	1.062	0.986	0.928	0.730	0.718	0.564	0.956	0.712
360	0.908	0.754	0.774	0.772	0.724	0.704	0.674	0.840	0.710
420	1.068	1.026	0.996	0.966	0.796	0.762	0.592	0.954	0.776
480	0.798	0.808	0.804	0.772	0.790	0.700	0.642	0.898	0.750
540	0.800	0.830	0.882	0.806	0.852	0.700	0.656	0.934	0.774
600	1.082	1.048	0.914	0.904	0.906	0.694	0.626	0.916	0.714
660	1.052	1.022	0.986	0.928	0.906	0.682	0.668	0.868	0.710

Table A.5 Sediment concentration (g/l) data for Test 5.

Time (min)	Station C (elevation, cm)					Station A	Station B	Station D	Station E
	1.5	3.0	5.0	8.0	13.0				
240	0.000	0.000	0.000	0.000	0.000	0.000	0.000	0.000	0.000
255	1.030	0.315	0.285	0.175	0.165	0.050	0.050	0.090	0.696
270	1.099	0.655	0.545	0.405	0.405	0.160	0.070	0.610	0.815
300	1.155	0.735	0.665	0.605	0.600	0.205	0.110	0.900	1.055
360	1.250	0.830	0.875	0.765	0.760	0.240	0.395	1.070	1.120
420	1.245	1.060	1.080	0.980	0.900	0.260	0.375	1.025	1.132
480	1.285	1.000	1.000	1.015	1.008	0.283	0.390	1.020	1.145
495	1.080	1.085	0.900	0.930	0.275	0.295	0.365	0.870	0.990
510	0.680	0.625	0.610	0.520	0.215	0.285	0.385	0.475	0.650
540	0.425	0.370	0.365	0.340	0.165	0.245	0.325	0.340	0.385
600	0.170	0.185	0.145	0.130	0.000	0.175	0.140	0.140	0.180
660	0.165	0.179	0.155	0.110	0.000	0.075	0.110	0.120	0.160
720	0.145	0.175	0.145	0.090	0.000	0.005	0.110	0.100	0.120

Table A.6 Sediment concentration (g/l) data for Test 6.

Time (min)	Station C (elevation, cm)					Station A	Station B	Station D	Station E
	1.5	3.0	5.0	8.0	13.0				
0	0.000	0.000	0.000	0.000	0.000	0.000	0.000	0.000	0.000
15	1.001	0.252	0.273	0.201	0.174	0.042	0.060	0.088	0.623
30	1.032	0.413	0.425	0.445	0.392	0.123	0.058	0.109	0.854
60	1.134	0.697	0.634	0.609	0.434	0.201	0.127	0.320	0.974
120	1.305	0.792	0.778	0.602	0.592	0.237	0.209	0.803	0.978
180	1.376	0.958	0.902	0.808	0.660	0.287	0.257	0.813	0.963
240	1.291	0.832	0.831	0.815	0.708	0.278	0.333	0.810	0.954
255	1.080	0.985	0.790	0.800	0.254	0.251	0.321	0.680	0.690
270	0.996	0.825	0.810	0.593	0.215	0.285	0.385	0.457	0.325
300	0.725	0.410	0.353	0.230	0.165	0.234	0.353	0.324	0.258
360	0.570	0.358	0.154	0.321	0.013	0.185	0.232	0.214	0.198
420	0.465	0.264	0.166	0.110	0.023	0.081	0.108	0.103	0.086
480	0.345	0.175	0.143	0.090	0.019	0.015	0.113	0.097	0.063
495	1.041	0.325	0.258	0.179	0.156	0.040	0.054	0.090	0.560
510	1.101	0.649	0.554	0.410	0.403	0.136	0.059	0.601	0.651
540	1.146	0.753	0.656	0.625	0.602	0.187	0.107	0.899	0.905
600	1.394	0.732	0.757	0.756	0.658	0.234	0.229	1.080	1.022
660	1.454	0.951	0.876	0.798	0.703	0.226	0.217	1.052	1.013
720	1.439	0.800	0.901	0.703	0.708	0.238	0.179	1.063	1.021

Table A.7 Dye concentration (mg/l) data for Test 1.

Time (min)	Station C (elevation, cm)					Station A	Station B	Station D	Station E
	1.5	3.0	5.0	8.0	13.0				
0	0.251	0.213	0.251	0.251	0.154	0.023	0.023	0.154	0.049
15	0.235	0.208	0.202	0.208	0.208	0.181	0.181	0.181	0.101
30	0.235	0.208	0.208	0.208	0.208	0.181	0.181	0.181	0.101
60	0.235	0.208	0.208	0.208	0.154	0.181	0.181	0.181	0.127
120	0.235	0.181	0.181	0.181	0.154	0.181	0.181	0.181	0.127
180	0.235	0.181	0.218	0.208	0.154	0.181	0.181	0.181	0.127
240	0.245	0.213	0.235	0.218	0.218	0.181	0.181	0.181	0.127
255	0.316	0.322	0.305	0.316	0.256	0.273	0.316	0.251	0.197
270	0.316	0.289	0.322	0.316	0.289	0.316	0.316	0.262	0.235
300	0.344	0.333	0.322	0.322	0.305	0.333	0.316	0.316	0.251
360	0.372	0.399	0.366	0.344	0.372	0.372	0.383	0.383	0.273
420	0.427	0.416	0.427	0.411	0.399	0.372	0.366	0.344	0.316
480	0.427	0.399	0.399	0.372	0.399	0.372	0.372	0.366	0.322
495	0.416	0.416	0.399	0.427	0.372	0.372	0.388	0.399	0.344
510	0.427	0.427	0.399	0.372	0.372	0.327	0.327	0.322	0.316
540	0.372	0.399	0.372	0.372	0.372	0.316	0.316	0.316	0.316
600	0.372	0.372	0.372	0.383	0.372	0.316	0.372	0.372	0.316
660	0.372	0.372	0.372	0.372	0.372	0.316	0.344	0.316	0.316
720	0.344	0.344	0.36	0.366	0.372	0.372	0.344	0.344	0.316

Table A.8 Dye concentration (mg/l) data for Test 2.

Time (min)	Station C (elevation, cm)					Station A	Station B	Station D	Station E
	0.5	2.0	4.0	7.0	12.0				
0	0.075	0.075	0.075	0.075	0.075	0.075	0.075	0.075	0.075
15	0.316	0.112	0.075	0.101	0.075	0.127	0.049	0.372	0.208
30	0.372	0.154	0.101	0.101	0.091	0	0.049	0.427	0.208
60	1.553	1.553	0.684	0.181	0.101	0.023	0.101	0.399	0.181
120	1.445	1.374	1.553	0.372	0.154	0.101	0.262	1.202	0.235
180	3.15	1.481	0.969	0.503	0.262	0.181	0.399	0.684	0.208
240	3.83	1.7	0.937	0.937	0.427	0.316	0.562	0.777	0.262
	Station C (elevation, cm)					Station A	Station B	Station D	Station E
	-	0.5	2.5	5.5	10.5				
255	-	3.665	1.002	0.809	0.562	2.818	0.684	1.002	0.316
270	-	4.482	1.41	0.841	0.654	1.626	2.333	1.775	0.344
300	-	4.807	1.41	1.202	1.339	1.202	1.134	1.929	0.456
360	-	5.448	1.775	1.626	1.626	1.851	1.481	2.007	0.593
420	-	5.448	2.047	1.851	1.79	2.681	1.663	2.047	0.809
480	-	5.154	2.25	2.007	2.007	1.929	1.851	2.007	0.937
	Station C (elevation, cm)					Station A	Station B	Station D	Station E
	-	0.5	2.5	5.5	10.5				
495	-	5.299	2.504	2.087	2.007	2.168	2.047	1.929	1.002
510	-	5.299	2.504	2.209	2.168	2.333	2.25	2.047	1.101
540	-	5.299	2.818	2.504	2.504	2.636	2.592	2.292	1.339
600	-	5.299	3.118	2.868	2.892	2.748	2.636	1.929	1.7
660	-	5.299	3.118	2.868	2.892	2.748	2.636	1.929	1.7
720	-	5.299	3.118	2.868	2.892	2.748	2.636	1.929	1.7

Table A.9 Dye concentration (mg/l) data for Test 3.

Time (min)	Station A (elevation, cm)				Station B (elevation, cm)			
	1.0	3.0	5.0	11.0	1.0	3.0	5.0	11.0
0	0.009	0.009	0.009	0.009	0.009	0.009	0.009	0.009
15	0.009	0.009	0.009	0.02	0.02	0.02	0.032	0.037
30	0.044	0.044	0.032	0.032	0.032	0.044	0.056	0.054
60	0.056	0.056	0.054	0.047	0.032	0.227	0.105	0.081
120	0.13	0.13	0.118	0.113	0.105	0.258	0.245	0.235
180	0.142	0.219	0.203	0.142	0.155	0.285	0.206	0.206
240	0.142	0.219	0.206	0.168	0.168	0.339	0.285	0.232
255	0.206	0.258	0.245	0.245	0.285	0.394	0.366	0.339
270	0.009	0.009	0.009	0.009	0.009	0.009	0.009	0.009
300	0.009	0.009	0.009	0.009	0.009	0.009	0.020	0.020
360	0.044	0.043	0.046	0.044	0.064	0.032	0.032	0.032
420	0.055	0.056	0.055	0.056	0.076	0.054	0.047	0.032
480	0.099	0.100	0.103	0.100	0.130	0.118	0.113	0.105
495	0.140	0.144	0.145	0.142	0.219	0.203	0.142	0.155
510	0.141	0.141	0.141	0.142	0.219	0.206	0.168	0.168
540	0.206	0.208	0.213	0.206	0.285	0.258	0.245	0.245
600	0.250	0.265	0.241	0.253	0.532	0.422	0.361	0.285
660	0.252	0.249	0.249	0.258	0.450	0.394	0.394	0.394
720	0.431	0.458	0.459	0.450	0.600	0.479	0.450	0.417

Table A.9 Dye concentration (mg/l) data for Test 3 (continued).

Time (min)	Station C (elevation, cm)				Station D (elevation, cm)				Station E (elevation, cm)			
	1.0	3.0	5.0	11.0	1.0	3.0	5.0	11.0	1.0	3.0	5.0	11.0
0	0.009	0.009	0.009	0.009	0.009	0.009	0.009	0.009	0.206	0.199	0.210	0.205
15	0.020	0.032	0.037	0.056	0.068	0.056	0.081	0.081	0.180	0.171	0.181	0.180
30	0.094	0.056	0.054	0.054	0.151	0.105	0.081	0.061	0.162	0.162	0.158	0.161
60	0.127	0.105	0.081	0.081	0.209	0.172	0.155	0.105	0.152	0.146	0.157	0.147
120	0.258	0.245	0.235	0.180	0.200	0.180	0.168	0.155	0.135	0.130	0.133	0.132
180	0.285	0.206	0.206	0.180	0.255	0.155	0.155	0.155	0.130	0.135	0.132	0.134
240	0.339	0.285	0.232	0.206	0.268	0.268	0.168	0.168	0.130	0.134	0.128	0.133
255	0.394	0.366	0.339	0.285	0.339	0.298	0.285	0.271	0.206	0.211	0.196	0.208
270	0.529	0.444	0.408	0.311	0.405	0.311	0.311	0.285	0.256	0.254	0.246	0.261
300	0.538	0.508	0.480	0.450	0.422	0.372	0.366	0.366	0.296	0.281	0.297	0.291
360	0.598	0.568	0.479	0.453	0.499	0.465	0.422	0.400	0.358	0.361	0.368	0.342
420	0.638	0.538	0.518	0.450	0.588	0.538	0.508	0.450	0.406	0.407	0.395	0.426
480	0.644	0.614	0.583	0.538	0.538	0.528	0.503	0.450	0.450	0.431	0.430	0.452
495	0.598	0.598	0.568	0.568	0.508	0.514	0.479	0.471	0.473	0.475	0.453	0.449
510	0.583	0.568	0.538	0.523	0.494	0.485	0.465	0.458	0.473	0.468	0.457	0.490
540	0.584	0.569	0.534	0.526	0.491	0.486	0.468	0.452	0.480	0.466	0.491	0.457
600	0.587	0.565	0.539	0.522	0.496	0.484	0.469	0.450	0.472	0.467	0.462	0.466
660	0.590	0.570	0.540	0.529	0.493	0.487	0.463	0.449	0.473	0.479	0.452	0.473
720	0.582	0.567	0.542	0.519	0.497	0.482	0.466	0.445	0.469	0.476	0.468	0.473

Table A.10 Dye concentration (mg/l) data for Test 4.

Time (min)	Station C (elevation, cm)					Station A	Station B	Station D	Station E
	1.0	2.5	4.5	7.5	12.5				
0	0.009	0.009	0.009	0.009	0.009	0.009	0.009	0.009	0.009
30	0.009	0.009	0.009	0.009	0.009	0.009	0.020	0.020	0.020
60	0.044	0.043	0.046	0.044	0.064	0.032	0.032	0.032	0.094
120	0.055	0.056	0.055	0.056	0.076	0.054	0.047	0.032	0.127
180	0.099	0.100	0.103	0.100	0.130	0.118	0.113	0.105	0.258
240	0.140	0.144	0.145	0.142	0.219	0.203	0.142	0.155	0.285
300	0.141	0.141	0.141	0.142	0.219	0.206	0.168	0.168	0.339
360	0.206	0.208	0.213	0.206	0.285	0.258	0.245	0.245	0.394
420	0.250	0.265	0.241	0.253	0.532	0.422	0.361	0.285	0.529
480	0.252	0.249	0.249	0.258	0.450	0.394	0.394	0.394	0.538
540	0.431	0.458	0.459	0.450	0.600	0.479	0.450	0.417	0.598
600	0.561	0.559	0.580	0.568	0.629	0.538	0.511	0.501	0.638
660	0.592	0.610	0.603	0.607	0.629	0.598	0.568	0.551	0.644

Table A.11 Dye concentration (mg/l) data for Test 5.

Time (min)	Station C (elevation, cm)					Station A	Station B	Station D	Station E
	1.5	3.0	5.0	8.0	13.0				
0	0.161	0.127	0.142	0.048	0.039	0.081	0.056	0.180	0.125
15	0.166	0.193	0.085	0.037	0.032	0.083	0.032	0.176	0.122
30	0.220	0.208	0.081	0.070	0.054	0.103	0.082	0.208	0.128
60	0.260	0.202	0.163	0.090	0.056	0.180	0.105	0.233	0.110
120	0.248	0.231	0.185	0.155	0.080	0.239	0.178	0.265	0.128
180	0.311	0.308	0.258	0.219	0.081	0.232	0.232	0.271	0.130
240	0.326	0.305	0.277	0.262	0.108	0.270	0.265	0.298	0.151
255	0.422	0.419	0.391	0.285	0.263	0.450	0.344	0.541	0.372
270	0.724	0.692	0.626	0.485	0.394	0.468	0.511	0.660	0.450
300	0.692	0.676	0.660	0.631	0.595	0.425	0.694	0.730	0.585
360	0.724	0.756	0.730	0.674	0.657	0.550	0.714	0.872	0.732
420	0.792	0.799	0.826	0.679	0.786	0.694	0.768	0.891	0.738
480	0.887	0.856	0.856	0.675	0.783	0.793	0.793	0.950	0.840
495	0.796	0.792	0.789	0.679	0.656	0.839	0.944	0.996	0.927
510	0.824	0.730	0.676	0.670	0.692	0.864	0.869	0.964	0.990
540	0.730	0.730	0.730	0.673	0.724	0.856	0.859	0.964	0.892
600	0.839	0.839	0.786	0.673	0.724	0.792	0.889	0.992	0.930
660	0.819	0.891	0.768	0.670	0.714	0.812	0.890	0.982	0.980
720	0.785	0.785	0.724	0.678	0.679	0.814	0.886	0.995	0.996

Table A.12 Dye concentration (mg/l) data for Test 6.

Time (min)	Station C (elevation, cm)					Station A	Station B	Station D	Station E
	1.5	3.0	5.0	8.0	13.0				
0	0.159	0.119	0.132	0.084	0.041	0.078	0.065	0.172	0.119
15	0.542	0.319	0.312	0.314	0.273	0.124	0.252	0.332	0.227
30	0.844	0.534	0.502	0.497	0.432	0.204	0.523	0.558	0.432
60	1.287	0.743	0.603	0.604	0.593	0.414	0.697	0.738	0.545
120	1.415	0.932	0.93	0.974	0.957	0.889	1.073	1.126	1.054
180	1.595	1.274	1.226	1.279	1.286	1.073	1.224	1.412	1.375
240	1.645	1.584	1.564	1.574	1.556	1.285	1.395	1.684	1.575
255	1.596	1.579	1.475	1.424	1.434	1.326	1.439	1.593	1.559
270	1.624	1.492	1.476	1.445	1.465	1.336	1.428	1.584	1.549
300	1.53	1.53	1.465	1.465	1.434	1.312	1.426	1.61	1.562
360	1.639	1.539	1.435	1.424	1.424	1.335	1.435	1.574	1.573
420	1.619	1.491	1.484	1.464	1.454	1.335	1.425	1.574	1.556
480	1.585	1.485	1.478	1.446	1.475	1.336	1.425	1.603	1.558
495	1.839	1.584	1.545	1.538	1.558	1.403	1.547	1.696	1.529
510	2.158	1.674	1.695	1.75	1.598	1.443	1.618	1.806	1.605
540	2.183	1.698	1.873	1.819	1.803	1.506	1.602	1.827	1.69
600	2.202	1.839	1.876	1.874	1.859	1.657	1.849	2.093	1.786
660	2.374	1.958	1.964	1.964	1.974	1.748	1.958	2.148	1.948
720	2.462	2.03	2.028	2.075	2.075	1.823	2.108	2.283	2.154

Table A.13 Temperature mesurements (°C).

Time (hr)	Test 1	Test2	Test 3	Test 4	Test 5	Test 6
0	18.0	16.0	13.5	13.0	12.0	13.6
1	18.3	16.1	13.8	13.4	12.2	13.8
2	18.5	16.2	14.0	13.7	12.4	14.0
3	19.0	16.5	14.2	14.0	12.6	14.2
4	19.0	16.8	14.5	14.3	12.8	14.4
5	19.2	17.0	14.8	14.6	13.0	14.5
6	19.5	17.0	15.0	14.9	13.3	14.7
7	20.0	17.0	15.3	15.0	13.6	14.9
8	20.0	17.0	15.7	15.3	13.8	15.0
9	20.0	17.0	16.0	15.6	14.0	15.1
10	20.0	17.0	16.0	16.0	14.0	15.2
11	20.0	17.0	16.0	16.3	14.0	15.3
12	20.0	17.0	16.0	16.6	14.0	15.3
Mean	19.3	16.7	15.0	14.8	13.2	14.6

APPENDIX B
SIMULATED AND MEASURED SUSPENDED SEDIMENT
AND DYE CONCENTRATION PROFILES

B.1 Suspended Sediment Profiles

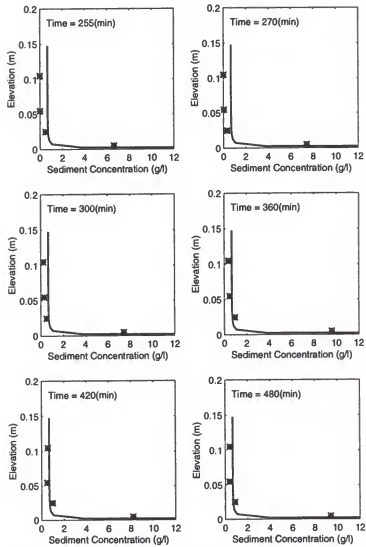

Figure B.1 Comparison between simulated and measured suspended sediment profiles in Test 2-2. Solid line represents model simulation results and asterisks are measured data.

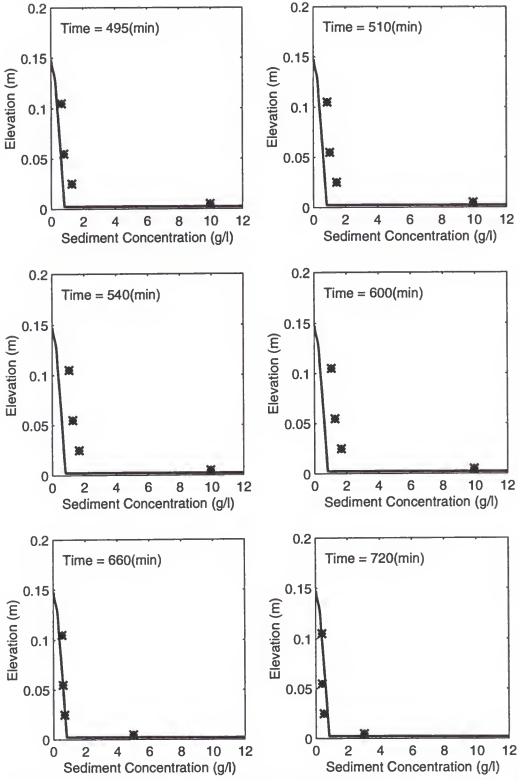

Figure B.2 Comparison between simulated and measured suspended sediment profiles in Test 2-3. Solid line represents model simulation results and asterisks are measured data.

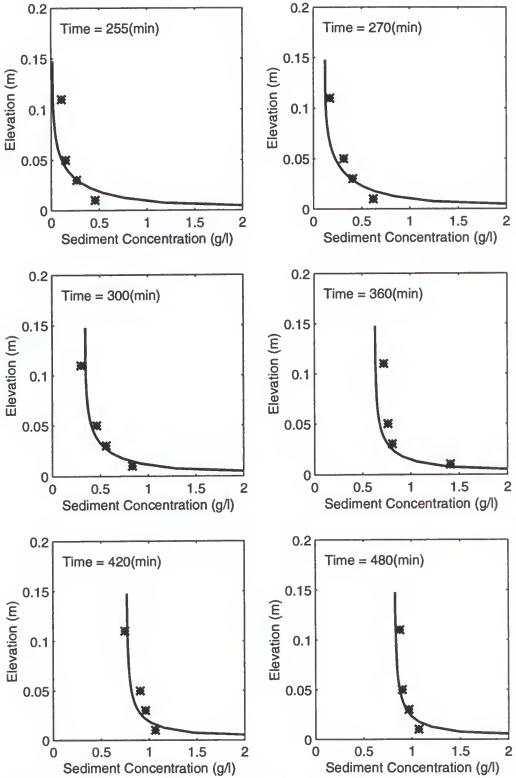

Figure B.3 Comparison between simulated and measured suspended sediment profiles in Test 3-2. Solid line represents model simulation results and asterisks are measured data.

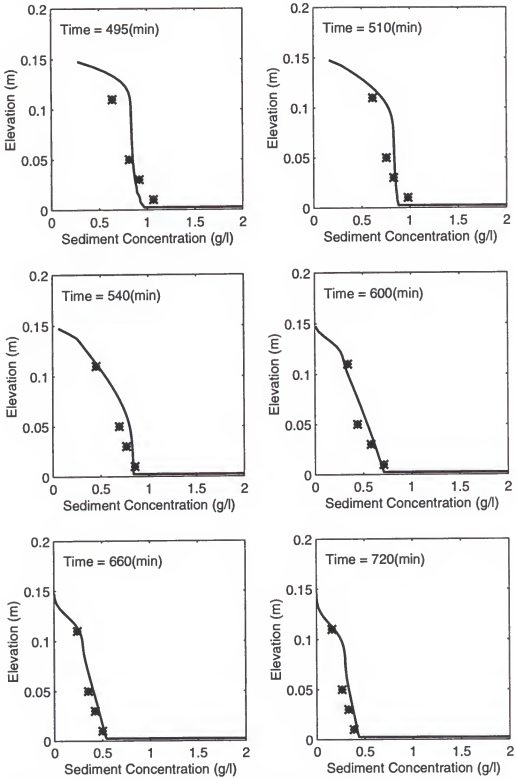

Figure B.4 Comparison between simulated and measured suspended sediment profiles in Test 3-3. Solid line represents model simulation results and asterisks are measured data.

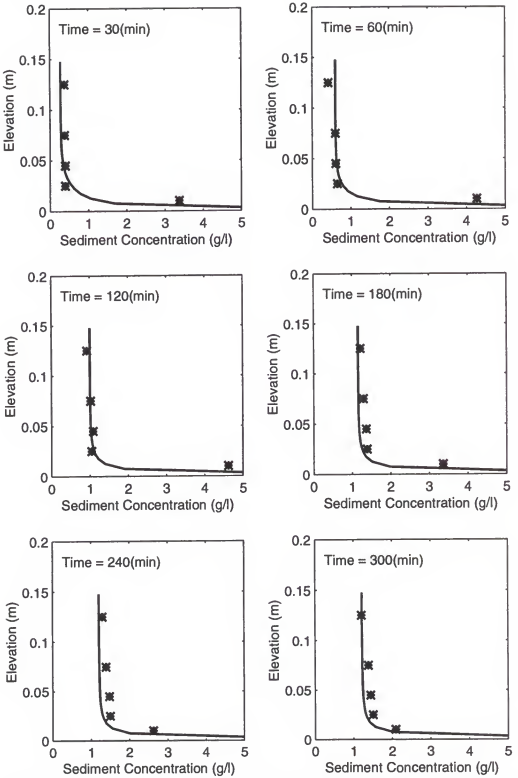

Figure B.5 Comparison between simulated and measured suspended sediment profiles in Test 4-1 during time range of 0 ~ 300 min. Solid line represents model simulation results and asterisks are measured data.

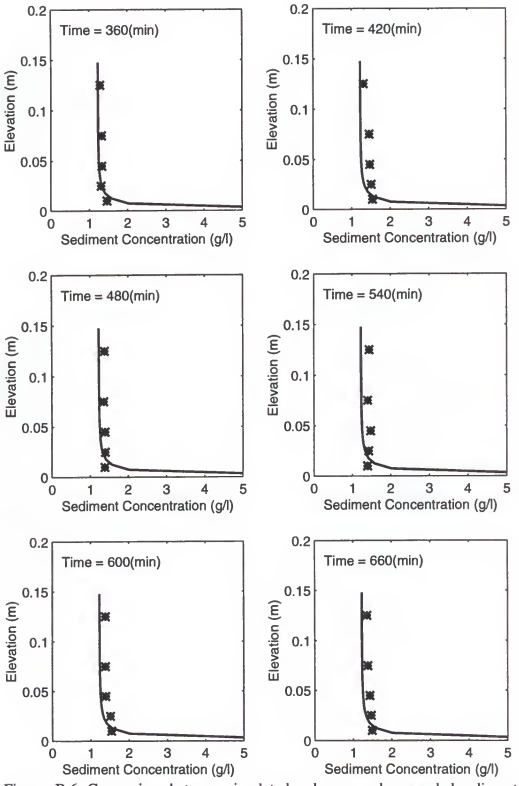

Figure B.6 Comparison between simulated and measured suspended sediment profiles in Test 4-1 during time range of 300 ~ 660 min. Solid line represents model simulation results and asterisks are measured data.

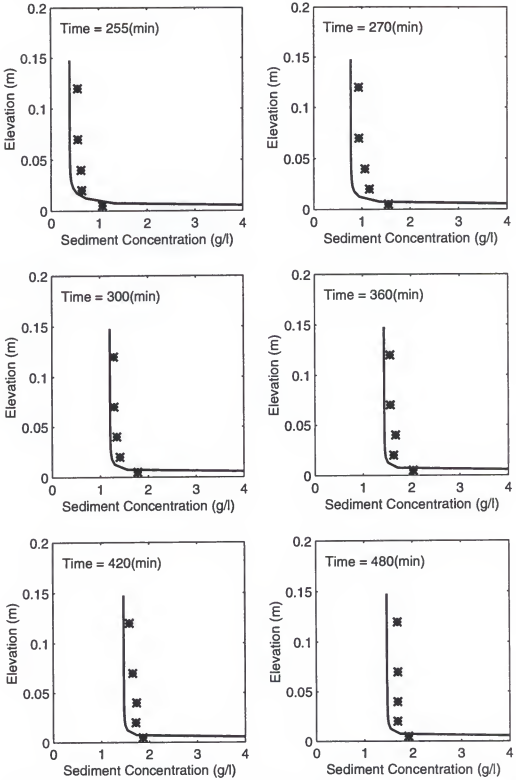

Figure B.7 Comparison between simulated and measured suspended sediment profiles in Test 5-2 during time range of 240 ~ 480 min. Solid line represents model simulation results and asterisks are measured data.

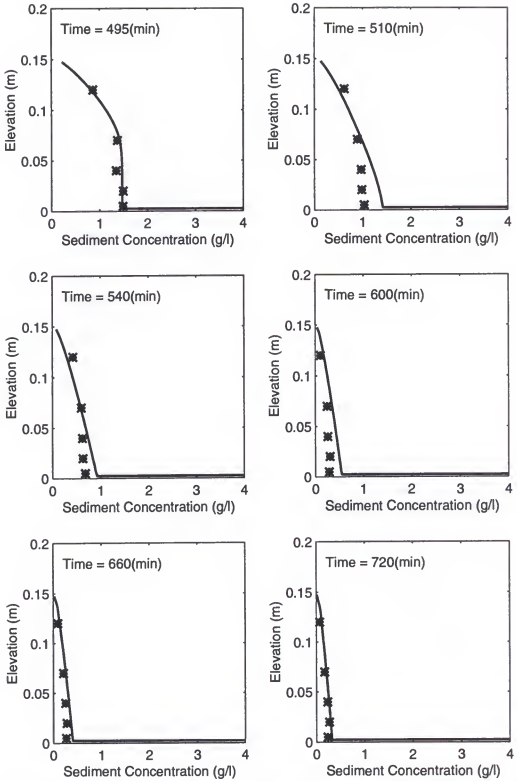

Figure B.8 Comparison between simulated and measured suspended sediment profiles in Test 5-3 during time range of 480 ~ 720 min. Solid line represents model simulation results and asterisks are measured data.

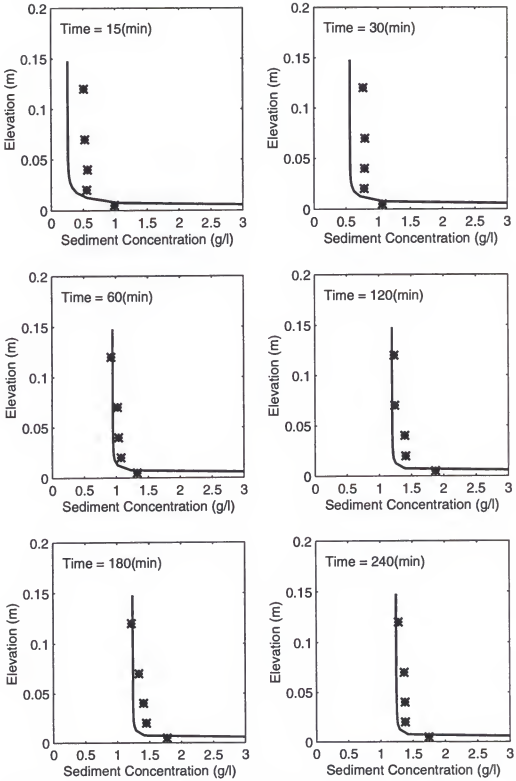

Figure B.9 Comparison between simulated and measured suspended sediment profiles in Test 6-1 during time range of 0 ~ 240 min. Solid line represents model simulation results and asterisks are measured data.

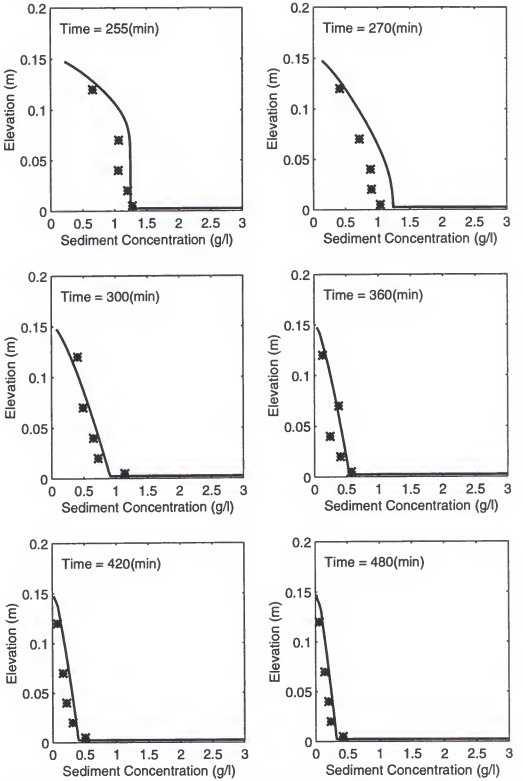

Figure B.10 Comparison between simulated and measured suspended sediment profiles in Test 6-2 during time range of 240 ~ 480 min. Solid line represents model simulation results and asterisks are measured data.

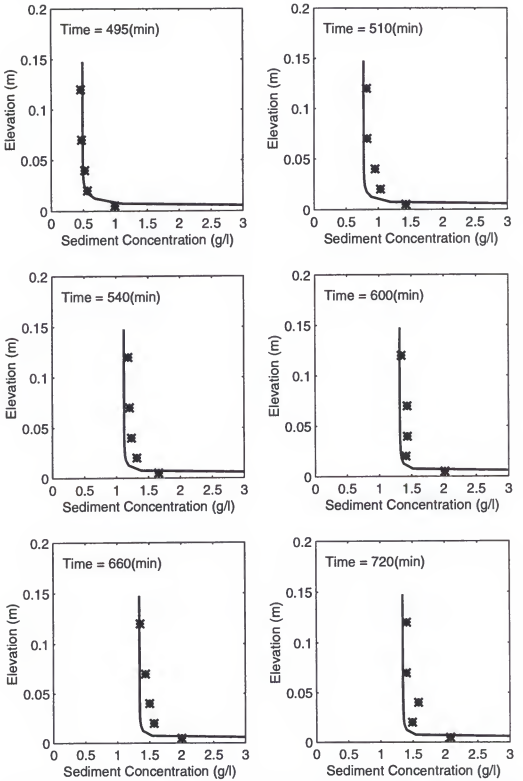

Figure B.11 Comparison between simulated and measured suspended sediment profiles in Test 6-3 during time range of 480 ~ 720 min. Solid line represents model simulation results and asterisks are measured data.

B.2 Dye Concentration Profiles in Water

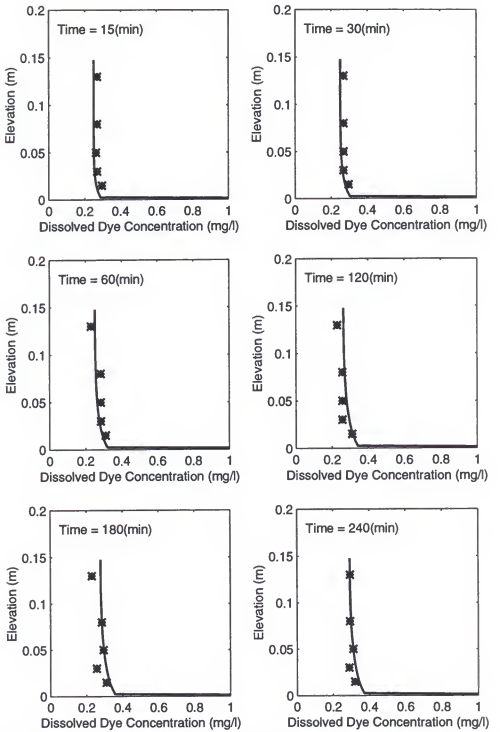

Figure B.12 Comparison between simulated and measured dye profiles in Tests 1-1. Solid line represents model simulation results and asterisks are measured data.

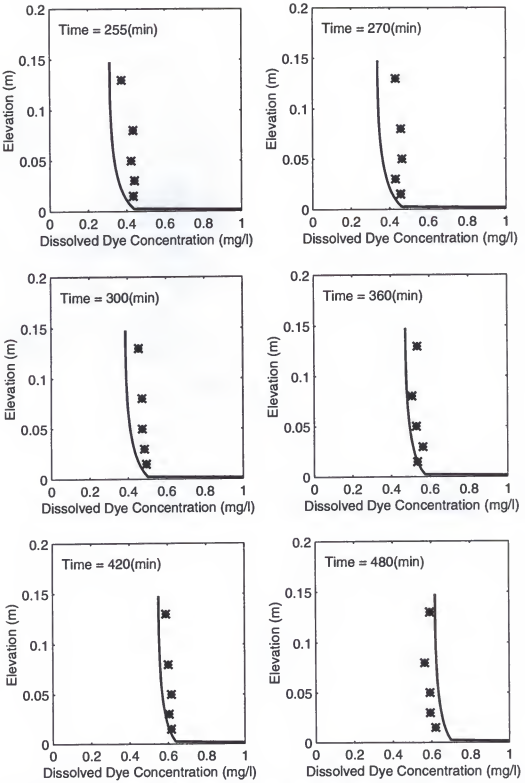

Figure B.13 Comparison between simulated and measured dye profiles in Tests 1-2. Solid line represents model simulation results and asterisks are measured data.

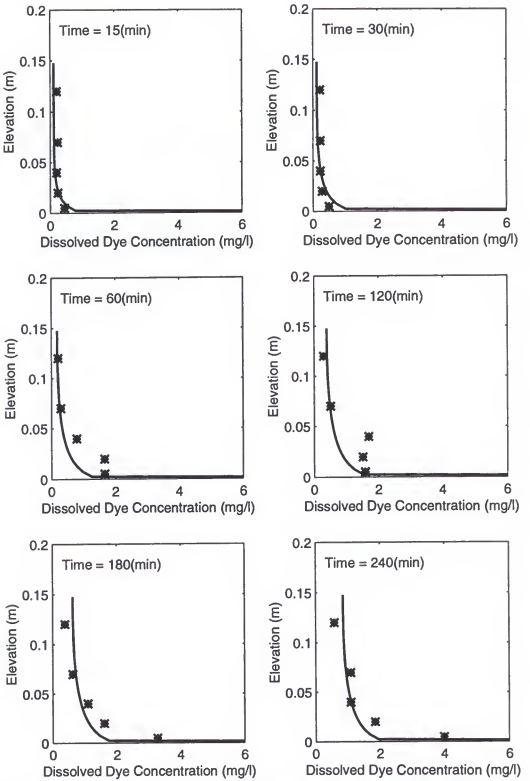

Figure B.14 Comparison between simulated and measured dye profiles in Tests 2-1. Solid line represents model simulation results and asterisks are measured data.

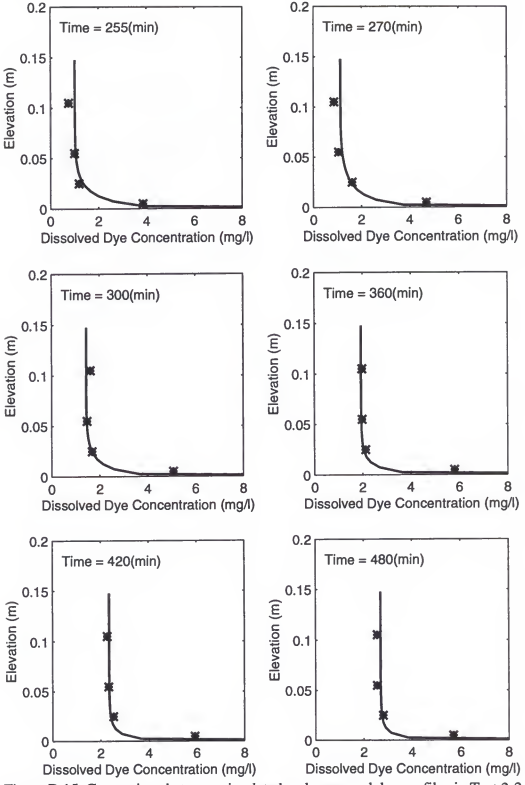

Figure B.15 Comparison between simulated and measured dye profiles in Test 2-2. Solid line represents model simulation results and asterisks are measured data.

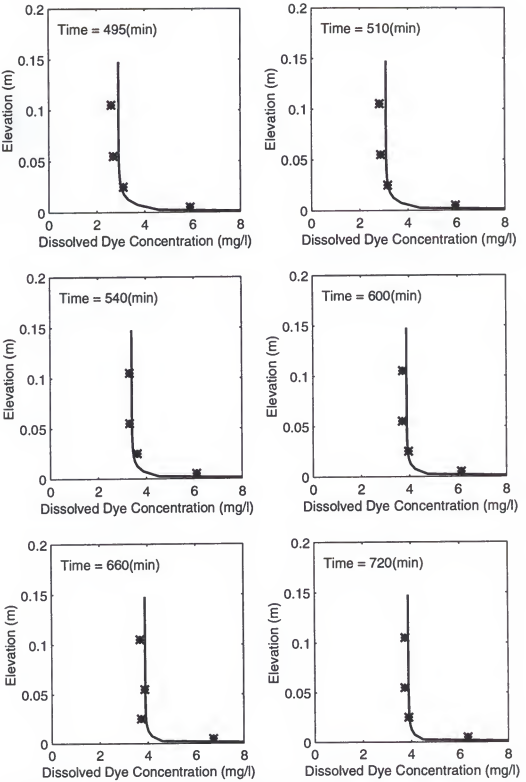

Figure B.16 Comparison between simulated and measured dye profiles in Test 2-3. Solid line represents model simulation results and asterisks are measured data.

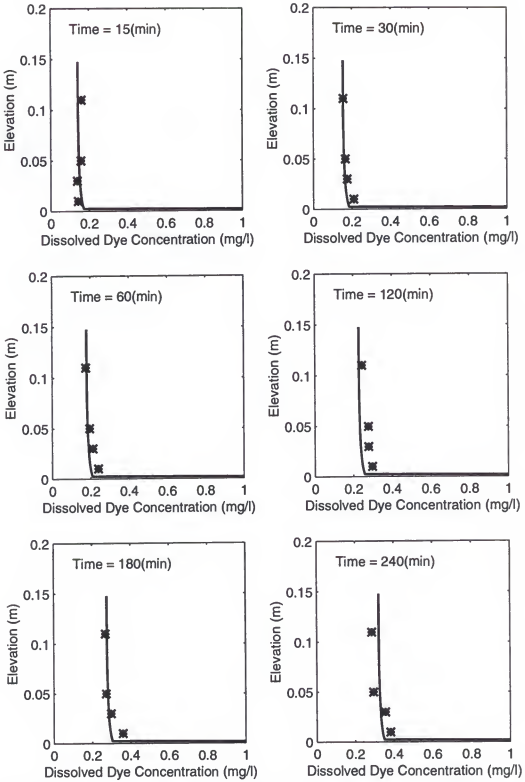

Figure B.17 Comparison between simulated and measured dye profiles in Test 3-1. Solid line represents model simulation results and asterisks are measured data.

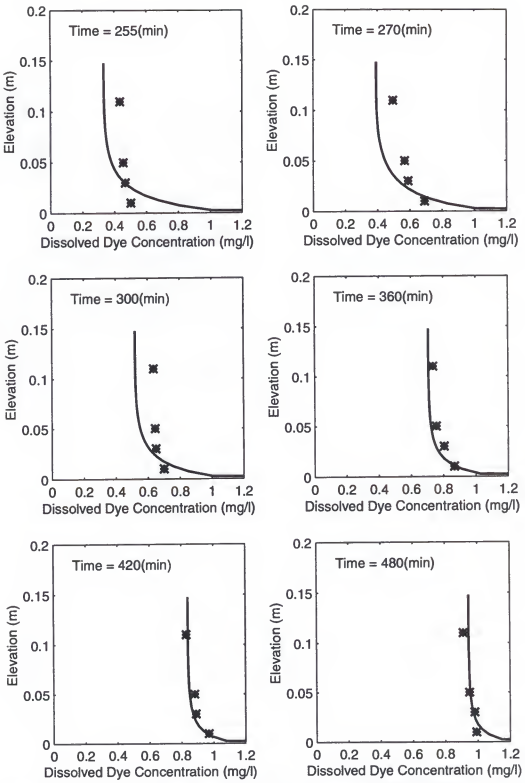

Figure B.18 Comparison between simulated and measured dye profiles in Test 3-2. Solid line represents model simulation results and asterisks are measured data.

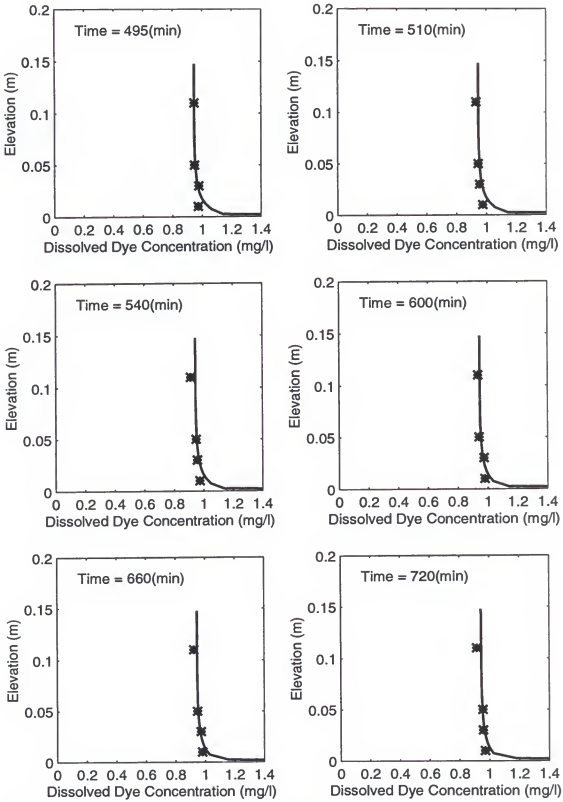

Figure B.19 Comparison between simulated and measured dye profiles in Test 3-3. Solid line represents model simulation results and asterisks are measured data.

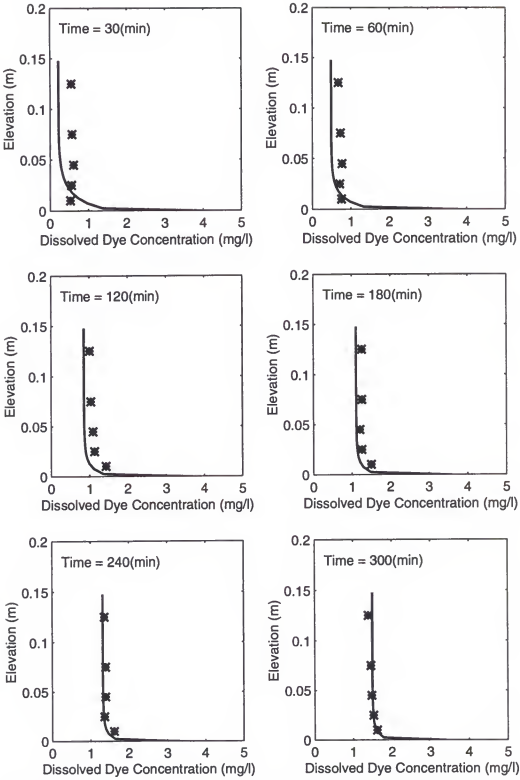

Figure B.20 Comparison between simulated and measured dye profiles in Test 4 during time range of 0 ~ 300 min. Solid line represents model simulation results and asterisks are measured data.

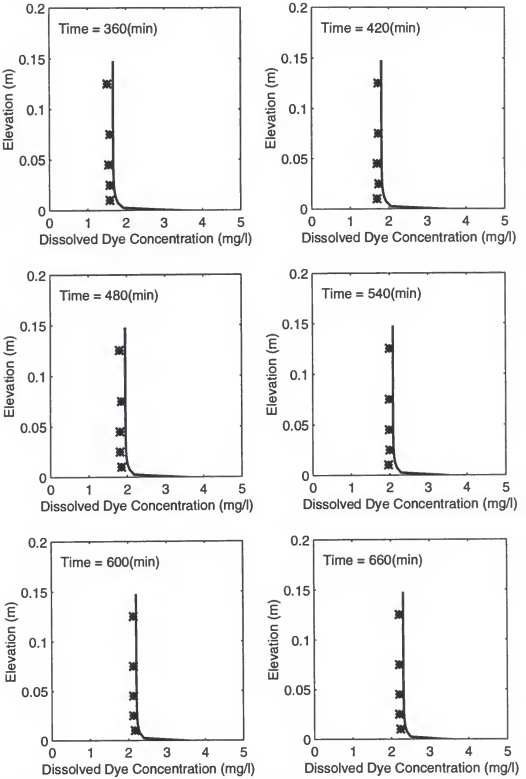

Figure B.21 Comparison between simulated and measured dye profiles in Test 4 during time range of 300 ~ 660 min. Solid line represents model simulation results and asterisks are measured data.

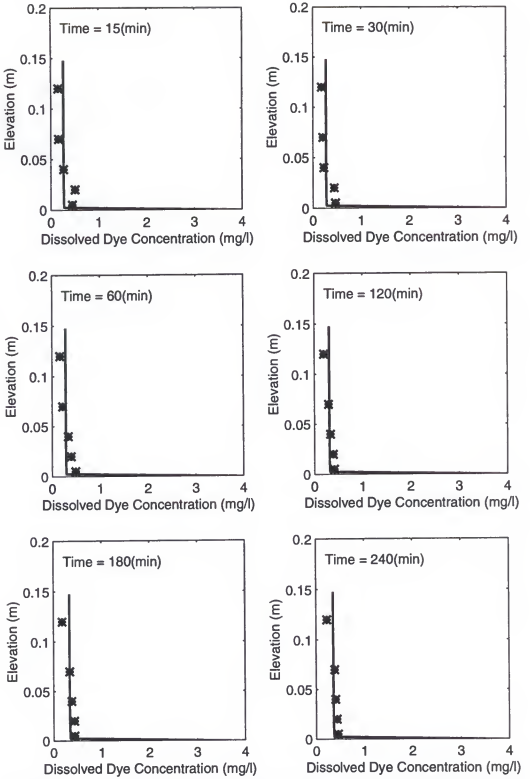

Figure B.22 Comparison between simulated and measured dye profiles in Test 5-1 during time range of 0 ~ 240 min. Solid line represents model simulation results and asterisks are measured data.

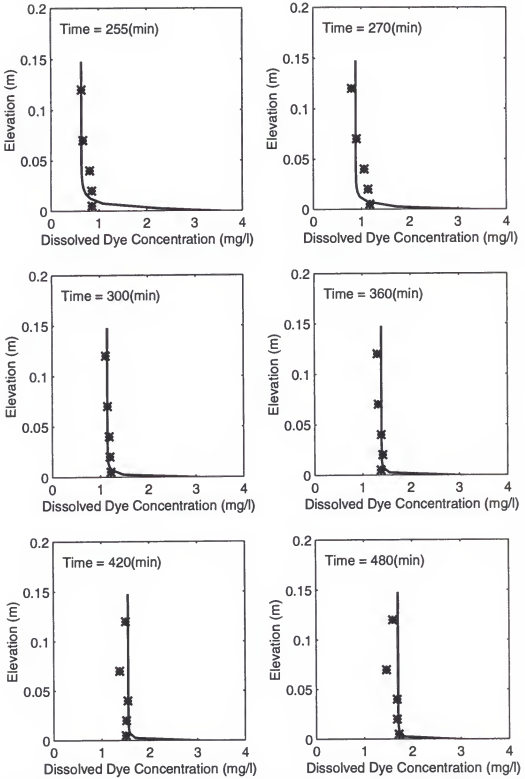

Figure B.23 Comparison between simulated and measured dye profiles in Test 5-2 during time range of 240 ~ 480 min. Solid line represents model simulation results and asterisks are measured data.

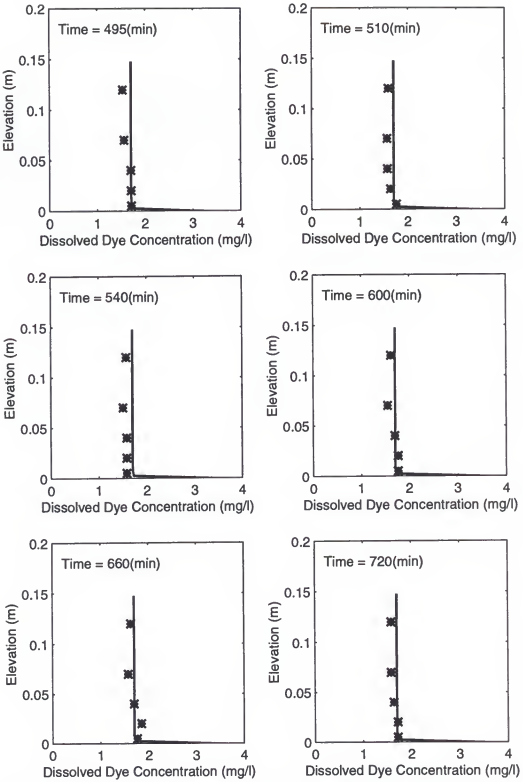

Figure B.24 Comparison between simulated and measured dye profiles in Test 5-3 during time range of 480 ~ 720 min. Solid line represents model simulation results and asterisks are measured data.

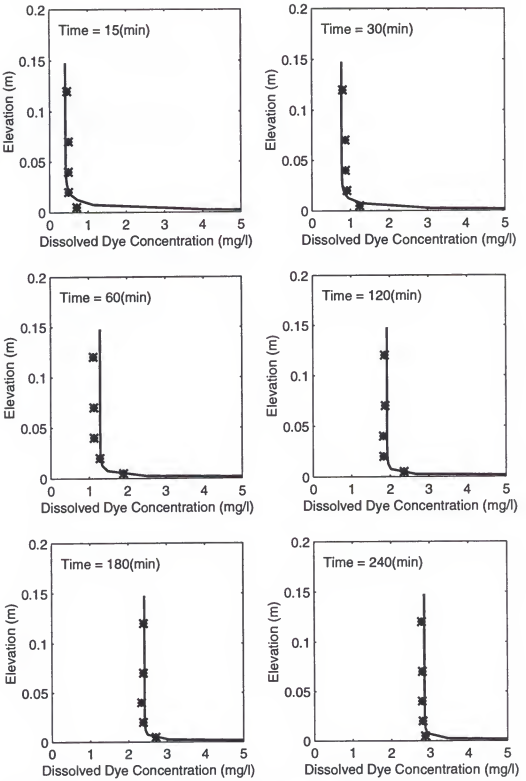

Figure B.25 Comparison between simulated and measured dye profiles in Test 6-1 during time range of 0 ~ 240 min. Solid line represents model simulation results and asterisks are measured data.

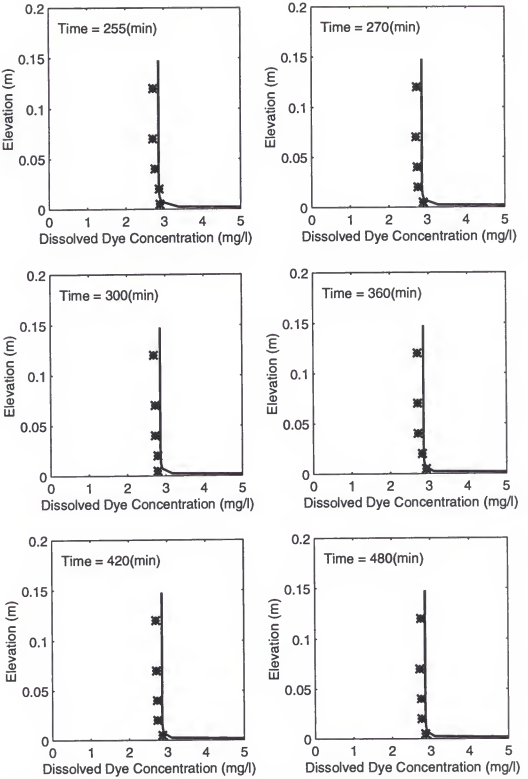

Figure B.26 Comparison between simulated and measured dye profiles in Test 6-2 during time range of 240 ~ 480 min. Solid line represents model simulation results and asterisks are measured data.

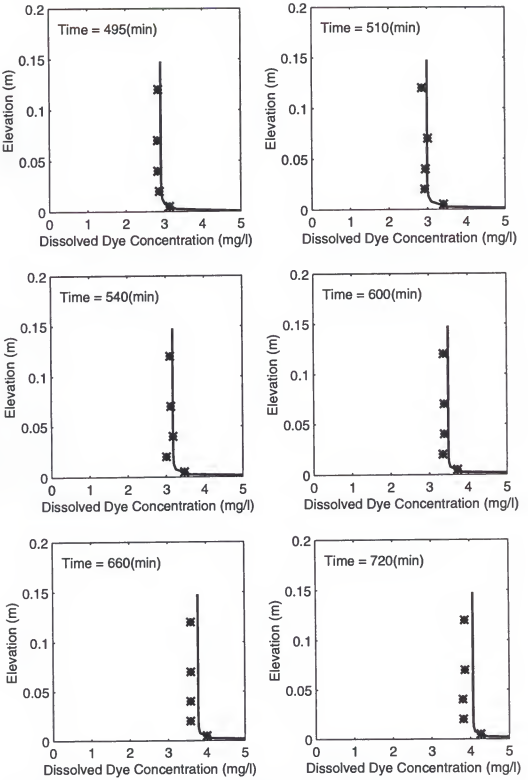

Figure B.27 Comparison between simulated and measured dye profiles in Test 6-3 during time range of 480 ~ 720 min. Solid line represents model simulation results and asterisks are measured data.

BIBLIOGRAPHY

Ambrose R.A., Woll T.A., Martin J.L., 1993. The Water Quality Analysis Simulation Program, WASP5, Part A: Model Documentation. Environmental Research Laboratory, Athen, GA. 209p.

Anderson, M. P., 1979. Using models to simulate the movement of contaminates through groundwater flow systems. CRC Critical Review in Environmental Control, 9(2), 97-156.

Basmadjian D. and Quan F., 1988. Distribution of chemicals in rivers during contamination and recovery. Journal of Environmental Engineering, 113(6), 1185-1201.

Bear, J., 1972. Dynamics of Fluids in Porous Media, American Elsevier Publishing Company, New York, 764p.

Bedford, K. W., Wai, O., Libicki C. M. and Evra III R. V., 1987. Sediment entrainment and deposition measurements in Long Island Sound. Journal of Hydraulic Engineering, 113(10), 1325-1342.

Berner R.A., 1980. Early Diagenesis: A Theoretical Approach. Princeton University Press, Princeton, NJ, 253p.

Biot, M. A., 1956. Theory of propagation of elastic waves in a fluid-saturated porous solid. I. Low-frequency range. Journal of Acoust. Soc. Am., 28, 168-191.

Bissham, G., Subramanian, V., Ramanathan, A. L. and Van Grieken, R., 1991. Heavy metal distribution in the Godavari River Basin, Environmental Geology and Water Science, 16(3), 117-126.

Boudreau, B. P. and Guinasso, N. L., 1982. The influnce of a diffusive sublayer on accretion, dissolution, and diagenesis at the sea floor. The Dynamic of Environment of the Ocean Floor, Fanning, K. A. And Manheim, F. T. (eds.), Lexington Books, Lexington, MA, 115-146.

Bowman, B. T. and Sans, W. W., 1977. Adsorption of parathion, fenitrothion, methylparathion, aminoparathion, and paraoxon by Na+, Ca+, and Fe3+

montmorillonite suspensions. Soil Science Society of American Journal, 69, 2818-2829.

Burton G.A., 1991. Annual review: assessing the toxicity of freshwater sediments. Environmental Toxicology and Chemistry, 10, 1585-1627.

Bretschneider, C. L. and Reid, R. O., 1954. Modification of wave height due to bottom friction, percolation, and reflection. Technical Memorandum 45, Beach Erosion Board, 1, 36p.

Brownawell, B. J., Flood, R. D. and Wang, X., 1994. The role of seasonal resuspension in contaminant cyccling in Lake Ontario. Great Lakes Research Review, 1(1), 29-36.

Burkholder, H. C., 1976. Method and data for predicting nuclide migration in geologic media. In: Proceedings of International Symposium on Management of Wastes from the LWR Fuel Cycle, Denver, Colorado, 11-16 July, 658-666.

Butman, B., 1994. Contaminant transport in massachusetts bay. Public Issues in Energy and Marine Geology, U.S. Geological Survey, Branch of Atlantic Marine Geology, Woods Hole, MA, 4p.

Carpenter, S. H., Thompson, L. J. and Bryant, W. R., 1973. Viscoelastic properties of marine sediments. Proceedings of 5th Offshore Technology Conference, Houston, 777-788.

Chen, X. J., 1994. Effects of Hydrodynamics and Sediment Transport Processes on Nutrient Dynamics in Shallow Lakes and Estuaries. Ph.D. Dissertation, University of Florida, Gainesville, 256p.

Cho, C. M., 1971. Convective transport of ammonium with nitrification in soil. Canadian Journal of Soil Science, 51, 339-350.

Chou, H. T., 1989. Rheological response of cohesive sediments to water waves. Ph.D. Dissertation, University of Califonia, Berkeley, 149p.

Costa, R. C. F., 1989. Flow-Fine Sediment Hysteresis in Sediment-Stratified Coastal Waters. Report UFL/COEL-89/011, Coastal and Oceanographic Engineering Department, University of Florida, Gainesville, 172p.

Dalrymple, R. A. and Liu, P. L.-F., 1978. Wave over soft muds, a two layer fluid mud model. Journal of Physical Oceanography, 8, 1121-1131.

Das, B. M., 1983. Fundamentals of Soil Dynamics. Elsevier, New York, 185-210.

Davison, J .M., Rieck, C.E. and Santelmann, P.W., 1968. Influence of water flux and porous material on the movement of selected herbicides. Soil Science Society of American Proceedings, 32, 629-633.

Dawson, T. H., 1978. Wave propagation over a deformable sea floor. Ocean Engineering, 5, 227-234.

Dean, R. G. and Dalrymple, R. A., 1991. Water Wave Mechanics for Engineers and Scientists, World Scientific Publishing Co., Englewood Cliffs, NJ, 353p.

DePinto J.V., 1994. Role of mass balance modeling in research and management of toxic chemicals in the Great Lakes: the Green Bay mass balance study. Great Lakes Research Review, 1(1), 1-8.

DePinto, J. V., Theis, T. L., Young, T. C. and Leach, S. T., 1994. Predicting Metals Partitioning During Resuspension Events. In: Transport and Transformation of Contaminants Near the Sediment-Water Interface, J.V. DePinto, W. Lick, and J.F., Paul (eds.), Lewis Publisher, Boca Raton, 177-204.

de Wit, P. J., 1994a. Liquefaction and erosion of mud due to waves and current--Experiments on china clay. Report 10-92, Department of Civil Engineering, Delft University of Technology, Delft, The Netherlands, 126p.

de Wit, P. J., 1994b. Liquefaction and erosion of mud due to waves and current--Experiments on Westwald clay. Report 2-93, Department of Civil Engineering, Delft University of Technology, Delft, The Netherlands, 103p.

Dean, R. G. and Dalrymple, R.A., 1991. Water Wave Mechanics for Engineers and Scientists. World Scientific, Singapore. 353p.

Di Toro, D. M., Mahony, J. D., Hansen, D. J., Scott, K. J., Hinks, M. B., Mayr, S. M. and Redmond, M. S., 1989. Toxicity of cadmium in sediments: The role of acid volatile sulfide. Environmental Toxicology and Chemistry, 9, 1487-1502.

Dyer K. R., 1986. Coastal and Estuarine Sediment Dynamics, Wiley, New York, 357p.

Eadie B.J. and Robbins J.A., 1987. The role of particulate matter in the movement of contaminants in the Great Lakes. In: Sources and Fate of Aquatic Pollutants, R.A. Hites and S.J. Eisenreich (ed), American Chemical Society, Washington, DC, 319-364.

Enfield, C. G. and Bledsoe, B. E., 1975. Fate of wastewater phosphorous in soil. Journal of Irrigation and Drainage Division, ASCE, 101(IR3), 145-155.

Enfield, C. G., Harlin, C. C. and Bledsoe, B. E., 1976. Comparison of five kinetic mpdels for orthophosphate reactions in mineral soils. Soil Science Society of American Journal, 40, 243-249.

Engelund, F. and Wan, Z.-H., 1984. Instability of hyperconcentrated flow. Journal of Hydraulic Engineering, 110(3), 219-232.

Faas, R. W., 1995. Mudbanks of the southwest coast of India. III: Role of non-Newtonian flow properties in the generation and maintenance of mudbanks. Journal of Coastal Research, 11(3), 911-917.

Faust, C. R. and Mercer, J. W., 1980. Groung-water modeling recent developements. Ground Water, 15(5), 365-371.

Feng, J., 1992. Laboratory experiments on cohesive soil bed fluidization by water waves. M.S. Thesis, University of Florida, Gainesville, 109p.

Fertis, D. G., 1973. Dynamics and Vibration of Structure, A Wiley Interscience Publication, Jonh Wiley & Sons.

Fick, A, 1955. Über diffusion. Poggendorff's Annalen der Physik, 95, 59-86.

Fiskell, J. G. A., Mansell, R. S., Selim, H. M. and Martin, F. G., 1979. Kinetic behavior or phosphate sorption by acid, sandy soil. Journal of Environmental Quality, 8, 579-584.

Fitter, A. H. and Sutton, C. D., 1975. The use of the Freundlich isotherm for soil phosphate sorption data. Journal of Soil Science, 26, 241-246.

Foda, M. A., 1989. Sideband damping of water waves over a soft bed. Journal of Fluid Mechanics, 201, 189-201.

Foda, M. A., Tzang S. Y. and Chou, H. T., 1993. A non-linear model for the fluidization of marine mud by wave. Journal of Geophysical Research, 98, 7039-7047.

Freeze, R. A. and Chery, J. A., 1979. Groundwater, Prentice Hall, Englewood Cliffs, NJ, 604p.

French, R. H., 1979. Interfacial stability in channel flow. Journal of the Hydraulics Division, ASCE, 105(8), 955-979.

French, R. H. and McCutcheon, S. C., 1983. Vertical momentum transfer in continuously stratified channel flow. Water Resources Center, Desert Research Institute, Las Vegas, Nevada, 39p.

Gade, H. G., 1957. Effects of a non-rigid, impermeable bottom on plane surface waves in shallow water. M.S. Thesis, Texas A & M University, College Station, 35p.

Gade, H. G., 1958. Effects of a nonrigid impermeable bottom on plane surface wave in shallow water. Journal of Marine Research, 16, 61-82.

Garcia-Miragaya, J. and Page, A. L., 1976. Influence of ionic strength and inorganic complex formation on the sorption of trace amounts od Cd by montmorillonite. Soil Science Society of America Proceedings, 40, 658-663.

Glasstone, S., 1962. Physical Chemistry. Macmillan, London, 1320p.

Grant, W. D. and Madsen, O. S., 1979. Combined wave and current interaction with a rough bottom. Journal of Geophysical Research, 17(4), 303-313.

Grim, R. E., 1968. Clay Mineralogy. Mcgraw-Hill, Inc., New York, 596p.

Grissinger, E. H., 1966. Resistance of selected clay systems to erosion by water. Water Resources Research, 2(1), 131-138.

Gupta, S. P. and Greenkorn, R. A., 1973. Dispersion during flow in porous media with bilinear assorption. Water Resources Research, 9, 1357-1368.

Hachiya, K., Sasaki, M., Ikeda, T., Mikami, N. and Yasunaga, T., 1984. Static and kinetic studies of adsorption-desorption of metal ions on a γ-Al_2O_3 surface. 2. Kinetic study by means of pressure-jump technique. Journal of Physical Chemistry, 88, 27-31.

Harrison, W. D. and Osterkamp, T. E., 1978. Heat and mass transport processes in subsea permafrost, 1, an analysis of molecular diffusion and its consequences. Journal of Geophysical Reserch, 83(C9), 4707-4712.

Hart, B. T., and Davies, S. H. R., 1981. Trace metal speciation in three Victorian lakes. Australian Journal of Marine and Freshwater Research, 32, 175-189.

Harter, R. D., 1968. Adsorption of phosphorous by lake sediment. Soil Science Society of America Proceedings, 32, 679-683.

Harter, R. D., 1979. Adsorption of copper and lead by Ap and B2 horizons of several northeastern United States soils. Soil Science Society of American Journal, 43, 679-683.

Hayes, K. F. and Leckie, J. O., 1986. Mechanism of lead ion adsorption at the goethite-water interface. In: Geochemical Processes at Mineral Surfaces, J.A. Davis (ed.), American Chemical Society, Washington DC, 683-690.

Hayes, K. F. and Leckie, J. O., 1987. Modeling ionic strength effects on cation adsorption at hydrous oxide/solution interfaces. Journal of Colloid and Interfacial Science, 115, 564-572

Hayter E.J. and Pakala C.V., 1989. Transport of inorganic contaminants in estuarial waters. Journal of Coastal Research, SI5, 217-230.

Hinze, J. O., 1959. Turbulence. McGraw-Hill Book Company, Inc., New York, 595p.

Holzman, B., 1943. The influence of stability on evaporation. Boundary Layer Problem in the Atmosphere and Ocean, W. G. Valentine, ed., New York Academic of Sciences, New York, Vol.144, 13-18.

Homma, M. and Horikawa, K., 1962. Suspended sediment due to wave action. Proceedings of the 8th Conference of Coastal Engineering, Mexico City.

Homma, M., Horikawa, K. and Kajima, R., 1965. A study of suspended sediment due to wave action. Coastal Engineering in Japan, 8.

Hornsby, A. G. and Davison, J. M., 1973. Solution and adsorbed fluometuron concentration distribution in a water-saturated soil: experimental and predicted evaluation. Soil Science Society of American Proceedings, 37, 823-828.

Hsiao, S. V. and Shemdin, O. H., 1980. Interaction of ocean waves with a soft bottom. Journal of Physical Oceanography, 10, 605-610.

Huber, W. C. and Dickinson R. E., 1991. Modeling of phosphorus dynamics in Lake Okeechobee, Florida, in UDT'91, C. Maksimovic (ed), Elsevier Applied Science, 203-216.

Hwang K.-N., 1989. Erodibility of fine sediment in wave-dominated environments. M.S. Thesis, University of Florida, Gainesville, FL, 159p.

Hwang P. A. and Wang H., 1982. Wave kinematics and sediment suspension at wave breaking point. Technical Report No. 13, Department of Civil Engineering, University of Delaware, Newwark, DE, 173p.

Ippen, A. T. and Harleman, D. R. F., 1951. Steady State Characteristics of Subsurface Flow. Proceedings of Natural Bureau Standards Semicentennial Symposium on Gravity Waves, 79-93

Isobe, M., Huyuh T. N. and Watanabe, A., 1992. A study on mud mass transport under waves based on an empirical rheology model. Proceedings of the 23rd International Conference on Coastal Engineering, 3, ASCE, New York, 3093-3106.

James, A. E., Williams D. J. A. and Williams P. R., 1988. Small strain, low shear rate rheometry of cohesive sediments. In: Physical Processes in Estuaries, J. Dronkers and W. van Leussen (eds.), Springer-Verlag, Berlin, 488-500.

Jarrell, W. M. and Dowson, M. D., 1978. Sorption and availability of molybdenum in soils of western Oregon. Soil Science Society of America Journal, 42, 412-415.

Jiang, F., 1993. Bottom mud transport due to water waves. Ph.D. Dissertation, University of Florida, Gainesville, 222p.

Jiang, F. and Mehta, A. J., 1995. Mudbanks of the southwest coast of India. IV: Mud viscoelastic properties. Journal of Coastal Research, 11(3), 918-926.

Jiang, F. and Mehta, A. J., 1996. Mudbanks of the southwest coast of India. V: Wave attenuation. Journal of Coastal Research (accepted for publication).

Jiang, L., Kioka, W. and Ishida, A., 1990. Viscous damping of cnoidal waves over fluid-mud seabed. Journal of Waterway, Port, Coastal, and Ocean Engineering, 116(4), 470-491.

Jiang, L. and Zhao, Z., 1989. Viscous damping of solitary waves over fluid-mud seabeds. Journal of Waterway, Port, Coastal, and Ocean Engineering, 115(3), 345-362.

Josson, I. G., 1966. Wave boundary layer and friction factors. Proceedings of the 10th Coastal Engineering Conference, ASCE, Vol. 1, pp 127-148.

Kamphuis, J. W., 1975. Friction factor under oscillatory waves. Journal of Waterways, Harbors and Coastal Engineering Division, ASCE, 101, 135-144.

Karickhoff, S. W., 1980. Sorption kinetics of hydrophobic pollutants in natural sediments. In: Contaminants and Sediments, R.A. Baker (ed.), Butterworths, Stoneham, MA, 193-205.

Kato, H. and Phillips, O. M., 1969. On the penetration of a turbulent layer into a stratified fluid. Journal of Fluid Mechanics, 37, 753-768.

Keedwell, M. J., 1984. Rheology and Soil Mechanics, Elsevier, London, 339p.

Kelly, W. E. and Gularte, R. C., 1981. Erosion resistence of cohesive soils. Journal of Hydraulic Division, ASCE, 107(10), 1211-1224.

Kemp, G. P., 1986. Mud Deposition at the Shore Surface: Wave and Sediment Dynamics on the Chenier plain of Louisiana. Ph.D. Dissertation, Louisiana State University, 159p.

Kemp, G. P. and Wells, 1987. Observations of shallow-water waves over a fluid mud bottom: implications to sediment transport. Proceedings of Coastal Sediments'87, Vol. 1, ASCE, New York, 363-377.

Keulegun, G. H., 1949. Intrenal Instability and Mixing in Stratified Flows. Journal of Research of National Burreau of Standands, 43, 487-500.

Kirby, R., 1986. Suspended fine cohesive sediment in the Severn estuary and Inner Bristol channel, U.K.. Report ETSU-STP-4042, Department of Atomic Energy, Harwell, United Kingdom, 243p.

Kirby, R., Hobbs, C. H., and Mehta, A. J., 1989. Fine sediment regime of Lake Okeechobee, Florida. Report UFL/COEL-89/009, Coastal and Oceanographic Engineering Department, University of Florida, Gainesville, 77p.

Kirby, R., Hobbs, C. H., and Mehta, A. J., 1994. Shallow Stratigraphy of Lake Okeechobee, Florida: a preliminary reconnaissance. Journal of Coastal Research, 10(2), 339-350.

Kirby, R. and Parker, W. R., 1977. The physical characteristics and environmental significance of fine sediment suspensions in estuaries. Estuaries, Geophysics and the Environment, National Research Council, NAS, USA, Studies in Geophysics, 110-120.

Kranenburg, C., 1994. An entrainment model for fluid mud. Report 93-10, Communications on Hydraulic and Geotechnical Engineering, Civil Engineering Department, Delft University of Technology, The Netherlands, 10p.

Krone, R. B., 1962. Flume studies of the transport of sediment in estuarial shoaling process. Final Report, Hydraulic Engineering Laboratory and Sanitary Engineering Research Laboratory, University of Califonia, Berkeley, Califonia, 110p.

Krumbein, W. C. and Monk, G. D., 1942. Permeability as a function of size parameters of unconsolidated sand. Technical Publications, 1492, American Institute of Minerals and Metallurigic Engineering, New York, 1-11.

Kuo, S. and Lotse, E. G., 1974. Kinetics of phosphate adsorption by calcium carbonate and Ca-kaolinite. Soil Science Society of American Proceedings, 38, 50-54.

Kynch, G. J., 1952. A Theory of sedimentation. Transactions of the Faraday Society, 48, 166-176.

Lai, S. and Jurinak, J. J., 1972. Cation adsorption in one-dimensional flow through soils: a numerical solution. Water Resources Research, 8, 99-107.

Lai, S., Jurinak, J. J., and Wagenet, R. J., 1978. Multicomponent cation adsorption during convective-dispersive flow through soils: experimental study. Soil Science Society of America Journal, 42, 240-243.

Lapidus, L. and Amundson, N. R., 1952. Mathematics of adsorption in beds. VI. The effect of longitudinal diffusion in ion exchange and chromatographic columns. Journal of Physical Chemistry, 56, 984-988.

Le Hir, P., 1994. Fluid and sediment "integrated" modeling application to fluid mud flows in estuaries. 4th Nearshore and Estuarine Cohesive Sediment Transport Conference, INTERCOH'94, Wallingford, England, 12p.

Leistra, M. and Dekkers, W. A., 1977. Some models for the adsorption kinetics of pesticides in soils. Journal of Environmental Science Health, B12, 85-103.

Li, Y., 1986. Experiment studies on tansport and settling properties of cohesive sediment. M. S. Thesis, Hohai University, Nanjing, China. 120p (in Chinese with English abstract).

Li, Y., Feng J. and Mehta A. J., 1994. Mud fluidization by water waves. 4th Nearshore and Estuarine Cohesive Sediment Transport Conference, INTERCOH'94, Wallingford, England, 18p.

Li, Y.-H. and Gregory, S., 1974. Diffusion of ions in sea water and in the deepsea sediments. Geochim. et Cosmochim. Acta, 38, 703-714.

Lindenberg, J., van Rijn, L. C., and Winterwerp, J. C., 1989. Some experiments on wave-induced liquefaction of soft cohesive soils. Journal of Coastal Research, SI5, 127-137.

Liu, K. F. and Mei, C. C., 1989. Effects of wave-induced friction on a muddy seabed modelled as a Bingham-plastic fluid. Journal of Coastal Research, 5(4), 777-789.

Long, E. R., Wolfe, D., Carr, R. S., Scott, K. J., Thursby, G. B., Windom, H. L., Lee, R., Calder, F. D., Sloane, G. M. and Seal, T., 1994. Magnitude and extent of sediment toxicity in Tampa Bay, Florida. NOAA Technical Memorandum NOS ORCA 78, Nation Status and Trends Program, NOAA, Silver Springs, Maryland, 198p.

Maa, P.-Y., 1986. Erosion of soft mud by waves. Ph.D. Dissertation, University of Florida, Gainesville, 296p.

Maa, P.-Y. and Mehta, A. J., 1987. Mud erosion by waves: a laboratory study. Continental Shelf Research, 7(11/12), 1267-1268.

MacPherson, H., 1980. The attenuation of water waves over a non-rigid bed. Journal of Fluid Mechanics, 97(4), 721-742.

Madsen, O. S., 1974. Stability of a sand bed under breaking waves. Proceedings of 14th Coastal Engineering Conference, ASCE, New York, 2, 777-794.

Mallard, W. W. and Dalrymple, R. A., 1977. Water waves propagating over a deformable bottom. Proceedings of the Offshore Technology Conference, OTC 2895, Houston, 141-146.

Malvern, L. E., 1969. Introduction to the Mechanics of a Continuous Medium. Prentice-Hall, Englewood Cliffs, NJ, 731p.

Manheim, F., 1994. The Legacy of contaminanted sediments in Boston Harbor. Public Issues in Energy and Marine Geology, U.S. Geological Survey, Branch of Atlantic Marine Geology, Woods Hole, MA, 4p.

MacPherson, H., 1980. The attenuation of water waves over a non-rigid bed. Journal of Fluid Mechanics, 97(4), 721-742.

Mathew, J., 1992. Wave-mud interaction in mudbanks. Ph.D. Dissertation, Cochin University of Science and Technology, Cochin, Kerala, India, 139p.

Mathew, J. Baba, M. and Kurian, N. P., 1995. Mudbanks of the southwest coast of india. I: Wave characteristics. Journal of Coastal Research, 11(1), 168-178.

Mathew, J. Baba, M. and Kurian, N. P., 1995. Mudbanks of the southwest coast of india. II: Wave-mud interactions. Journal of Coastal Research, 11(1), 179-187.

McDuff, R. E. and Ellis, R. A., 1979. Determining diffusion coefficients in marine sediments: a Laboratory study of the validity of resistivity techniques. Journal of America of Science, 279, 666-675.

Mehta, A. J., 1986. Characterization of cohesive sediment properties and transport processes in estuaries. Esturine Cohesive Sediment Dynamics, A. J. Mehta, (ed.), Springer-Verlag, Berlin, 290-325.

Mehta, A.J., 1988. Laboratory studies on cohesive sediment deposition and erosion. Physical Processes in Estuaries, J.Dronkers and W. Van Leussen, (eds.), Springer-Verlag, Berlin, 427-445.

Mehta, A. J., 1989. On estuarine cohesive sediment suspension behavior. Journal of Geopgysical Research, 94(C4), 14303-14314.

Mehta, A. J., 1991. Understanding fluid mud in a dynamic environment. Geo-Marine Letters, 11(3/4), 113-118.

Mehta, A. J. and Jiang, F., 1990. Some observations on bottom mud motion due to waves. Report UFL/COEL-90/008, Coastal and Oceanographic Engineering Department, University of Florida, Gainesville, 85p.

Mehta, A. J. and Jiang, F., 1993. Some observations on water wave attenuation over nearshore underwater mudbank and mud berm. Report UFL/COEL/MP-93/01, Coastal and Oceanographic Engineering Department, University of Florida, Gainesville, 45p.

Mehta, A. J., Lee, S. C. and Li, Y., 1994. Fluid mud and water waves, A brief review of interactive processes and simple modeling approaches. Report UFL/COEL/MP-94/01, Coastal and Oceanographic Engineering Department, University of Florida, Gainesville, 87p.

Mehta, A. J. and Lott, J. W., 1987. Sorting of fine sediment during deposition. Coastal Sediment '87, Special Conference on Advances in Understanding of Coastal Sediment Process, Nicholas Kraus, (ed.), ASCE, New York, 348-362.

Mehta, A. J. and Maa, P. Y., 1986. Wave over mud: modeling erosion. Proceedings of 3rd International Symposium on River Sedimentation, University of Mississippi, University, MS, 588-601.

Mehta, A. J., Partheniade,s E., Dixit, J. G. and Mcanally W. H., 1982. Properties of deposited kaolinite in a long flume. Proceedings of the Conference on Applying Research to Hydraulic Practice, ASCE, New York, 594-603.

Mehta, A. J. and Srinivas R., 1993. Observations on the entrainment of fluid mud by shear flow. Nearshore and Estuarine Cohesive Sediment Transport, A.J. Mehta (ed.), American Geophysical Union, Washington, DC, 224-246.

Mehta, A. J., Williams D. J. A, Williams, P .R. and Feng, J., 1995. Tracking dynamical changes in mud bed due to waves. Journal of Hydraulic Engineering, 121(6), 504-506.

Mehta A.J. and Jiang F., 1992. Some observations on water wave attenuation over Nearshore underwater mudbanks and mud berms. Report UFL/COEL/MP-91/01, Coastal and Oceanographic Engineering Department, University of Florida, Gainesville, FL, 45p.

Mei, C. C. and Liu, K. F., 1987. A Bingham plastic model for muddy sea bed under long waves. Journal of Geophysical Research, 92(C13), 14581-14594.

Mimura, N., 1993. Rates of erosion and deposition of cohesive sediments under wave action. Nearshore and Estuarine Cohesive Sediment Transport, A.J. Mehta (ed), American geophysical Union, Washington, DC, 247-264.

Moore, M. J. and Long, R. R., 1971. An experimental investigation of turbulent stratified shearing flow. Journal of Fluid Mechanics, 10, 496-508.

Munk W. H. and Anderson E. R., 1948. Notes on a theory of the thermocline. Journal of Marine Research, 1, 276-295.

Nathwani, J. S. and Phillips, C. R., 1977. Adsorption-desorption of selected hydrocarbons in crude oil in soils. Chemosphere, 4, 157-162.

Nelsen, J. E., 1972. Vertical turbulent mixing in stratified flow--A comparision of previous experiments. Report No. WHM-3, Hydraulic Engineering Laboratory, University of Califonia, Berkeley, 98p.

Novak, L. T., 1977. A method for the study of interphase mass transfer at very low Reynolds numbers in packed beds. Journal of AIChE, 23, 398-400.

Novak, L. T. and Petschauer, F. J., 1979. Kinetics of the reaction between orthophosphate ions and muskegon dune sand. Journal of Environmental Quality, 8, 312-318.

Nriagu, J. O., Wong, H. K. T. and Snodgrass, W. J., 1983. Historical records of metal pollution in sediments of Toronto and Hamilton Harbours. Journal of Great Lakes Research, 9(3), 365-373.

O'Connor D.J., 1988a. Models of sorptive toxic substances in freshwater systems. I: basic equations. Journal of Environmental Engineering, 114(3), 507-532.

O'Connor D.J., 1988b. Models of sorptive toxic substances in freshwater systems. II: lakes and reservoirs. Journal of Environmental Engineering, 114(3), 533-551.

O'Connor D.J., 1988c. Models of sorptive toxic substances in freshwater systems. III: streams and rivers. Journal of Environmental Engineering, 114(3), 552-574.

Oddson, J. K., Letey, J. and Weeks, L. V., 1970. Predicted distribution of organic chemicals in solution and adsorbed as a function of position and time for various chemical and soil properties. Soil Science Society of American Proceedings, 34, 412-417.

Onish, Y., 1981. Sediment-contaminant transport model. Journal of Hydraulics Engineering, 107(9), 1089-1107.

Overman, A. L., Chu, R. L. and Leseman, W. G., 1976. Phosphorous transport in a packed bed reactor. Journal of Water Pollute Control Fed., 48, 880-888.

Partheniades, E., 1965. Unified view of wash load and bed material load. Journal of Hydraulic Engineering, 103(9), 1037-1057.

Parker, W. R. and Kirby, R., 1982. Time dependent properties of cohesive sediment deposits. Journal of Hydraulic Engineering, 111(10), 1308-1326.

Parchure, T. M. and Mehta, A. J., 1985. Erosion of soft cohesive sediment deposits. Journal of Hydraulic Engineering, 111(10), 1308-1326.

Perkins, T. K. and Johnson, O. C., 1963. A review of diffusion and dispersion in porous media. Society of Petroleum Engineers Journal 3, 70-84.

Petrie, C. J. S., 1978. Elongational Flows, Pitman, London, 254p.

Reible, D.D and Savant-Malhiet, S.A., 1993. Comparison of physical transport processes in noncohesive river sediments. Journal of Environmental Engineering, 119(1), 90-102.

Ren, R. S. and Zheng, X. C., 1985. Experiment Studies on settling velocity and rheological properties of cohesive sediment from changjiang estuary. Scientific Information of Hohai University, 11, (in Chinese), 10-18.

Richardson, J. F. and Zaki, W. N., 1954. The sedimenttation of a suspension of uniform spheres under conditions of viscous flow. Chemical Engineering Science, 3, 65-72.

Roberts, M., 1993. Development of a mathematical model of fluid mud in the coastal zone. Proceeding of the Institution of Civil Engineers, Water, Maritime and Energy, 101, 173-181.

Ross, M. A., 1988. Vertical structure of estuarine fine sediment suspensions. Ph.D Dissertation, University of Florida, Gainesville, 206p.

Rossby, C. G. and Montgomery, R. B., 1935. The layer of friction influence in wind and ocean currents. Physical Oceanography and Meteorology, 3(3), 1-17.

Sakakiyama, T. and Bijker, E. W., 1989. Mass transport velocity in mud layer due to progressive waves. Journal of Waterway, Port, Coastal, and Ocean Engineering, 115(5), 614-633.

Sanford, L. P. and Halka, J. P., 1993. Assessing the paradigm of mutually exclusive erosion and deposition of mud, with examples from upper Chesapeake Bay. Marine Geology, 114, 37-57.

Scarlatos, P. D. and Mehta, A. J., 1993. Some observations on erosion and entrainment of estuarine fluid muds. Residual Currents and Long-term Transport, R.T. Cheng (ed.), Springer-Verlag, New York, 321-332.

Scarlatos, P. D. and Mehta, A. J., 1993. Instability and entrainment mechanisms at the stratified fluid mud-water interface. Nearshore and Estuarine Cohesive Sediment Transport, A.J. Mehta (ed.), American Geophysical Union, Washington, DC, 205-223.

Scott, H. D. and Phillips, R. E., 1972. Diffusion of selected herbicides in soil. Soil Science Society of America Journal, 36, 714-719.

Selim, H. M, Davidson, J. M. and Rao, P. S. C., 1977. Transport of reactive solutes through multilayered soils. Soil Science Society of America Journal, 41, 3-10.

Selly, R. C., 1988. Applied Sedimentology, Academic Press, London, 446p.

Shah, D. B., Coulman, G. A., Novak, L. T. and Ellis, B. G., 1975. A mathematical model for phosphorus movement in soils. Journal of Environmental Quality, 4, 87-92.

Shaikh, A., Ruff, J. F., and Abt, S. R., 1988. Erosion rate of compacted Na-montmorillonite soils. Journal of Geotechnical Engineering, 114(3), 296-305.

Sheng, Y. P., 1986. Modeling bottom boundary layer and cohesive sediment dynamics in estuarine and coastal waters. Estuarine Cohesive Sediment Dynamics, A. J. Mehta, (ed.), Springer-Verlag, Berlin, 360-400.

Sheng, Y. P., 1986. Hydrodynamics, sediment transport and their effects on phosphorus dynamics in Lake Okeechobee. Nearshore and Estuarine Cohesive Sediment Transport, A. J. Mehta, (ed.), 558-571.

Shibayama, T., Aoki, T. and Sato S., 1989. Mud mass transport rate due to waves: a viscoelastic model. Proceedings of the 23rd IAHR Congress, Ottawa, Canada, B567-B574.

Shibayama, T., Okuno, M. and Sato S., 1990. Mud transport in mud layer due to wave action. Proceedings of the 22nd Coastal Engineering Conference, ASCE, New York, 3, 3037-3049.

Shibayama, T., Takikawa, H. and Horikawa, K., 1986. Mud mass transport due to waves. Coastal Engineering in Japan, 29, 151-161.

Shukla, U. C. and Mittal, S. B., 1979. Characterization of Zinc adsorption in some soils of India. Soil Science Society of America Journal, 42, 878-882.

Sidle, R. C., Kardos, L. T. and van Genuchten, 1977. Heavy metals transport model in a sludge-treated soil. Journal of Environmental Quality, 6, 438-443.

Singh, B. and Sekhon, G. S., 1977a. Adsorption, desorption and solubility relationships of lead and cadmium in some alkaline soils. Journal of Soil Science, 28, 271-275.

Singh, B. and Sekhon, G. S., 1977b. The effect of soil properties on adsorption and desorption of zinc by alkaline soils. Soil Science, 124, 366-369.

Sisko, A. W., 1958. The flow of lubricating greases. Industrial Engineering Chem., 50, 1789-1792.

Srinivasan, P. and Mercer, J. W., 1988. Simulation of biodegradation and sorption processes in ground water. Ground Water, 26(2), 192-198.

Street, J. J., Lindsay, W. L. and Sabey, B. R., 1977. Solubility and plant uptake of cadimium in soils amended with cadimium and sewage sludge. Journal of Environmental Quality, 6, 72-77.

Suhayda, J. N., 1986. Interaction between surface waves and muddy bottom sediments. In: Estuarine Cohesive Sediment Dynamics, A. J. Mehta, ed., Springer-Verlag, Berlin, 401-428.

Taki, K., 1990. Hydraulic study on the rate of resuspension of mud due to free surface water flow. Ph. D. Thesis, Chuo University, Tokyo, 180p (in Japanese).

Theis, T. L., Young, T. C., and DePinto, J. V., 1988. Factors affect metal partitioning during resuspension of sediments from the Detroit River. Journal of Great Lakes Research, 14, 216-226.

Theis, T. L, Iyer, R. and Kaul, L. W., 1988. Kinetic studies of cadmium adsorption on geothite. Environmental Science Technology, 18, 43-48.

Thimakorn P., 1983. Resuspension of clays under waves. Seabed Mechanics, B. Denness (ed), Graham & Trotman, London, 191-196.

Tsuruya, H, Nakano, S. and Takahama, J., 1987. Interaction between surface waves and a multi-layered mud bed. Report of the Port and Harbor Research Institute, Ministry of Transport, Japan, 26(5), 137-173.

Tubman, M. and Suhayda, J. N., 1976. Wave action and bottom movements in fine sediments. Proceedings of the 15th International Coastal Engineering Conference, ASCE, New York, 1168-1183.

van Bladel, R. and Moreale, A., 1977. Adsorption of herbicide-derived p-chloroaniline residues in soils: a predictive equation. Journal of Soil Science, 28, 93-102.

van De Pol, R. M., Wierenga, P. J. and Nielsen, D. R., 1977. Solute movement in a field soil. Soil Science Society of America Journal, 41, 10-13.

van Olphen, H., 1963. Clay Colloid Chemistry. John Wiley & Sons, Inc., New York, 317p.

Vanoni, V. A., 1975. Sedimentation engineering. Report of Engineering Practice No.54, ASCE, New York, 771p.

Vanderborgh J.P., Wollast R., and Billen G., 1977a. Kinetic models of diagenesis in disturbed sediments. Part 1, Mass transfer properties and silica diagenesis. Limnology and Oceanography, 22(5), 787-793.

Vilker, V. L, 1980. Simulating virus movement in soils. In: Modeling Wastewater Renovation Land Treatment, I.K. Iskander (ed.), Wiley Interscience Publication, John Wiley & Sons, New York.

Vilker, V. L. and Burge, W. D., 1980. Adsorption mass transfer model for virus transport in soils. Water Resources, 14, 783-790.

Welty J.R., Wicks C.E. and Wilson R.E., 1969. Fundamentals of Momentum, Heat and Mass Transfer, John Wiley & Sons, Inc., New York, 712p.

Wells, J. T. and Kemp, G. P., 1986. Interaction of Surface Waves and Cohesive Sediments: Field Observation and Geologic Significance. Estuarine Cohesive Sediment Dynamics, A. J. Mehta (ed.), Springer-Verlag, New York, 43-65.

White, R. E. and Taylor, A. W., 1977. Reactions of soluble phosphate with acid soils: the interpretation of adsorption-desorption isotherms. Journal of Soil Science, 28, 314-328.

Wilkinson, W. L., 1960. Non-Newtonian Fluid: Fluid Mechanics, Mixing and Heat Transfer, Pergamon Press, New York, 152p.

Williams, D. J. A. and Williams, P. R., 1992. Laboratory experiments on cohesive soil bed fluidization by water waves, Part II: *In-situ* rheometry for determining the dynamic response of bed. Report UFL/COEL-92/015, Coastal and Oceanographic Engineering Department, University of Florida, Gainesville, FL, 28p.

Winterwerp, J. C., 1994. On the erosion of fluid mud layers by entrainment. 4th Nearshore and Estuarine Cohesive Sediment Transport Conference, INTERCOH'94, Wallingford, England, 11p.

Wolanski, E. J., Chappell, P. R. and Bertessy, R., 1988. Fluidization of mud in estuaries. Journal of Geophysical Research, 93(C3), 2351-2361.

Wolanski E., Gibbs R. J., Mazda Y., Mehta A. J. and King B., 1992. The role of turbulence in the settling of mud flocs. Journal of Coastal Research, 8(1), 35-46.

Wu, S. C. and Gschwend, P. M., 1986. Sorption Kinetics of hydrophobic organic compounds to natural sediments and soils. Environmental Science Technology, 20, 717-725.

Wu, S. C. and Gschwend, P. M., 1988. Numerical Modeling of sorption kinetics of organic compounds to soil and sediment particles. Water Resources Research, 24(8), 1373-1383.

Xian-Chen, S., Yang, M. S., and Feng, H. H., 1991. Heavy metals in the water and sediments of Guan-Ting Reservior, IAHS Publications, 203, 367-374

Yaron, B., 1978. Some aspects of surface interactions of clays with organophosphorus pesticides. Soil Science, 125, 210-216.

BIOGRAPHICAL SKETCH

Yigong Li (Wally) was born on November 21, 1964, in Nanjing, China. He received his Bachelor of Engineering degree in civil engineering with special emphasis in port and coastal engineering from the Department of Navigation, Waterway and Ocean Engineering at Hohai University, in 1986, and the Master of Engineering degree from the Coastal and Ocean Engineering Research Institute at Hohai University, in 1989. Soon after he got his Master's degree, he began to work as an engineer in the Institute. In 1992, the opportunity for further studies in United States for the Ph.D. degree came through sponsorship by Professor Ashish J. Mehta through a Graduate Research Assistantship. He came to the United States and entered the Graduate School of the University of Florida and the Department of Coastal and Oceanographic Engineering. After nearly four years of study and work, he earned the Doctor of Philosophy degree, and looks forward to contributing his newly acquired knowledge in addressing various engineering and research problems.

I certify that I have read this study and that in my opinion it conforms to acceptable standards of scholarly presentation and is fully adequate, in scope and quality, as a dissertation for the degree of Doctor of Philosophy.

Ashish J. Mehta, Chairman
Professor of Coastal and Oceanographic Engineering

I certify that I have read this study and that in my opinion it conforms to acceptable standards of scholarly presentation and is fully adequate, in scope and quality, as a dissertation for the degree of Doctor of Philosophy.

Robert G. Dean
Graduate Research Professor of Coastal and Oceanographic Engineering

I certify that I have read this study and that in my opinion it conforms to acceptable standards of scholarly presentation and is fully adequate, in scope and quality, as a dissertation for the degree of Doctor of Philosophy.

Y. Peter Sheng
Professor of Coastal and Oceanographic Engineering

I certify that I have read this study and that in my opinion it conforms to acceptable standards of scholarly presentation and is fully adequate, in scope and quality, as a dissertation for the degree of Doctor of Philosophy.

Kirk Hatfield
Associate Professor of Civil Engineering

I certify that I have read this study and that in my opinion it conforms to acceptable standards of scholarly presentation and is fully adequate, in scope and quality, as a thesis for the degree of Doctor of Philosophy.

Brij M. Moudgil
Professor of Materials Science and Engineering

This thesis was submitted to the Graduate Faculty of the College of Engineering and to the Graduate School and was accepted as partial fulfillment of the requirements for the degree of Doctor of Philosophy.

May, 1996

Winfred M. Phillips
Dean, College of Engineering

Karen A. Holbrook
Dean, Graduate School